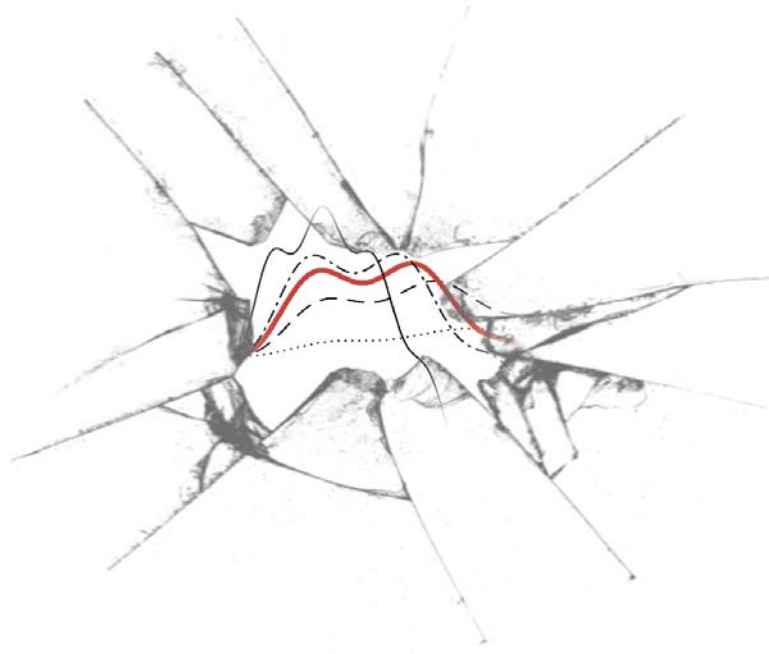




LUND
UNIVERSITY



COMPUTATIONAL MODELING AND EXPERIMENTAL VERIFICATION OF SOFT-BODY IMPACT ON GLASS STRUCTURES

ERNEST BJÖRKLUND
and AXEL CHRISTOFFERSSON

Structural
Mechanics

Master's Dissertation

DEPARTMENT OF CONSTRUCTION SCIENCES
DIVISION OF STRUCTURAL MECHANICS

ISRN LUTVDG/TVSM--20/5246--SE (1-187) | ISSN 0281-6679

MASTER'S DISSERTATION

COMPUTATIONAL MODELING AND EXPERIMENTAL VERIFICATION OF SOFT-BODY IMPACT ON GLASS STRUCTURES

ERNEST BJÖRKLUND and AXEL CHRISTOFFERSSON

Supervisor: Professor **KENT PERSSON**, Division of Structural Mechanics, LTH.
Assistant Supervisors: **LINUS ANDERSSON**, MSc, and Dr **MARCIN KOZLOWSKI**, Division of Structural
Mechanics, LTH, together with **BJÖRN LUNDIN**, MSc, Scanscot Technologies AB .
Examiner: Professor **PER-ERIK AUSTRELL**, Division of Structural Mechanics, LTH.

Copyright © 2020 Division of Structural Mechanics,
Faculty of Engineering LTH, Lund University, Sweden.
Printed by V-husets tryckeri LTH, Lund, Sweden, June 2020 (*PI*).

For information, address:
Division of Structural Mechanics,
Faculty of Engineering LTH, Lund University, Box 118, SE-221 00 Lund, Sweden.
Homepage: www.byggmek.lth.se

Abstract

Glass has become ubiquitous in architecture and structures. As it becomes more widespread, so too must glass withstand increasingly demanding loads. Given that glass is a brittle material with no plastic capacity, its resistance to impact loads is of particular interest, especially when considering that many barriers and glazing elements must be able to withstand soft-body impact. The means for verifying this resistance to soft-body impact is often experimental, such as through European Standard EN 12600, which specifies a test method for impact by pendulum action and subsequent classification of the glass based on its performance. The method is expensive and cumbersome, and only allows for one type of fastener configuration for the glass. Therefore, the purpose of this thesis is to investigate the viability of a numerical method for verifying the resistance of an arbitrary glass panel to soft-body impact.

The numerical study is carried out using the finite element program Abaqus. This consists of high-fidelity models alongside reduced models. The latter are created in an effort to reduce computational costs. To verify the results, the models are compared to data extracted from an extensive experimental campaign carried out at LTH. Both the experimental campaign and the finite element models consider a variety of glass thicknesses, both monolithic and laminated, various interlayer materials, three different fastener configurations, and five different drop heights for the pendulum impactor. For pedagogical reasons, a semi-analytical model of the glass-impactor system is also derived, yielding a damped 2DOF system.

The results of the finite element simulations are in good agreement with their experimental counterparts: the stress maxima deviate by approximately 9% for the high-fidelity models, and 6% for the reduced dynamic models. However, the transient events themselves are not in agreement, which is likely a result of a mismatch in the stiffness-damping interplay, as well as the simplifications made with respect to material modeling. For practical purposes, however, the stress maxima are of greater interest, and these were captured reasonably well. The models were further reduced by implementing equivalent static loads; the results are less accurate, but, as a proof-of-concept, are not fully disqualified, and deserve more research.

The results demonstrated that numerical methods, that is to say finite element modeling, is, indeed, a viable approach for designing glass structures to resist soft-body impact. This creates a foundation for future research in the area, the ultimate result of which will be significant cost-savings for the industry.

Sammanfattning

Glas som byggnadsmaterial blir alltmer vanligt inom industrin och, liksom en regnmätare under skånsk vinter, fortsätter dess användning öka i rask takt. Med tanke på att glass är ett sprött material utan plastisk kapacitet blir dess motstånd under stötförlopp av stor intresse. Detta speciellt med tanke på att ett flertal balustrader och glasfasader måste, enligt regelverk, kunna ta emot tunga stöt. Ofta kontrolleras sådana glaselement m.h.a. standarden SS EN 12600. Denna utformar en testmetod för verifikation mot tung stöt, m.h.a. en impaktor med pendelrörelse, för att sedan kunna klassificera glaset. Metoden är dock dyr och opraktisk i större utsträckning. Vidare tar den endast hänsyn till en typ av infästning. Således finns det ett påtagligt behov av att undersöka lämpligheten av numeriska metoder för att kunna bekräfta ett godtyckligt glaselement mot tung stöt.

Den numeriska studien utförs i finita element programmet Abaqus. Denna består av detaljerade modeller samt reducerade modeller. De senare upprättas i syfte att begränsa beräkningskostnaderna. För att kunna bekräfta resultaten, jämförs spänningarna med data extraherade från en omfattande experimentell undersökning som har utförts vid LTH. Både den experimentella undersökningen och finita elementmodellerna redogör för ett antal olika glastjocklekar, monolitiska såväl som laminerade, olika mellanskiktmaterial, tre olika infästningar, samt fem olika fallhöjder hos pendelimpaktorn. Detta kompletteras med en halvanalytisk studie av systemet, där en 2DOF modell härleds fram och undersöks.

Resultaten påvisar att finita elementsimuleringarna uppnår god överensstämmelse med sina experimentella motparter: de maximala huvudspänningarna avviker ca 9 % hos de detaljerade modellerna, medan avvikelsen ligger på ca 6 % hos de reducerade dynamiska modellerna. Dock är själva utformningen på tidsförloppen felaktiga, vilket anses bero på förenklingar som påverkar samspelet mellan systemets styvhet och dämpning, vidare på förenklingarna hos materialmodellerna. Emellertid är det huvudsakligen de maximala spänningarna som antar störst intresse när det gäller glas och dessa har fångats med god noggrannhet. Modellerna reducerades ytterliga genom att införa statistiskt ekvivalenta laster; resultaten ger sämre överensstämmelse men anses vara godkända som ett första steg inom forskningen.

Resultaten påvisar att numeriska metoder är lämpliga vid dimensionering av glaskonstruktioner mot tung stöt. Detta skapar ett underlag för framtida kostnadsbesparande och praktiskt underlättande dimensioneringsverktyg, utformade för näringslivet.

Preface

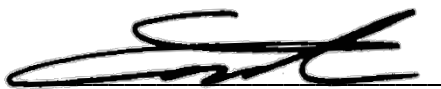
We would like to thank our supervisors, professor Kent Persson and PhD candidate Linus Andersson at the LTH Division of Structural Mechanics; Björn Lundin (MSc) at Scanscot Technology AB; and Marcin Kozłowski (PhD) at the Silesian University of Technology. Without their advice and expertise, the final form of this thesis would have been markedly different.

We are also grateful to Johan Köllfors (MSc), and everyone else at Scanscot, for making our thesis work over the past few months a genuine highlight of recent memory, and a resounding crescendo to our five years of study at LTH.

Finally, we would like to extend our thanks to Arvid Nordquist's Dark Mountain roast for unfalteringly escorting us along the path of enlightenment, and to the WMF Group for its model machine WMF 1200 S, article number 03.1210.0200—a buttress of indefatigable quality and reliability in these otherwise uncertain times.

29 May, 2020

Lund, Sweden



Ernest Björklund



Axel Christoffersson

Table of Contents

- 1 Introduction.....1
 - 1.1 Background.....1
 - 1.2 Research Motivation.....3
 - 1.3 Purpose and Research Objectives.....3
 - 1.4 Scope and Delimitations4
 - 1.5 Disposition5

- 2 Method7
 - 2.1 General Approach.....7
 - 2.2 Experiments8
 - 2.3 Semi-analytical Model11
 - 2.4 Numerical Modeling11

- 3 Architectural Glass.....13
 - 3.1 Materials Science.....13
 - 3.2 Mechanical Properties.....15
 - 3.3 Flat Glass Variants and Glazing Products.....18

- 4 Technical Standards and Academic Research on Glass Subjected to Impact Loading.....21
 - 4.1 Design Codes and Technical Standards21
 - 4.2 Academic Research.....23

- 5 Experimental Setup and Results25
 - 5.1 Setup.....25
 - 5.2 Results28

- 6 Semi-analytical Model33
 - 6.1 General Overview33
 - 6.2 System Assembly and Equations of Motion35
 - 6.3 Eigenanalysis.....36

6.4	Modal Analysis.....	38
6.5	Input Parameters	42
6.6	Case Study and Stress Derivation	45
6.7	Parametric Study	48
7	The Finite Element Method.....	51
7.1	General Overview	51
7.2	Derivation of Structural Dynamic Finite Element Formulation.....	52
7.3	Dynamics	57
7.4	Nonlinearity	57
7.5	Solver Schemes.....	59
7.6	Convergence	60
7.7	Applicability to the Study.....	60
7.8	Selected Element Families and Their Applications	61
8	Finite Element Modeling of High-fidelity Designs	67
8.1	General Overview	67
8.2	Frame Beams	68
8.3	Glass Specimens	69
8.4	Impactor	71
8.5	Design of Simply Supported Connection	76
8.6	Design of Bolted Connection	79
8.7	Design of Clamped Connection.....	82
8.8	Summary of Material Input Parameters and Element Selection	84
8.9	Convergence	85
9	Finite Element Modeling of Reduced Designs	89
9.1	General Overview	89
9.2	Design of Reduced Dynamic Models	89
9.3	Design of Reduced Models with Equivalent Static Loads	91
10	Results and Analysis	95
10.1	General Overview	95
10.2	Dynamic Model Results	96
10.3	Maximum Stresses and Equivalent Static Results.....	108
10.4	Stress Deviations.....	111

11	Discussion	115
11.1	Dynamic Results Discussion	115
11.2	Equivalent Static Model Results Discussion	118
11.3	Material Modeling and Nonlinearity	119
12	Conclusion	123
12.1	Chief Conclusions	123
12.2	Engineering Implications	124
12.3	Limitations and Avenues for Further Research	124
13	References	127
A	Processed Experimental Data: Principal Stress at Glass Specimen Impact Location	131
B	Processed Experimental Data: Acceleration of Glass Specimen at Impact Location	143
C	Derivation of Beam Deflection Response to Atypical Load Configurations	155
D	Collated Results: Out-of-plane Acceleration of Glass Specimens	163
E	Equivalent Static Loads	175
F	Stress Deviations	179

List of Notations and Symbols

Latin

a	nodal displacement vector
c	$N \times N$ damping matrix, alternatively a vector containing arbitrary constants
c_d	wave speed through material
C	damping matrix
D	constitutive matrix
E	Young's modulus
E_c	modulus of compression
I	moment of inertia
k_i	stiffness of spring i
k	$N \times N$ stiffness matrix
K	modal stiffness matrix
L_e	length of finite element
N	global shape function matrix
m_i	mass of body i
m	$N \times N$ mass matrix
M	modal mass matrix
q_n	modal coordinate for mode n
q	$1 \times N$ modal coordinate vector
$\dot{\mathbf{q}}$	$1 \times N$ modal coordinate vector derivative
$\ddot{\mathbf{q}}$	$1 \times N$ modal coordinate vector second derivative

S	stress tensor
t	traction vector
u	$1 \times N$ displacement vector
$\dot{\mathbf{u}}$	$1 \times N$ velocity vector
$\ddot{\mathbf{u}}$	$1 \times N$ acceleration vector
w	column vector containing weight functions

Greek

α_R	mass proportional damping ratio
β_R	stiffness proportional damping ratio
δ	deformation
ζ_n	modal damping ratio.
ζ	$N \times N$ diagonalized damping matrix containing modal damping ratios.
ν	Poisson's ratio
ρ	mass density
σ	stress
Φ_n	$N \times 1$ natural vibration mode column vector corresponding to the n th natural frequency and associated with the contribution of the n th mode of vibration the system response, where $n = \{1, 2, \dots, N\}$
Φ	$N \times N$ matrix containing each deflection mode column vector Φ_n
Ω	$N \times N$ diagonalized matrix of a system's natural frequencies
Ω_D	$N \times N$ diagonalized matrix of a system's natural frequencies of damped vibration
ω_n	n th natural frequency
ω_{nD}	n th natural frequency of damped vibration
$\tilde{\nabla}$	matrix differential operator

List of Tables

Table 1-1: Fastener configurations investigated during the experimental campaign.	4
Table 2-1: investigated setup and glass specimen permutations. Note that Setup 2 has outlying planar dimensions. * Note: the interlayer thickness was later increased to 1.60 mm in the FE models, see Section 8.3.	8
Table 3-1: Typical chemical composition, by weight, of soda-lime glass, and sources of raw material. Source: Gonçalves, 2015.....	14
Table 3-2: Elastic properties of soda-lime glass, compiled from various sources.	16
Table 3-3: Dissonance between theoretical strength and values used in structural glass design. Source: Falk, et al. (2011).	17
Table 5-1: Estimated dynamic stiffness of the impactor for various drop heights.....	30
Table 6-1: Estimated dynamic stiffness of the impactor for drop heights used in the experimental campaign.	42
Table 6-2: Glass lumped masses and stiffnesses used in the 2DOF model.	44
Table 8-1: Effective Young’s modulus as a function of temperature and load duration for the interlayer materials PVB and SGP. Supplier data is provided for the temperatures 20 °C and 25 °C; interpolation yields the values for 22 °C (shaded cells). Source: Kuraray, 2020.	69
Table 8-2: Constituent materials of a typical EU rubber tire. Mass proportions are sourced from Sienkiewicz, et al. (2012).	72
Table 8-3: Summary of input parameters for the materials used in the high-fidelity finite element models. EPDM rubber lacks a density value because it is modeled as a gasket, which does not require a density input.	84
Table 8-4: Summary of element selection used in the high-fidelity finite element models....	85
Table 9-1: Spring stiffnesses and torsion coefficients for the reduced setups.....	91

Table 10-1: Arrangement of the collated results.....	96
Table 10-2: Deviation in modeled principal stress from the experimental results, averaged for each glass specimen type across impactor drop heights. Multiplying the factors with the corresponding experimental stress gives the stress outputted by the model.	112
Table 10-3: Average deviation in modeled principal stress from experimental results, averaged across all glass specimen types and impactor drop heights. Multiplying the factors with the corresponding experimental stress gives the stress outputted by the model. * Note: only accounts for the simply supported setup.....	113
Table 11-1: Case study of computational cost relative to deviation from experimental stress. The case is 10 mm monolithic glass fastened to the simply supported setup, with a 300 mm impactor drop height.....	119

List of Figures

Figure 1-1: Experimental setup for testing soft-body impact loading on glass specimens, in accordance with European standard EN 12600, where 1 is the main frame, 2 is the clamping frame, 3 is the impactor, 4 is an optional support member, and 5 is an optional suspension device. Source: CEN, 2002.....	2
Figure 1-2: Principal appearance of the studied fastener configurations: simply supported (left), bolted (center), and clamped (right).	4
Figure 2-1: Measuring instruments used during the experimental campaign: accelerometer attached to the impactor (left); accelerometer and strain gauge positioned in the center of the glass specimen. i.e. the impact location (center); strain gauges positioned near the fasteners (right) in order to measure the stress concentrations...9	9
Figure 2-2. Experimental setup of the static compression test (left) and the dynamic rigid impact test (right).....	10
Figure 3-1: Molecular structure of a crystalline solid (quartz, left) and a glassy material (soda-lime glass, right). Note the absence of symmetry in the latter.	13
Figure 3-2: Schematic overview of the interaction between electromagnetic radiation and material upon the former hitting the material surface.....	15
Figure 3-3: Principal breakage patterns of annealed (left) and tempered glass (right). Source: Custom Glass Products, 2020.	17
Figure 3-4: Typology of architectural glass products and their disposition within the production process.....	18
Figure 3-5: Residual stress profile (envelope) through the thickness t of a tempered glass specimen.	19
Figure 5-1: Examples of the experimental setup, with simply supported (left) and bolted (right) fastener configurations.	26
Figure 5-2: Close-ups of the bolt (left) and the bolted connection (right).	27

Figure 5-3: Close-ups of the clamp (left) and the clamped connection (right). The clamp is attached to the flange of a C-beam.....	27
Figure 5-4: Examples of the processed experimental data. The data are derived from a strain gauge and an accelerometer during the experimental campaign. The data sets correspond to simply supported monolithic specimens with a thickness profile of 10 mm.	29
Figure 5-5: Experimental results of the displacement-controlled static compression test performed on one of the impactor tires.	30
Figure 5-6: Experimental results of the dynamic rigid impact test performed on the dual-tire impactor.	31
Figure 6-1: Discretization of the glass-impactor system into a 2DOF system.	35
Figure 6-2: Freebody diagrams of the masses in the 2DOF system.....	35
Figure 6-3: Symmetrically discontinuous loading of a simply supported beam (top) and a beam fixed at both ends (bottom).	43
Figure 6-4: Deformation response of the glass to impact loading in the numerical model. It is judged to be closer to that of a beam fixed at both ends rather than a simply supported beam.....	44
Figure 6-5: Case study: deformation response of the glass-impactor 2DOF system, assuming a 10 mm thick monolithic glass specimen fastened to the simply supported setup, and a 300 mm drop height.....	46
Figure 6-6: Case study: stress on the glass surface computed using a beam analogy and the displacements outputted by the 2DOF model.	47
Figure 6-7: Parametric study on the governing parameters in the 2DOF model. Legend entries correspond to the weights (or percentages) that are multiplied with the base case of a 10 mm thick monolithic glass specimen and 300 mm drop height.....	49
Figure 7-1: Engineering as an idealized workflow, with the finite element method targeting the lattermost step. Adapted from Ottosen & Petersson (1992).	51
Figure 7-2: Discretization of a model geometry into finite elements. Adapted from Dassault Systèmes (2020).	52
Figure 7-3: Schematic overview of the degree to which nonlinear effects are present in problem areas, as viewed with respect to the time domain. Adapted from Dassault Systèmes (2016).	59

Figure 7-4: Five-node tetrahedron (left) and eight-node hexahedral (brick) solid elements (right). Source: Dassault Systèmes, 2015.	62
Figure 7-5: Axisymmetric conventional shell elements, with normal vectors displayed. Note that these are three-dimensional, with thicknesses defined independently of the element formulation. Source: Dassault Systèmes, 2015.....	62
Figure 7-6: Normal and thickness direction for continuum solid shell elements. Source: Dassault Systèmes, 2020.	64
Figure 7-7: Spatial representation of a gasket element (left) and an 8-node gasket element (right). Source: Dassault Systèmes, 2015.	64
Figure 8-1: Schematic overview of the analysis steps used to simulate the high-fidelity FE models.....	67
Figure 8-2: Comparison of experimental setup (left) and high-fidelity FE models (center, right). The beams are assembled with S2S ties to capture the rigidity of the true bolted connection, while the fixed boundary conditions capture the bolts to the yellow steel superstructure.....	68
Figure 8-3: Extrapolation of effective Young’s moduli for the load duration 27 ms. PVB is a log-log curve; SGP is a log curve.....	70
Figure 8-4: Finite element model of the dual-tire impactor: whole (left) and section cut (right).....	71
Figure 8-5. Static compression test rebuilt in Abaqus.	73
Figure 8-6: Comparison of experiments and FE model during the static compression test on one of the impactor tires.	73
Figure 8-7: Dynamic rigid impact test rebuilt in Abaqus.	74
Figure 8-8: Comparison of experiments and FE model during the dynamic rigid impact test for the dual-tire impactor.....	75
Figure 8-9: Condensed comparison of the experimental and FE model during the dynamic rigid impact test, showing only the maximum accelerations and the times at which they occur. The black dashpots link the results with common drop heights.	76
Figure 8-10: Simply supported high-fidelity FE model seen isoparametrically (left) and from the side (right). The magenta strips shown in the side view represent the rubber strips.....	77

Figure 8-11: Schematic cross-section of the simply supported fastener assembly modeled in Abaqus. The connector beam simulated the bolt.	78
Figure 8-12: Close-up of simply supported connection in Abaqus. The gray is steel, the turquoise is glass, the dark red is the interlayer, and the magenta are the rubber strips.....	78
Figure 8-13: Bolted high-fidelity FE model seen isoparametrically (left) and close-up of the bolted connection. The gray is steel, the turquoise is glass, the purple is the interlayer, and the magenta are the rubber bolt gussets.	80
Figure 8-14: Schematic cross-section of the bolt fastener assembly modeled in Abaqus.	81
Figure 8-15: Clamped high-fidelity FE model seen isoparametrically (left) and from the side (right), with the C-beams removed.	82
Figure 8-16: Clamped setup seen from above (top), and close-up of the clamped connection (bottom).	83
Figure 8-17: Finite element meshes of the three high-fidelity models: simply supported (left); bolted (center); clamped (right).....	86
Figure 8-18: Spatial convergence of the impactor, showing relative change in the acceleration output variable from the previous iteration. Note that the scale is logarithmic.	86
Figure 8-19: Spatial convergence of the glass, showing relative change in the stress output variable from the previous iteration. Note that the scale is logarithmic.	87
Figure 8-20: Spatial convergence of the glass, showing relative change in the stress output variable from the previous iteration. Note that the scale is logarithmic.	88
Figure 9-1: Reduced dynamic model designs: simply supported (left), bolted (center), and clamped (right). Springs are positioned at the vertical edges of the glass, along the centerline.	90
Figure 9-2: Reduced model designs with equivalent static loads: simply supported (left), bolted (center), and clamped (right).	91
Figure 10-1: Collated results of principal stress at glass specimen impact location for various impactor drop heights. The data sets correspond to simply supported monolithic specimens with a thickness profile of 8 mm.	98

Figure 10-2: Collated results of principal stress at glass specimen impact location for various impactor drop heights. The data sets correspond to simply supported monolithic specimens with a thickness profile of 10 mm.	99
Figure 10-3: Collated results of principal stress at glass specimen impact location for various impactor drop heights. The data sets correspond to simply supported monolithic specimens with a thickness profile of 12 mm.	100
Figure 10-4: Collated results of principal stress at glass specimen impact location for various impactor drop heights. The data sets correspond to simply supported laminated specimens with a thickness profile of 8 mm ESG/TVG + 1.6 mm PVB + 8 mm ESG/TVG.	101
Figure 10-5: Collated results of principal stress at glass specimen impact location for various impactor drop heights. The data sets correspond to simply supported laminated specimens with a thickness profile of 8 mm ESG/TVG + 1.6 mm SGP + 8 mm ESG/TVG.	102
Figure 10-6: Collated results of principal stress at glass specimen impact location for various impactor drop heights. The data sets correspond to bolted laminated specimens with a thickness profile of 6 mm ESG + 1.6 mm SGP + 6 mm ESG.	103
Figure 10-7: Collated results of principal stress at glass specimen impact location for various impactor drop heights. The data sets correspond to clamped laminated specimens with a thickness profile of 5 mm ESG + 1.6 mm PVB + 5 mm ESG.	104
Figure 10-8: Collated results of principal stress at glass specimen impact location for various impactor drop heights. The data sets correspond to clamped laminated specimens with a thickness profile of 5 mm ESG + 1.6 mm SGP + 5 mm ESG.	105
Figure 10-9: Collated results of principal stress at glass specimen impact location for various impactor drop heights. The data sets correspond to clamped laminated specimens with a thickness profile of 6 mm ESG + 1.6 mm PVB + 6 mm ESG.	106
Figure 10-10: Collated results of principal stress at glass specimen impact location for various impactor drop heights. The data sets correspond to clamped laminated specimens with a thickness profile of 6 mm ESG + 1.6 mm SGP + 6 mm ESG.	107
Figure 10-11: Collated results of maximum principal stress at glass specimen impact location for various impactor drop heights. The data sets correspond to the simply supported setup.....	109

Figure 10-12: Collated results of maximum principal stress at glass specimen impact location for various impactor drop heights. The data sets correspond to the simply supported setup.....	110
Figure 10-13: Collated results of maximum principal stress at glass specimen impact location for various impactor drop heights. The data sets correspond to the simply supported setup.....	111
Figure 11-1: Effects of damping on free vibration. Source: Chopra (2014).	116
Figure 11-2: Shock spectra for a half-cycle sine pulse force for five damping values. Source: Chopra (2014).	117

1 Introduction

“To achieve great things, two things are necessary: a plan, and not quite enough time.”

—Leonard Bernstein

The introductory chapter presents the background serving as motivation for the research documented in the following pages. This establishes the overarching purpose, from which research objectives are then derived. These research objectives map out how the purpose will be fulfilled, with the implicit objective being a worthwhile contribution to the study of the aforementioned problem. The scope is then delimited, and the report’s disposition presented.

1.1 Background

The history of glass encompasses a time period of geological proportions, having formed naturally throughout the ages as a result of high-temperature, rapid-cooling spectacles such as volcanic eruptions and meteor impacts (Bourhis, 2008). Human civilization has since moved on from using prehistoric obsidian and rudimentary glassblowing techniques; instead, most glass is now produced on an industrial scale and by industrial means. One of the chief reasons behind the industrialization of glass production is its widespread use as a building material. Indeed, glass is a material that has seen its use in construction expand rapidly with the advent of modern architecture and technical breakthroughs such as soda-lime-silica compositions, laminated glazing, and insulating glass units. Today, emphasis is steadily moving towards the use of glass as a structural, that is to say loadbearing, element. This shift in focus, combined with its ubiquity in building enclosures, balustrades, and other barriers, has resulted in more demanding technical requirements and design specifications.

Among these requirements are those stipulating that glass sheeting, when installed according to specific configurations, be capable of withstanding soft-body impact loads. For instance, Swedish regulation states that, for glass surfaces with a vertical drop height exceeding 2 m to the underlying ground, or if the distance between the glazed surface and the bottom floor is less than 0.6 m, attention must be given to ensuring that the risk of falling through the glass be restricted (National Board of Housing, Building and Planning, 2019). One such method for achieving this risk mitigation is by verification with a test method described by the European

Standard EN 12600, adopted by the Swedish National Board of Housing, Building and Planning in 2003. This method consists of a pendulum test in which a 50 kg impactor is released such that it falls with a pendulum movement and strikes the glass surface, see Figure 1-1. Following impact, the damage is assessed and the glass is classified according to its performance (CEN, 2002). This method prescribes the fastener configuration to a fixed boundary condition along all edges, and does not allow for other boundary conditions.

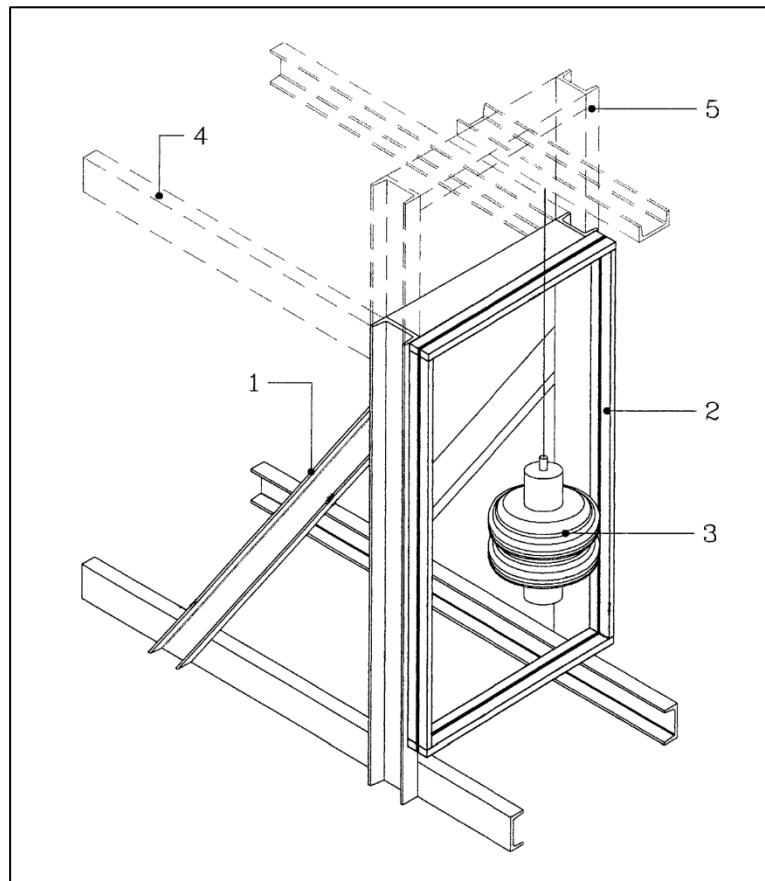


Figure 1-1: Experimental setup for testing soft-body impact loading on glass specimens, in accordance with European standard EN 12600, where 1 is the main frame, 2 is the clamping frame, 3 is the impactor, 4 is an optional support member, and 5 is an optional suspension device. Source: CEN, 2002.

Given the ever-increasing popularity of glass for use in barriers, performing the pendulum test can quickly become cumbersome (and expensive). Indeed, the 50 kg impactor is meant to simulate the load effect of a human body colliding with the glass, implying that experimental verification is a requirement not just for specialty components, but also for the glass facades that have become endemic to urban environments. As a result, alternative methods for determining the capacity of an arbitrary glass unit to withstand an impact load are of mounting interest to the industry. Even so, it is ill-advised to limit such alternative methods to the all-edge fixed boundary condition prescribed by EN 12600; after all, the fasteners applied to a glazing unit upon practical installation are seldom rigid along all four edges. Thus, a key element of deriving alternative methods for soft-body impact loading on glass is making those methods applicable to a more universal set of fastener configurations.

1.2 Research Motivation

As demonstrated by the background, it is clear that there is a need to develop a non-experimental method for verifying the resistance of glass units to soft-body impact loading. The pendulum test used today is expensive, time-consuming, and does not account for the true fixings used on the glass unit upon installation. Moreover, contemporary approaches to simulating soft-body impact on glass structures numerically are under-researched and prohibitively computationally expensive.

The issue of fastener variability in the glass unit is of particular importance if a more universal and accessible method is to be developed. This has been a significant deterrent to developing a numerical method in the past because it entails a major experimental undertaking if the universality of the numerical method is to be verified. In that spirit, an experimental campaign was carried out at LTH, in 2018, in which glass panels were tested using the pendulum method, but were mounted with different fixings (Kozłowski, et al., 2020). Those included vertical simple supports, linear clamps, local clamp fixings, and point fixings (bolts). In addition, different glass unit types were tested, including monolithic specimens of variable thickness, laminated specimens of variable thickness and interlayer material, along with variable specimen dimensions. There is therefore ample empirical data for use as a benchmark in developing a numerical method for assessing the response of a glass unit to an appropriate soft-body impact load.

1.3 Purpose and Research Objectives

The purpose of this thesis is to investigate the viability of a numerical method for verifying the resistance of an arbitrary glass panel to soft-body impact. This purpose is discretized according to the following research objectives:

- Process and analyze the empirical data obtained through the experimental campaign.
- Investigate the essential mechanics of the glass-impactor system under impact loading by developing a semi-analytical model and carrying out a subsequent parameter study.
- Develop a high-fidelity finite element model of the glass-impactor system that accurately captures the behavior measured in the experimental campaign. Such a model may include, for instance: nonlinear material effects, such as hyperelasticity and viscoelasticity; nonlinear geometric effects; pneumatic cavity behavior; and contact conditions.
- Explore the feasibility of a reduced finite element model that captures the behavior of the glass-impactor system, while weighing computational efficiency against reasonable tolerances.

1.4 Scope and Delimitations

The experimental campaign, carried out at LTH, was undertaken to investigate soft-body impact of glass specimens with variable fastener configurations. These configurations are described by the six setups provided in Table 1-1.

Table 1-1: Fastener configurations investigated during the experimental campaign.

Setup	Fastener configuration
I	Simply supported along vertical edges
II	Simply supported along all edges
III	Point-fixed (bolted) at corners
IV	Clamp-fixed at corners
V	Cantilevered along bottom edge by means of a steel shoe
VI	Cantilevered along bottom edge by means of four-point fixings

It is noted that setup V has already been modeled (Kozłowski, 2019; Kozłowski, et al., 2020). Furthermore, setup V is qualitatively similar to setup VI, as is setup I to setup II. In an effort to curb superfluous work, the scope is therefore delimited to the study of setups I, III, and IV. The principal appearance of these fastener configurations is illustrated in Figure 1-2.

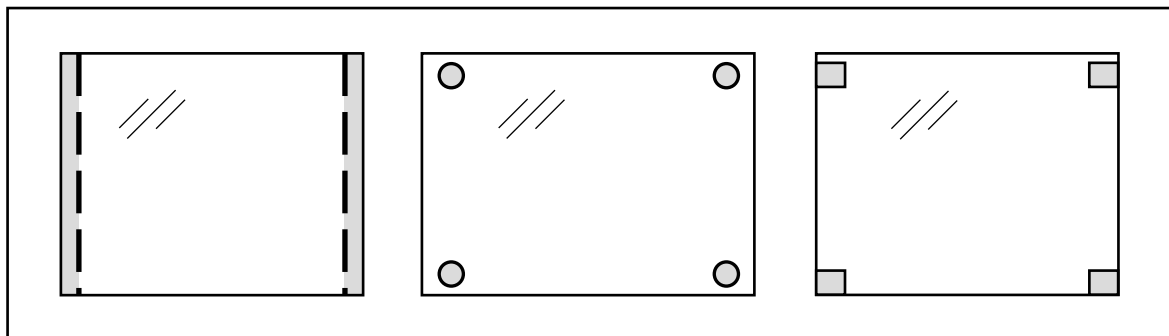


Figure 1-2: Principal appearance of the studied fastener configurations: simply supported (left), bolted (center), and clamped (right).

During the experimental campaign, tests were also carried out that investigated the post-breakage behavior and strength of the glass specimens. Post-breakage response is disregarded in this thesis; only the pre-failure response of the glass is studied.

A semi-analytical investigation of the glass-impactor system is of interest, as this may shed light on otherwise opaque behaviors exhibited by the finite element models. The semi-analytical models are not developed with the intention of capturing the true behavior of the system as accurately as possible; rather, they are designed as a resource that can be consulted throughout the remainder of the study.

1.5 Disposition

Referring to the research objectives outlined earlier, the disposition of the thesis is established according to:

- A detailed accounting of the research method is given in Chapter 2.
- An annotated summary of architectural glass, covering materials science, mechanical properties, and applications, is provided in Chapter 3.
- Chapter 4 continues the literature review by presenting the governing design codes and technical standards for structural glass, along with the prevailing literature on the numerical modeling of glass under impact loading.
- The experimental setup is described in Chapter 5, after which experimental data are presented and processed.
- Chapter 6 derives a semi-analytical model of the glass-impactor system in an effort to elucidate the dynamics undergirding the system response.
- An abridged theoretical review of the finite element method is provided in Chapter 7, with emphasis on when to include nonlinearity, dynamic effects, alongside a review of element types pertinent to the study.
- The design of the high-fidelity finite element models is described in Chapter 8.
- The detailed finite element models are reduced in Chapter 9
- The results from the experimental campaign, semi-analytical model, and finite element simulations are compared in Chapter 10.
- The implications of and shortcomings in the results are discussed in Chapter 11.
- Chapter 12 concludes the study by summarizing the implications of the results and suggesting avenues for future research.

2 Method

“Never mind the maneuvers, just go straight at them.”

—Horatio Nelson

The method chapter details the approach that was applied during the study. It encompasses the overarching strategy that was implemented, alongside the methods deployed with respect to engineering simplifications, experimental processing, semi-analytical modeling, and the finite element modeling of both the high-fidelity and the reduced models.

2.1 General Approach

Given that the overarching purpose of the study is to evaluate the viability of a numerical method for verifying the resistance of an arbitrary glass panel to soft-body impact, it is crucial that this numerical method be compared with ulterior data. To that end, the results of the finite element simulations were compared with the results of the experimental campaign and the semi-analytical model. Only after that was accomplished, could work begin on reducing the finite element models to their essential components. The results of these reduced models were also compared to the other data sets.

The purpose of the study entails understanding the material behavior of glass. In line with this, Chapter 3 compiles information from noted authors and textbooks on the properties of glass, alongside presenting an annotated catalogue of glazing products. Understanding these properties and products guided some of the engineering simplifications made in the numerical models. In a similar fashion, previous research was catalogued in Chapter 4 to highlight some of the common modeling techniques used for impact loads on glass.

The three setups that were studied were installed with glass specimens of varying profiles, see Table 2-1. The monolithic specimens were the focus of the first phase of analysis. Once these were modeled successfully, attention shifted to the laminated specimens. This strategy was formulated because it was presumed that the material and mechanical complexity of the interlayers would inhibit the modeling process, unless it had been established beforehand that the simpler monolithic specimens were behaving within acceptable tolerances.

2 Method

Table 2-1: investigated setup and glass specimen permutations. Note that Setup 2 has outlying planar dimensions. * Note: the interlayer thickness was later increased to 1.60 mm in the FE models, see Section 8.3.

Setup	Fastener configuration	Profile type	Interlayer	Profile [mm]	Planar dimensions [mm ²]
1	Simply supported along vertical edges	Monolithic	–	8	1000 × 800
		Monolithic	–	10	1000 × 800
		Monolithic	–	12	1000 × 800
		Laminated	PVB	8 + 1.52 + 8*	1000 × 800
		Laminated	SGP	8 + 1.52 + 8*	1000 × 800
2	Point-fixed (bolted) at corners	Laminated	SGP	6 + 1.52 + 6*	1100 × 800
3	Clamp-fixed at corners	Laminated	PVB	5 + 1.52 + 5*	1000 × 800
		Laminated	SGP	5 + 1.52 + 5*	1000 × 800
		Laminated	PVB	6 + 1.52 + 6*	1000 × 800
		Laminated	SGP	6 + 1.52 + 6*	1000 × 800

2.2 Experiments

The experimental campaign was carried out at LTH, in 2018 (Kozłowski, et al., 2020). For each setup and glass type, the impact test was performed for the following five drop heights of the impactor: 100 mm, 200 mm, 300 mm, 400 mm, and 500 mm. Considering that there were 10 glass types which were tested across the various setups, this means that 50 data stream permutations were treated. Moreover, for each drop height, the glass specimen was subjected to three impact trials, i.e. a total of 150 data sets were processed for the experimental component of the study.

The behavior of both the glass specimens and the impactor were measured during the experimental campaign. The data were collected from: accelerometers attached to the impactor and the center of the glass specimen; and strain gauges positioned along the glass specimens, which collected data every 0.83 ms, see Figure 2-1. Even after processing, the accelerometer data for the impactor were deemed too volatile to be of any practical utility as a benchmark for the finite element results. However, the strain gauges and, to some extent, the glass accelerometer, yielded usable data once processed.

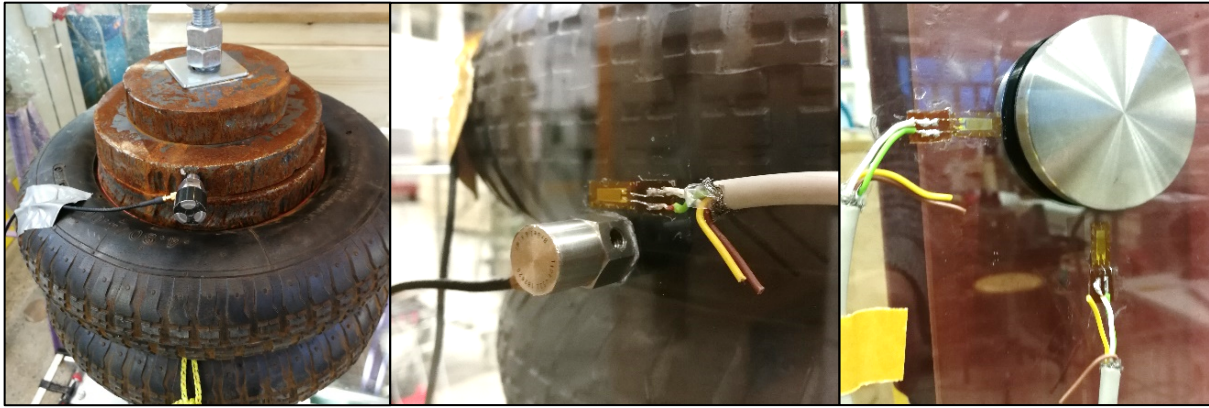


Figure 2-1: Measuring instruments used during the experimental campaign: accelerometer attached to the impactor (left); accelerometer and strain gauge positioned in the center of the glass specimen. i.e. the impact location (center); strain gauges positioned near the fasteners (right) in order to measure the stress concentrations.

2.2.1 Data Processing

The accelerometer data were processed in MATLAB using first order polynomial Savitzky-Golay filtering. This filtration technique uses a linear least-squares method to fit adjacent data points to the curve of a prescribed low-degree polynomial, with the output being a smoother curve. In this instance, the polynomial order was set to one. Note that the filtered curve is likely to display accelerations that are smaller than the recorded values (Bang-Jian, et al., 2018).

The strain data were processed in MATLAB, but without filtration. Assuming linearity and utilizing $\sigma = \varepsilon E$, each data point was computed into stress. The Young's modulus was set to $E = 72$ GPa, see Section 3.2.1. This is a possible source of error in the method, perhaps of decisive importance, because the true Young's modulus was never verified experimentally for the glass specimens in question.

Scrutiny of the strain data reveals a large spread of the measured values. This becomes particularly prevalent when comparing data sets of the same fastener configuration and for otherwise identical glass specimens, save for the treatment of the glass. In one such instance, one data set corresponded to heat-strengthened glass, while another corresponded to fully tempered glass—neither of these treatment processes affects the modulus of elasticity, see Section 3.3, yet the strains deviated from one another by approximately 12%. This confirms a significant spread in the experimental data. This was considered when comparing the experimental results with the numerical simulations later on in the study.

2.2.2 Experimental Verification of the Dual-tire Impactor

Two independent tests were performed on the dual-tire impactor during the experimental campaign:

- Static compression test: performed on a single tire that was dismantled from the impactor assembly and subjected to displacement-controlled compression, see Figure

2-2. The loading apparatus continuously recorded both the force and the displacement during the test.

- Dynamic rigid impact test: the dual-tire impactor was attached to a pendulum and released from five different drop heights, see Figure 2-2, in accordance with EN 12600 (CEN, 2002). An accelerometer was mounted onto the impactor that measured its acceleration during the pendulum movement and subsequent impact with the rigid surface. In actuality, the rigid surface was a rigid steel beam.

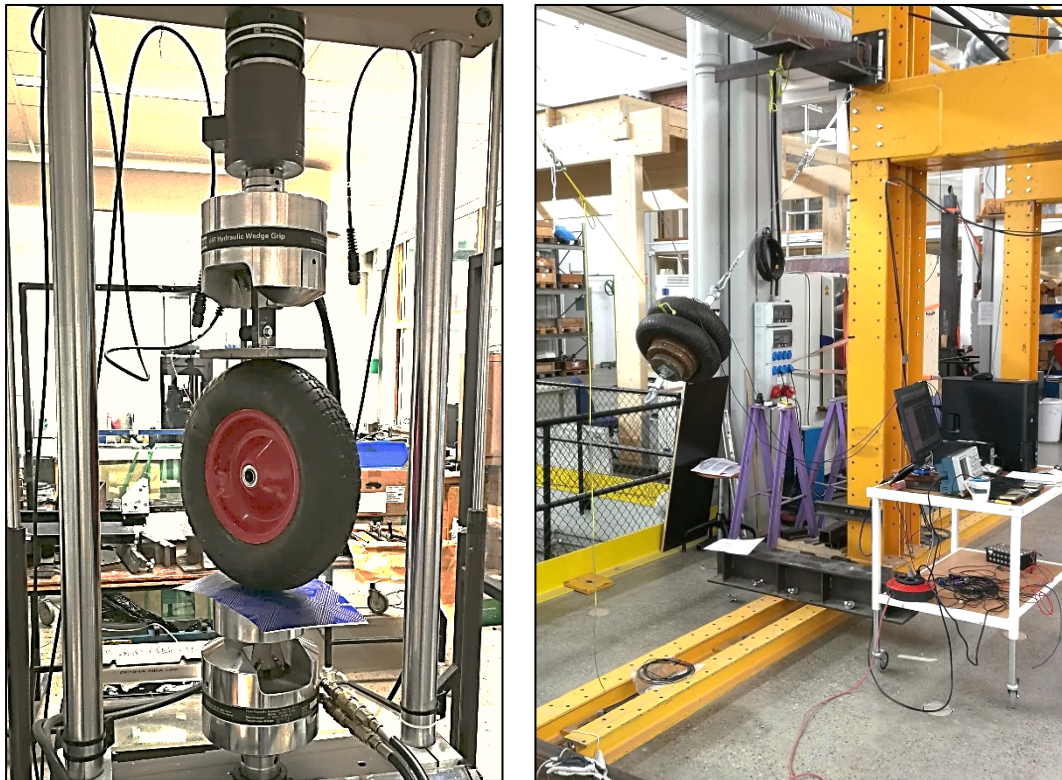


Figure 2-2. Experimental setup of the static compression test (left) and the dynamic rigid impact test (right).

Data from both of these tests were used to calibrate the impactor in the numerical model. This is a valuable piece of the puzzle when recreating the impactor numerically because the hyperelastic material is one of many parameters that complicates its modeling. Even so, caution was taken even after the numerical impactor exhibited comparable behavior to that measured in the tests because the tests only consider static behavior and impactor acceleration. In other words, the tests do not consider, for instance, stress, even though the focus of the numerical component of the study was on the stresses in the glass. It is therefore possible that good agreement between the experimental and numerical impactor was achieved with respect to static behavior and acceleration, but not with respect to stress.

EN 12600 stipulates that the impactor should be inflated to 350 kPa, and this was also verified to be the case for the independent tests, and was also accounted for in the numerical model (CEN, 2002; Kozłowski, et al., 2020).

2.3 Semi-analytical Model

The chief objective of the semi-analytical model was to demonstrate the essential mechanics of the glass-impactor system. To that end, a pedagogical approach was adopted, in which mathematical derivations are annotated and presented clearly. Idealizations, such as beam analogies, are employed to further facilitate a pedagogical presentation of the system dynamics.

The semi-analytical model was also an opportunity to carry out a parametric study of the system that was less cumbersome than if it had been carried out with the numerical models. The results of this parametric study provide a visual catalog on the influence that each component has on the system's behavior, which is why the study is also presented.

2.4 Numerical Modeling

The numerical component of the study was carried out in the finite element program Abaqus. Given that the simulated system covers impact loading, there is some ambiguity on whether to use an implicit or explicit solver. This ambiguity is eliminated by scrutinizing the stability limit that is characteristic of the explicit solver. This takes the form of an estimated stable time increment Δt_{stable} , beyond which the explicit solver will be unlikely to produce affable results (Dassault Systèmes, 2015). This stability condition can be expressed as

$$\Delta t_{\text{stable}} = \frac{L^e}{c_d} \quad (2-1)$$

where L^e is the element length and c_d is the wave speed of the material, which is calculated according to

$$c_d = \sqrt{\frac{E}{\rho}} \quad (2-2)$$

Glass is of discernable interest in the study, and has the approximate material parameters $E = 70$ GPa and $\rho = 2500$ kg/m³, see Section 3.2.1. Assuming an inordinately large element size of 5 cm for the glass specimen, a generous stability limit is estimated, using Eq. (2-1) and (2-2), to be

$$\Delta t_{\text{stable}} = \frac{0.05}{\sqrt{70 \cdot 10^9 / 2500}} = 9.45 \cdot 10^{-6} \text{ s} \approx 0.01 \text{ ms}$$

which, assuming that the course of events to be simulated lasts ~ 100 ms, suggests that the number of required time increments is on the order of 10^4 . This is not a sustainable projection, and thus the explicit solver is abandoned in favor of the implicit solver.

2.4.1 Input Data

Care was taken to derive the input parameters analytically or to source them from reliable literature, such as supplier data, technical standards, engineering textbooks, and research articles. If the finite element models continued to exhibit divergent behavior, certain input parameters were then adjusted accordingly, but only if those parameters did not have fully established values, such as the rubber components and the interlayer materials.

As much as possible, efforts were made to streamline the models by applying simplified, linear values to otherwise nonlinear parameters, such as modeling the viscoelastic interlayers with equivalent moduli of elasticity.

2.4.2 Verification of Finite Element Models

To verify the realistic behavior of the simulated impactor, both the static compression test setup and the dynamic rigid impact test setup were recreated in Abaqus. The results were then compared with their experimental counterparts.

The behavior of the glass specimens in the three test setups is of governing interest to the overarching objective of the study. This behavior, specifically its response upon contact with the dual-tire impactor, was verified by extracting the principal stresses from Abaqus and comparing them to the data sourced from the strain gauges during the experimental campaign. The same procedure was carried out for the acceleration of the glass.

2.4.3 High-fidelity and Reduced Finite Element Models

High-fidelity finite element models were built in the first phase of the numerical study, in which the complete construction of the experimental setup was included. Once a sufficient degree of accuracy had been obtained from the high-fidelity models, work shifted towards reducing the models. This took the form of both reduced dynamic models and reduced models using equivalent static loads. The former replaced the setup with translational and rotational springs of equivalent stiffness but maintained the impactor and the transient aspect of the impact loading. The equivalent static models also removed the impactor and eliminated the dynamic simulations, replacing them with an equivalent load acting on the center of the glass specimens. This equivalent load was determined using two different methods. The first method derived a dynamic amplification factor while the second method used data from the previous tests directly.

3 Architectural Glass

“Nothing is built on stone; all is built on sand, but we must build as if the sand were stone.”

—Jorge Luis Borges

Architectural glass refers to glass elements that are used as building components, such as for glazing and interior barriers. This chapter presents the essential materials science on architectural glass, describing its chemical, physical, and mechanical properties, after which an annotated catalog of glazing products is accounted for, in which their production, functions, and applications are described.

3.1 Materials Science

There are myriad definitions mapping out the criteria for what constitutes a glassy material, many of which are misleading. Referring to a comprehensive definition from materials science, a material can be considered a glass, or as being in a glassy state, if it is a dense, isotropic, and homogenous noncrystalline solid, one that lacks any internal phase boundaries (Conradt, 2019). In short, glass materials, when observed at the atomic level, are characterized by the absence of any translational symmetry (Greaves, 1985), see Figure 3-1.

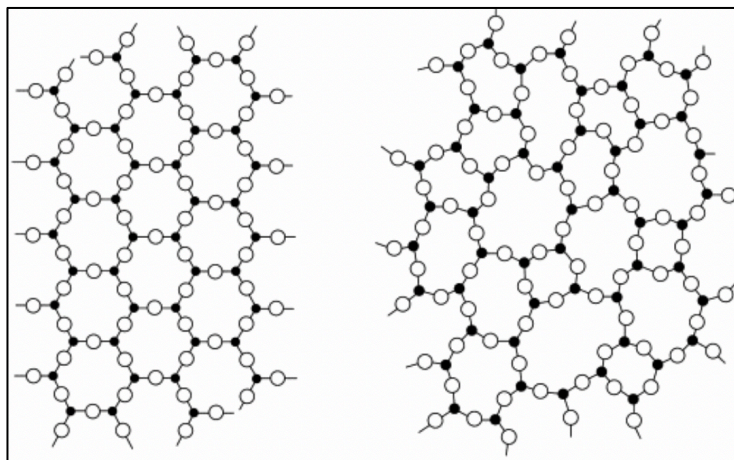


Figure 3-1: Molecular structure of a crystalline solid (quartz, left) and a glassy material (soda-lime glass, right). Note the absence of symmetry in the latter.

3 Architectural Glass

There is an abundance of chemical compositions that fulfill these criteria, but, for the purposes of architectural glass, the most prevalent of these is the soda-lime silicate scheme (Belis, et al., 2019). This scheme constitutes the molecular structure of what is commonly referred to as soda-lime glass, the archetypal chemical composition of which is provided in Table 3-1. The effect of the sodium ions is to disrupt the otherwise regular lattice silica structure, thereby inhibiting the material from crystalizing; the aluminum oxide is added to improve the chemical durability of the glass.

Table 3-1: Typical chemical composition, by weight, of soda-lime glass, and sources of raw material. Source: Gonçalves, 2015.

Chemical name	Chemical formula	Soda-lime composition [%]	Raw material source
Silicon dioxide (silica)	SiO ₂	71.9	Sand (quartz)
Sodium oxide	Na ₂ O	12.5	Feldspar (“soda”)
Calcium oxide	CaO	9.8	Limestone (“lime”)
Magnesium oxide	MgO	2.4	Dolomite
Potassium oxide	K ₂ O	1.8	Potassium carbonate
Aluminum oxide	Al ₂ O ₃	1.6	Feldspar

A defining characteristic of all glasses, including soda-lime glass, is the temperature at which it transitions from an amorphous material in a rigid state to an amorphous material that exhibits plastic behavior (Gonçalves, 2015). This point is termed the transition temperature, T_g , and it is of interest because, below this point, the material is brittle, demonstrating only a limited capacity to absorb mechanical energy. The response of the glass to loading can thus be used to ascertain whether the material is above or below the transition temperature. Of note is that soda-lime glass has a transition temperature of approximately 560 °C (a more precise value is governed by the chemical composition of the specific glass specimen in question).

As is true for many materials, soda-lime glass is homogenous at a macroscale. However, what distinguishes the homogeneity of soda-lime glass from materials such as timber is the scale at which this holds true: even at an atomic level, soda-lime glass remains homogenous, which cannot be said for the cellulose fibers that make up timber. Additionally, glass is an isotropic material, which streamlines its application in structural design.

As an architectural material, glass is most commonly deferred to for its optical performance, and it is for this reason that glass has become so popular in the industry. For glass, as with any arbitrary (smooth) material, the interaction that takes place between it and the electromagnetic radiation that hits its surface is a function of: the light R reflecting off of the

surface; the light S scattering through the material; the light A being absorbed by the material; and the light T transmitting through and out of the material, see Figure 3-2.

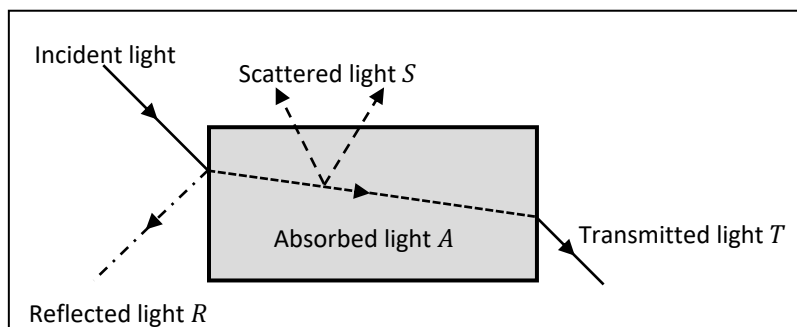


Figure 3-2: Schematic overview of the interaction between electromagnetic radiation and material upon the former hitting the material surface

By treating these variables as proportions of the total light interaction with the material, this interaction can be modeled as $R + S + A + T \equiv 1$. For materials such as soda-lime glass, the scattering S is negligible, while the transmission T is high. Even so, the transmission varies with the radiation wavelength as well as, specifically for architectural glass, the specimen thickness and chemical composition, the laminate properties, and the surface treatment. For normal flat glass, the transmission is high when the wavelength corresponds to visible light; but for infrared radiation, the transmission is considerably lower, and becomes negligible at ultraviolet wavelengths. This explains why a person cannot be practically sunburned by looking through a window, even though they can feel the heat radiating from the sun.

3.2 Mechanical Properties

Among the arsenal of modern construction materials, glass exhibits a distinctive material response to mechanical perturbation. It is therefore prudent to examine a selection of those properties that induce this behavior.

3.2.1 Deformation Response to Loading

Below the transition temperature, glass is a brittle material that exhibits a linearly elastic response to loading. On a molecular level, this means that the atoms are displaced from their equilibrium positions without breaking their bonds; upon unloading, the atoms return to their original equilibrium positions, and the material reverts to its original geometry.

The modulus of elasticity for soda-lime glass encompasses a narrow range of values, thanks to its standardized industrial production, see Table 3-2. Of note is that Eurocode lists a value of $E = 70$ GPa, which is used in structural design. However, this is the characteristic value, i.e. the 98th percentile of the collated annual extreme values for the random variable E . If the intention is, instead, to capture the most probable behavior of the glass element, a somewhat higher value is of interest, say 72 GPa.

Table 3-2: Elastic properties of soda-lime glass, compiled from various sources.

Young's modulus [GPa]	Poisson's ratio [-]	Source
70–73	0.23	Belis, et al., 2019
70–74	0.22	Bourhis, 2008
70–75	–	Burström & Nilvér, 2018
70–75	0.23	Button & Pye, 1993
70 (characteristic)	0.20 (characteristic)	CEN, 2016
63–77 (range)	0.20–0.25 (range)	
70–75	0.21	Falk, et al., 2011

Linear elastic response is the only deformation behavior exhibited by glass; once the stress surpasses the elastic domain, the material collapses because glass has no plastic capacity, i.e. it is not able to redistribute load upon local failure. Thus, the only deformation properties that are of interest are its modulus of elasticity and its Poisson's ratio. Furthermore, the total lack of a plastic capacity means that phenomena such as creep, stress relaxation, and fatigue are not applicable to glass at normal temperatures (Bourhis, 2008; Gonçalves, 2015).

There are numerous industrial methods used in glass production to manipulate its mechanical properties, such as heat-strengthening and tempering, see Section 3.3. However, these are concerned with implanting stress envelopes onto the material in order to manipulate its strength properties and post-breakage behavior, as opposed to modifying its deformation response. Thus, they have a negligible effect on the modulus of elasticity.

3.2.2 Strength and Failure Modes

The structural design of glass in ultimate limit state is a function of the material specimen's surface character (Rodichev & Veer, 2016). This is a result of the surface flaws that are, despite the highly standardized nature of glass production, ubiquitous to the material. Indeed, the theoretical strength of an atomically flawless glass specimen is high, with a tensile strength of approximately 20 GPa (Bourhis, 2008). (For the sake of comparison, the tensile strength of structural steel is 2 GPa.) As is the case for all brittle materials, however, the true strength is much lower, see Table 3-3; design codes recommend designing glass to withstand between 45 and 120 MPa in bending stress, depending on the glass type (Belis, et al., 2019). This conservatism is a direct result of the prevalence of surface flaws (defects).

Table 3-3: Dissonance between theoretical strength and values used in structural glass design. Source: Falk, et al. (2011).

Strength	Theoretical value [MPa]	Design value [MPa]
Compressive	~21,000	880–930
Tensile	~21,000	30–90
Bending	~21,000	30–100

The surface flaws come in many shapes and sizes, and can be traced to just as many sources, from mechanical perturbation to various stages in the manufacturing process (Rodichev & Veer, 2016). These surface flaws act as a conduit for crack development, which can rapidly drain the strength of the material. Once a crack is implanted onto the surface, even one as small as a microcrack, the energy required to propagate it is easily exceeded by the energy accumulated in the material when it is deformed elastically in the region of the crack, even if that deformation is minimal (Gonçalves, 2015). Thus, surface flaws create the conditions for cracks, thus compromising the loadbearing integrity of the glass specimen.

The failure mode of a glass specimen is determined, in part, by whether the material has been tempered, see Section 3.3. Glass that has only undergone annealing, i.e. glass that is not tempered, exhibits a comparatively low-energy fracture pattern, see Figure 3-3, while its tempered cousin is characterized by more explosive behavior. The latter is a result of the stress envelope that is definitive of tempered glass: a surface crack finds itself in the compressive zone, which, if allowed to propagate to the inner tensile zone, immediately increases the fracture energy, thereby yielding an explosive fracture pattern. However, the larger glass shards created by fractured annealed glass are sharper, and therefore more dangerous, than the glass dice created by breaking a tempered glass specimen. Post-breakage laminated glass is safer still because the fractured glass splinters tend to adhere to the polymer interlayer instead of collapsing onto the ground.



Figure 3-3: Principal breakage patterns of annealed (left) and tempered glass (right). Source: Custom Glass Products, 2020.

3.3 Flat Glass Variants and Glazing Products

Considering its myriad applications, it is no surprise that architectural glass is available in a multitude of types and finishes. Flat glass, in particular, has numerous finishing treatments that can be applied to it in the final stages of production, thus significantly altering its mechanical behavior, see Figure 3-4.

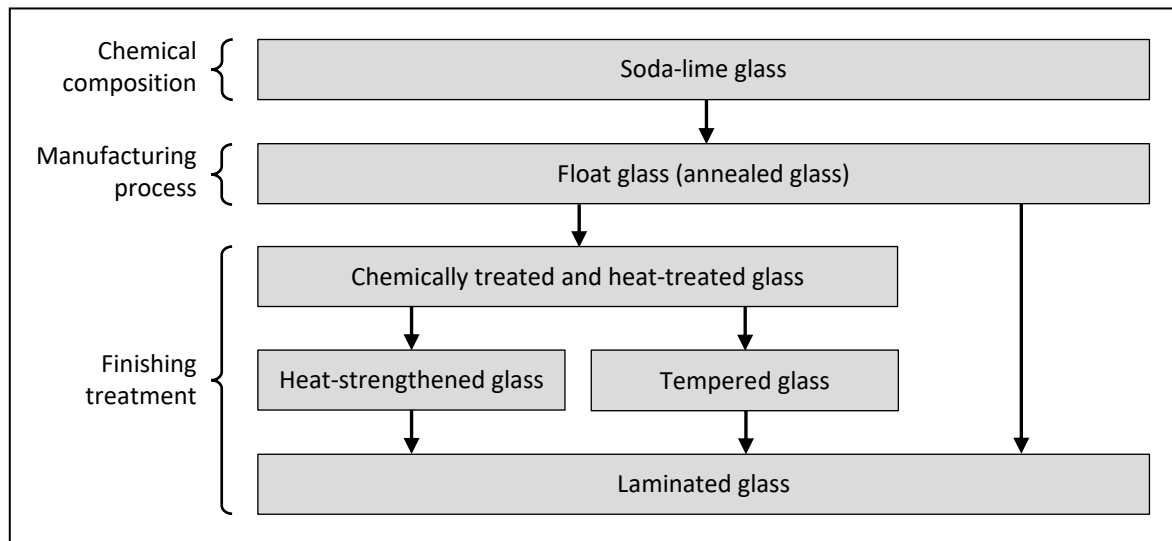


Figure 3-4: Typology of architectural glass products and their disposition within the production process.

3.3.1 Float Glass and Annealed glass

The flat glass panes used in most architectural applications are manufactured using the float process. Its namesake is derived from a particular stage in the manufacturing process wherein the raw materials that constitute soda-lime glass are poured into a molten tin bath, which, due to the higher density of the tin, causes the glass melt to rise to the surface and float. If properly executed, the glass melt forms a perfectly flat, uniform sheet, the thickness of which can be tailored to suit one's needs by adjusting the perimeter of the tin bath, and thereby the area of the melt. While floating, the glass melt is cooled from approximately 1050 °C to 600 °C (Gonçalves, 2015).

The high temperatures of the glass melt, if not handled carefully, can quickly induce unwanted internal stresses in the final specimens. The problem becomes particularly astute when considering that, if uncontrolled, the glass cools much too rapidly from its temperature of 600 °C, upon exiting the float chamber, to the ambient temperature. Therefore, all float glass enters an annealing chamber upon exiting the float chamber. When annealing, the material is slowly cooled in a controlled environment. Any post-processing, such as hole-drilling or lamination, typically take place after the annealing is complete. The glass sheets are then laser-cut to the appropriate size and readied for shipment.

3.3.2 Tempered Glass

Tempered, or toughened, glass refers to glass specimens that have been chemically or thermally treated, post-annealing, to improve its mechanical performance. The objective is to imprint a stress envelope onto the glass such that the surface becomes compressed while the interior is subjected to tension, see Figure 3-5. (This is entirely analogous with the residual stresses that are characteristic of steel beam profiles.) This is desirable because the strength of glass, being a brittle material, is governed by its tensile capacity and by the flaws that permeate its surface; the application of a compressive stress field to the surface, which locks the surface flaws into a permanent state of compression (Belis, et al., 2019). In so doing, the characteristic strength is significantly improved, from 45 MPa for annealed glass to approximately 100 MPa for its tempered counterpart. This, alone, means that tempered glass is of significant interest to the industry.

Beyond improved strength, the breakage pattern of tempered glass also deviates from that of annealed glass. While the latter shatters into sharp shards, the breakage pattern of the former is dense, breaking into blunt, dice-like fragments. As a result, tempered glass is often referred to as safety glass (Laniel, et al., 2019).

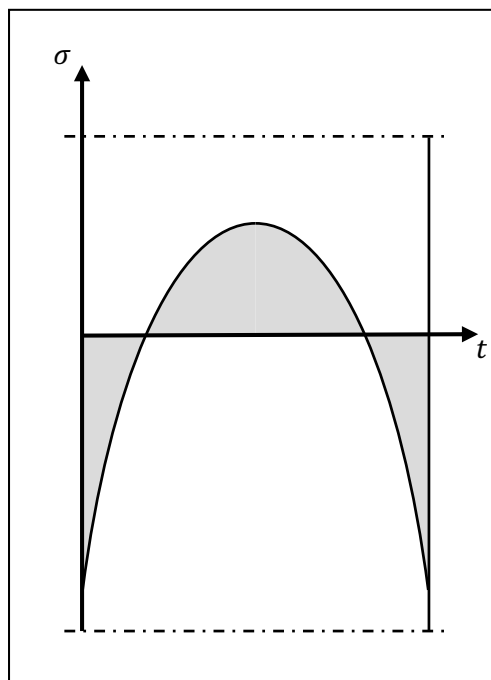


Figure 3-5: Residual stress profile (envelope) through the thickness t of a tempered glass specimen.

Most tempering is thermal, in which annealed glass is reheated to manufacturing-level temperatures, approximately 680 °C, and then rapidly cooled. The faster the cooling, the greater the tempering effects, in terms of both the added strength to the glass material and the improved safety to its fracture behavior.

3.3.3 Heat-strengthened Glass

Both tempering and heat strengthening are forms of heat treatment. The chief difference between the two is in the cooling rate of the glass. The cooling is slower for heat-strengthened glass, thereby inducing a residual stress profile through the specimen thickness that is less pronounced than if it had been tempered (Belis, et al., 2019). Heat-strengthened glass fractures similarly to annealed glass (Kinsella, 2018).

3.3.4 Laminated Glass

Laminated glass refers to a specimen assembly of alternating glass plies and polymeric sheets, although always bounded by the former, not the latter (Belis, et al., 2019). The polymeric sheets are referred to as interlayers, and are most commonly sourced from viscoelastic polymers, such as PVB. Laminated glass specimens are produced by placing the glass-polymer assembly in a heated autoclave. This creates an environment of 800 kPa and roughly 140 °C, thereby attaching the assembly members to one another through adhesion. This significantly improves its deformation response to loading, although this presumes full composite action, i.e. full shear transfer between the composite layers, which is far from always the case in reality. The usual culprit behind incomplete composite action is the interlayer.

There is a catalog of polymers available for use as interlayers in laminated glass products. The choice of polymer is determined by the specifications set for the laminated specimen in question, including architectural qualities, such as opacity and daylight control, acoustics, thermal insulation, and structural performance. The interlayers are highly viscoelastic and thermoplastic. For instance, the mechanical performance of PVB, the most common interlayer polymer, is only valid for the temperature range 10 °C to 45 °C (Gonçalves, 2015). Likewise, its stiffness decreases with a factor on the order of 10^2 when loading increases from only a couple of seconds to 24 hours (Kuraray, 2020). This reduction in stiffness can be transformed into a function of the interlayer's capacity to transfer shear stress, which is inversely proportional to the load duration. Thus, the smaller the load duration, the more the composite response of the laminated specimen is preserved, which is why laminated glass is ubiquitous as a safety glass—after all, loads such as bullets, explosions, and soft-body impacts are all relatively short-term. It is therefore prudent to investigate the viscoelastic properties of the interlayer when analyzing the mechanical behavior of laminated glass.

4 Technical Standards and Academic Research on Glass Subjected to Impact Loading

“Regelverket är för omfattande.”

—Göran Persson

This chapter reviews the work that has been done on analyzing and designing glass. The review is divided into two Sections: the first presents the prevailing technical standards and design codes that pertain to glass and its design with respect to impact; the second Section examines previous academic research on the same topic, particularly with an eye towards European standard EN 12600.

4.1 Design Codes and Technical Standards

4.1.1 Design Codes for Glass

For EU member states, there are two sets of design codes that steer structural design: these apply either on a national level or for the European Union as a whole.

The Eurocodes are harmonized technical rules specifying the conduct of structural design within the European Union. No such standard has been approved by the European Commission for glass design, but one is currently in development (Joint Research Center of the European Commission, 2014). The formative Eurocode on glass includes stipulations on everything from material parameters to beam and plate design. The formative code is explicit in stating that secondary structural elements (e.g. glazing) must be designed with attention to protection against impact, and in so doing safeguard the robustness and safety of the structure/element.

Consistent with national codes, the document recommends that, in its final form, the glass Eurocode should specify the verification of secondary structures for, among other things, dynamic impact loading. To do this, either testing should be carried out according to EN 12600 or numerical methods should be adopted. The latter can take the form of either a transient

finite element simulation of EN 12600 or as an appropriate double-mass-oscillator combined with beam or plate theory (Joint Research Center of the European Commission, 2014). (Consistent with these recommendations, a two-degree-of-freedom system, i.e. a double-mass-oscillator, is investigated in Chapter 6, while finite element models are the subject of Chapters 8 and 9.)

National design codes for glass exist in numerous EU member states, including Germany, Austria, the Czech Republic and Italy. The impact requirements for glass set by each of these design codes are variable. Most rely on EN 12600, or an analogous national standard, for classifying and verifying glass with respect to soft-body impact. The national codes also recommend finite element analysis as a tool for designing glass against dynamic loading.

4.1.2 European Standard on Experimental Verification of Soft-body Impact

European Standard EN 12600 outlines a test method for soft-body impact on glass and subsequent classification of the glass based on its performance (CEN, 2002). The test apparatus consists of an impactor that is hung from a wire so as to enable pendulum action against a glass pane that is fixed on all sides. The glass is secured by being fixed to a rigid frame. To safeguard against stress concentrations and local fracture of the glass, rubber strips are installed between the frame and the glass (CEN, 2002).

The impactor comprises a steel core that is surrounded by two rubber tires, inflated to 350 kPa, totaling 50 kg in mass (CEN, 2002). The dual-tire impactor is hung from a steel wire that is fixed to a bracket above the main frame, thereby enabling pendulum action against the glass. In so doing, the impactor can strike the glass specimen at its geometric center with variable energy by adjusting the drop height, that is to say by adjusting the starting position of the pendulum body (CEN, 2002).

The standard provides for three principal classes with corresponding drop heights, namely 190 mm, 450 mm, and 1200 mm (CEN, 2002). After being struck by the impactor four times, the response of the glass is evaluated and categorized according to its mode of breakage for each drop height. Three such breakage modes are specified:

- Type A: numerous cracks appear forming separate fragments with sharp edges, some of which are large, typical of annealed glass.
- Type B: numerous cracks appear, but the fragments hold together and do not separate, typical of laminated glass.
- Type C: disintegration occurs, leading to a large number of small particles that are relatively harmless, typical of toughened glass.

The standard does not set requirements based on the intended use of the glass, nor does it allow for other boundary conditions.

4.2 Academic Research

Soft-body impact on glass and EN 12600 have been the subject of numerous studies in the academic literature. Several have modeled the test apparatus numerically, with high-detail models of the dual-tire impactor and hyperelastic material models for the tire rubber and interlayer polymer (Boeykens & Van den Bosch, 2014; Pelfrane, et al., 2016). The numerical results are in good agreement with their experimental counterparts, but they increasingly deviate as drop height decreases: for 700 mm drop height, the force and impact time deviate by approximately 7%, while for 200 mm drop height they deviate by approximately 20%. The authors attribute the phenomenon to flaws in the experimental testing procedure.

Still others have modeled the dual-tire impactor from EN 12600 and applied it to glass with ulterior boundary conditions, principally a free-standing balustrade (Kozłowski, 2019; Kozłowski, et al., 2020). (These articles draw experimental data from the same source as this thesis and use a similar methodology.) The maximum stresses captured by the numerical model are well within an acceptable range, deviating from the experiments by approximately 5%.

Another approach has been to utilize modal analysis of the glass in operating conditions to estimate its performance during impact (Ramos, et al., 2015). This has yielded good agreement between experimental and numerical accelerations. However, only a 100 mm drop height was tested.

Other authors have investigated the applicability of reduced models to glass impact, such as with Ritz vectors (Fröling, 2013). Studying a glass pane fixed at all sides and a free-standing balustrade, a single Ritz vector did not capture the maximum stresses accurately. However, two Ritz vectors were found to be sufficient, deviating approximately 10% from the respective finite element simulations.

5 Experimental Setup and Results

“Nobody can say what a variable is.”

—Hermann Weyl

The first Section of this chapter presents the experimental test setups. Emphasis is placed on the connections used to fasten the glass to the steel frame during the experimental campaign, as these have a decisive effect on the modeling, and thereby the results. The second Section presents the experimental data.

5.1 Setup

The experimental setup was built to meet the requirements set out in EN 12600, see Figure 1-1. That standard is only concerned with one boundary condition, i.e. the four-sided fixed boundary condition. In this study, three ulterior boundary conditions—fastener configurations—are investigated. These are neither based on nor intended to comply with the above standard.

The test apparatus consists of three parts:

- A primary frame: this is built using HEB160 steel beams, connected rigidly with bolts.
- A fastening frame: this is the setup variable, as the method used to fasten the glass specimens to the primary frame are determined by the fastener configuration.
- A 50 kg dual-tire impactor: it is hung from a steel wire to enable pendulum action against the center of the glass specimen.

The setup was fixed to the ground by bolting the lower HEB160 beam to a rigid steel structure, see Figure 5-1. Likewise, the upper beam of the setup was fastened to the same steel rigid structure in the back, improving rigidity.



Figure 5-1: Examples of the experimental setup, with simply supported (left) and bolted (right) fastener configurations.

The simply supported connection was created by mounting C160-beams vertically to the I-beams of the primary frame. A gap was left for the glass specimen between the surfaces of the C- and I-beams. Only one line of bolts was used to fasten the C-beams to the primary frame, and these were not positioned along the centerline of the C-beam. As a result of the asymmetry, pretensioning of the bolts generated a rotation in the C-beam. The precise angle of rotation is unknown, but it has been deemed to be significant. Finally, an EPDM rubber strip was placed between the glass and the steel beams to insure against wanton damage to the glass.

The bolted connection was achieved by placing a bolt through a predrilled hole in each corner of the glass, see Figure 5-2. The bolts were fastened with two nuts: one behind the glass to induce pretension in the glass-bolt head connection, and one behind the vertical HEB-beam to secure the bolts to the primary frame. The insides of the bolt heads were lined with 2 mm thick EPDM rubber to ensure a safe connection, see thereby protecting the glass.

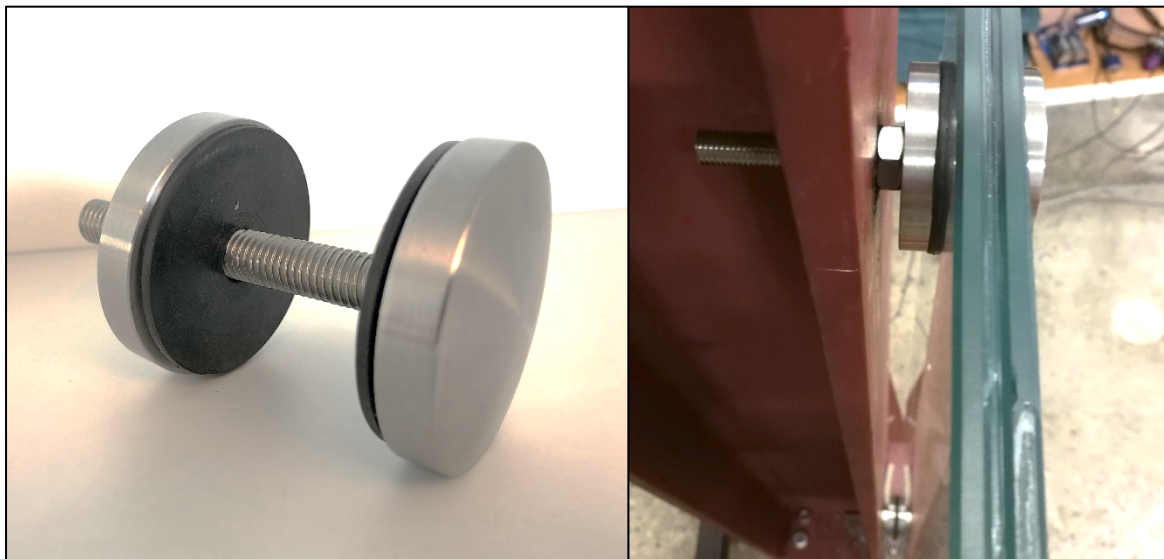


Figure 5-2: Close-ups of the bolt (left) and the bolted connection (right).

The clamped connection required fixing perpendicular to the main frame, see Figure 5-3. Thus, the C-beams from Setup 1 were reintroduced, translated outwards from the frame center such that the edge of the C-beam was lined up with the centerline of the vertical I-beams. The clamps were bolted into the flange of the C-beam. Consistent with the bolts of setup two, the inside of the clamps was lined with a thin 2 mm EPDM gusset.

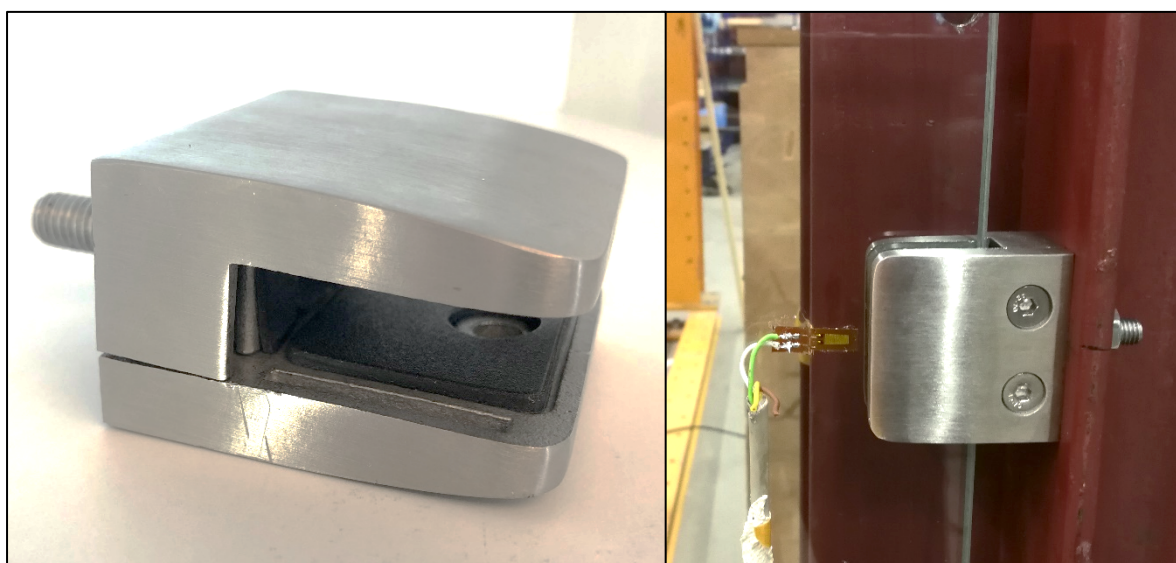


Figure 5-3: Close-ups of the clamp (left) and the clamped connection (right). The clamp is attached to the flange of a C-beam.

The dual-tire impactor was built in accordance with EN 12600. Two pneumatic tires were mounted onto a solid steel core, amassing 50 kg, including the pressurized air. The tires were inflated to 350 kPa, which was controlled after each hit. To achieve pendulum action, the impactor was hung from a rope, which in turn was connected to a steel wire. This may have created a hinge in the pendulum. The pendulum was calibrated to ensure that, while at rest,

the impactor circumference was between 5 and 15 mm away from the glass surface. This ensures that impact occurs with maximum velocity and minimum angle from the horizontal.

In terms of data acquiring, acceleration and strain was collected for the setups. Two accelerometers were used; one placed on the steel core of the impactor, and the other in the center of the backside of the glass. Strain was measured using horizontally oriented strain gauges, located on the glass next to the accelerometer. Additional strain gauges were used for setup two and three, located in the corners of the glass, next to its fixing device.

Interlayer thickness has been found to be somewhat thicker than advertised by the supplier (Fors, 2014). This is likely to have been the case for the glass specimens used in the experimental campaign, as well: by comparing the masses provided by the glass manufacturer with masses calculated based on nominal densities and thicknesses, a discrepancy was found. This discrepancy is eliminated when the thickness of the interlayer is increased from the nominal 1.52 mm to 1.60 mm. Although the interlayer is only a small proportion of the total specimen mass, its contribution to the stiffness is far more significant.

5.2 Results

5.2.1 Experimental Campaign

Both the strain and the out-of-plane acceleration of the glass specimen were measured at the impact location. Once the data was processed, each hit series (i.e. all impacts corresponding to the same glass specimen, fastener configuration, and drop height) was collated. The hit series were averaged in order to obtain a representative data set of the glass specimen's transient behavior. Examples of this are shown in Figure 5-4. All of the processed stresses and accelerations from the experimental campaign are presented in a similar manner in Annex A and Annex B, respectively. For those cases in which a particular data series is corrupt or yields unrealistic results, the series was discarded and is not included in the averaged data series.

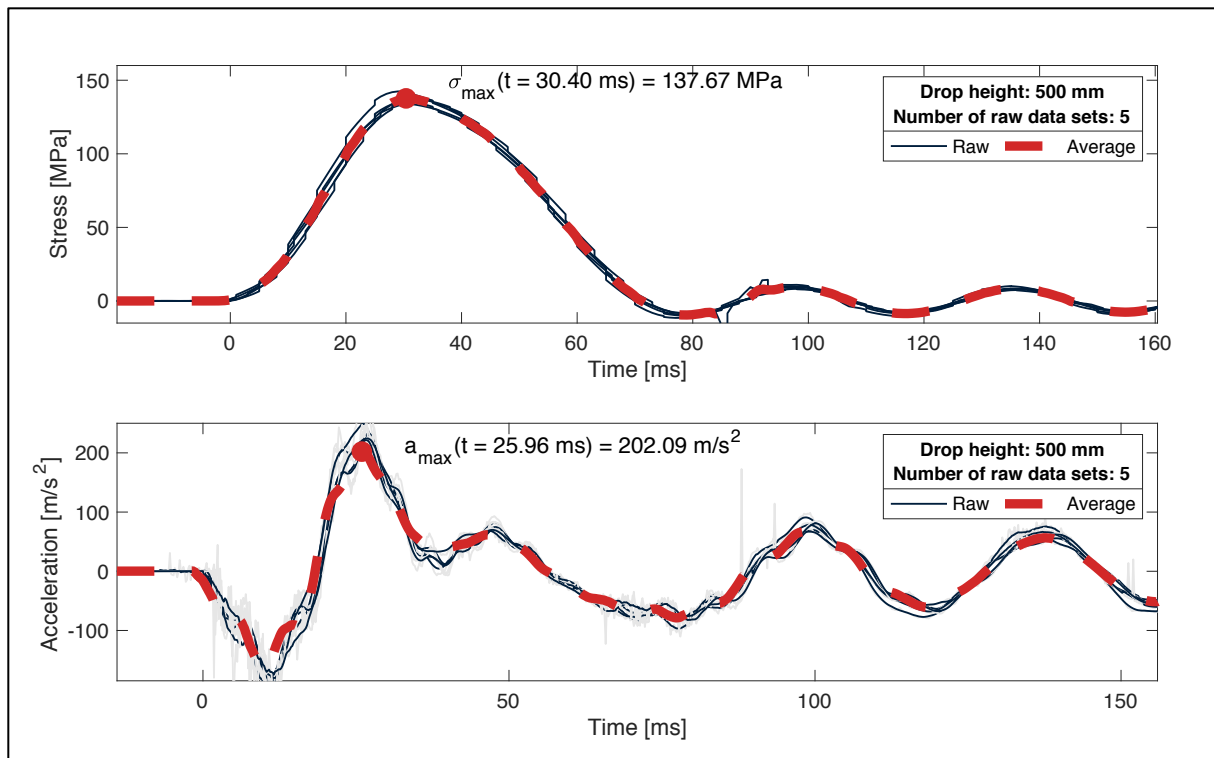


Figure 5-4: Examples of the processed experimental data. The data are derived from a strain gauge and an accelerometer during the experimental campaign. The data sets correspond to simply supported monolithic specimens with a thickness profile of 10 mm.

5.2.2 Impactor Tests

The impactor was subjected to two tests in order to verify that its behavior was in accordance with that mandated by EN 12600, see Section 2.4.2. The first of these tests is the displacement-controlled static compression test, the results of which are shown in Figure 5-5. The test yielded consistent results across multiple data sets, which denotes a promising degree of reliability.

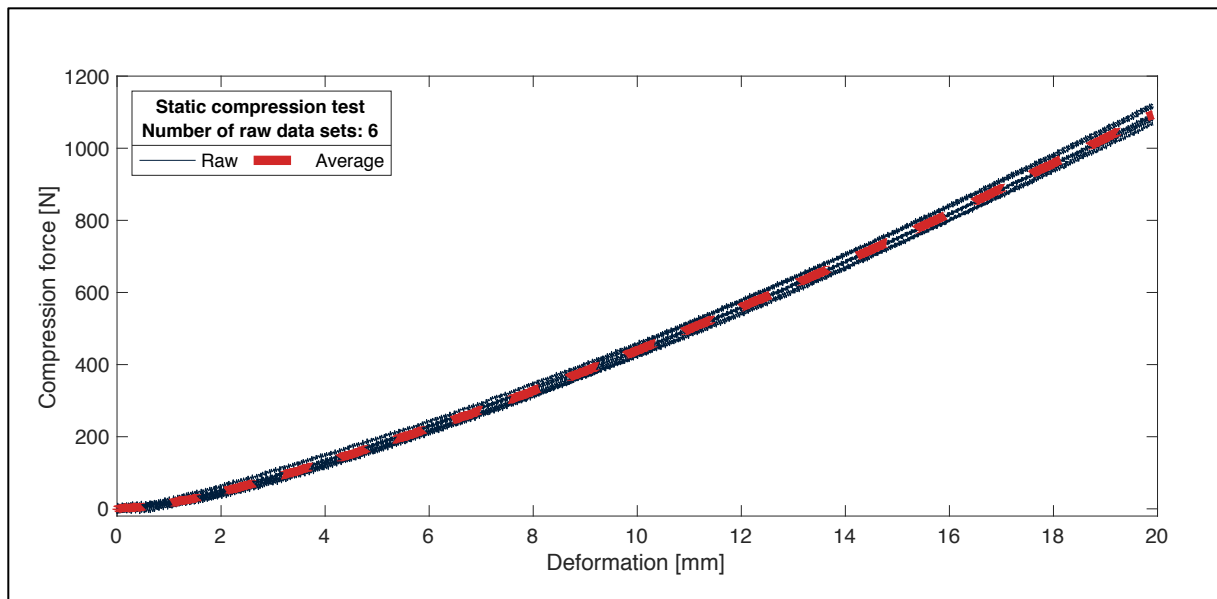


Figure 5-5: Experimental results of the displacement-controlled static compression test performed on one of the impactor tires.

The second test is the dynamic rigid impact test, the results of which are shown in Figure 5-6. Here, too, the test data sets exhibit only minor deviations from one another.

Of note is that the dynamic rigid impact test can be used to estimate the stiffness of the impactor, which is of interest for any semi-analytical calculations. Noting that $\omega = \sqrt{k/m}$, rewriting the expression for the period of a sinusoidal signal gives

$$T = \frac{2\pi}{\omega}$$

$$\Rightarrow k_{\text{dyn}} \approx m \left(\frac{2\pi}{T} \right)^2 \tag{5-1}$$

Using Eq. (5-1) and the data illustrated in Figure 5-6, the dynamic stiffness is estimated for the tested drop heights, see Table 5-1.

Table 5-1: Estimated dynamic stiffness of the impactor for various drop heights.

Drop height [mm]	Half-period [ms]	Dynamic stiffness [kN/m]
100	39	324
200	37	360
300	35	403
450	33	453
700	31	514

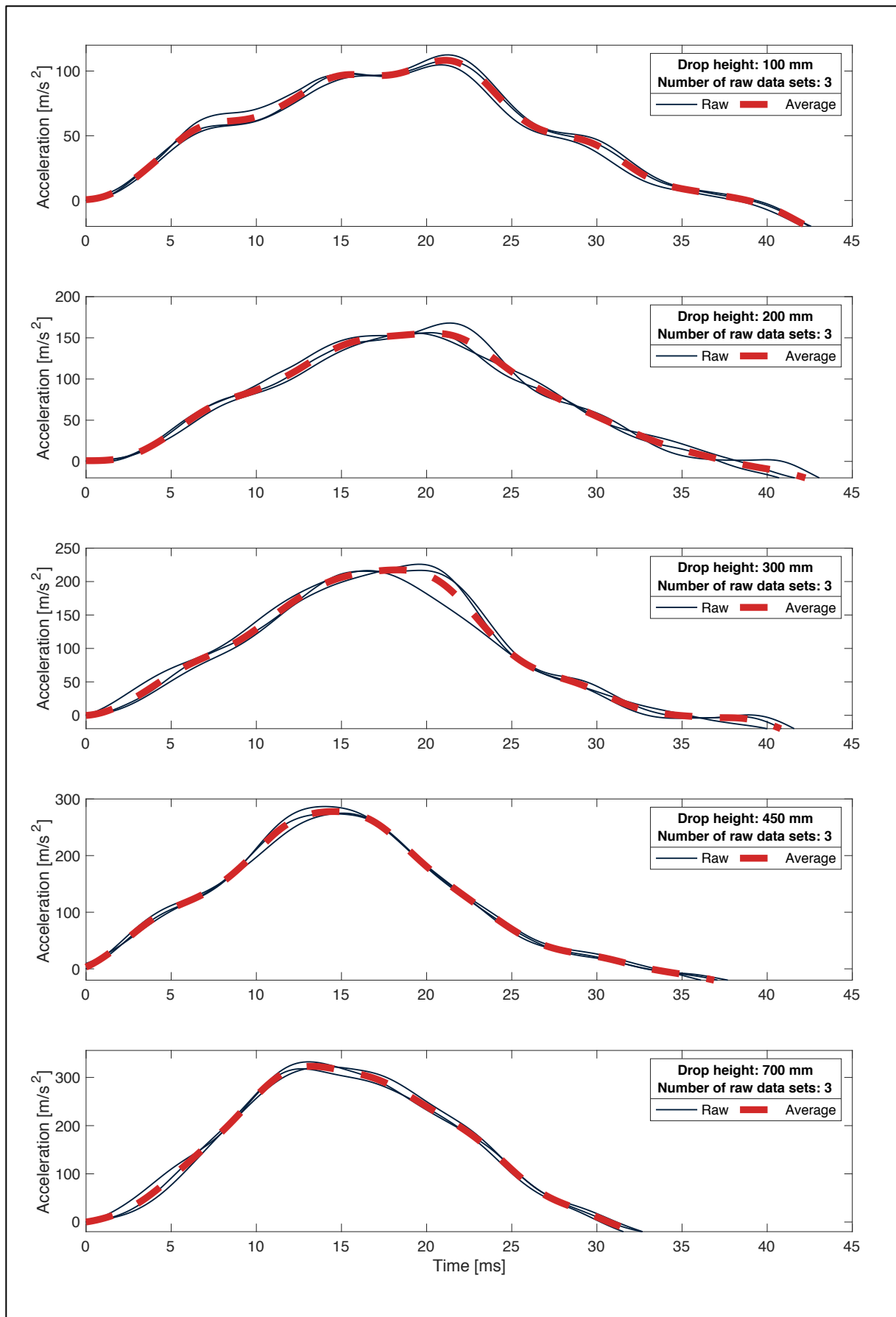


Figure 5-6: Experimental results of the dynamic rigid impact test performed on the dual-tire impactor.

6 Semi-analytical Model

“An ideal math talk should have one proof and one joke and they should not be the same.”

—Ron Graham

In an effort to elucidate the underlying mechanics at play in the glass-impactor system, this chapter adopts a comparatively qualitative approach to describing the dynamic behavior of the system. This is accomplished by condensing the complexity intrinsic to the experimental setup into two components: the glass panel and the impactor. More precisely, the system is discretized into two degrees of freedom, after which its behavior when subjected to an impact load is studied. This behavior is modeled by likening it to the system’s free vibration response, which is captured analytically by means of modal analysis. Finally, the model is studied parametrically and select results are presented.

6.1 General Overview

Most of the dynamic systems found in nature are continuous, with the quantity of their degrees of freedom tending towards infinity. This tendency presents an obvious hindrance to their technical study. The difficulty is compounded by the mathematics, inherent to these systems, dictating that they be modeled by means of partial differential equations—these are often difficult, if not outright impossible, to solve. As a result, another avenue of approach is required if the investigation of such systems is to be rendered more practicable.

One such avenue is through the discretization of the continuous system into a multi-degree-of-freedom (MDOF) system, in which each degree of freedom corresponds to one possible form of motion linked to a particular mass. In mathematical terms, this means that the system’s vibration behavior is instead captured by ordinary differential equations, which lend themselves to more amenable solution methods than their partial differential cousins.

Notwithstanding the discretization, one mathematical obstruction persists: the differential equations remain coupled, but, for economic reasons, it is highly desirable to uncouple them. This can be accomplished by invoking linear algebra, where it is well known that any set of N independent vectors can be used as a basis for expressing any other vector of the order N . In the present context of a dynamic system, having been modeled as a set of discrete points

(degrees of freedom), the system can therefore also be modeled with the aid of a basis. The choice of basis now assumes importance.

It is noted that a critical property of any vibrating system is that its behavior, however arbitrary, can be expressed as a superposition of its harmonics. It is therefore extrapolated that the vibration behavior of a dynamic system can be expressed as the superposition of its natural vibration modes $\boldsymbol{\phi}_n$. These natural modes therefore constitute a basis (and the deflection shapes are time invariant). More explicitly, the $\boldsymbol{\Phi}$ -basis describes the system displacements through

$$\mathbf{u}(t) = \sum_{n=1}^N \boldsymbol{\phi}_n q_n(t) = \boldsymbol{\Phi} \mathbf{q}(t) \quad (6-1)$$

where $\mathbf{q}(t) = [q_1, q_2, \dots, q_N]^T$ are the modal coordinates. This is of interest because, in mathematical terms, the differential equations have now been uncoupled, and the displacements can be solved with linear algebra. This method is termed classical modal analysis. One limitation with it is that it places certain requirements on the system with respect to damping, namely (Chopra, 2014):

- the damping ratios ζ_n may not exceed 20%;
- the structure's subsystems may not exhibit wildly differing levels of damping.

It is safe to assume that neither of these conditions are violated in the case of the glass-impactor dynamic system. Indeed, it is presumed that the system exhibits classical damping.

In short, modal analysis can be used to establish the dynamic response of an MDOF system to any disruption to static equilibrium, such as through external loading or by means of initial displacement and/or the imparting of initial velocities. The latter class of disruptions is of particular interest, given that it pertains to free vibration. The execution of such a modal analysis, with respect to free vibration, is summarized with the following sequence:

1. Establish the equations of motion describing the system's free vibration response, see Section 6.2.
2. Using Eigenanalysis, calculate the natural frequencies ω_n of the system, alongside the corresponding natural vibration modes $\boldsymbol{\phi}_n$, see Section 6.3.
3. For each natural vibration mode $\boldsymbol{\phi}_n$, determine its contribution $\mathbf{u}_n(t)$ to the system response by computing the matching modal coordinate $q_n(t)$, see Section 6.4. Then compute the total system response $\mathbf{u}(t)$ by superimposing the modal displacements $\mathbf{u}_n(t)$.
4. Define the structural properties of the system, see Section 6.5. This involves determining the masses m_i and stiffnesses k_i of the system, alongside estimating the damping ratios ζ_n associated with each vibration mode $\boldsymbol{\phi}_n$, where $n = \{1, 2, \dots, N\}$.

6.2 System Assembly and Equations of Motion

The glass-impactor system is discretized into two degrees of freedom, such that the glass and impactor are each represented by a single mass m_i , and each mass is permitted one form of motion, u_i , see Figure 6-1. The masses are linked together by constituent springs k_i and viscous damping coefficients c_i . Taken together, these parts form a two-degree-of-freedom (2DOF) system, where the indices 1 and 2 represent the glass and impactor, respectively.

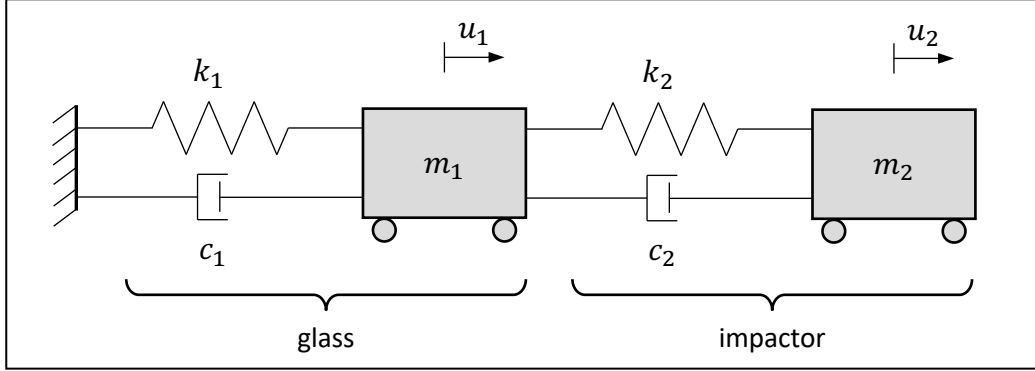


Figure 6-1: Discretization of the glass-impactor system into a 2DOF system.

For each degree of freedom, an additional equation is required to describe the behavior of the system. Freebody diagrams of each mass illustrate the forces acting on each mass, see Figure 6-2.

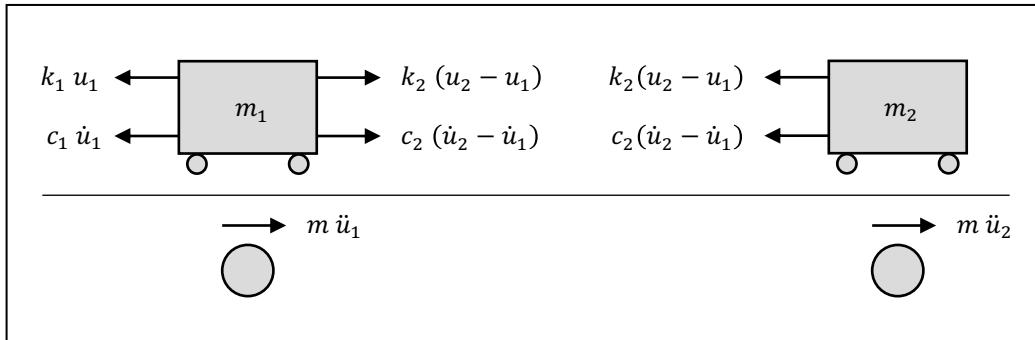


Figure 6-2: Freebody diagrams of the masses in the 2DOF system.

Utilizing Newton's Second Law of Motion, the equation of motion for each mass is derived:

$$\begin{cases} -k_1 u_1 + k_2 (u_2 - u_1) - c_1 \dot{u}_1 + c_2 (\dot{u}_2 - \dot{u}_1) = m_1 \ddot{u}_1 \\ -k_2 (u_2 - u_1) - c_2 (\dot{u}_2 - \dot{u}_1) = m_2 \ddot{u}_2 \end{cases}$$

$$\Leftrightarrow \begin{cases} m_1 \ddot{u}_1 + (c_1 + c_2) \dot{u}_1 - c_2 \dot{u}_2 + k_1 u_1 + k_2 (u_2 - u_1) = 0 \\ m_2 \ddot{u}_2 - c_2 \dot{u}_1 + c_2 \dot{u}_2 + k_2 (u_2 - u_1) = 0 \end{cases} \quad (6-2)$$

Written in matrix form, Eq. (6-2) becomes

$$\begin{bmatrix} m_1 & 0 \\ 0 & m_2 \end{bmatrix} \begin{bmatrix} \ddot{u}_1 \\ \ddot{u}_2 \end{bmatrix} + \begin{bmatrix} c_1 + c_2 & -c_2 \\ -c_2 & c_2 \end{bmatrix} \begin{bmatrix} \dot{u}_1 \\ \dot{u}_2 \end{bmatrix} + \begin{bmatrix} k_1 + k_2 & -k_2 \\ -k_2 & k_2 \end{bmatrix} \begin{bmatrix} u_1 \\ u_2 \end{bmatrix} = \begin{bmatrix} 0 \\ 0 \end{bmatrix}$$

$$\Leftrightarrow \mathbf{m}\ddot{\mathbf{u}} + \mathbf{c}\dot{\mathbf{u}} + \mathbf{k}\mathbf{u} = \mathbf{0} \quad (6-3)$$

The equations of motion for the 2DOF system have now been derived and formulated in matrix form, where

$$\mathbf{m} = \begin{bmatrix} m_1 & 0 \\ 0 & m_2 \end{bmatrix}; \quad \ddot{\mathbf{u}} = \begin{bmatrix} \ddot{u}_1 \\ \ddot{u}_2 \end{bmatrix};$$

$$\mathbf{c} = \begin{bmatrix} c_1 + c_2 & -c_2 \\ -c_2 & c_2 \end{bmatrix}; \quad \dot{\mathbf{u}} = \begin{bmatrix} \dot{u}_1 \\ \dot{u}_2 \end{bmatrix};$$

$$\mathbf{k} = \begin{bmatrix} k_1 + k_2 & -k_2 \\ -k_2 & k_2 \end{bmatrix}; \quad \mathbf{u} = \begin{bmatrix} u_1 \\ u_2 \end{bmatrix}$$

Eq. (6-3) is applicable for any viscously damped MDOF system. Having formulated the equations of motion, the overarching objective now is to solve the equations for the system deformation response \mathbf{u} .

6.3 Eigenanalysis

The equations of motion for a viscously damped MDOF system undergoing free vibration are given by Eq. (6-3). This constitutes a system of second-order linear ordinary differential equations, the quantity of which is equivalent to the order N of the matrices composing the equations of motion, that is to say, the number of degrees of freedom N . Under the assumption that the free vibration motion of the system is simple harmonic, a reasonable trial solution for this system of differential equations is

$$\mathbf{u} = [\mathbf{A} \cos \Omega t + \mathbf{B} \sin \Omega t] \Phi \quad (6-4)$$

where $\{\mathbf{A}, \mathbf{B}\} \in \mathbb{R}$ for classically damped systems. It follows that the first and second order derivatives of this trial solution are, respectively,

$$\dot{\mathbf{u}} = \Omega [\mathbf{A} \sin \Omega t - \mathbf{B} \cos \Omega t] \Phi$$

$$\ddot{\mathbf{u}} = -\Omega^2 [\mathbf{A} \cos \Omega t + \mathbf{B} \sin \Omega t] \Phi$$

Insertion of the trial solution and its derivatives into the equations of motion, Eq. (6-3), gives the unwieldy expression

$$[\mathbf{k} - \Omega^2 \mathbf{m}] \Phi [\mathbf{A} \cos \Omega t + \mathbf{B} \sin \Omega t] + \mathbf{c} \Omega [\mathbf{A} \sin \Omega t - \mathbf{B} \cos \Omega t] \Phi = \mathbf{0} \quad (6-5)$$

However, it is noted that for damped systems in which the damping ratios $\zeta_n < 0.2$, as in the present case, the damping term may be neglected (Chopra, 2014). Furthermore, the

homogeneity of Eq. (6-5) allows the constants $[\mathbf{A} \cos \Omega t + \mathbf{B} \sin \Omega t]$ to be discarded. Thus, Eq. (6-5) reduces to

$$[\mathbf{k} - \Omega^2 \mathbf{m}] \Phi = \mathbf{0} \quad (6-6)$$

This is a set of N homogenous algebraic equations, and can have both trivial and nontrivial solutions. The former is given by $\Phi = \mathbf{0}$, which is uninteresting because it implies that there is no motion in the system. However, Eq. (6-6) also constitutes an eigenvalue problem, for which nontrivial solutions exist on the condition that

$$\det[\mathbf{k} - \Omega^2 \mathbf{m}] = 0 \quad (6-7)$$

which, for the case with \mathbf{k} and \mathbf{m} defined according to Section 6.2, gives

$$\begin{vmatrix} k_1 + k_2 - m_1 \omega_n^2 & -k_2 \\ -k_2 & k_2 - m_2 \omega_n^2 \end{vmatrix} = 0$$

$$\Leftrightarrow k_1 k_2 - k_1 m_2 \omega_n^2 + k_2^2 - k_2 m_2 \omega_n^2 - k_2 m_1 \omega^2 + m_1 m_2 \omega^4 - k_2^2 = 0 \quad (6-8)$$

This characteristic equation is of the fourth order. The analytical solution yields the eigenvalues ω_n^2 , where $n = \{1,2\}$. In turn, Eq. (6-8) thereby yields the natural frequencies of the system, and are of the form

$$\omega_n = \sqrt{\frac{k_1 m_2 + k_2 m_2 + k_2 m_1 \pm \sqrt{(k_1 m_2 + k_2 (m_1 + m_2))^2 - 4 k_1 k_2 m_1 m_2}}{2 m_1 m_2}} \quad (6-9)$$

The associated eigenvectors Φ , that is to say, the natural vibration modes of the system, are given by inserting the diagonalized matrix of eigenvalues, Ω , and solving Eq. (6-6). (The resulting analytical expression is unwieldy and is therefore not presented here.)

To verify the results, it is recalled that eigenvectors must be orthogonal to one another. Note that this is consistent with the presumption that the natural vibration modes constitute a basis. (If this eigenvector orthogonality were not the case, then the natural vibration modes would not constitute a basis; a physical consequence would be that the work done by the i th-mode inertia forces when going through the j th-mode displacements would be nonzero, which is illogical.) For the natural frequencies $\omega_i \neq \omega_j$, modal orthogonality may be verified by referring to the eigenvalue problem in Eq. (6-6) and invoking linear algebra:

$$\Phi_i \perp \Phi_j \Leftrightarrow \begin{cases} \Phi_i^T \mathbf{k} \Phi_j = 0 \\ \Phi_i^T \mathbf{m} \Phi_j = 0 \end{cases}$$

where $i \neq j$. In this instance, there are only two degrees of freedom, and thus $i = 1, j = 2$.

6.4 Modal Analysis

Returning to the equations governing the free vibration response of a damped system, Eq. (6-3), it is observed that this is a set of homogenous and linear ordinary differential equations of the second order. The homogeneity implies that the general solution is equal to the homogenous solution,

$$\begin{cases} \mathbf{u} = \mathbf{u}_h + \mathbf{u}_p \\ \mathbf{u}_p = \mathbf{0} \end{cases} \Leftrightarrow \mathbf{u} = \mathbf{u}_h \quad (6-10)$$

It is therefore sufficient to determine the homogenous solution in order to arrive at a general solution to the equations of motion. Thus, a method is required that yields the homogenous solution while also uncoupling the differential equations. The first step is to uncouple the differential equations.

6.4.1 Transformation into Diagonalized System Using Modal Equations

Recalling that the displacements of an MDOF system may be expressed with the help of a time-invariant basis Φ such that

$$\mathbf{u}(t) = \Phi \mathbf{q}(t) \quad (6-11)$$

it is clear that $\mathbf{u} = \Phi \mathbf{q}$, $\dot{\mathbf{u}} = \Phi \dot{\mathbf{q}}$, and $\ddot{\mathbf{u}} = \Phi \ddot{\mathbf{q}}$. Accordingly, the equations of motion are rewritten as

$$\mathbf{m}\Phi\ddot{\mathbf{q}} + \mathbf{c}\Phi\dot{\mathbf{q}} + \mathbf{k}\Phi\mathbf{q} = \mathbf{0} \quad (6-12)$$

Premultiplying Eq. (6-12) by Φ^T gives

$$\mathbf{M}\ddot{\mathbf{q}} + \mathbf{C}\dot{\mathbf{q}} + \mathbf{K}\mathbf{q} = \mathbf{0} \quad (6-13)$$

where the orthogonality of the natural modes yields the diagonal matrices

$$\mathbf{M} \equiv \Phi^T \mathbf{m} \Phi \quad (6-14a)$$

$$\mathbf{K} \equiv \Phi^T \mathbf{k} \Phi \quad (6-14b)$$

$$\mathbf{C} \equiv \Phi^T \mathbf{c} \Phi \quad (6-14c)$$

Despite the damping present in the system, this diagonality is made possible by the fact that the damping exhibited by the system is classical (proportional). As a result, the differential equations are now fully uncoupled. Deriving homogenous solutions to the differential equations is now rendered practicable.

6.4.2 Solution to Homogenous Linear Differential Equation of the Second Order

Referring to one-dimensional calculus, it is well known that a differential equation of the form $y'' + ay' + by = 0$ has the solution

$$y = e^{\alpha x}(A \cos \beta x + B \sin \beta x) \quad (6-15)$$

where α and β are nonzero constants such that

$$\lambda = \alpha \pm i\beta \quad (6-16)$$

and where λ is a solution to the associated characteristic equation

$$\lambda^2 + a\lambda + b = 0 \quad (6-17)$$

Applying this method to the problem at hand, it is now of interest to rewrite Eq. (6-13) such that

$$\ddot{\mathbf{q}} + \frac{\mathbf{C}}{\mathbf{M}}\dot{\mathbf{q}} + \frac{\mathbf{K}}{\mathbf{M}}\mathbf{q} = \mathbf{0} \quad (6-18)$$

The resulting characteristic equations to Eq. (6-18) are

$$\lambda^2 + \frac{\mathbf{C}}{\mathbf{M}}\lambda + \frac{\mathbf{K}}{\mathbf{M}} = \mathbf{0} \quad (6-19)$$

where λ is a diagonal matrix containing the roots λ_i . It is recalled that all of the terms in Eq. (6-18) are diagonal matrices of the order N . Furthermore,

$$\begin{cases} \mathbf{C} = 2\boldsymbol{\zeta}\mathbf{M}\boldsymbol{\Omega} \\ \mathbf{K} = \boldsymbol{\Omega}^2\mathbf{M} \end{cases} \quad (6-20)$$

where $\boldsymbol{\zeta}$ is a vector containing the modal damping ratios ζ_n . The roots of Eq. (6-19) are thereby derived using the quadratic equation:

$$\begin{aligned} \lambda &= \frac{1}{2} \left[-\frac{\mathbf{C}}{\mathbf{M}} \pm \sqrt{\frac{\mathbf{C}^2}{\mathbf{M}^2} - 4\frac{\mathbf{K}}{\mathbf{M}}} \right] = \\ &= \frac{1}{2} \left[-\frac{2\boldsymbol{\zeta}\mathbf{M}\boldsymbol{\Omega}}{\mathbf{M}} \pm \sqrt{\frac{(2\boldsymbol{\zeta}\mathbf{M}\boldsymbol{\Omega})^2}{\mathbf{M}^2} - 4\frac{\boldsymbol{\Omega}^2\mathbf{M}}{\mathbf{M}}} \right] = \\ &= \frac{1}{2} \left[-2\boldsymbol{\zeta}\boldsymbol{\Omega} \pm \sqrt{4\boldsymbol{\zeta}^2\boldsymbol{\Omega}^2 - 4\boldsymbol{\Omega}^2} \right] = \\ &= -\boldsymbol{\zeta}\boldsymbol{\Omega} \pm \boldsymbol{\Omega}\sqrt{\boldsymbol{\zeta}^2 - 1} = \\ &= -\boldsymbol{\zeta}\boldsymbol{\Omega} \pm i\boldsymbol{\Omega}\sqrt{1 - \boldsymbol{\zeta}^2} \end{aligned} \quad (6-21)$$

Comparing Eq. (6-21) to Eq. (6-16), it is clear that

$$\begin{cases} \boldsymbol{\alpha} = -\zeta \boldsymbol{\Omega} \\ \boldsymbol{\beta} = \boldsymbol{\Omega} \sqrt{1 - \zeta^2} \equiv \boldsymbol{\Omega}_D \end{cases} \quad (6-22)$$

where $\boldsymbol{\Omega}_D$ is termed the natural frequencies of damped vibration matrix. The homogenous solution to the set of differential equations given by Eq. (6-18) is thereby determined to be

$$\mathbf{q} = e^{-\zeta \boldsymbol{\Omega} t} [\mathbf{A} \cos[\boldsymbol{\Omega}_D t] + \mathbf{B} \sin[\boldsymbol{\Omega}_D t]] \quad (6-23)$$

where $\{\mathbf{A}, \mathbf{B}\} \in \mathbb{R}$ and are prescribed by the initial conditions of the system. Extracting these constants is the next objective.

6.4.3 Initial Conditions

Analysis has thus far revealed that the displacement response of the MDOF system is given by

$$\mathbf{u}(t) = \boldsymbol{\Phi} \mathbf{q}(t) \quad (6-24)$$

where the modal coordinates have been derived to be

$$\mathbf{q} = e^{-\zeta \boldsymbol{\Omega} t} [\mathbf{A} \cos[\boldsymbol{\Omega}_D t] + \mathbf{B} \sin[\boldsymbol{\Omega}_D t]] \quad (6-25)$$

The initial conditions of the system describe the kinematics that initiate the motion of the system. The conditions therefore take the form of

$$\mathbf{u} = \mathbf{u}(t = 0), \quad \dot{\mathbf{u}} = \dot{\mathbf{u}}(t = 0) \quad (6-26)$$

Recalling that $\boldsymbol{\Phi}$ constitutes a base in the modal expansion, the initial conditions are analogous to

$$\mathbf{q} = \mathbf{q}(t = 0), \quad \dot{\mathbf{q}} = \dot{\mathbf{q}}(t = 0) \quad (6-27)$$

Linking these conditions back to Eq. (6-25), the constants \mathbf{A} and \mathbf{B} are determined to be

$$\begin{aligned} & \begin{cases} \mathbf{q}(t = 0) = e^0 [\mathbf{A} \cos[\mathbf{0}] + \mathbf{B} \sin[\mathbf{0}]] \\ \dot{\mathbf{q}}(t = 0) = e^0 [\mathbf{A} [-\zeta \boldsymbol{\Omega} \cos[\mathbf{0}] - \boldsymbol{\Omega}_D \sin[\mathbf{0}]] + \mathbf{B} [-\zeta \boldsymbol{\Omega} \sin[\mathbf{0}] + \boldsymbol{\Omega}_D \cos[\mathbf{0}]]] \end{cases} \\ \Leftrightarrow & \begin{cases} \mathbf{q}(t = 0) = \mathbf{A} + \mathbf{0} \\ \dot{\mathbf{q}}(t = 0) = \mathbf{A} [-\zeta \boldsymbol{\Omega} - \mathbf{0}] + \mathbf{B} [\mathbf{0} + \boldsymbol{\Omega}_D] \end{cases} \\ \Leftrightarrow & \begin{cases} \mathbf{A} = \mathbf{q}(t = 0) \\ \mathbf{B} = \frac{\dot{\mathbf{q}}(t = 0) - \zeta \boldsymbol{\Omega} \mathbf{q}(t = 0)}{\boldsymbol{\Omega}_D} \end{cases} \end{aligned} \quad (6-28)$$

It is further noted that, as a result of orthogonality, the (initial) modal coordinates can be expressed as

$$\begin{cases} \mathbf{q}(t=0) = \frac{\mathbf{\Phi}^T \mathbf{M} \mathbf{u}(t=0)}{\mathbf{\Phi}^T \mathbf{M} \mathbf{\Phi}} \\ \dot{\mathbf{q}}(t=0) = \frac{\mathbf{\Phi}^T \mathbf{M} \dot{\mathbf{u}}(t=0)}{\mathbf{\Phi}^T \mathbf{M} \mathbf{\Phi}} \end{cases} \quad (6-29)$$

thereby linking the modal coordinates directly to the initial conditions.

Having determined the constants \mathbf{A} and \mathbf{B} , the modal coordinates can thus be expressed as

$$\mathbf{q} = e^{-\zeta \Omega t} \left[\mathbf{q}(t=0) \cos[\Omega_D t] + \frac{\dot{\mathbf{q}}(t=0) - \zeta \Omega \mathbf{q}(t=0)}{\Omega_D} \sin[\Omega_D t] \right] \quad (6-30)$$

The analysis is now at a stage at which both the natural vibration modes and the modal coordinates have been sufficiently derived. They can now be reintegrated into the modal expansion.

6.4.4 Modal Expansion

Analysis has thus far revealed that the displacement response of an MDOF system is given by

$$\mathbf{u}(t) = \mathbf{\Phi} \mathbf{q}(t) \quad (6-31)$$

where the natural vibration modes $\mathbf{\Phi}$ are a function of the natural frequencies Ω , yielded by the eigenanalysis, and the modal coordinates \mathbf{q} , derived to be

$$\mathbf{q} = e^{-\zeta \Omega t} \left[\mathbf{q}(t=0) \cos[\Omega_D t] + \frac{\dot{\mathbf{q}}(t=0) - \zeta \Omega \mathbf{q}(t=0)}{\Omega_D} \sin[\Omega_D t] \right] \quad (6-32)$$

Returning to Eq. (6-31), the contribution of each mode n to the displacement response \mathbf{u} is given by

$$\mathbf{u}(t) = \sum_{n=1}^N \mathbf{\Phi}_n q_n(t) \quad (6-33)$$

A method has now been derived for computing the displacement response of a MDOF system while also decoupling the contributions made by each mode, thus enabling each mode to be analyzed independently. Of note is that the system response can be computed entirely through the deployment of a few key input parameters, namely:

- the masses m_i of the system;
- the stiffnesses k_i of the system;
- the modal damping ratios ζ_n of the system;
- the initial conditions, i.e. the kinematics that initiate the motion of the system (free vibration response).

6.5 Input Parameters

Having derived a general method for studying the displacements of a MDOF system, focus now returns to the problem at hand, i.e. the glass-impactor 2DOF system. Of interest is to determine the masses, stiffnesses, damping ratios, and initial conditions of the system.

6.5.1 Impactor

European standard EN 12600 stipulates that the mass of the dual-tire impactor be 50 kg, and that its stiffness is approximately 400 kN/m (CEN, 2002). While the mass is a relatively certain parameter, the stiffness, however, is only an approximation. Referring back to Section 5.2.2, the dynamic impactor stiffness is estimated as a function of drop height (impact velocity), and is therefore utilized for the 2DOF model, see Table 6-1. Note that k_{dyn} is interpolated for the drop heights $h = \{400, 500\}$ mm using data from Table 5-1.

Table 6-1: Estimated dynamic stiffness of the impactor for drop heights used in the experimental campaign.

Drop height [mm]	Dynamic stiffness [kN/m]
100	324
200	360
300	403
400	435
500	464

6.5.2 Glass Specimens

Setup 1, i.e. the experimental setup which fastened the glass along its vertical edges between the I- and C-beams, is used as the principal case study to derive the glass input parameters. Both the mass and the stiffness of the glass specimen are estimated by idealizing the setup into a beam subjected to symmetrically discontinuous loading, see Figure 6-2, where c represents the loading from the dual-tire impactor. Considering that the glass seems to have been fastened very tightly between the I- and C-beams, it can be presumed that the behavior of the glass is a point that lies somewhere on a spectrum that, for the given load configuration, is bounded by a simply supported response and a fixed response.

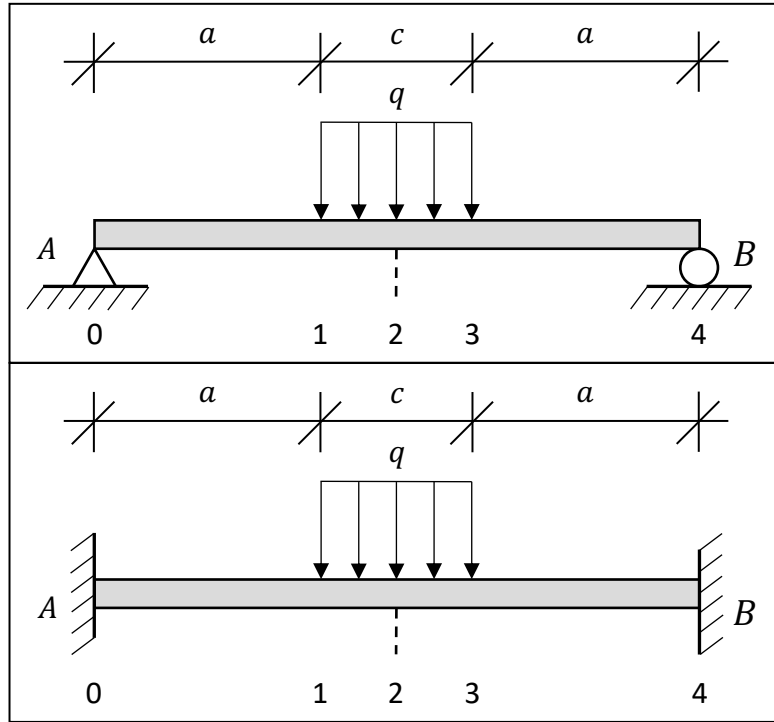


Figure 6-3: Symmetrically discontinuous loading of a simply supported beam (top) and a beam fixed at both ends (bottom).

Neither of these cases is a standard beam load configuration, indicating that beam tables are an insufficient resource here. As such, the Euler-Bernoulli beam equation is used to derive an analytical solution for the prospective load configurations. These derivations are of only tangential relevance to the problem at hand, but are, for the sake of completeness, presented in Annex C. Expressed using the notation shown in Figure 6-2, the derivations yield the maximum deflections for the respective beams, which are used to calculate equivalent stiffnesses:

$$\begin{cases} v_{\text{simple}}(x = L/2) = \frac{q}{24EI} \left(-\frac{1}{2}L^3 c + \frac{1}{4}L c^3 - \frac{1}{16}c^4 \right) \\ v_{\text{fixed}}(x = L/2) = \frac{q}{192EI} \left(-L^3 c + L c^3 - \frac{1}{2}c^4 \right) \end{cases}$$

$$\Rightarrow \begin{cases} k_{\text{simple}} = \frac{q c}{v_{\text{simple}}(x = L/2)} \\ k_{\text{fixed}} = \frac{q c}{v_{\text{fixed}}(x = L/2)} \end{cases} \quad (6-34)$$

The more realistic stiffness of the glass is a combination of these two beam stiffnesses. A weighting factor w , where $0 \leq w \leq 1$, is introduced, such that

$$\begin{cases} w = 0 \Leftrightarrow \text{glass beam is fully simply supported} \\ w = 1 \Leftrightarrow \text{glass beam is fully fixed at both ends} \end{cases} \quad (6-35)$$

6 Semi-analytical Model

By combining Eq. (6-34) and Eq. (6-35), the stiffness of the glass can be reduced to a single equation:

$$k_{\text{glass}} = w k_{\text{fixed}} + (1 - w) k_{\text{simple}} \quad (6-36)$$

Eq. (6-36) requires the weighting factor w , the loaded area c , and general beam data such as the bending stiffness EI . The latter is calculated analogously to any other beam cross-section, where $E = 72$ GPa; in the case of the laminated specimens, equivalent profile thicknesses are derived to account for the composite action (Serafinavicius, et al., 2013). The loaded length is set to $c = 0.2$ m (roughly half of the dual-tire impactor diameter). Scrutinizing the deformation response of the glass in the numerical simulations, see Figure 6-4, the glass is deemed to be closer to the behavior of a fixed beam rather than a simply supported one, say $w \approx 3/4$.

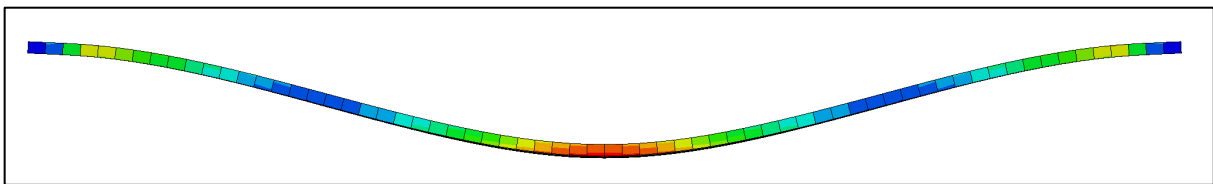


Figure 6-4: Deformation response of the glass to impact loading in the numerical model. It is judged to be closer to that of a beam fixed at both ends rather than a simply supported beam.

Likewise, the mass of the glass is lumped. It is common engineering practice in structural dynamics to set the lumped mass of a simply supported beam and beam fixed at both ends to $0.5 m_{\text{tot}}$ and $0.4 m_{\text{tot}}$, respectively. For $w = 0.75$, the lumped mass thus becomes $0.425 m_{\text{tot}}$.

The glass input parameters are presented in Table 6-2.

Table 6-2: Glass lumped masses and stiffnesses used in the 2DOF model.

Fastener configuration	Glass profile [mm]	Lumped mass [kg]	Stiffness [kN/m]	
Simply supported	8	6.800	465	
	10	8.500	908	
	12	10.200	1570	
	8 + 1.6 PVB + 8	14.144	4760	
	8 + 1.6 SGP + 8	14.144	4890	
Bolted	6 + 1.6 SGP + 6	12.716	1660	
	Clamped	5 + 1.6 PVB + 5	9.044	1380
		5 + 1.6 SGP + 5	9.044	1400
Clamped	6 + 1.6 PVB + 6	10.744	2210	
	6 + 1.6 SGP + 6	10.744	2260	

6.5.3 Modal Damping Ratios

In a 2DOF model, there are two modal damping ratios—both of these are unknown. It is safe to assume that the damping ratio for the first mode, ζ_1 , can be set to zero. The second damping ratio is assumed to be caused by the steel frame and the joints of the experimental setup. (Glass has negligible damping properties.) This is set to $\zeta_2 = 0.02$, which is roughly consistent with the literature on bolted steel structures subjected to loads not in excess of 50% loadbearing capacity (ASCE, 2017).

6.5.4 Initial Conditions

Two sets of initial conditions are possible, but it is known that the initial displacements of the system are zero, i.e. $\mathbf{u}(t = 0) = \mathbf{0}$, while the initial velocities $\dot{\mathbf{u}}(t = 0)$ are calculated using the impactor drop height h and the law of conservation of energy,

$$\begin{aligned} m_1 g h &= \frac{1}{2} m_1 v^2 \\ \Rightarrow v &= \sqrt{2 g h} \end{aligned} \quad (6-37)$$

Referring back to the coordinates introduced in Figure 6-1, the initial velocities become

$$\dot{\mathbf{u}}(t = 0) = \begin{bmatrix} 0 \\ -\sqrt{2 g h} \end{bmatrix} \quad (6-38)$$

6.6 Case Study and Stress Derivation

To better concretize the implications of the work derived in this chapter, a case study is presented. For a monolithic glass specimen, thickness 10 mm, which is fastened to the simply supported setup, the stiffness is $k_{\text{glass}} = 1570$ kN/m and the mass is $m_{\text{glass}} = 8.5$ kg. Assuming a 300 mm drop height for the impactor, the stiffness is $k_{\text{imp}} = 403$ kN/m and the initial velocity is $\dot{u}_{\text{imp}} = -2.42$ m/s, with a mass $m_{\text{imp}} = 50$ kg. Plotting the displacement response \mathbf{u} in time yields Figure 6-5. It is immediately obvious that the impactor deformation is significantly larger than that of the glass, which is a promising result.

The contributions made by each mode to the response of the glass are also plotted, for convenience. It is clear that the first mode is governing for the principal shape of the glass curve, which is to be expected, and that the damping $\zeta_2 = 0.02$ reduces the influence of the second mode on the displacement response over time. But for such a short event, this phenomenon has only a slight effect on the deformations.

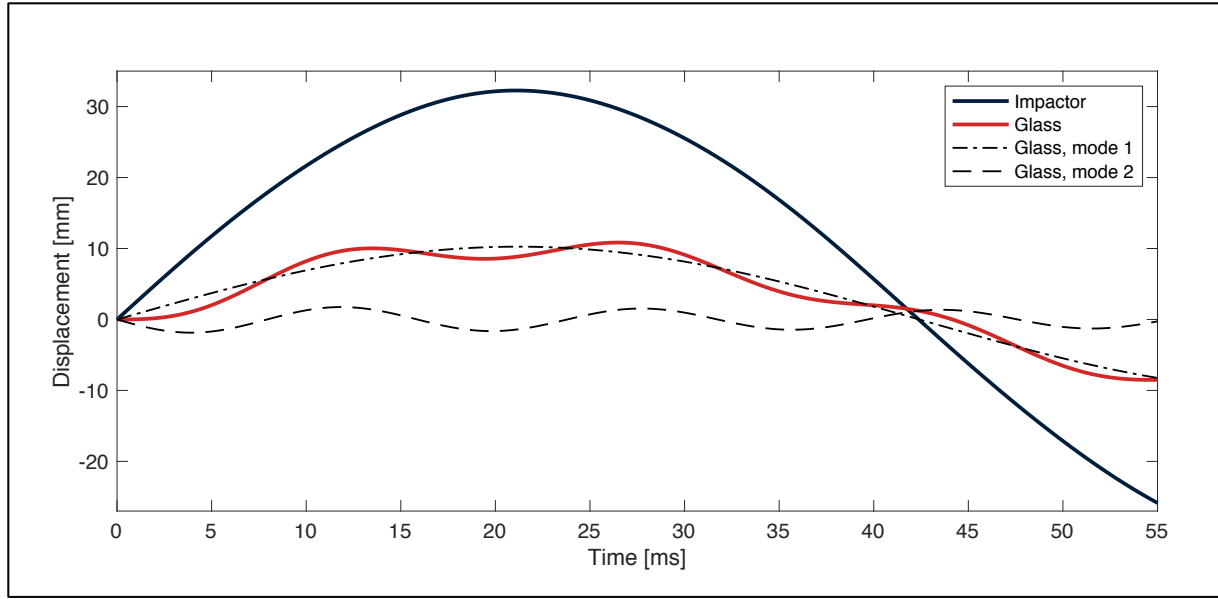


Figure 6-5: Case study: deformation response of the glass-impactor 2DOF system, assuming a 10 mm thick monolithic glass specimen fastened to the simply supported setup, and a 300 mm drop height.

Interesting though they may be, the displacements of the glass-impactor system are of only tangential relevance to the ultimate objectives of the study—the experimental campaign logged stresses, not deformations. It is therefore prudent to derive a method for transforming the displacements in the semi-analytical model into stress. This is approached in a fashion analogous to the derivation of the glass stiffnesses in Section 6.5.2, i.e. by means of a beam analogy.

For a Euler-Bernoulli beam, the normal stress at the upper edge of a particular section cut can be expressed as a function of the moment in the same section cut,

$$\sigma_{\text{edge}} = \frac{M}{I} y_{\text{edge}} \xrightarrow{\text{rectangular}} 6 \frac{M}{b h^2} \quad (6-39)$$

For the case at hand, the second cut is given by $x = L/2$, and the corresponding moment functions, derived in Annex C and expressed in terms of the beam length L and the loaded length c , are

$$\begin{cases} M_{\text{simple}} = q \left(-\frac{c^2}{8} + \frac{cL}{4} - \frac{L^2}{8} + \frac{Lx}{2} - \frac{x^2}{2} \right)_{x=L/2} \rightarrow q \left(\frac{cL}{4} - \frac{c^2}{8} \right) \\ M_{\text{fixed}} = q \left(-\frac{c^3}{24L} - \frac{c^2}{8} + \frac{cL}{8} - \frac{L^2}{8} + \frac{Lx}{2} - \frac{x^2}{2} \right)_{x=L/2} \rightarrow q \left(\frac{cL}{8} - \frac{c^2}{8} + \frac{c^3}{24L} \right) \end{cases} \quad (6-40)$$

Again, the weighting factor $w = 0.75$ is invoked such that

$$M_{\text{glass}} = w M_{\text{fixed}} + (1 - w) M_{\text{simple}} \quad (6-41)$$

By inserting Eq. (6-41) into Eq. (6-39), the stress at the section edge of the beam can be expressed in terms of the distributed load q . By invoking Hooke's Law, it is convenient to rewrite the distributed load q in terms of the beam stiffness and the displacement, i.e.

$$F = q c = k_{\text{glass}} u_{\text{glass}} \quad (6-42)$$

This is sufficient to establish an expression for the stress at the glass surface that is a function of the precomputed displacement response and the loading characteristics, i.e.

$$\sigma_{\text{glass}} = \sigma_{\text{glass}}(k_{\text{glass}}, u_{\text{glass}}) \quad (6-43)$$

This function is nothing more than a scale factor multiplied with u_{glass} , see Figure 6-6, which is reasonable. For the given case study of a 10 mm monolithic glass specimen fastened to the simply supported setup and subjected to an impactor load dropped from 300 mm, the figure illustrates that the maximum stress is 92 MPa, which can be compared to the corresponding experimental value of 110 MPa.

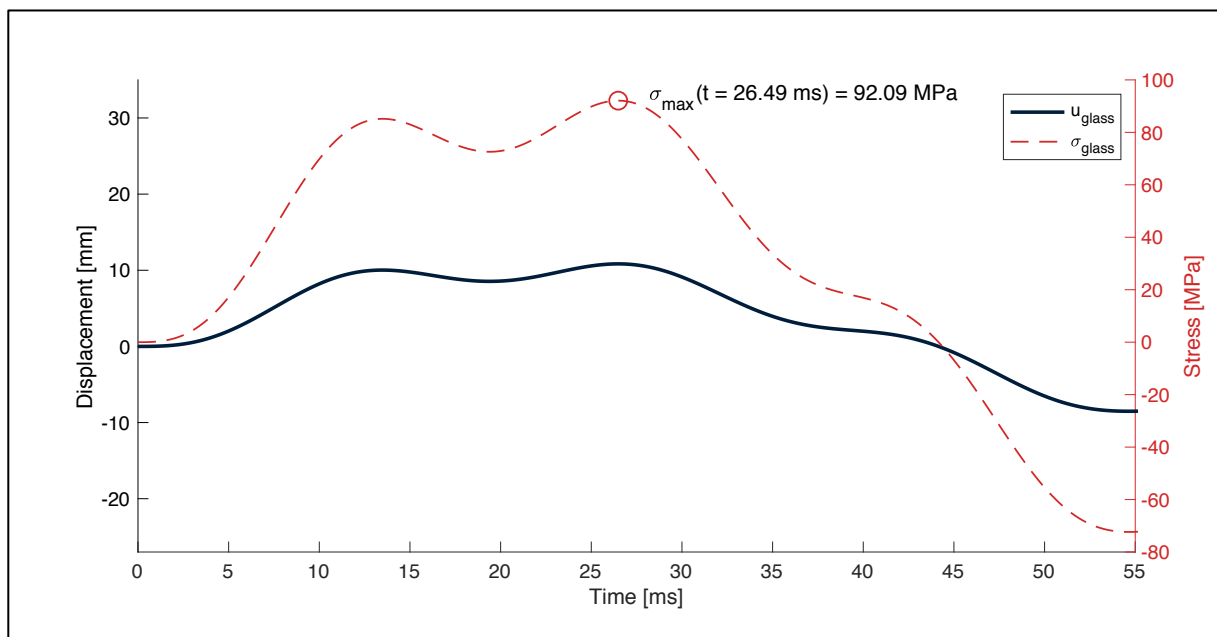


Figure 6-6: Case study: stress on the glass surface computed using a beam analogy and the displacements outputted by the 2DOF model.

Figure 6-6 amplifies the double impact phenomenon present in the 2DOF model. Indeed, glancing at the result above and comparing it to the experimental results in Annex A, there are glaring differences in the shape of the impact event. There are many reasons for why this may be the case, not the least of which is the multitude of idealizations made in the 2DOF model. Furthermore, inherent to the 2DOF model is its linear behavior, which is far from realistic when compared to the experimental case. However, the emphasis of the semi-analytical model rests on a pedagogical, analytical approach, rather than a fully realistic one.

6.7 Parametric Study

To further shed light on the dynamics of the glass-impactor system, a parametric study is carried out with respect to the system masses, stiffnesses, damping, and initial conditions. The influence of each of these parameters is investigated by plotting the modified glass stress. The same base case found in Section 6.6 is used, i.e. 10 mm thick monolithic glass specimen fastened to the simply supported setup, and subjected to impact loading from a 300 mm drop height. The results are collated in Figure 6-7.

Both the system masses and the stiffnesses influence the period and the amplitude of the stress curves. This is to be expected: the natural frequency is expressed in terms of m_i and k_i , and it is the natural frequency that determines the period of the signal. Moreover, the natural frequency steers the natural vibration modes, which in turn describe the displacement response; a modified natural frequency therefore has the effect of changing the displacement response, and in so doing directly changing the shape of the stress curves.

Citing the equation $\omega = \sqrt{k/m}$ helps clarify why adding mass to the system has the opposite effect on the periods of the stress curves as those exercised by the stiffnesses. Recalling that

$$T = \frac{2\pi}{\omega} = 2\pi\sqrt{\frac{m}{k}} \quad (6-44)$$

it is obvious that added mass should increase the period; correspondingly, added stiffness decreases it. This is corroborated by the results of the parametric study.

The effect of the second modal damping ratio ζ_2 is comparatively mute, which is to be expected for an impact load and for damping ratios below 20%. The stress curves follow the same centerline in the plot, and the deviations from this centerline decrease as the damping increases. This is precisely the intended effect when damping is introduced to a system. Though not plotted, it can be surmised that the amplitude of the stress curves decreases at an ever-faster rate as the damping is increased.

Modification of the impactor velocity has the effect of a stress scale factor, which can be surmised by noting that the periods of the curves are identical to one another, yet the amplitude increases in tandem with the velocity. This is to be expected: an increased impact velocity implies greater energy in the system, but does not change the spring stiffnesses, and thus the fundamental event remains unchanged in character, albeit modified in amplitude.

Having reviewed the results of the parametric study, it is clear that, if the objective is to utilize the semi-analytical model to obtain realistic results, it is the mass and the stiffness in the system that play a decisive role. (The effect of damping is limited for such a short event, while the impactor velocity is a comparably certain parameter.) The question can then be raised as to whether the row of idealizations made in the derivations above, such as full linearity and beam analogies, filter out too much detail to accurately capture the response of the system.

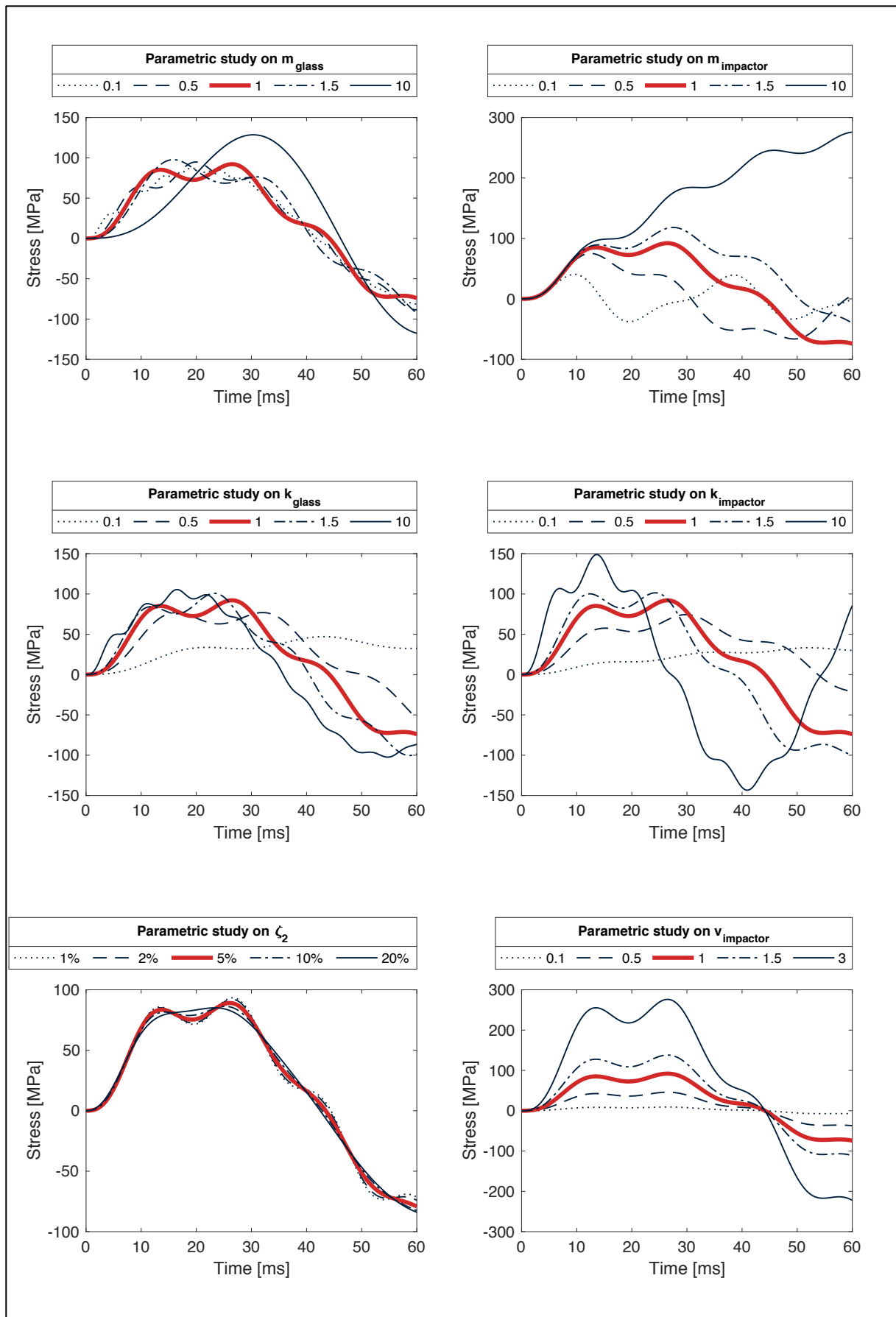


Figure 6-7: Parametric study on the governing parameters in the 2DOF model. Legend entries correspond to the weights (or percentages) that are multiplied with the base case of a 10 mm thick monolithic glass specimen and 300 mm drop height.

7 The Finite Element Method

“Although this may seem a paradox, all exact science is dominated by the idea of approximation.”

—Bertrand Russell

This chapter introduces the finite element method as a means for solving engineering problems. An archetypal derivation of the method is presented, after which aspects such as solution schemes, nonlinearity, dynamics, and convergence are discussed. Finally, a selective library of finite elements that are of relevance to the study is provided.

7.1 General Overview

Engineering is concerned with the solving, by efficient means, of problems of the real world through the practical application of the pure sciences. By reducing a real-world problem to a tangible and isolated model, the behavior induced by a scientific phenomenon can be expressed as a differential equation; the solution to such an equation can be captured in a cost-effective manner through numerical approximation. It is from this pedigree that the finite element method has been developed, targeting the lattermost step of this idealized workflow, see Figure 7-1.

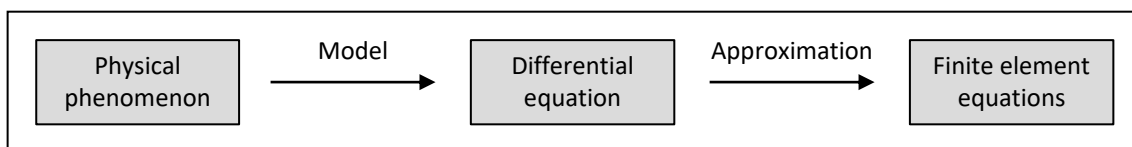


Figure 7-1: Engineering as an idealized workflow, with the finite element method targeting the lattermost step. Adapted from Ottosen & Petersson (1992).

The finite element method is deployed to approximate the behavior described by a differential equation for a certain region (body). It draws its namesake from the manner in which this is accomplished, i.e. by dividing up the region into a certain number of elements with predefined properties. The behavior of each element can then be computed according to a numerical approximation of the differential equation in question. From this, the behavior of the entire region can be studied (Ottosen & Petersson, 1992; Plumbridge, et al., 2003). For the behavior

of the region to be captured accurately, the discretization from a continuous region into finite elements must be carried out at a sufficiently high resolution, see Figure 7-2.

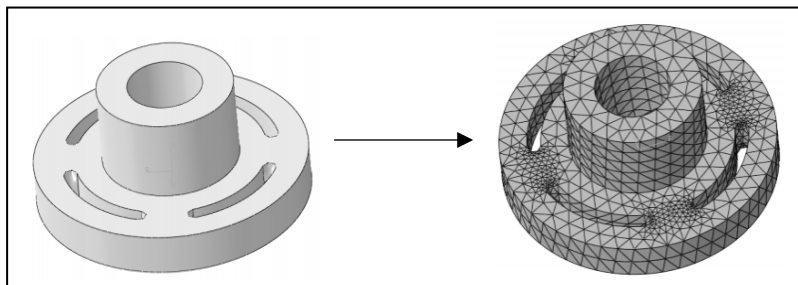


Figure 7-2: Discretization of a model geometry into finite elements. Adapted from Dassault Systèmes (2020).

Each finite element is defined by its geometry, material parameters, couplings and constraints to the environment, and so on. The response of each finite element to the physical and/or chemical phenomena to which it is subjected is given by its degrees of freedom. Thus, a degree of freedom can represent anything from spatial translation to heat flow to electrical potential (Dassault Systèmes, 2020). In structural applications, it is normally kinematic variables (e.g. displacement, velocity, and acceleration) and static variables (e.g. normal force, shear force, and bending moment) that are of interest. From these, the stresses resulting from a particular load scenario of the structure can be scrutinized for the purposes of design and verification.

As with any approximation, there is a balancing act inherent to the finite element method, in which the fidelity of the solution must be weighed against the computational costs. There are numerous strategies for curbing the latter while still maintaining acceptable levels of accuracy, including:

- neglect of dynamics, see Section 7.3;
- neglect of nonlinear effects, see Section 7.4;
- choice of solver scheme, see Section 7.5;
- degree of solution convergence, see Section 7.6;
- and choice of element type, see Section 7.8.

7.2 Derivation of Structural Dynamic Finite Element Formulation

The derivation of the finite element formulation is now showcased using an idealized problem, namely an arbitrary three-dimensional body (solid) with mass density ρ and constituted by a linear elastic material. It is subjected to body forces \mathbf{b} and inertial forces $\rho\ddot{\mathbf{u}}$. These induce the displacements \mathbf{u} , strains $\boldsymbol{\varepsilon}$, and stresses $\boldsymbol{\sigma}$ with respect to the body. Citing Newton's Second Law of Motion, the resulting equation of motion can be expressed as

$$\tilde{\nabla}^T \boldsymbol{\sigma} + \mathbf{b} = \rho\ddot{\mathbf{u}} \quad (7-1)$$

where

$$\tilde{\mathbf{V}}^T = \begin{bmatrix} \frac{\partial}{\partial x} & 0 & 0 & \frac{\partial}{\partial y} & \frac{\partial}{\partial z} & 0 \\ 0 & \frac{\partial}{\partial y} & 0 & \frac{\partial}{\partial x} & 0 & \frac{\partial}{\partial z} \\ 0 & 0 & \frac{\partial}{\partial z} & 0 & \frac{\partial}{\partial x} & \frac{\partial}{\partial x} \end{bmatrix}; \quad \boldsymbol{\sigma} = \begin{bmatrix} \sigma_{xx} \\ \sigma_{yy} \\ \sigma_{zz} \\ \tau_{xy} \\ \tau_{xz} \\ \tau_{yz} \end{bmatrix}; \quad \mathbf{b} = \begin{bmatrix} b_x \\ b_y \\ b_z \end{bmatrix}; \quad \text{and } \ddot{\mathbf{u}} = \frac{\partial^2}{\partial t^2} \begin{bmatrix} u_x \\ u_y \\ u_z \end{bmatrix} \quad (7-2)$$

Noting that the constitutive equation is given by Hooke's Law, $\boldsymbol{\sigma} = \mathbf{D} \boldsymbol{\varepsilon}$, and that the kinematic relationship is given by $\boldsymbol{\varepsilon} = \tilde{\mathbf{V}} \mathbf{u}$, the stresses in Eq. (7-1) can be expressed as

$$\boldsymbol{\sigma} = \mathbf{D} \tilde{\mathbf{V}} \mathbf{u}$$

i.e. as a function of the constitutive matrix \mathbf{D} and the displacements \mathbf{u} . For a linear elastic material, the former is given by

$$\mathbf{D} = \frac{E}{(1+\nu)(1-2\nu)} \begin{bmatrix} 1-\nu & \nu & \nu & 0 & 0 & 0 \\ \nu & 1-\nu & \nu & 0 & 0 & 0 \\ \nu & \nu & 1-\nu & 0 & 0 & 0 \\ 0 & 0 & 0 & \frac{1-2\nu}{2} & 0 & 0 \\ 0 & 0 & 0 & 0 & \frac{1-2\nu}{2} & 0 \\ 0 & 0 & 0 & 0 & 0 & \frac{1-2\nu}{2} \end{bmatrix} \quad (7-3)$$

(In cases of plane strain or plane stress, this can be reduced to a 4×4 matrix, thus simplifying the problem considerably.) Note that Eq. (7-1) is the strong form of the differential equation, but deriving the finite element formulation from the weak form is preferable. To obtain the weak form, Eq. (7-1) is premultiplied with a vector containing the weight functions $\mathbf{w} = [w_x \ w_y \ w_z]^T$ such that

$$\mathbf{w}^T \tilde{\mathbf{V}}^T \boldsymbol{\sigma} + \mathbf{w}^T \mathbf{b} = \mathbf{w}^T \rho \ddot{\mathbf{u}} \quad (7-4)$$

The formulation of the weight functions \mathbf{w} can be determined later. To account for the entire body, Eq. (7-4) is integrated over its volume V , i.e.

$$\int_V \mathbf{w}^T \tilde{\mathbf{V}}^T \boldsymbol{\sigma} dV + \int_V \mathbf{w}^T \mathbf{b} dV = \int_V \mathbf{w}^T \rho \ddot{\mathbf{u}} dV \quad (7-5)$$

It is pertinent to reformulate the stress term $\boldsymbol{\sigma}$ in Eq. (7-5) in terms of the body's surface S so as to permit the prescription of boundary conditions to the equations. To do this, the surface

traction vector \mathbf{t} is introduced as $\mathbf{t} = \mathbf{S} \mathbf{n}$, where \mathbf{S} is the stress tensor and \mathbf{n} is the unit normal vector, i.e.

$$\mathbf{t} = \begin{bmatrix} \sigma_{xx} & \sigma_{xy} & \sigma_{xz} \\ \sigma_{yx} & \sigma_{yy} & \sigma_{yz} \\ \sigma_{zx} & \sigma_{yz} & \sigma_{zz} \end{bmatrix} \begin{bmatrix} n_x \\ n_y \\ n_z \end{bmatrix} = \begin{bmatrix} t_x \\ t_y \\ t_z \end{bmatrix} \quad (7-6)$$

By employing Gauss's divergence theorem and inserting Eq. (7-6), the term containing the stresses $\boldsymbol{\sigma}$ in Eq. (7-5) becomes

$$\int_V \mathbf{w}^T \tilde{\nabla}^T \boldsymbol{\sigma} dV = \int_S \mathbf{w}^T \mathbf{t} dS - \int_V (\tilde{\nabla} \mathbf{w})^T \boldsymbol{\sigma} dV \quad (7-7)$$

Insertion of Eq. (7-7) into Eq. (7-5) yields the weak form,

$$\int_S \mathbf{w}^T \mathbf{t} dS - \int_V (\tilde{\nabla} \mathbf{w})^T \boldsymbol{\sigma} dV + \int_V \mathbf{w}^T \mathbf{b} dV = \int_V \mathbf{w}^T \rho \ddot{\mathbf{u}} dV \quad (7-8)$$

To establish the finite element formulation of Eq. (7-8), the weight functions \mathbf{w} are now defined. To do this, Galerkin's method is employed, i.e. \mathbf{w} are defined as functions of the global shape functions \mathbf{N} and arbitrary constants \mathbf{c} ,

$$\mathbf{w} = \mathbf{N} \mathbf{c} \quad (7-9)$$

For three dimensions, the global shape function matrix \mathbf{N} is given by

$$\mathbf{N} = \begin{bmatrix} N_1 & 0 & 0 & N_2 & 0 & 0 & \cdots & N_n & 0 & 0 \\ 0 & N_1 & 0 & 0 & N_2 & 0 & \cdots & 0 & N_n & 0 \\ 0 & 0 & N_1 & 0 & 0 & N_2 & \cdots & 0 & 0 & N_n \end{bmatrix} \quad (7-10)$$

where each shape function N_i , $i = \{1, 2, \dots, n\}$, is defined by the choice of the finite element. Thus, element characteristics such as geometry, along with the number and placement of nodes, influence \mathbf{N} and thereby the computational costs.

For convenience, $\mathbf{B} = \tilde{\nabla} \mathbf{N}$ is introduced. As a result, terms containing the matrix differential operator $\tilde{\nabla}$ can be succinctly redefined as

$$\tilde{\nabla} \mathbf{u} = \boldsymbol{\varepsilon} = \mathbf{B} \mathbf{a} \quad (7-11a)$$

$$\tilde{\nabla} \mathbf{w} = \mathbf{B} \mathbf{c} \quad (7-11b)$$

In so doing, the weak form expressed in Eq. (7-8) is rewritten, using Eq. (7-9) and (7-11), as

$$\mathbf{c}^T \left(\int_S \mathbf{N}^T \mathbf{t} dS - \left(\int_V \mathbf{B}^T \mathbf{D} \mathbf{B} \boldsymbol{\sigma} dV \right) \mathbf{a} + \int_V \mathbf{N}^T \mathbf{b} dV \right) = \mathbf{c}^T \left(\int_V \mathbf{N}^T \rho \mathbf{N} dV \right) \ddot{\mathbf{a}} \quad (7-12)$$

However, recalling that the constants \mathbf{c} are arbitrary, Eq. (7-12) is simplified to

$$\int_S \mathbf{N}^T \mathbf{t} dS - \left(\int_V \mathbf{B}^T \mathbf{D} \mathbf{B} \boldsymbol{\sigma} dV \right) \mathbf{a} + \int_V \mathbf{N}^T \mathbf{b} dV = \left(\int_V \mathbf{N}^T \rho \mathbf{N} dV \right) \ddot{\mathbf{a}} \quad (7-13)$$

The traction vector \mathbf{t} refers to forces acting on the surface and through section cuts of the body. Thus, the static boundary conditions are prescribed as

$$\mathbf{t} = \mathbf{h} \text{ on the surface } \Gamma_h \quad (7-14)$$

Likewise, the kinematic boundary condition is prescribed as

$$\mathbf{u} = \mathbf{g} \text{ on the surface } \Gamma_g \quad (7-15)$$

Utilizing Eq. (7-14) and (7-15), the surface force can be rewritten as

$$\int_S \mathbf{N}^T \mathbf{t} dS = \int_{\Gamma_h} \mathbf{N}^T \mathbf{h} dS + \int_{\Gamma_g} \mathbf{N}^T \mathbf{t} dS \quad (7-16)$$

For convenience, the following definitions are now introduced:

$$\int_V \mathbf{N}^T \mathbf{b} dV = \mathbf{f}_b \quad (7-17a)$$

$$\int_{\Gamma_h} \mathbf{N}^T \mathbf{h} dS = \mathbf{f}_s \quad (7-17b)$$

$$\int_{\Gamma_g} \mathbf{N}^T \mathbf{t} dS = \mathbf{f}_r \quad (7-17c)$$

These correspond to the body forces, the applied surface forces, and the reaction forces, respectively. Note that $\mathbf{f} = \mathbf{f}_b + \mathbf{f}_s + \mathbf{f}_r$. Insertion of Eq. (7-17) into Eq. (7-13) thus yields

$$\mathbf{f}_s + \mathbf{f}_r - \left(\int_V \mathbf{B}^T \mathbf{D} \mathbf{B} \boldsymbol{\sigma} dV \right) \mathbf{a} + \mathbf{f}_b = \left(\int_V \mathbf{N}^T \rho \mathbf{N} dV \right) \ddot{\mathbf{a}}$$

$$\Leftrightarrow \left(\int_V \mathbf{N}^T \rho \mathbf{N} dV \right) \ddot{\mathbf{a}} + \left(\int_V \mathbf{B}^T \mathbf{D} \mathbf{B} \boldsymbol{\sigma} dV \right) \mathbf{a} = \mathbf{f}_b + \mathbf{f}_s + \mathbf{f}_r \quad (7-18)$$

Further definitions are now made,

$$\int_V \mathbf{N}^T \rho \mathbf{N} dV = \mathbf{M} \quad (7-19a)$$

$$\int_V \mathbf{B}^T \mathbf{D} \mathbf{B} \boldsymbol{\sigma} dV = \mathbf{K} \quad (7-19b)$$

These are termed the mass matrix and stiffness matrix, respectively. Insertion of Eq. (7-19) into Eq. (7-18) finally yields

$$\mathbf{M} \ddot{\mathbf{a}} + \mathbf{K} \mathbf{a} = \mathbf{f}_b + \mathbf{f}_s + \mathbf{f}_r$$

$$\Leftrightarrow \mathbf{M} \ddot{\mathbf{a}} + \mathbf{K} \mathbf{a} = \mathbf{f} \quad (7-20)$$

Eq. (7-20) is the finite element formulation of a three-dimensional body in a structural dynamic context. (Note the similarities to the equation of motion typical of a basic mechanics problem.) It is also possible to include damping in this formulation. Consider Rayleigh damping, i.e.

$$\mathbf{C} = \alpha \mathbf{M} + \beta \mathbf{K} \quad (7-21)$$

Analogous to the expressions derived in Chapter 6, the damping in Eq. (7-21) can be added to Eq. (7-20) such that

$$\mathbf{M} \ddot{\mathbf{a}} + \mathbf{C} \dot{\mathbf{a}} + \mathbf{K} \mathbf{a} = \mathbf{f} \quad (7-22)$$

However, for the purposes of the derivation, the damping is superfluous. What matters is that Eq. (7-20), alternatively Eq. (7-22), can be solved algebraically to yield an approximate solution to the governing differential equations that defined the original problem. In so doing, the work required to obtain an answer is substantially reduced.

In practice, performing the derivation above is not part of the end user's workflow in a finite element simulation. Rather, the computer carries out a similar process to solve the prescribed problem. There are numerous methods for doing this with an eye towards curbing computational costs. Chief among them are the degree to which dynamic and nonlinear effects should be neglected.

7.3 Dynamics

Any and all phenomena in the physical world can be said to be strictly dynamic in the sense that they vary over time. For practical (technical) purposes, however, it is warranted to distinguish between dynamic and static events, or problems. The latter are characterized by time invariant behavior, that is to say they exhibit behavior that can be idealized into models that are not time dependent. This is not possible for dynamic events, which are instead characterized by significant inertial forces that vary rapidly over time (Dassault Systèmes, 2020). If these forces and their implied accelerations are not captured with sufficiently high detail, the physics of the problem being studied breaks down, yielding inaccurate results (Dassault Systèmes, 2014). Note that the inertial forces must be both significant and vary rapidly time—if only one of these properties applies, the problem can, in all likelihood, be simplified into a static (or quasi-static) problem. For instance:

- Blood pressure pulsations have small inertial forces and are consistent over time; the problem can thus be characterized as quasi-static.
- Gravity does not vary rapidly over time, despite inducing relatively large inertial forces; gravitational load (dead load) can thus be characterized as static.

Beyond inertial effects, a dynamic problem also permits consideration of damping. Damping refers to the energy in a system dissipating over time and is present for all physical problems (Moreland, 2009). It can oftentimes be neglected but warrants consideration if it plays an outsized role in modifying the vibration behavior of the system in question.

Just as the spatial domain of the problem, the geometry, is discretized into elements when performing a finite element procedure, so too must the temporal domain be discretized if the problem is dynamic (Dassault Systèmes, 2020). To do this, the time for the event to take place is divided into distinct time increments; for each increment, the equations of motion are solved. Since the state of the problem at an increment t_i is also dependent on its state at time increment t_j , $i \neq j$, it is obvious enough that the size of the time increment Δt plays a governing role with respect to the accuracy of the simulation results.

7.4 Nonlinearity

All bodies exhibit some degree of nonlinearity in their response to physical phenomena (Dassault Systèmes, 2020). This is especially the case with structures, which often use highly nonlinear materials, are deformed such that the geometric response is nonlinear, and are bounded by nonlinear contact conditions (e.g. friction). Consistent with the theme thus far demonstrated in this chapter, the question is not whether a particular structural response is nonlinear, but rather whether or not the response can be approximated as linear without exceeding the tolerances stipulated by the relevant professional and legal bodies.

Assuming that those tolerances are not breached, the advantages to using linear models are intuitive. To name a few, linear mechanical problems have unique solutions, can be scaled linearly in behavior, and grant the freedom to use principles of superposition. None of these are unconditional properties of nonlinear problems. Moreover, computational cost is considerably reduced when treating a problem as linear. The process of evaluating whether a problem can be reasonably approximated as linear can be condensed into three criteria (Dassault Systèmes, 2020):

- Geometric linearity: the strains and rotations are small.
- Material linearity: the material properties do not change during the simulation.
- Boundary linearity: the contact conditions do not change during a linear analysis.

Geometric nonlinearity is brought about by large deflections, deformations, and rotations; instability phenomena; and preloading in the system. Observe that these are, however, general guidelines. Indeed, the nonlinear sensitivity of a system to deformation is not necessarily correlated with the magnitude of the deformation, although this is commonly the case (Peksen, 2018). The fundamental behavior of a geometrically nonlinear system response is that the projected system behavior is determined by the actual loading taking place. In other words, the stiffness of the system becomes a function of the deformation taking place (Plumbridge, et al., 2003).

For most materials, the response of a body to a highly limited loading range can be modeled as linear elastic, including hyperelastic materials such as rubber (which are otherwise described holistically by multi-order polynomials). However, this simplification breaks down with more generalized (realistic) loads. At that point, the effects of nonlinear elastic behavior, plasticity, material damage, and failure mechanisms begin to play an outsized role in the system response (Dassault Systèmes, 2020). Relationships such as these cannot be adequately modeled as linear, and thus material nonlinearity must be considered. If they are instead neglected, the analysis forsakes any capacity to forecast phenomena such as cracking, crushing, plastic hinge formation, and so on. The difficulty is compounded by materials that are dependent on load history, such as viscoelastic materials, i.e. a material for which deformation is dependent upon strain rate, or creep phenomena (Plumbridge, et al., 2003). In those instances, the analysis must be dynamic because the relationship between time and deformation becomes nonlinear.

When considering nonlinearity, it is normally materials and geometry that first spring to mind. However, a third category is equally crucial: boundary nonlinearity, that is to say contact between distinct components in a system or with the external environment (variable boundary conditions). The contact surface between two bodies is described exclusively by a nonlinear relationship upon enforcement of the load, and this nonlinearity is highly discontinuous, that is to say computationally expensive (Dassault Systèmes, 2020). Even friction, which is colloquially modeled through simple material constants for basic mechanics

problems, is nonlinear. Indeed, the tangential forces brought about by two bodies in contact moving relative to one another are time variant. In other word, friction, is dependent on the load history, inducing nonlinearities (Plumbridge, et al., 2003).

Nonlinear systems are, in contrast to linear systems, solved iteratively. The loading is divided across the time domain if dynamic, or a timeless equivalent if static. This is discussed in greater detail in the next Section.

7.5 Solver Schemes

Dynamic finite element problems can be solved using one of two schemes: an implicit solver or an explicit solver. The solver schemes differ in the manner in which they solve the equations of motion for each time increment. The choice of solver scheme is dependent on the nature of the problem being studied, principally with respect to the dynamic behavior and the degree of nonlinearity present in the problem.

For the implicit solver, the dynamic quantities present at time t are computed using values from the time t , as well as from the previous time increment, $t - \Delta t$. To do this, the implicit solver relies on iterative computations, chiefly through a Newton-Raphson procedure, to solve the nonlinear equations modeling the problem. The greater the nonlinearities, the more cumbersome this iterative procedure becomes (Dassault Systèmes, 2020). As a result, the implicit solver is ideal for problems that exhibit limited nonlinear behavior, as well as for problems where the response period of interest is significantly longer that the vibration frequency of the model, see Figure 7-3.

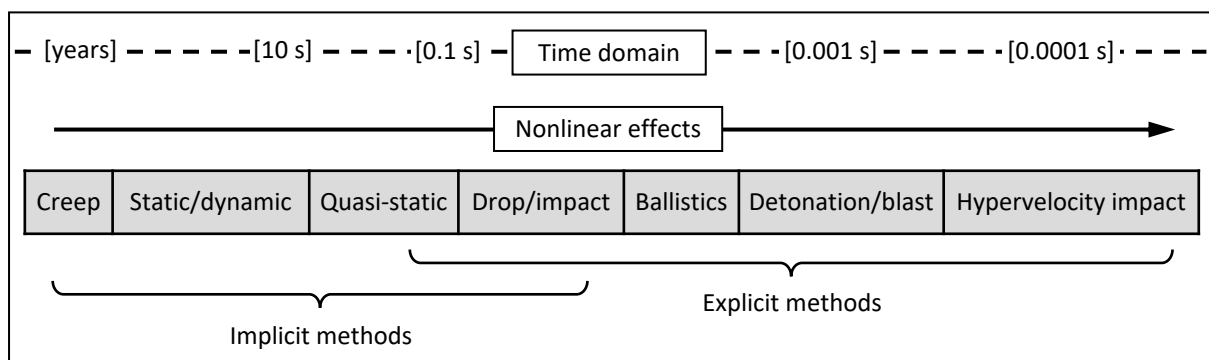


Figure 7-3: Schematic overview of the degree to which nonlinear effects are present in problem areas, as viewed with respect to the time domain. Adapted from Dassault Systèmes (2016).

Instead of relying on input data from both time increment t and the previous increment $t - \Delta t$, the explicit solver computes the dynamic quantities at t only using known data from $t - \Delta t$ (Flow Science, 2020). As a result, neither iterations nor convergence checks are required (Dassault Systèmes, 2020). The tradeoff is obvious, namely that the explicit solver is far more sensitive to the size of the time increment. In turn, a stable time increment is largely governed by the wave propagation speed in the model, i.e. a function of the mesh size and material properties (Dassault Systèmes, 2015; Dattakumar & Ganeshan, 2017). In cases where

many iterations are required by the implicit solver, such as when contact or material nonlinearity are present, the explicit solver can be more efficient. As a result, the explicit solver is favorable for highly time-dependent problems, such as high-speed dynamic events, e.g. impacts, ballistics, blasts and wave propagation analysis.

7.6 Convergence

The discretization of any continuous system will result in a solution that deviates from its continuous, that is to say true, counterpart. This becomes readily apparent by considering something as simple as an integral in one-dimensional calculus: a Riemann sum can be used to estimate the area under a curve, the integral, by dividing it into strips; the thinner the strips, the more accurate the estimate of the area becomes. Analogous to this procedure, the discretization of a real problem into a finite element model, both with respect to space and to time, implies deviations from the true behavior of the system. Indeed, disregarding all other factors, discretization will tend to stiffen the model excessively (Dutt, 2015). The way forward is not to reduce the size of the finite elements and the time increments such that they become infinitesimal, as this would be prohibitively computationally expensive. Rather, steps must be taken to ensure that the numerical solution has converged on the true solution to an acceptable degree (Dassault Systèmes, 2020).

Spatial convergence implies assigning a sufficiently fine finite element mesh to the model. If the exact solution is unknown, the only means of doing this is to adjust the mesh size iteratively (Dassault Systèmes, 2020). Care must also be taken to contextualize the relative deviations in output with respect to the corresponding costs, normally measured in CPU seconds.

In the time domain, the size of the time increments also affects the output. While the size of the convergent time increment is partially determined by the choice of solver scheme, see Section 7.5., it is generally the case that greater nonlinearities in a model necessitate a smaller time increment. Abaqus provides reliable automatic time incrementation, but this scheme can often jump past output extrema in the model, such as stress, which may warrant manual overriding of the maximum permitted time increment Δt_{max} .

7.7 Applicability to the Study

Having reviewed some of the essential theory and practice in the finite element method, it is prudent to recontextualize the information to the problem at hand, namely the glass-impactor system. This problem is dynamic—the dual-tire impactor strikes the glass in a short time frame, with an inertial force that is proportional to a mass of 50 kg. It is therefore reasonable to analyze the problem dynamically in Abaqus. Moreover, the problem is nonlinear:

- there are numerous nonlinear materials in the system, such as the tire rubber surrounding the impactor;
- the boundaries are nonlinear, with friction playing an important role between the impactor and the glass, and between the glass and the fastener rubber components;
- the geometry is nonlinear, with large deformations taking place in, for instance, the rubber of the impactor.

It is therefore reasonable to analyze the glass-impactor problem nonlinearly.

The choice of solver scheme has already been reviewed, see Section 2.4, with the results yielding an inclination towards the implicit solver. It is now of interest to discuss the element types that are relevant to the problem.

7.8 Selected Element Families and Their Applications

This Section presents a non-exhaustive library of element families that are of relevance to the finite element modeling of the glass-impactor system. The behavior of each element is described, alongside the typical applications of and uses for the element.

7.8.1 Solid Continuum Element

Solid continuum elements are an all-purpose family of elements and are archetypical in the finite element method. They can be utilized in both linear and nonlinear applications, including intricate contact formulations, coupled thermal-stress analyses, structural-acoustic applications, and fluid mechanics, electrical analysis, and much more.

For structural analysis, the tetrahedron and hexahedral (brick) formulations are common, see Figure 7-4. Tetrahedron elements provide efficient and accurate meshing of complex geometries, but they converge at a slower rate than quadrilaterals and have a tendency to be too stiff. Moreover, they can be unduly expensive to simulate if the underlying geometry is regular. In contrast, brick elements can mesh the same geometry more efficiently, with fewer elements per unit volume required, while still maintaining comparable levels of accuracy (Dassault Systèmes, 2015).

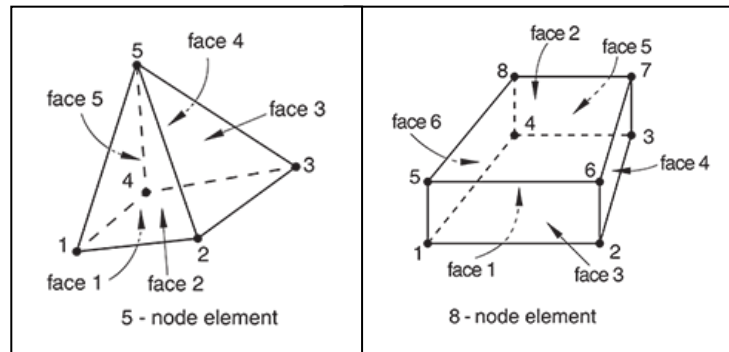


Figure 7-4: Five-node tetrahedron (left) and eight-node hexahedral (brick) solid elements (right). Source: Dassault Systèmes, 2015.

Assuming that a hexahedral element is selected, it is also important to consider the type of integration that is to be used, i.e. full-integration or reduced-integration elements (Dassault Systèmes, 2015). In general, full-integration elements are resistant to the effects of hourglassing, i.e. uncontrolled distortion due to zero energy, which can occur in first-order reduced-integration elements because they only have one integration point and are therefore unable to detect strain in bending. The phenomenon is eliminated if a sufficiently fine mesh is used, specifically in the thickness direction.

On the other hand, full-integration elements can exhibit overly stiff behavior due to shear locking and volumetric locking. This is caused by overconstraining of the elements in an effort to maintain constant element volume. The problem is effectively eliminated when using reduced-integration elements. Unsurprisingly, these elements are also cheaper to analyze.

7.8.2 Conventional Shell Element

For structures where one dimension, usually the thickness, is significantly smaller than the others, shell elements are of interest. Abaqus distinguishes between conventional and continuum shell elements. Focusing on the former, a conventional shell element is a three-dimensional body that is represented by a reference surface defined by its nodal coordinates. From the reference surface, the thickness is defined through the cross-sectional properties. The use of a reference surface to emulate three dimensions makes the shell element a computationally inexpensive choice.

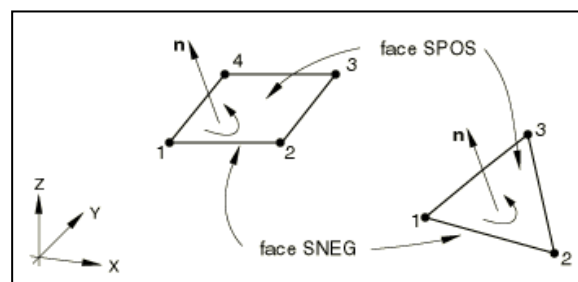


Figure 7-5: Axisymmetric conventional shell elements, with normal vectors displayed. Note that these are three-dimensional, with thicknesses defined independently of the element formulation. Source: Dassault Systèmes, 2015.

A conventional shell element can be formulated as either a 4- or 8-node quadrilateral, or as a 3- or 6-node triangular element. Each node has five degrees of freedom, accounting for translation in all directions and rotation about the in-plane axes. Three categories are available: thin, thick, and general-purpose shells.

Thin shell elements are based Kirchhoff's thin-plate theory, with corresponding assumptions. Firstly, the out-of-plane stress is assumed to be zero. Secondly, the normal to the undeformed reference plane remains straight and orthogonal during deformation (Liu & Quek, 2014). Thirdly, it is assumed that the neutral plane does not exhibit any in-plane deformation or stress. Thus, bending of the plate will cause deformation and corresponding stresses on each side of the neutral plane. The forces and moments result from the normal and shear stresses and are expressed in units per length, meaning that they vary over the plates section (Kelly, 2020).

The thick shell elements are based on Reissner-Mindlin plate theory. It is a refinement of the Kirchhoff plate, where shear deformation and inertia are also considered (Liu & Quek, 2014). This is a more accurate representation when the thickness of the plate increases (Ozer, 2007).

As for the general-purpose shell, it will provide solutions for both cases. Abaqus allows the element thickness to change by introducing it as a function of the elements in-plane deformation. For geometrically nonlinear analyses, the function includes an effective Poisson's ratio. With the in-plane stress component assumed to be zero, linear elasticity gives the strain component ε_{zz} as a function of the effective Poisson's ratio and the out-of-plane strain components. By taking the natural logarithm of the strain, the change in the elements thickness can be expressed in terms of change in area of the midplane and effective Poisson's ratio (Dassault Systèmes, 2015).

7.8.3 Continuum Solid Shell Element

A recent addition to the finite element library has been the continuum solid shell element, which provides accurate and efficient results for multilayer structures with very large aspect ratios (Vu-Quoc & Tan, 2003). This makes it suitable for the modeling of glass panes, both monolithic as well as laminated. The solid shell element is of the first order, holds 8 nodes, and has no rotational degrees of freedom. Shear locking is treated with the assumed natural strain method. It is a full-integration element that does not exhibit any hourglassing. And compared to continuum shell elements, they are not limited to plane stress (Vu-Quoc & Tan, 2003).

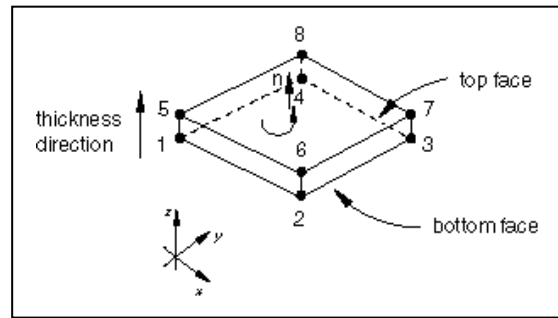


Figure 7-6: Normal and thickness direction for continuum solid shell elements. Source: Dassault Systèmes, 2020.

To reduce computational cost and improve versatility, the continuum solid shell element assumes a linear strain distribution through the thickness. This makes the element suitable for linear elastic materials, e.g. glass. However, this strain distribution also causes the element to fail one of the standard tests used for all elements in Abaqus, the three-dimensional patch test. The test is used to verify a three-dimensional element subjected to three different load cases by comparing its response to an analytical reference solution (Dassault Systèmes, 2015). Furthermore, the uncoupled behavior of the thickness direction and the in-plane direction entails high sensitivity to element orientation.

7.8.4 Gasket Element

Gasket elements are a specialty element family in Abaqus. They draw their namesake from the gasket sealing components that are common in machinery. Those components are designed to provide appropriate pressure-closure behaviors through their thickness (the thin direction of the gaskets). In so doing, the gasket maintains its sealing action as the structural components that encase it undergo deformations due to thermal and mechanical load (Dassault Systèmes, 2015). Simulating this behavior is difficult with solid continuum elements, and thus gasket elements have been designed to plug the gap.

The gasket element consists of two surfaces, a top and bottom face. These are separated by a given distance, the element thickness. The two surfaces control the thickness and transverse shear of the element, by relativizing their motion in each plane. The element's behavior is quantified by the stretching and shearing of the element midsurface, see Figure 7-7.

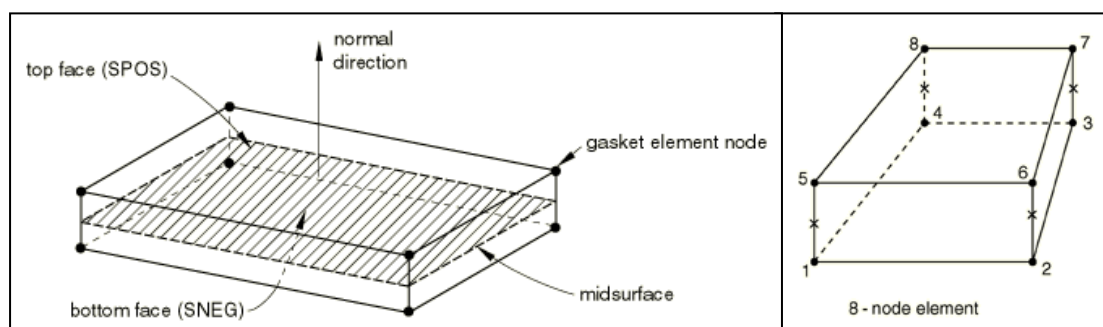


Figure 7-7: Spatial representation of a gasket element (left) and an 8-node gasket element (right). Source: Dassault Systèmes, 2015.

Abaqus offers two types, classes, of gasket elements. Elements in the first class retain translational degrees of freedom in all directions. The behavior in the thickness-direction, transverse shear and in-plane stress are uncoupled for this class, thus making it suitable for the purposes normally performed by a gasket in machinery.

In the second class, computationally efficient alterations to the elements in the first class are found. Here, it is assumed that all deformation occurs in the thickness direction. Subsequently, all other degrees of freedom are restricted. As a result, the element cannot account for in-plane stretching, thermally initiated deformation, nor transfer frictional or other tangential forces (Dassault Systèmes, 2015). Obviously, this does not make it suitable for most applications. However, it does mean that the gasket element becomes an excellent method for simulating components where the through-thickness behavior is governing and where the material is nearly incompressible. The typical example used for such cases is rubber sealings, discs, and so on, that are found in fastener components and structural seals.

8 Finite Element Modeling of High-fidelity Designs

“Computers are like Old Testament gods: lots of rules and no mercy.”

—Joseph Campbell

This chapter presents the engineering simplifications and modeling decisions made for the design of the high-fidelity finite element models. The model components, including the steel frame, impactor, glass specimens, and fasteners, are each described separately, after which the input data are compiled for convenience. Finally, a Section is included that validates the convergence of the model in both space and time.

8.1 General Overview

The high-fidelity models are built to include the primary frame, the fasteners, and the impactor. For each case, the analysis is split into two steps see Figure 8-1, and nonlinear geometry is activated. The “static, general” step allows the air pressure in the impactor to inflate the tires in a controlled setting, prior to impact. The second analysis step, the “dynamic, implicit” step, is where the impact loading took place. This is where the output variables, such as stress and acceleration, were extracted for comparison with the experimental results.

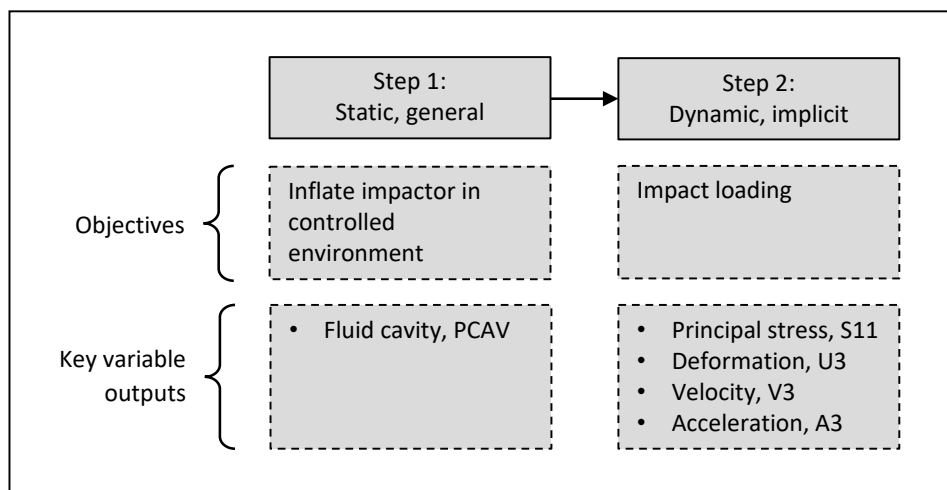


Figure 8-1: Schematic overview of the analysis steps used to simulate the high-fidelity FE models.

8.2 Frame Beams

The primary frame of the experimental setup consisted of four steel HEB160 beams. For two of the setups, an additional two steel C160 beams were included as part of the fasteners, see Chapter 5. These are all modeled as shell parts. Care is taken to ensure that the correct sections are assigned to the various beam faces, as they all have distinct thicknesses: the I-beam webs, flanges, and web stiffeners have shell thicknesses of 8 mm, 13 mm, and 10 mm, respectively, while the corresponding web and flange thicknesses for the C-beams are 7.5 mm and 10.5 mm, respectively. Industry-standard values are adopted for the linear elastic material model, i.e. $\rho = 7850 \text{ kg/m}^3$, $E = 210 \text{ GPa}$, and $\nu = 0.23$.

The primary frame is assembled entirely with surface-to-surface tie constraints. This is a stiff connection, with the ties constraining all degrees of freedom. Considering the stiffness of the connections in the experimental setup, this is a reasonable simplification, see Figure 8-2.

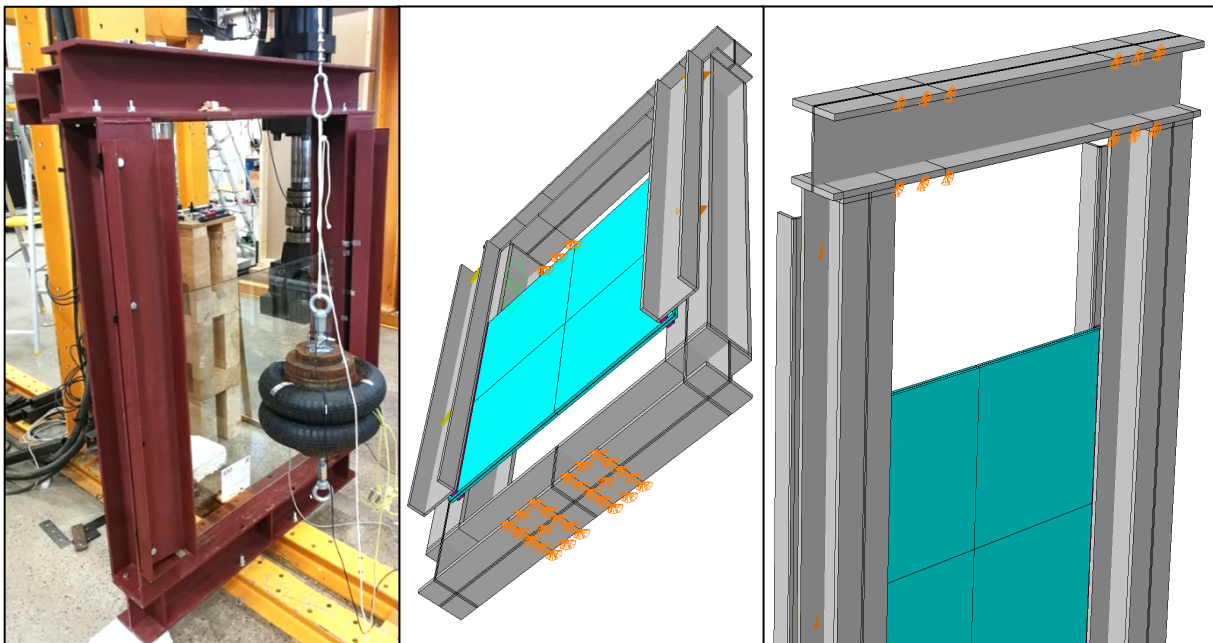


Figure 8-2: Comparison of experimental setup (left) and high-fidelity FE models (center, right). The beams are assembled with S2S ties to capture the rigidity of the true bolted connection, while the fixed boundary conditions capture the bolts to the yellow steel superstructure.

Boundary conditions are prescribed to the primary frame. In the experimental setup, out-of-plane horizontal beams were bolted to the upper frame element, heavily restricting its movement. The top beam is therefore fixed, in all degrees of freedom, at the points of contact with this steel superstructure, see Figure 8-2. Likewise, the bottom beam is fixed at its connection with the superstructure.

For reasons of computational economy, the beams are discretized using reduced integration shell elements (element name S4R) with an approximate element size of 20 mm. This element selection is consistent with best practice for the given load configuration, in which the beams were only subjected to loading in the normal direction of the shell surfaces.

8.3 Glass Specimens

A Young's modulus of 70 GPa is common in glass design; however, this bespeaks a characteristic design value, see Section 3.2.1. To better capture the statistical behavior of the glass, a higher modulus of elasticity, 72 GPa, is chosen. This modeling choice is consistent with other structural mechanical studies on glass (Fors, 2014; Fröling, 2013; Kinsella, 2018).

The interlayers in the laminated glass specimens were listed as 1.52 mm layers of polyvinyl butyral (PVB), alternatively SentryGlass® Plus (SGP). However, interlayer thickness has been found to be somewhat thicker than advertised by the supplier (Fors, 2014), which was also suspected to be the case for the specimens used in the experimental campaign, see Section 5.1. The interlayer thickness is therefore modeled with an increased thickness of 1.60 mm.

Both PVB and SGP are polymers that exhibit highly viscoelastic and thermoplastic behavior. As a result, their effective Young's moduli are a function of load duration and temperature. To capture these phenomena, supplier data for effective Young's moduli at various temperatures and load durations is interpolated for 22 °C (the temperature recorded during the experimental campaign), see Table 8-1.

Table 8-1: Effective Young's modulus as a function of temperature and load duration for the interlayer materials PVB and SGP. Supplier data is provided for the temperatures 20 °C and 25 °C; interpolation yields the values for 22 °C (shaded cells). Source: Kuraray, 2020.

Load duration [s]	Young's modulus for PVB [MPa]			Young's modulus for SGP [MPa]		
	20 °C	25 °C	22 °C	20 °C	25 °C	22 °C
1	37.0	7.9	25.4	629	511	582
3	20.0	4.4	13.8	612	485	561
5	14.0	3.5	9.8	606	474	553
10	9.4	2.7	6.7	594	456	539
30	5.1	2.1	3.9	581	433	522
60	3.7	1.8	2.9	567	413	505
300	2.2	1.5	1.9	549	340	465
600	1.9	1.4	1.7	525	334	449
1800	1.6	1.3	1.5	511	308	430
3600	1.5	1.2	1.4	493	294	413
21600	1.3	1.0	1.2	458	263	380

The temperature-interpolated values for the effective Young's modulus, $E_{\text{eff}}(T = 22\text{ }^{\circ}\text{C})$, are used as input data to extrapolate a corresponding E_{eff} for the load duration in question. It is noted that the load duration of the impactor against the glass is:

- a function of the drop height;
- a function of the glass specimen type;
- for the purposes of finding an effective Young's modulus, only of interest up the point at which the load function ceases to increase monotonically—in practice, this corresponds to the timepoint at which maximum stress occurs. After this point, the impactor begins to withdraw and the loading on the viscoelastic material relaxes.

All three of these conditions can be accounted for by assuming that the load duration for all experimental tests is approximately equal to the median timepoint at which maximum stress occurs. This median is calculated to be 27 ms. Utilizing this, the interpolated values are extrapolated, see Figure 8-3. Note that extrapolation is done for a log-log curve for PVB, and a log curve for SGP.

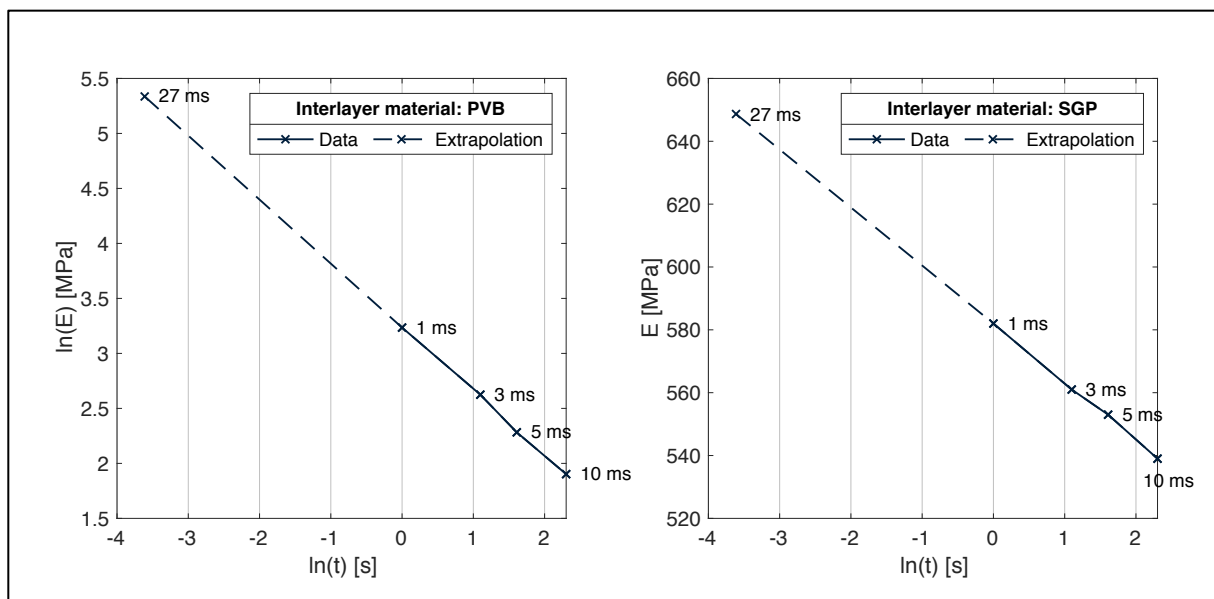


Figure 8-3: Extrapolation of effective Young's moduli for the load duration 27 ms. PVB is a log-log curve; SGP is a log curve.

Using Figure 8-3, the effective moduli of elasticity are computed to be 210 MPa for PVB and 650 MPa for SGP. However, it is noted that the supplier data is marked as being conservative (Kuraray, 2020), thus indicating that these values may be low. Finite element simulations support this assessment, indicating that the extrapolated values do not sufficiently capture the viscoelastic properties of the interlayers. As a result, the values are increased by a factor 2 for subsequent simulations, i.e. $E_{\text{eff,PVB}} = 210 \cdot 2 = 420$ GPa, and $E_{\text{eff,SGP}} = 650 \cdot 2 = 1300$ GPa. The Poisson's ratios are set to $\nu_{\text{PVB}} = 0.47$ and $\nu_{\text{PVB}} = 0.46$, which are common for these polymers.

The glass specimens are discretized with continuum solid shell elements (see Section 7.8.3). This is a reasonable element choice, considering that this element assumes a linear strain distribution through its thickness, which is consistent with the linear elastic models used for the glass and the interlayers. The laminated specimens are modelled with three layers of solid shells, again, in line with the elements intended purpose (Vu-Quoc & Tan, 2003).

8.4 Impactor

As reviewed in Section 4.2, myriad authors have successfully modeled the dual-tire impactor at a high level of detail. In an effort to limit computational cost, a more simplified approach is adopted for this study, in which only the tire rubber and steel weight are modeled. Components such as the nylon membrane are not modeled directly—instead, their influence is captured by modifying the stiffness of the rubber tire. Note that a cavity is created between the tires and the steel weight, see Figure 8-4, which is then filled with compressed air.

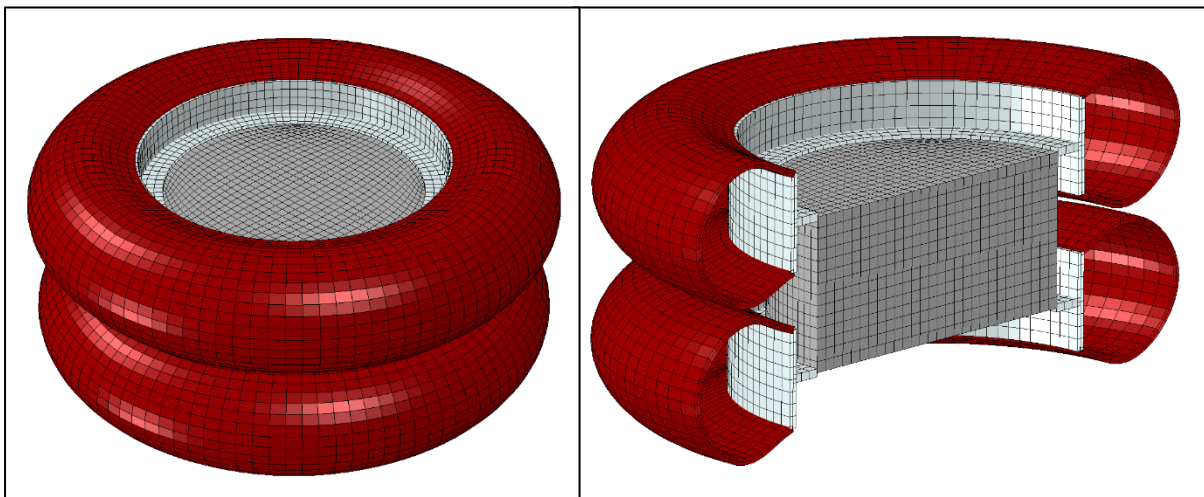


Figure 8-4: Finite element model of the dual-tire impactor: whole (left) and section cut (right).

The dual-tire impactor is discretized with shell elements for the rubber tires and with solid elements for the steel weight.

8.4.1 Mechanical Parameters

The density of the rubber tire is unknown. It is instead estimated by referring to the material mass proportions that constitute a typical 8.5 kg tire produced in the European Union, see

Table 8-2. By combining these data with densities typical for the constituent materials, the density of the rubber tire can be estimated to be $\rho_{\text{tire}} = 8.5 / 0.00644 \approx 1300 \text{ kg/m}^3$. To achieve a total impactor mass of 50 kg, a corresponding fictional density is then adopted for the steel body.

Table 8-2: Constituent materials of a typical EU rubber tire. Mass proportions are sourced from Sienkiewicz, et al. (2012).

Constituent material	Proportion of tire mass [-]	Mass [kg]	Material density [kg/m ³]	Volume [m ³]
Natural rubber	0.22	1.87	930	0.00201
Synthetic rubber	0.23	1.96	1100	0.00178
Carbon black	0.28	2.38	1800	0.00132
Steel	0.13	1.11	7800	0.00014
Fabric, fillers, etc.	0.14	1.19	~ 1000	0.00119
Total	1.00	8.50	⇒ ~ 1300	0.00644

Rubber is a hyperelastic material. In this case, its behavior is described using a Mooney-Rivlin material model of the first order. The constitutive parameters are inherited from testing of the material, and are set to $C_{10} = 15.828$ MPa, $C_{01} = -6.228$ MPa, and $D_1 = 5.700 \cdot 10^{-2}$ MPa⁻¹.

Rubber is infamous for its damped response to mechanical perturbation. The damping exhibited by the impactor is addressed through Rayleigh damping. The Rayleigh mass-proportional damping coefficient is set to $\alpha_R = 0$ while the Rayleigh stiffness-proportional damping coefficient is set to $\beta_R = 0.0028$. These values are determined iteratively according to the dynamic rigid impact tests, see Section 8.4.3.

8.4.2 Fluid Cavity

The dual-tire impactor is inflated to 350 kPa above atmospheric pressure. This is modeled as a fluid cavity in Abaqus. However, upon initiation of the analysis, the tire volume expands so as to attain equilibrium with the surrounding air pressure; this volume expansion entails a subsequent reduction in tire pressure. To account for this volume expansion, the input value for the cavity pressure must be greater than 350 kPa. Moreover, this marginal increase is a function of the mesh element size, as a coarser discretization yields a stiffer material, and therefore a smaller expansion in volume. Thus, the inputted air pressure must be iterated—it is finally set to 417 kPa, which is confirmed to decrease to 350 kPa in the static, general step by extracting the fluid cavity pressure output variable PCAV.

8.4.3 Verification of Impactor Behavior

An experimental static, displacement-controlled compression test was carried out on one of the inflated tires. The experiment was rebuilt in Abaqus, see Figure 8-5.

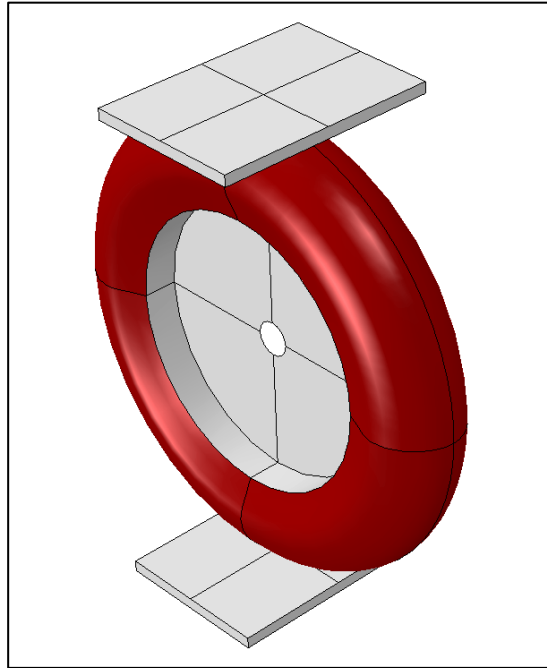


Figure 8-5. Static compression test rebuilt in Abaqus.

The experimental and simulated tests are compared through force-displacement data, see Figure 8-6. The results indicate high levels of conformity in the tire response to static compressive loading.

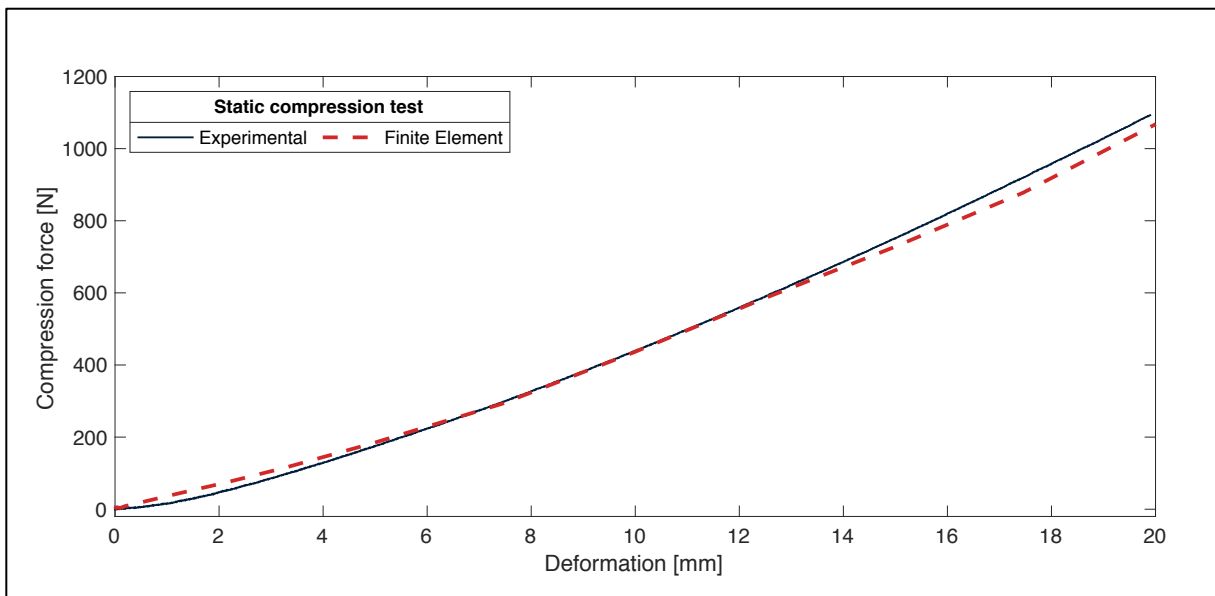


Figure 8-6: Comparison of experiments and FE model during the static compression test on one of the impactor tires.

The dual-tire impactor was further calibrated experimentally by means of dynamic rigid impact tests, see Section 5.2.2, in which the impactor collides with a rigid steel beam. An accelerometer mounted onto the impactor measured its accelerations during the pendulum movement and subsequent impact with the beam. The setup is recreated in Abaqus, see Figure 8-8.

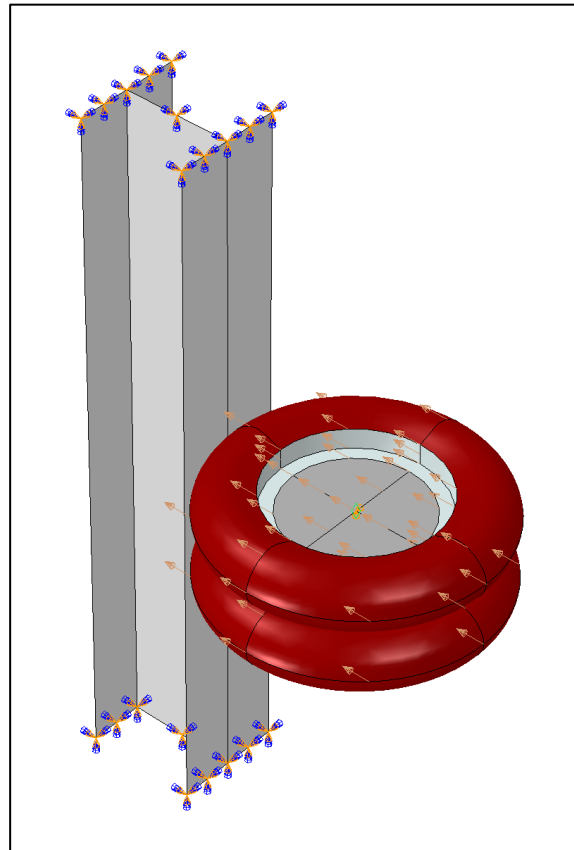


Figure 8-7: Dynamic rigid impact test rebuilt in Abaqus.

To verify the dynamic behavior of the impactor, the experimental accelerations and those outputted by the simulations are compared with one another for various drop heights of the impactor, see Figure 8-8. The results indicate high levels of conformity in the dynamic behavior of the impactor. However, it can be observed that the pulse time is somewhat longer for the simulated tire relative to the experimental one.

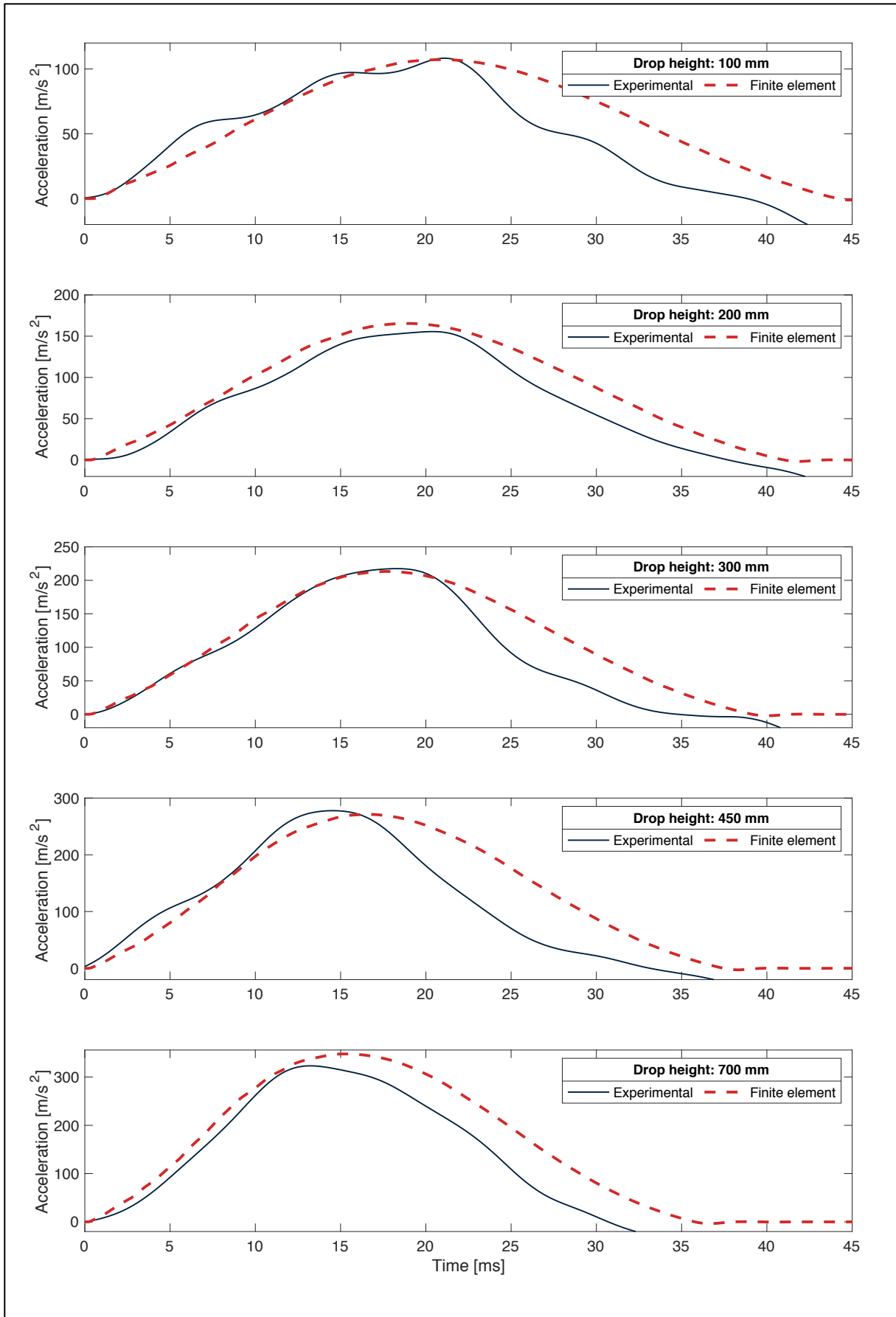


Figure 8-8: Comparison of experiments and FE model during the dynamic rigid impact test for the dual-tire impactor.

For convenience, the results are condensed into the maximum accelerations and the times at which these occur, see Figure 8-9. Here too, the results indicate acceptable levels of conformity, deviating from one another by a couple of milliseconds and, at worst, less than 30 m/s^2 .

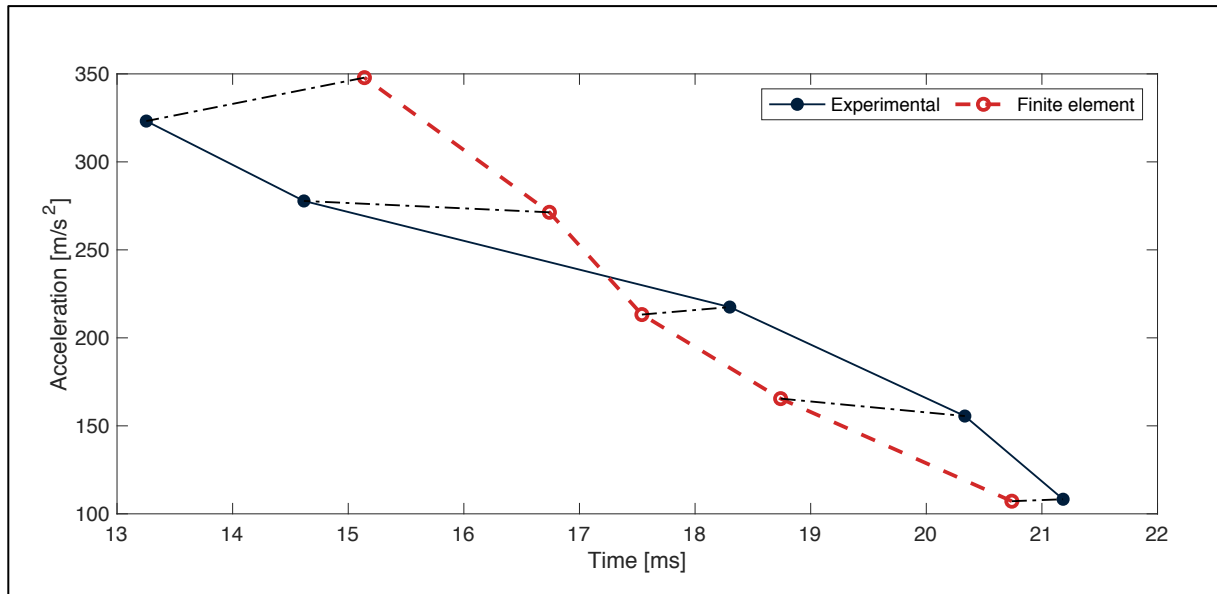


Figure 8-9: Condensed comparison of the experimental and FE model during the dynamic rigid impact test, showing only the maximum accelerations and the times at which they occur. The black dashpots link the results with common drop heights.

8.5 Design of Simply Supported Connection

The simply supported setup includes the primary frame and C-beams, between which are positioned rubber strips and the glass specimen, see Figure 8-10. There are a number of difficulties with accurately modeling this connection. The first of these is caused by the longitudinal rotation of the C-beams caused by asymmetrical pretensioning of the bolts, see Section 5.1. This is accounted for by increasing the stiffness of the connection between the C-beams and the primary frame I-beams. To do this, the bolts are modeled as beam connector elements. The connectors are not pretensioned, in large part to avoid the computational instability that would otherwise be introduced to the model.

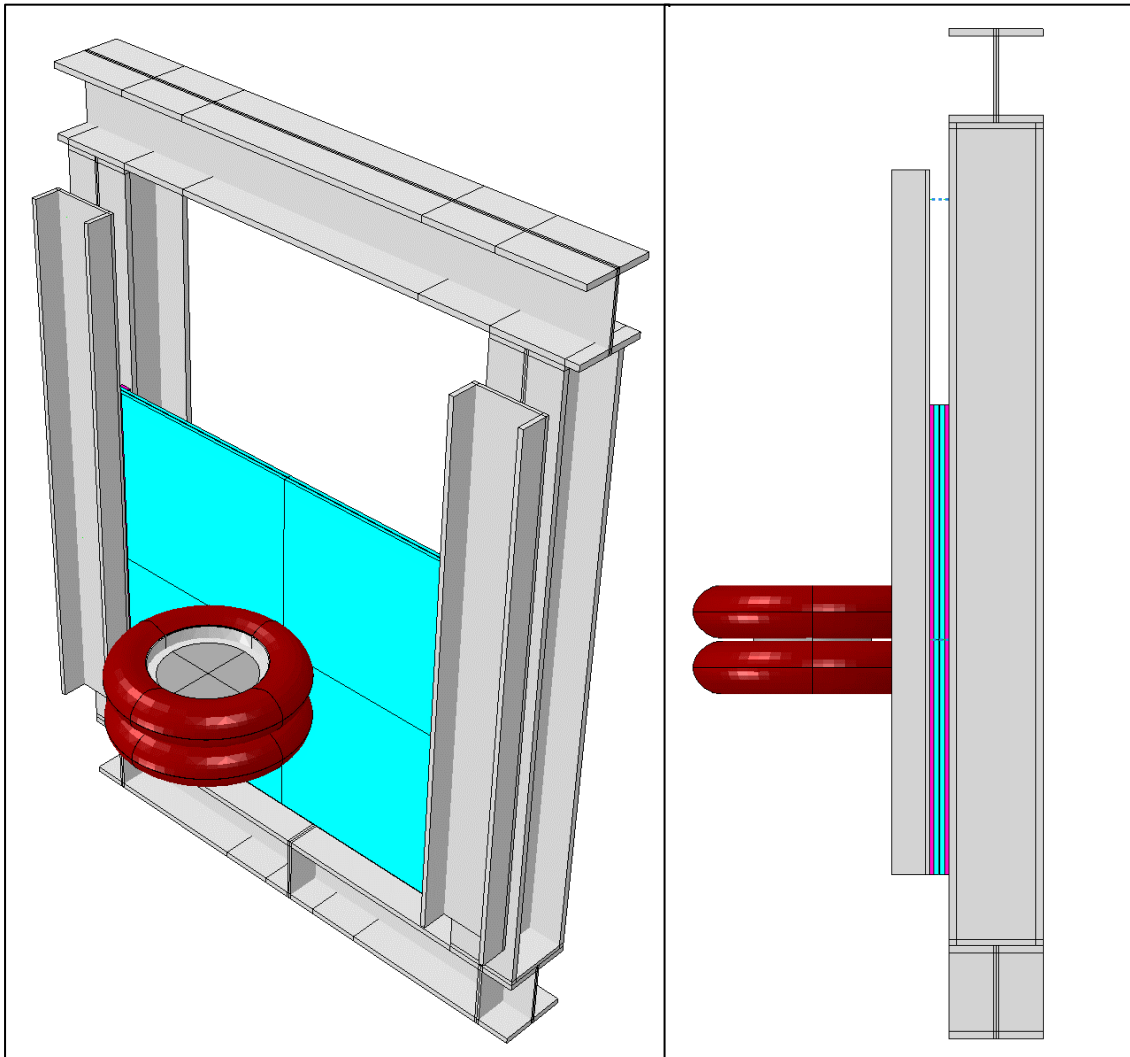


Figure 8-10: Simply supported high-fidelity FE model seen isoparametrically (left) and from the side (right). The magenta strips shown in the side view represent the rubber strips.

To compensate for the lack of pretensioning, tie constraints are assigned to the rubber strip surfaces facing the glass, while contact is defined for the rubber strip surfaces facing the C-beams and the HEB-beams, see Figure 8-11.

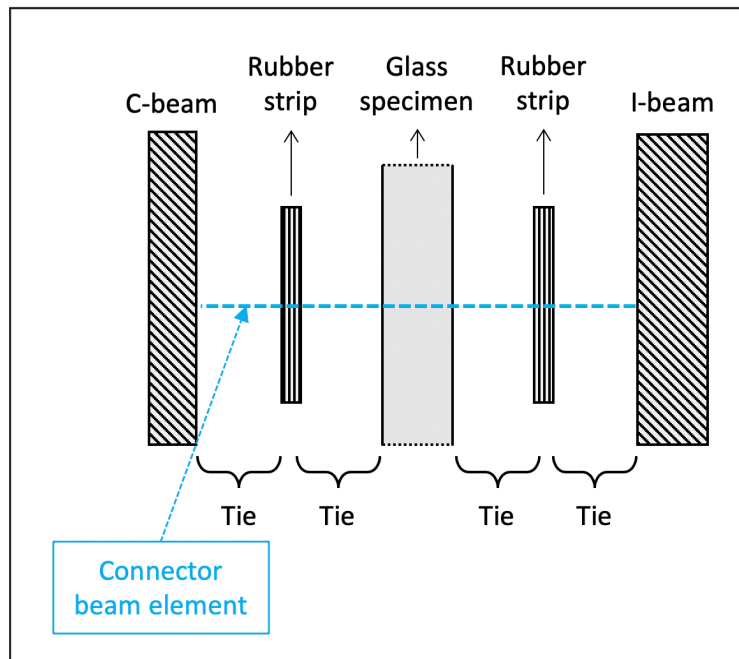


Figure 8-11: Schematic cross-section of the simply supported fastener assembly modeled in Abaqus. The connector beam simulated the bolt.

The second difficulty in modeling the connection is the rubber strips interlaid between the steel beams and the glass specimen, see Figure 8-12. Capturing the behavior of these strips is of decisive importance to the accuracy of the model. Ideally, its behavior would be inputted into Abaqus directly using material test data; such data were available, but in the form of tensile tests. These are of limited utility because the rubber is loaded exclusively in compression during the impact loading. Thus, another avenue of approach is required.

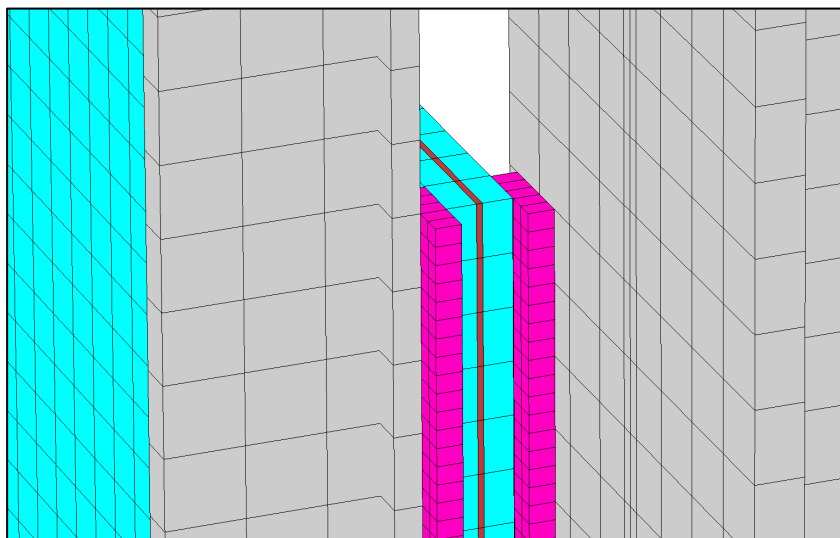


Figure 8-12: Close-up of simply supported connection in Abaqus. The gray is steel, the turquoise is glass, the dark red is the interlayer, and the magenta are the rubber strips.

Rubber is a hyperelastic material that is notoriously difficult to model linear-elastically. However, the rubber is subjected to out-of-plane compression, and there are simplified expressions available for estimating the effective compression modulus of a rubber element

with a prescribed geometry (Lindley, 1978). Simplifying the geometry of the rubber strips in question to an infinitely long strip, the compression modulus is approximated as

$$E_c = \frac{4}{3} E_0 (1 + k S^2) \quad (8-1)$$

where

E_0 is the initial Young's modulus;

k is a material constant that describes the compression characteristics of the rubber;

S is the shape factor.

To solve Eq. (8-1), the hardness of the rubber material used in the experimental campaign must be known. Unfortunately, this is not the case. However, referring to EN 12600, the hardness of the rubber is stipulated to be 60 ± 5 IRHD (CEN, 2002). Assuming 65 IRHD for the material in question, the initial Young's modulus becomes $E_0 = 9.4$ MPa, while $k = 0.52$ (Lindley, 1978). For a sufficiently long strip, with a 25 mm width and a 7 mm thickness, the shape factor is calculated to be

$$S = \frac{b L}{2 t L} \rightarrow \frac{b}{2 t} = \frac{25}{2 \cdot 7} = 1.79 \quad (8-2)$$

Insertion into Eq. (8-1) yields an effective compression modulus

$$\begin{aligned} E_c &= \frac{4}{3} \cdot 9.4 (1 + 0.52 \cdot 1.79^2) = \\ &= 33.3 \text{ MPa} \end{aligned} \quad (8-3)$$

The rubber strips are therefore modeled with a Young's modulus $E = 33$ MPa, and, characteristic of the near-incompressibility of rubber, with a Poisson's ratio $\nu = 0.499$. To better capture this incompressible behavior, the EPDM rubber strips are modeled as gaskets in Abaqus. Gasket elements capture incompressibility without compromising on computational efficiency, see Section 7.8.4 It is possible to define the deformation behavior of a gasket in Abaqus directly, but no such experimental information is available. As a result, the gasket is given linear elastic parameters, but nothing else—not even a density.

8.6 Design of Bolted Connection

The bolted setup contains four bolts attaching the glass specimen to the primary frame, see Figure 8-13. (The bolt model can also be compared to the photos in Section 5.1.) This implies that bolt holes were drilled into the glass, which generates stress concentrations. To capture this behavior in Abaqus, the model is also modeled with bolt holes, and the glass mesh is

refined in the areas immediately surrounding the bolt holes. Each bolt is modeled using four components:

- steel bolt heads/discs, modeled as cylindrical shells;
- rubber gussets, positioned between the bolt heads and the glass surface, modeled as gaskets;
- connector elements, with the connection type Axial + Align, positioned between the bolt heads;
- MPC Ties, positioned between the primary frame I-beams and the bolt heads.

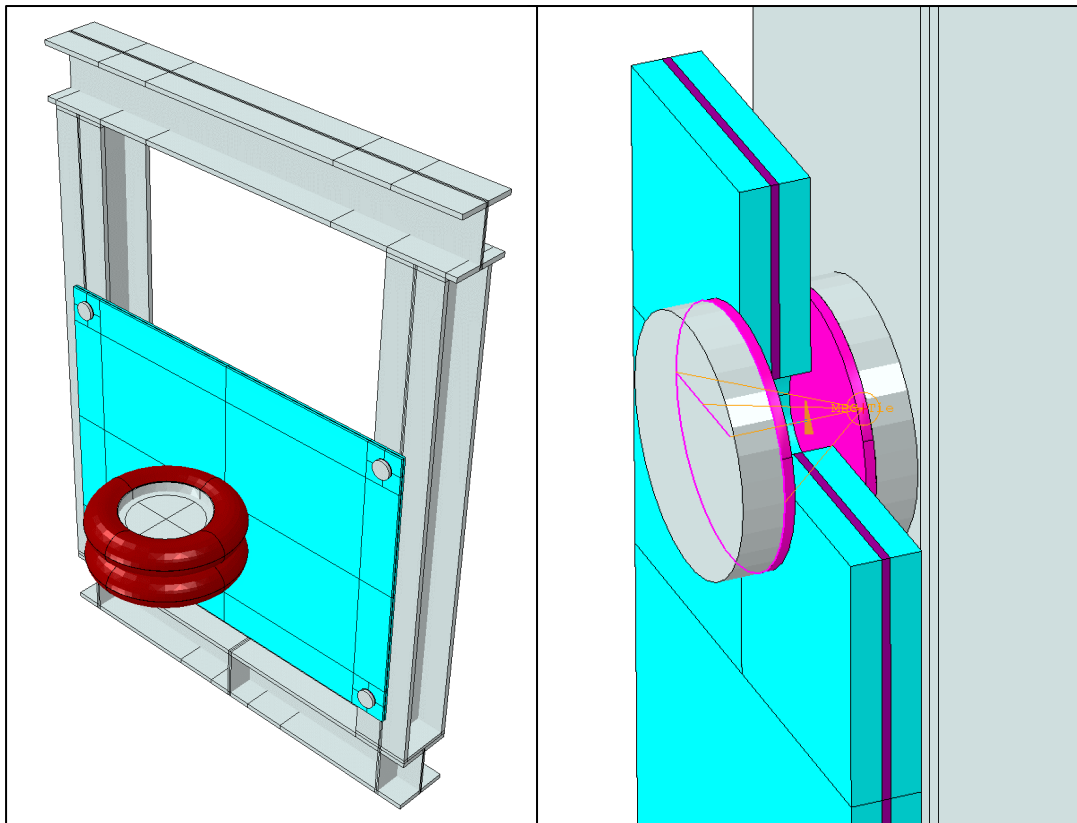


Figure 8-13: Bolted high-fidelity FE model seen isoparametrically (left) and close-up of the bolted connection. The gray is steel, the turquoise is glass, the purple is the interlayer, and the magenta are the rubber bolt gussets.

A schematic cross-section of this fastener assembly is illustrated in Figure 8-14. Tie constraints and contact interactions are applied alternately to the surfaces of the connection, which, together with the MPC Ties and connector elements, increase the fastener stiffness significantly. This is, in part, to compensate for the lack of pretensioning in the FE model.

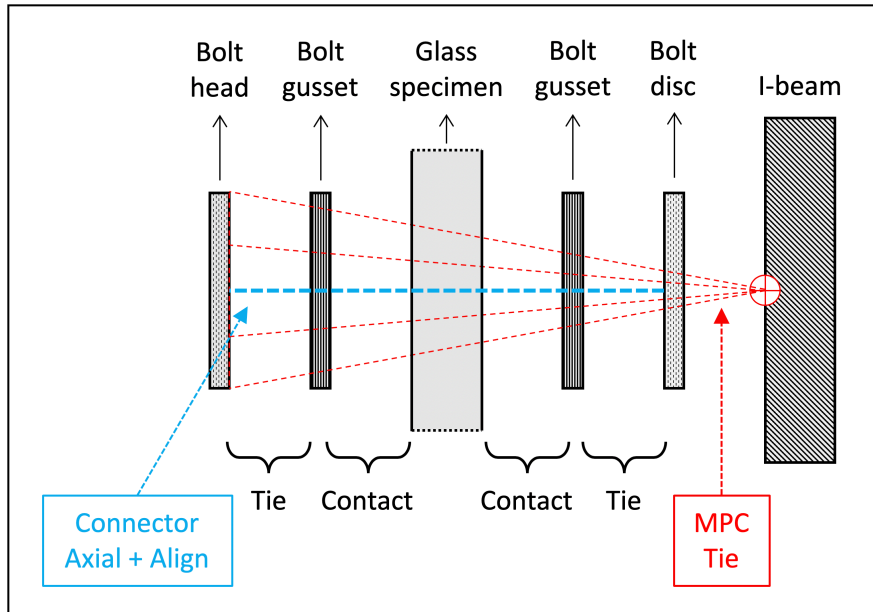


Figure 8-14: Schematic cross-section of the bolt fastener assembly modeled in Abaqus.

The Young's modulus of the rubber gussets is determined analogous to Section 8.5, in which simplified expressions are utilized to estimate the effective compression modulus of a rubber element with a prescribed geometry (Lindley, 1978). The compression modulus of the rubber bolt gussets is thereby approximated with

$$E_c = E_0 (1 + 2 k S^2) \quad (8-4)$$

The initial Young's modulus is $E_0 = 9.4$ MPa, while $k = 0.52$ (Lindley, 1978). For a circular disk of diameter $d = 50$ mm and thickness $t = 2$ mm, the shape factor is calculated to be

$$S = \frac{L B}{2 t (L + B)} \xrightarrow{\text{circular section}} \frac{d}{4 t} = \frac{50}{4 \cdot 2} = 6.25 \quad (8-5)$$

Insertion into Eq. (8-4) yields an effective compression modulus

$$\begin{aligned} E_c &= 9.4 (1 + 2 \cdot 0.52 \cdot 6.25^2) = \\ &= 391 \text{ MPa} \end{aligned} \quad (8-6)$$

However, for cases in which $E_c/E_\infty > 0.1$, where the bulk modulus of the rubber is $E_\infty = 1330$ MPa, the effective compression modulus should be modified to $E_{c,\text{mod}}$ (Lindley, 1978). Thus,

$$\begin{aligned} E_{c,\text{mod}} &= \frac{E_c}{1 + \frac{E_c}{E_\infty}} = \\ &= \frac{391}{1 + \frac{391}{1330}} = 302 \text{ MPa} \end{aligned} \quad (8-7)$$

The bolt gussets are therefore modeled with a Young's modulus $E = 302 \text{ MPa}$, and, characteristic of the near-incompressibility of rubber, with a Poisson's ratio $\nu = 0.499$. The rubber bolt gussets are discretized with gasket elements.

8.7 Design of Clamped Connection

The clamped setup contains four clamps attaching the glass specimen to the primary frame via the C-beams, see Figure 8-15. (The clamp model can also be compared to the photos in Section 5.1.)

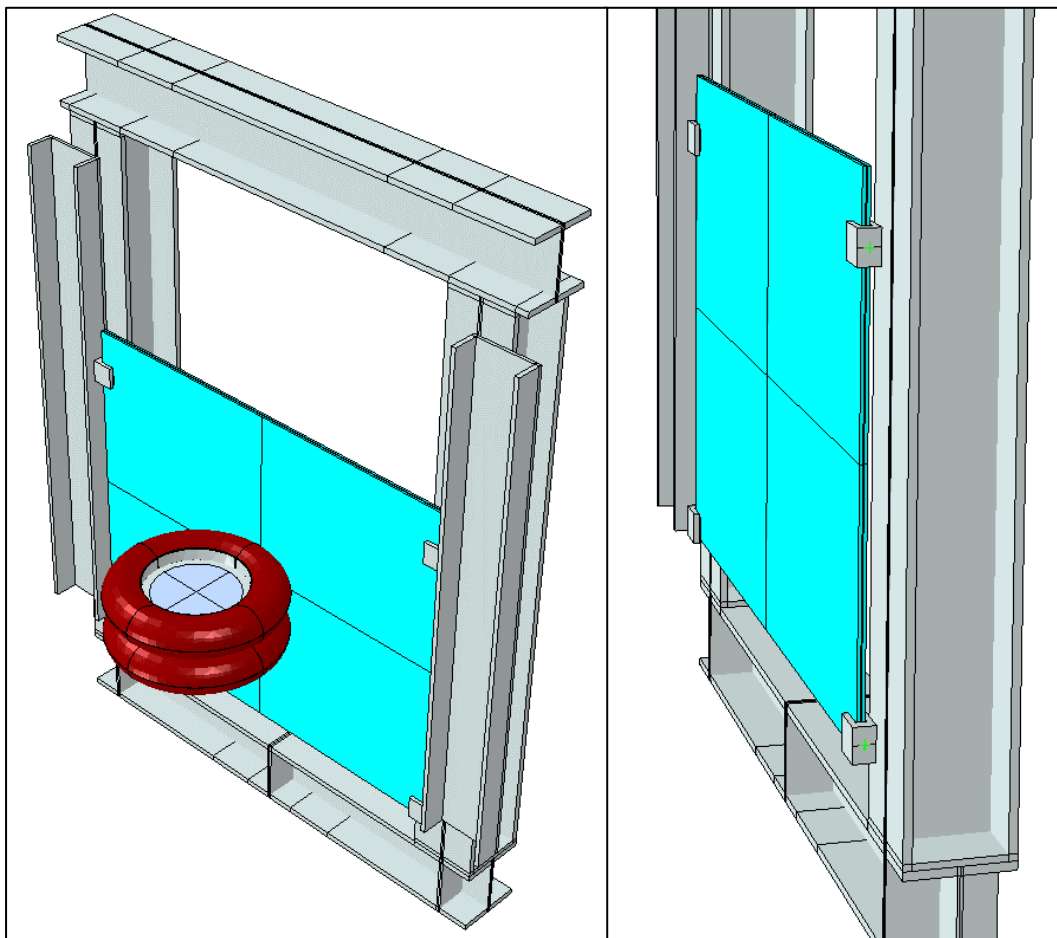


Figure 8-15: Clamped high-fidelity FE model seen isoparametrically (left) and from the side (right), with the C-beams removed.

A number of uncertainties characterize the third setup. Firstly, the position of the clamps is not precisely known, due to insufficient documentation, but the effect of moving the clamps a few mm along the plane is likely marginal. Close-ups of the modeled clamps are shown in Figure 8-16.

Secondly, upon investigation, it became clear that the minimum opening of the clamps was slightly larger than the thickness of the thinnest glass specimens. Thus, no pretension is possible for those specimens, although it is for the thicker specimens. Regardless, it is assumed that all glass specimens are fastened in such a manner that the prestress is negligible.

Thirdly, the connection between the clamps and the C-beam consisted of an 8 mm thick bolt, secured by a nut on the C-beam flange. It is assumed that this constitutes a rigid connection, which is modeled as a surface-to-surface tie constraint. The entirety of the surface that is in contact with the C-beam is tied, thereby achieving high rotational stiffness in the connection.

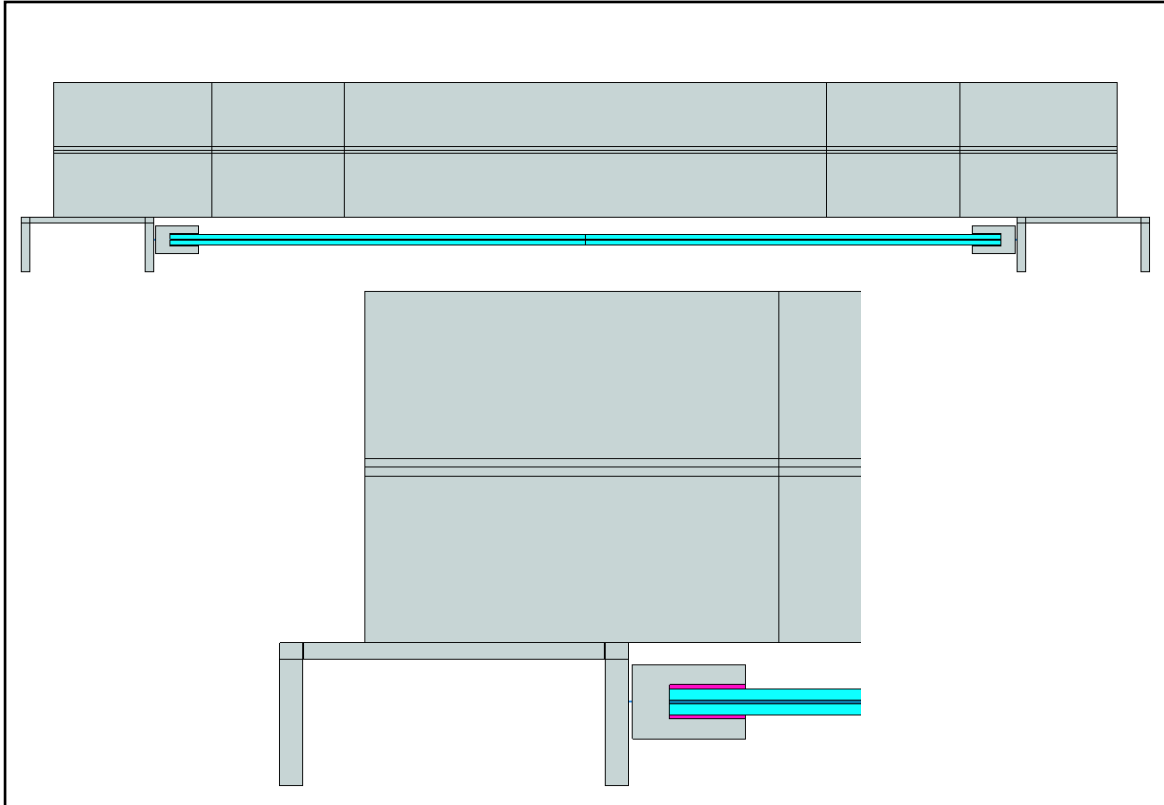


Figure 8-16: Clamped setup seen from above (top), and close-up of the clamped connection (bottom).

The rubber clamp gusset was designed to prohibit movement relative the steel. This is accounted for with a tie constraint between the rubber and the steel.

The Young's modulus of the rubber gussets is determined analogous to Section 8.5, in which simplified expressions are utilized to estimate the effective compression modulus of a rubber element with a prescribed geometry (Lindley, 1978). The compression modulus of the rubber clamp gussets is thereby approximated with

$$E_c = E_0 (1 + 2 k S^2) \quad (8-8)$$

The initial Young's modulus is $E_0 = 9.4$ MPa, while $k = 0.52$ (Lindley, 1978). For a square pad of side length $L = 38$ mm and thickness $t = 2$ mm, the shape factor is calculated to be

$$S = \frac{L B}{2 t (L + B)} \xrightarrow{\text{square section}} \frac{L}{4 t} = \frac{38}{4 \cdot 2} = 4.75 \quad (8-9)$$

Insertion into Eq. (8-8) yields an effective compression modulus

$$E_c = 9.4 (1 + 2 \cdot 0.52 \cdot 4.75^2) = 230 \text{ MPa} \quad (8-10)$$

However, for cases in which $E_c/E_\infty > 0.1$, where the bulk modulus of the rubber is $E_\infty = 1330 \text{ MPa}$, the effective compression modulus should be modified to $E_{c,\text{mod}}$ (Lindley, 1978). Thus,

$$\begin{aligned} E_{c,\text{mod}} &= \frac{E_c}{1 + \frac{E_c}{E_\infty}} = \\ &= \frac{230}{1 + \frac{230}{1330}} = 196 \text{ MPa} \end{aligned} \quad (8-11)$$

The clamp gussets are therefore modeled with a Young's modulus $E = 196 \text{ MPa}$, and, characteristic of the near-incompressibility of rubber, with a Poisson's ratio $\nu = 0.499$. The rubber bolt gussets are discretized with gasket elements.

8.8 Summary of Material Input Parameters and Element Selection

A summary of the material modeling is presented in Table 8-3, expressed in terms of the chosen material input parameters. Note that all elasticity models, save for the rubber tires, are linear in an effort to curb computational costs.

Material	Application	Density [kg/m ³]	Elastic properties	Damping [-]
Steel	Frame beams and impactor core	7850	$E = 210 \text{ GPa}$, $\nu = 0.3$	–
Glass	Soda-lime glass	2500	$E = 72 \text{ GPa}$, $\nu = 0.23$	–
PVB	Interlayer	1000	$E = 420 \text{ MPa}$, $\nu = 0.47$	–
SGP	Interlayer	1000	$E = 1300 \text{ MPa}$, $\nu = 0.46$	–
Tire rubber	Impactor tire	1300	Hyperelastic, Mooney-Rivlin: $C_{10} = 15.828 \text{ MPa}$ $C_{01} = -6.228 \text{ MPa}$ $D_1 = 5.700 \cdot 10^{-2} \text{ MPa}^{-1}$	Rayleigh damping: $\alpha_R = 0$ $\beta_R = 0.0028$
EPDM rubber	Setup 1: rubber strips	–	$E = 33.0 \text{ MPa}$, $\nu = 0.499$	–
	Setup 2: bolt gusset	–	$E = 302 \text{ MPa}$, $\nu = 0.499$	–
	Setup 3: clamp gusset	–	$E = 196 \text{ MPa}$, $\nu = 0.499$	–

Table 8-3: Summary of input parameters for the materials used in the high-fidelity finite element models. EPDM rubber lacks a density value because it is modeled as a gasket, which does not require a density input.

The element selection is summarized in Table 8-4, expressed in terms of their application throughout the high-fidelity finite element models. The 3D stress elements are reduced integration in an effort to curb computational cost.

Table 8-4: Summary of element selection used in the high-fidelity finite element models.

Element family	Element name	Element description	Application	Seed size [mm]
3D stress	C3D8R	An 8-node linear brick, reduced integration, hourglass control.	Impactor core	4
			Clamps	5
Shell	S4R	A 4-node doubly curved thin or thick shell, reduced integration, hourglass control, finite membrane strains.	Frame beams	20
			Impactor tires	4
			Bolt heads	5
Continuum solid shell	CSS8	An 8-node linear brick, incompatible modes, with assumed strain.	Soda-lime glass	15
			Interlayers	15
Gasket	GK3D8	An 8-node three-dimensional gasket element.	Rubber strips	5
			Bolt gussets	5
			Clamp gussets	5

8.9 Convergence

When investigating the extreme values for relatively short event such as impulse loading, it is important that the extrema behavior is captured accurately. Therefore, convergence of the models is studied to verify that the finite element meshes, shown in Figure 8-17, and the time increments converge spatially and transiently, respectively, on the true solution.

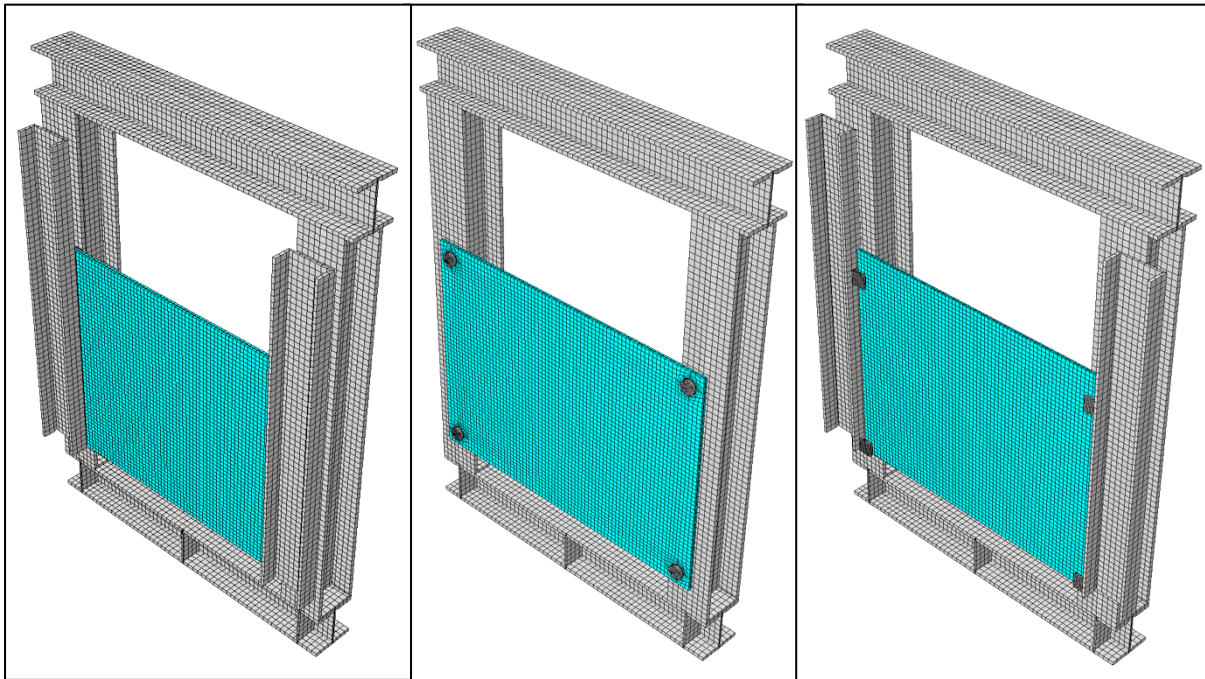


Figure 8-17: Finite element meshes of the three high-fidelity models: simply supported (left); bolted (center); clamped (right).

8.9.1 Spatial Convergence

The first element of the spatial convergence study is the impactor. Its mesh is verified by isolating it from the test setup and instead simulating it in the dynamic rigid impact tests. The results are processed by examining the relative change in output variable extrema, in this case acceleration maxima, from the previous iteration and comparing this to the total number of impactor elements required to complete the analysis step, see Figure 8-18. It is concluded that the impactor mesh converges to a sufficient degree at 6 mm global element size.

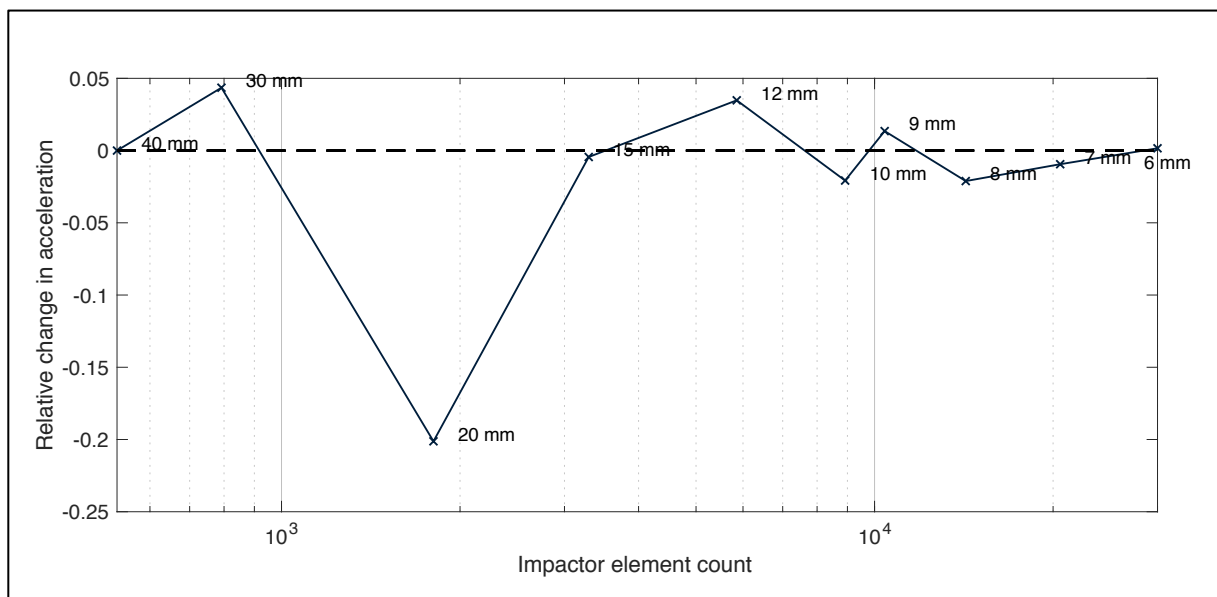


Figure 8-18: Spatial convergence of the impactor, showing relative change in the acceleration output variable from the previous iteration. Note that the scale is logarithmic.

Having determined the convergent impactor mesh, the dual-tire impactor is reintroduced to the high-fidelity models with a 6 mm global element size. Convergence of the glass element mesh is then studied, see Figure 8-19. The glass mesh converges quickly, and a 15 mm global element size is concluded to be sufficient.

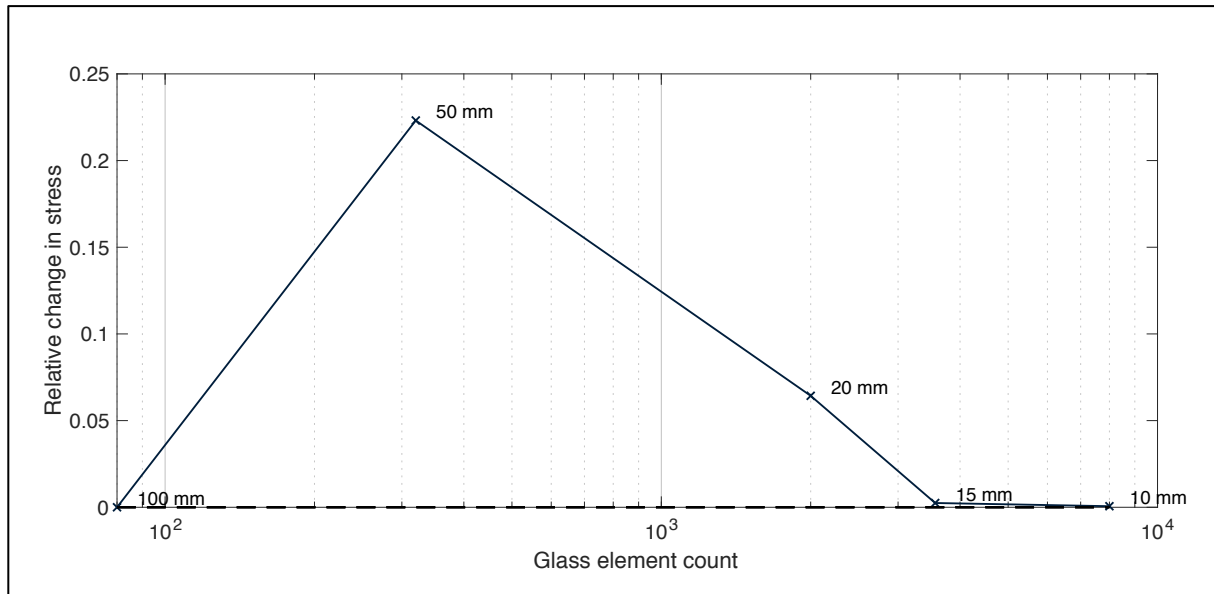


Figure 8-19: Spatial convergence of the glass, showing relative change in the stress output variable from the previous iteration. Note that the scale is logarithmic.

8.9.2 Transient Convergence

Determining the optimal time incrementation for the high-fidelity models is of decisive importance with respect to both precision of results and computational economy. Transient convergence is therefore studied by sequentially decreasing the maximum permitted time increment in the dynamic, implicit analysis step in the first test setup. The relative change in variable output extrema, in this case stress maxima, from the previous iteration is then compared to the total number of time increments required to complete the analysis step, see Figure 8-20. It is concluded that a 0.4 ms time increment yields an acceptable level of transient convergence vis-à-vis computational cost.

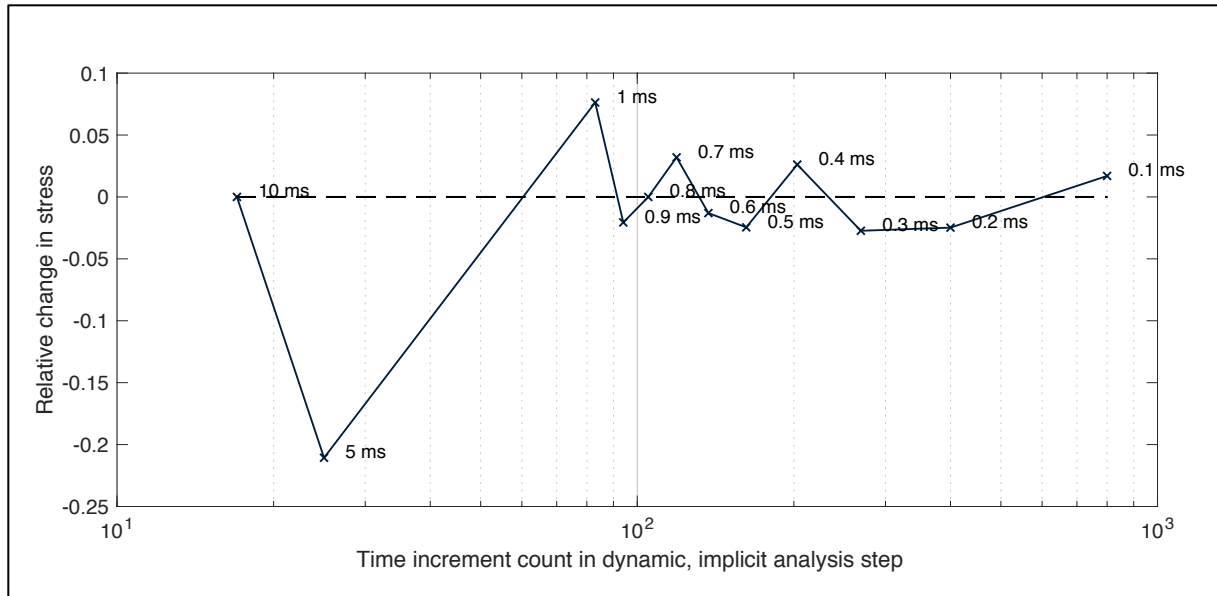


Figure 8-20: Spatial convergence of the glass, showing relative change in the stress output variable from the previous iteration. Note that the scale is logarithmic.

9 Finite Element Modeling of Reduced Designs

“Perfection is achieved, not when there is nothing left to add, but when there is nothing left to take away.”

—Antoine de Saint-Exupéry

This chapter describes the construction of, and input data to, the reduced finite element models. The first Section presents the reduced dynamic models, that is to say models that reduce the complexity inherent to the high-fidelity models while still executing the analysis in a dynamic, implicit step. The second Section describes the reduced models with equivalent static loads, that is to say models that are further simplified by replacing the impactor and the transient component with a static load multiplied with an amplification factor.

9.1 General Overview

A reduced numerical model aims to provide a computationally inexpensive route to obtaining accurate results of a given problem by means of idealizations and engineering assumptions. It is recalled that part of the research motivation of the study is to investigate potential avenues for designing glass structures to resist impact loading by way of streamlined numerical methods. It is therefore of interest to apply a reduced model methodology to the problem at hand; namely, accurately capturing the principal stresses exhibited by glass specimens as a result of soft-body impact loading. Two approaches are invoked: the first is a reduced dynamic model, after which a proof-of-concept is demonstrated with respect to an equivalent static model.

9.2 Design of Reduced Dynamic Models

The first set of reduced models retains the transient component of the simulations, i.e. the stresses continue to be computed in a dynamic, implicit analysis step. Reducing the high-fidelity models described in Chapter 8 is therefore chiefly concerned with eliminating inessential geometry and replacing them with equivalent springs. The objective is to eliminate all geometry in the model, save for the impactor and the glass itself, and while still maintaining accurate stress response, see Figure 9-1.

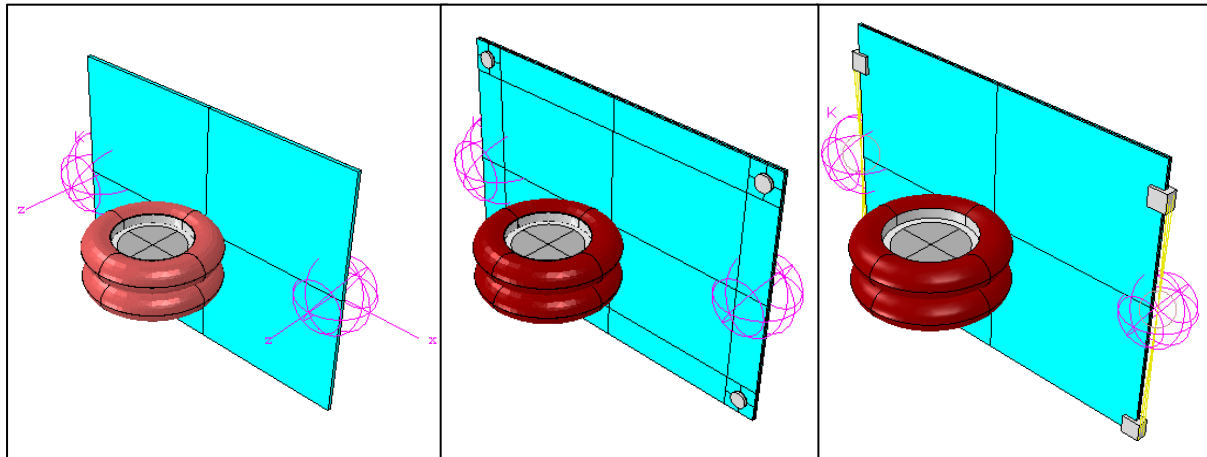


Figure 9-1: Reduced dynamic model designs: simply supported (left), bolted (center), and clamped (right). Springs are positioned at the vertical edges of the glass, along the centerline.

The primary frame remains unchanged for all fastener configurations. Simplifying its boundary conditions such that it is assumed to be rigid in the plane of the glass and that it is unable to rotate, it can be reduced to a single spring defined by an out-of-plane stiffness. To determine this stiffness, the frame is isolated in Abaqus and loaded uniformly with a force F , i.e. static condensation. Utilizing Hooke's Law, the stiffness k is derived by extracting the maximum deflection of the frame u_{frame} ,

$$F = k_{\text{frame}} u_{\text{frame}}$$

$$\Rightarrow k_{\text{frame}} = \frac{F}{u_{\text{frame}}} \quad (9-1)$$

Having reduced the primary frame, the remaining stiffness in the setup stems from the fasteners (and the glass). Each fastener configuration has a unique translational stiffness and rotational stiffness, i.e. a unique spring stiffness k_{fastener} and torsion coefficient κ_{fastener} . The former are calculated in a manner analogous to the primary frame, while the latter are determined iteratively. Once k_{fastener} is calculated for a particular setup, the total translational stiffness of the setup is calculated in series, i.e.

$$\frac{1}{k_{\text{tot}}} = \frac{1}{k_{\text{frame}}} + \frac{1}{k_{\text{fastener}}}$$

$$\Rightarrow k_{\text{tot}} = \left(\frac{1}{k_{\text{frame}}} + \frac{1}{k_{\text{fastener}}} \right)^{-1} \quad (9-2)$$

The final stiffnesses used in the reduced models are summarized in Table 9-1. These are prescribed to one spring positioned at each vertical edge of the glass, along its centerline.

Table 9-1: Spring stiffnesses and torsion coefficients for the reduced setups.

Setup	Stiffness [kN/m]	Torsion coefficient [kNm/rad]
Simply supported	51	150
Bolted	109	150
Clamped	109	580

For the bolted and clamped setups, the fastener geometry is maintained in the models to ensure that the stress concentrations continue to be captured accurately.

9.3 Design of Reduced Models with Equivalent Static Loads

The overarching design of the reduced dynamic models, with respect to the equivalent spring stiffnesses, is maintained in the next iteration of reduced models. The critical change in the geometry of the models is that the impactor is removed entirely and replaced with an equivalent, uniformly distributed, static load. The area on which this load acts is consistent with the idealizations employed in the semi-analytical model, see Section 6.5.2. This yields a $0.2 \times 0.2 \text{ m}^2$ loaded area, see Figure 9-2.

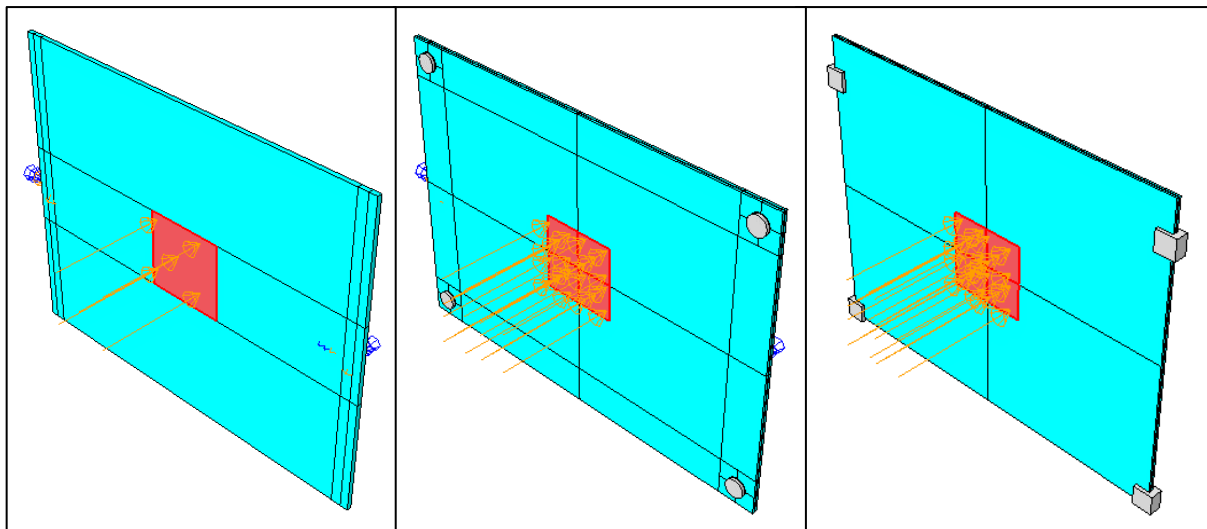


Figure 9-2: Reduced model designs with equivalent static loads: simply supported (left), bolted (center), and clamped (right).

Two methods are deployed to estimate the equivalent static load. Both methods presume that the glass behaves in a manner analogous to a beam, i.e. the results for the bolted and clamped setup are automatically rendered suspect. The methods are presented below.

9.3.1 Method 1: Amplified Impactor Self-weight Static Load

This method applies a dynamic impact factor (DIF) to the self-weight of the impactor. Consequently, the equivalent force is defined as

$$F_{eq} = mg \cdot n_{DIF} \quad (9-3)$$

For an impact load acting on a beam, i.e. a relatively stiff elastic body, approximations for the DIF are available (Akin, 2017). The factor can be calculated using

$$n_{DIF} = \sqrt{\frac{\eta v^2}{g \delta_{static}}} \quad (9-4)$$

where

v is the impactor velocity,

g is gravity,

η is the energy conservation in the system (1.0),

δ_{static} is the deflection of the glass due to static loading of the impactor.

The deflection δ_{static} is calculated as a beam analogy. That is, the glass panel is assumed to be a simply supported beam, loaded at midspan with a point load. The magnitude of the load is set by the self-weight of the impactor, i.e. $F = mg = 50g$. Thus, the deflection is given by:

$$\delta_{static} = \frac{FL^3}{48EI} \quad (9-5)$$

Naturally, this is a grave generalization of the problem. The hypothesis foundation lies within its applicability; the method can be utilized without any previous knowledge of the glass behavior.

It is clear that uncertainties are introduced to the system when the equivalent load, derived with beam theory, is applied in a numerical model. On this note, the validity of using exclusively beam theory, was investigated. Thus, the problem was described by a simply-supported beam subjected to the equivalent load obtained with (9-3). However, this approach was quickly neglected when calculations showed deviations of large magnitude.

Resulting parameters, such as equivalent force, are presented in Annex E. For the results of the static model, i.e. principal stress, refer to Section 10.4.

9.3.2 Method 2: Semi-analytical Static Load

This method utilizes the deformation response factor R_d from structural dynamics to estimate the equivalent static load. This factor describes the relationship between a static deformation and the resulting deflection if the load were to be applied dynamically (Chopra, 2014). It is defined as

$$R_d = \frac{u_{0,dyn}}{u_{0,stat}} \quad (9-6)$$

which, assuming linearity, is equivalent to

$$R_d = \frac{P_{0,dyn}}{P_{0,stat}} \quad (9-7)$$

Combining Eq. (9-6) and Eq. (9-7) thus yields

$$P_{0,dyn} = \frac{u_{0,dyn}}{u_{0,stat}} P_{0,stat} \quad (9-8)$$

Acknowledging that, through Hooke's Law,

$$u_{0,stat} = \frac{P_{0,stat}}{k_{stat}} \quad (9-9)$$

Eq. (9-8) and Eq. (9-9) finally yield

$$\begin{aligned} P_{0,dyn} &= \frac{u_{0,dyn}}{P_{0,stat}/k_{stat}} P_{0,stat} \\ \Rightarrow P_{0,dyn} &= u_{0,dyn} k_{stat} \end{aligned} \quad (9-10)$$

The equivalent load is thus the product of the stiffness of the setup, which is sourced from the beam analogy used in the semi-analytical model, see Table 6-2, and the deflection caused by dynamic loading. This deflection is interpreted as the maximum out-of-plane deformation of the glass when loaded dynamically. These values are extracted from the high-fidelity finite element models constructed in Chapter 8. In other words, the load used in the equivalent static models is estimated to be

$$F_{eq} = u_{FE,comp} k_{stat} \quad (9-11)$$

These loads are tabulated in E for the various setups and drop heights.

10 Results and Analysis

“Nature laughs at the difficulties of integration.”

—Pierre-Simon Laplace

This chapter collects the results from the experimental campaign, the high-fidelity finite element models, the reduced finite element models, and the semi-analytical models. Priority is given to presenting and analyzing the principal stresses outputted by each of these sources, and the agreement of the various data. The results of the dynamic models are presented, by setup, in the first Sections, after which the results of the equivalent static models are presented. In the final Section, the deviations in stress are tabulated and analyzed.

10.1 General Overview

The results outputted by the semi-analytical model and the finite element simulations become meaningful when compared to their experimental counterparts. This comparison takes place chiefly in the (principal) stress domain, as this variable is decisive when investigating structural glass. By superimposing the processed experimental data onto the principal stresses yielded by the finite element simulations, as well as the stress obtained from the semi-analytical model by means of a beam analogy, the agreement between the models can be scrutinized. This agreement can be deconstructed into two parameters: the maximum stress given by a particular model; and the character of the transient event itself, i.e. how quickly maximum stress is attained, whether double impacts take place, and so on. Both the transient events and the maximum stresses are visualized in the figures presented in this chapter.

Given the broad scope of the study, the arrangement of the results is presented in Table 10-1 for convenience.

Table 10-1: Arrangement of the collated results.

Fastener configuration	Glass profile [mm]	Transient event	Maximum Stress
Simply supported	8	Figure 10-1	Figure 10-11
	10	Figure 10-2	
	12	Figure 10-3	
	8 + 1.6 PVB + 8	Figure 10-4	
	8 + 1.6 SGP + 8	Figure 10-5	
Bolted	6 + 1.6 SGP + 6	Figure 10-6	Figure 10-12
Clamped	5 + 1.6 PVB + 5	Figure 10-7	Figure 10-13
	5 + 1.6 SGP + 5	Figure 10-8	
	6 + 1.6 PVB + 6	Figure 10-9	
	6 + 1.6 SGP + 6	Figure 10-10	

As a parenthesis, the experimental out-of-plane acceleration of the glass, processed according to Section 2.2.1, is superimposed onto those yielded by the high-fidelity finite element models, see Annex D. Unfortunately, there is poor agreement between these two data sets. Indeed, the dissonance in period times makes it clear that the numerical models do not accurately reflect the stiffness of the system, a relationship explained in Section 6.7.

10.2 Dynamic Model Results

The dynamic results are presented in Figures 10-1 to 10-10, i.e. they include all of the time series, including the experimental data, save for the reduced models with equivalent static loads. Studying the transient events illustrated in the figures, it is immediately obvious that, though there seems to be agreement in the ultimate stress, the character of the impact event is not consistent across the time series. Indeed, both the finite element simulations and the semi-analytical model exhibit significantly higher slopes than the experimental results. Put differently, the periods of the modeled impacts are smaller than the experimental ones. Assuming that the masses are correctly modeled, this suggests that the stiffness in the true setup is significantly lower than what has been modeled.

It is further clear that the reduced dynamic finite element models exhibit high levels of agreement with their high-fidelity cousins, which seems to vindicate the strategy of replacing the model geometry with equivalent springs. Moreover, the semi-analytical model, despite being intended as a pedagogical tool rather than an accurate model, also displays good

agreement with the other time series. The one caveat to this is the double peak phenomenon, which is only palpable for the semi-analytical model.

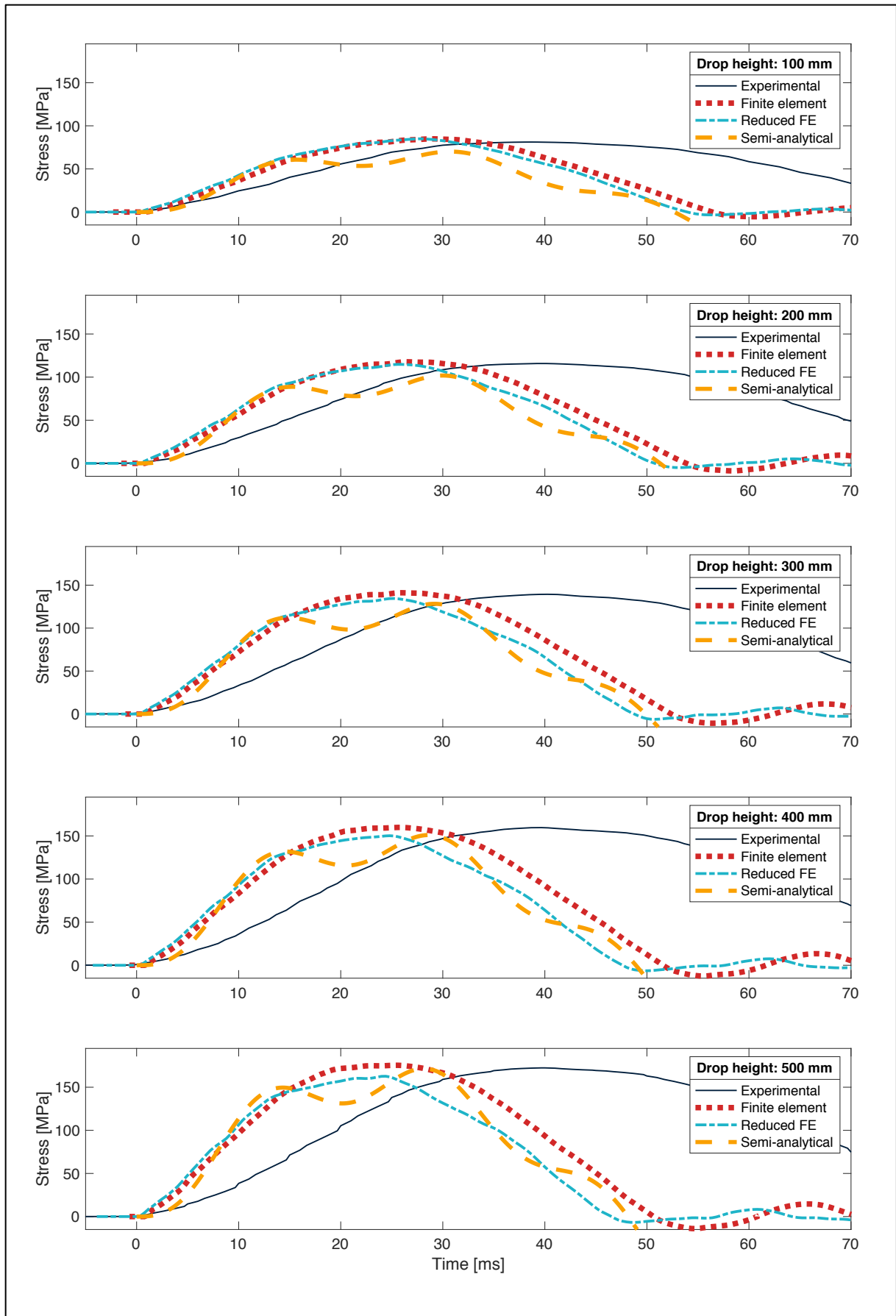


Figure 10-1: Collated results of principal stress at glass specimen impact location for various impactor drop heights. The data sets correspond to simply supported monolithic specimens with a thickness profile of 8 mm.

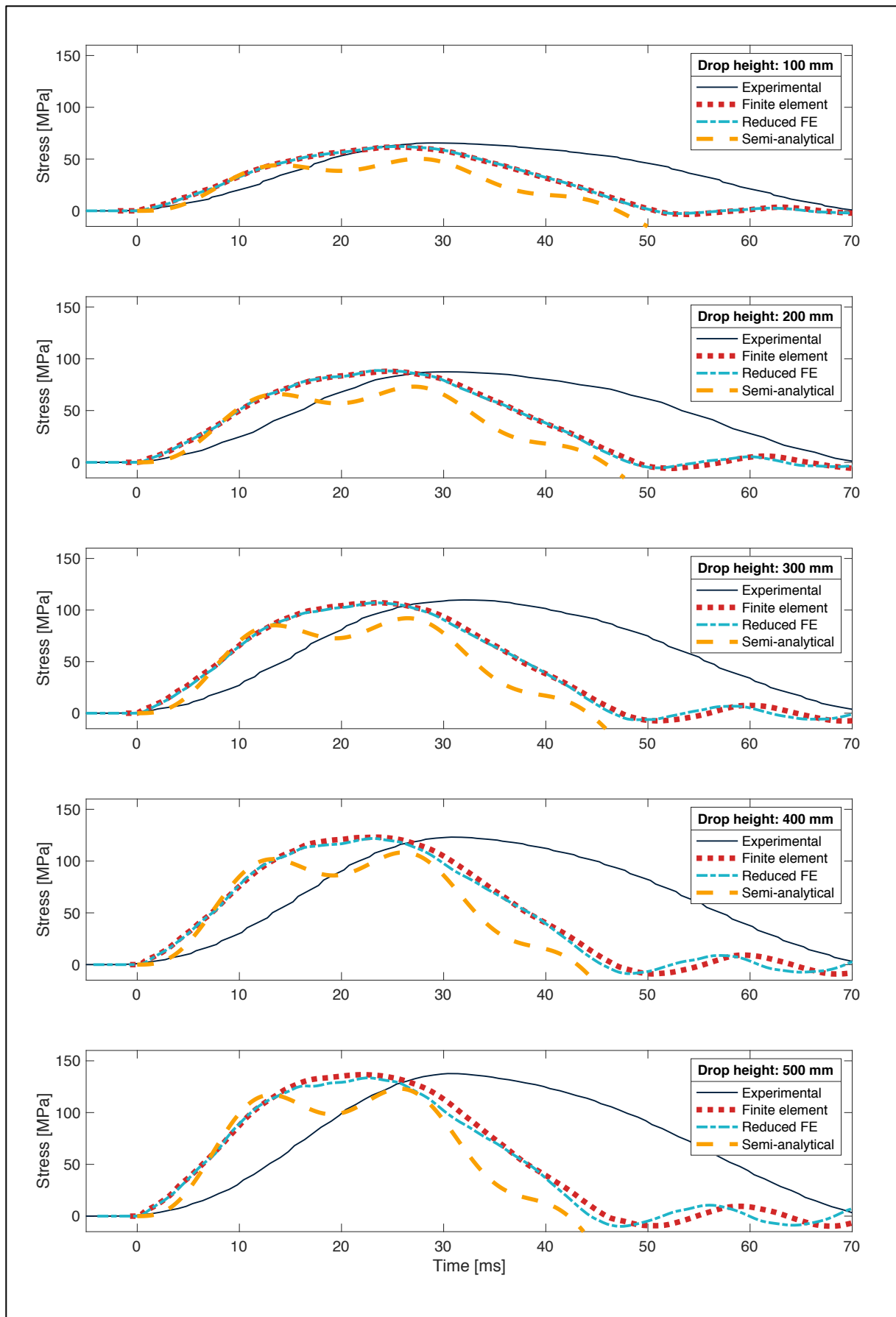


Figure 10-2: Collated results of principal stress at glass specimen impact location for various impactor drop heights. The data sets correspond to simply supported monolithic specimens with a thickness profile of 10 mm.

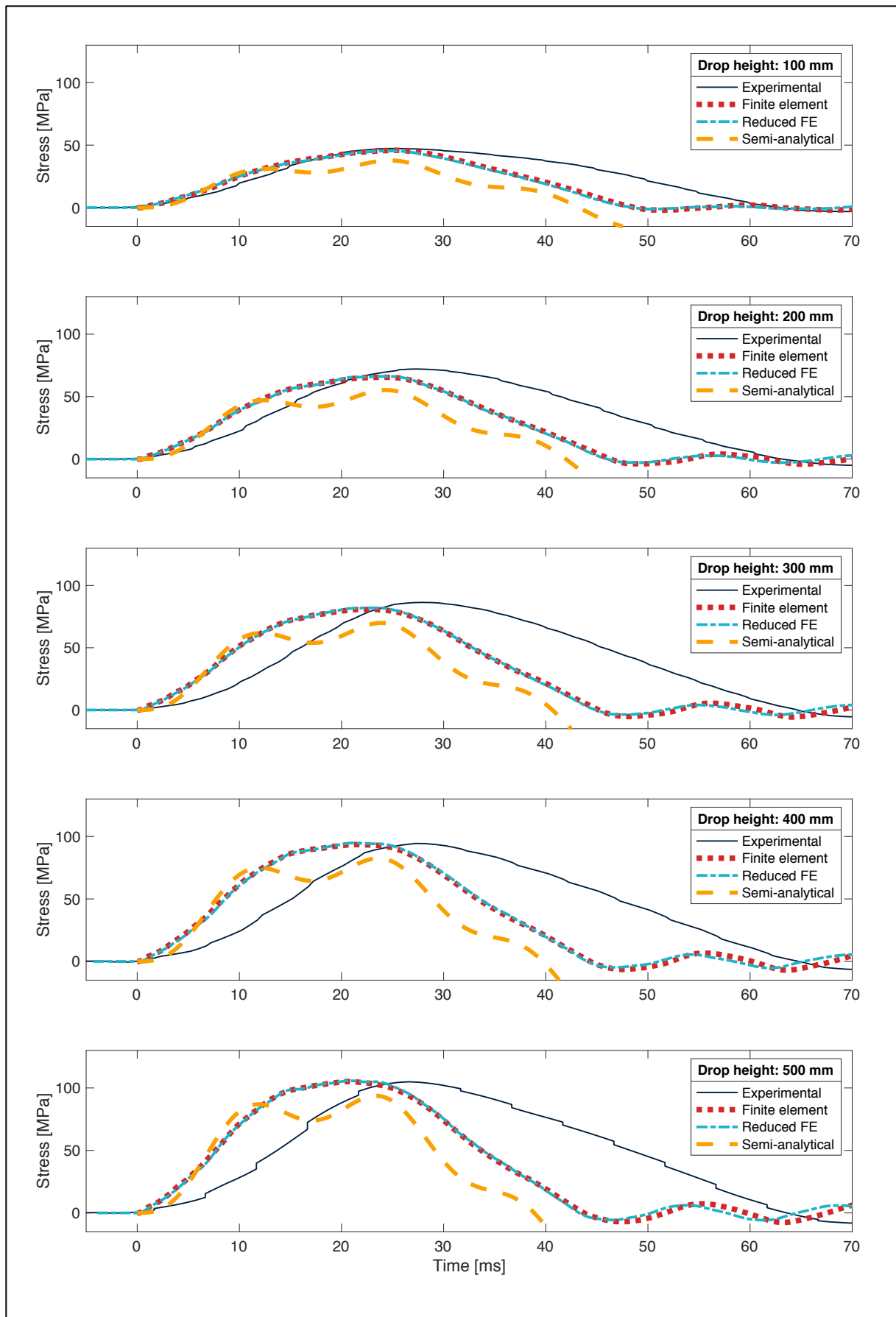


Figure 10-3: Collated results of principal stress at glass specimen impact location for various impactor drop heights. The data sets correspond to simply supported monolithic specimens with a thickness profile of 12 mm.

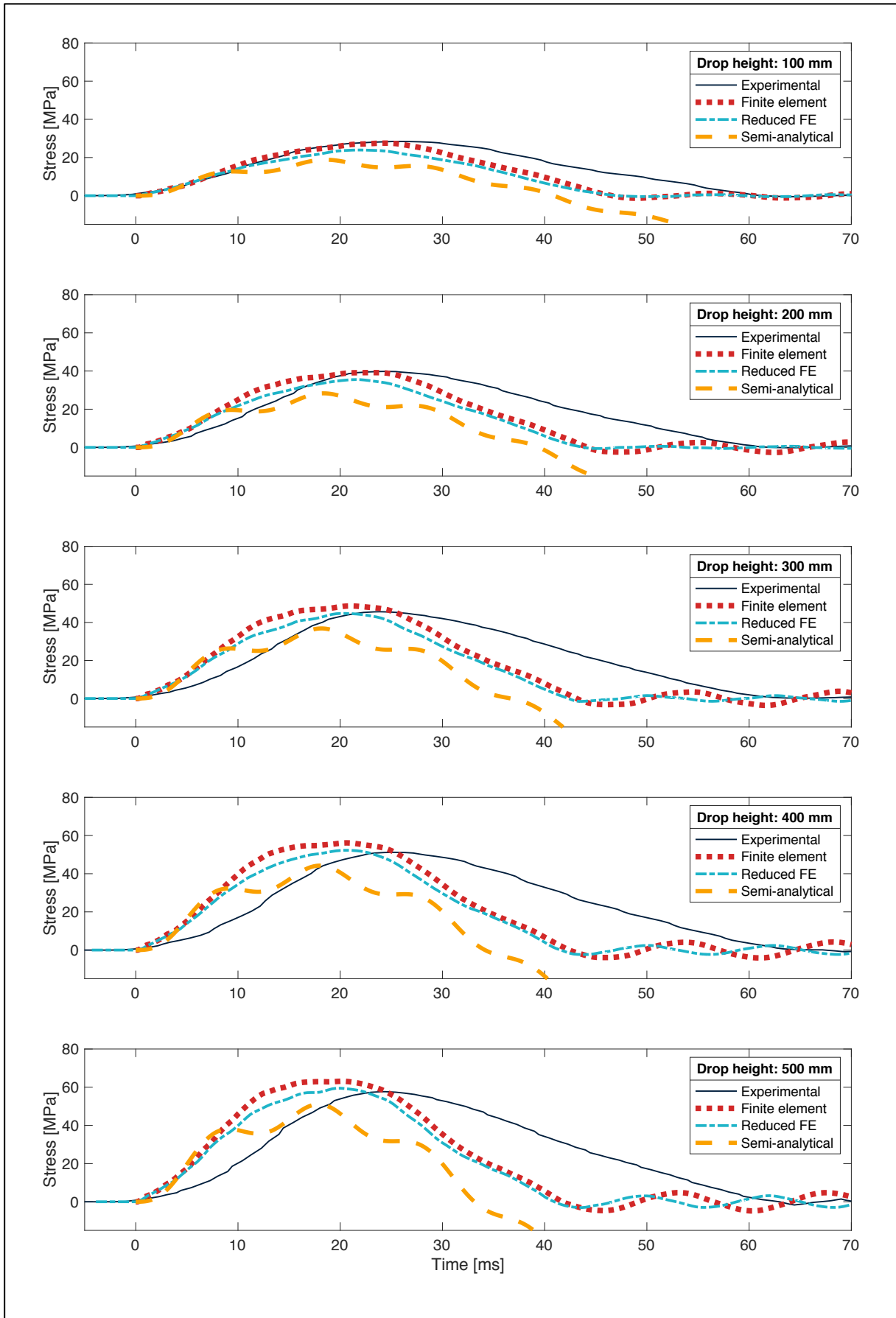


Figure 10-4: Collated results of principal stress at glass specimen impact location for various impactor drop heights. The data sets correspond to simply supported laminated specimens with a thickness profile of 8 mm ESG/TVG + 1.6 mm PVB + 8 mm ESG/TVG.

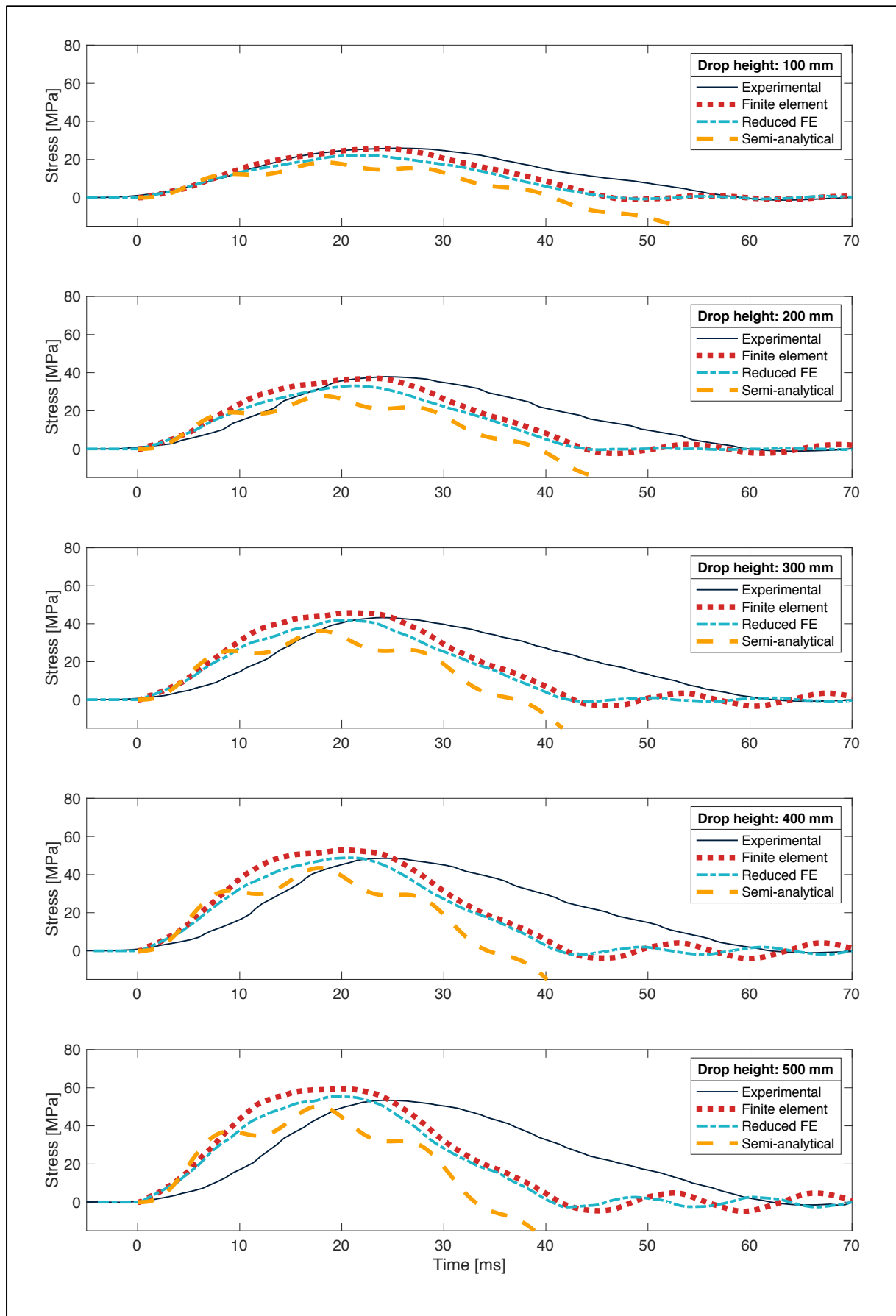


Figure 10-5: Collated results of principal stress at glass specimen impact location for various impactor drop heights. The data sets correspond to simply supported laminated specimens with a thickness profile of 8 mm ESG/TVG + 1.6 mm SGP + 8 mm ESG/TVG.

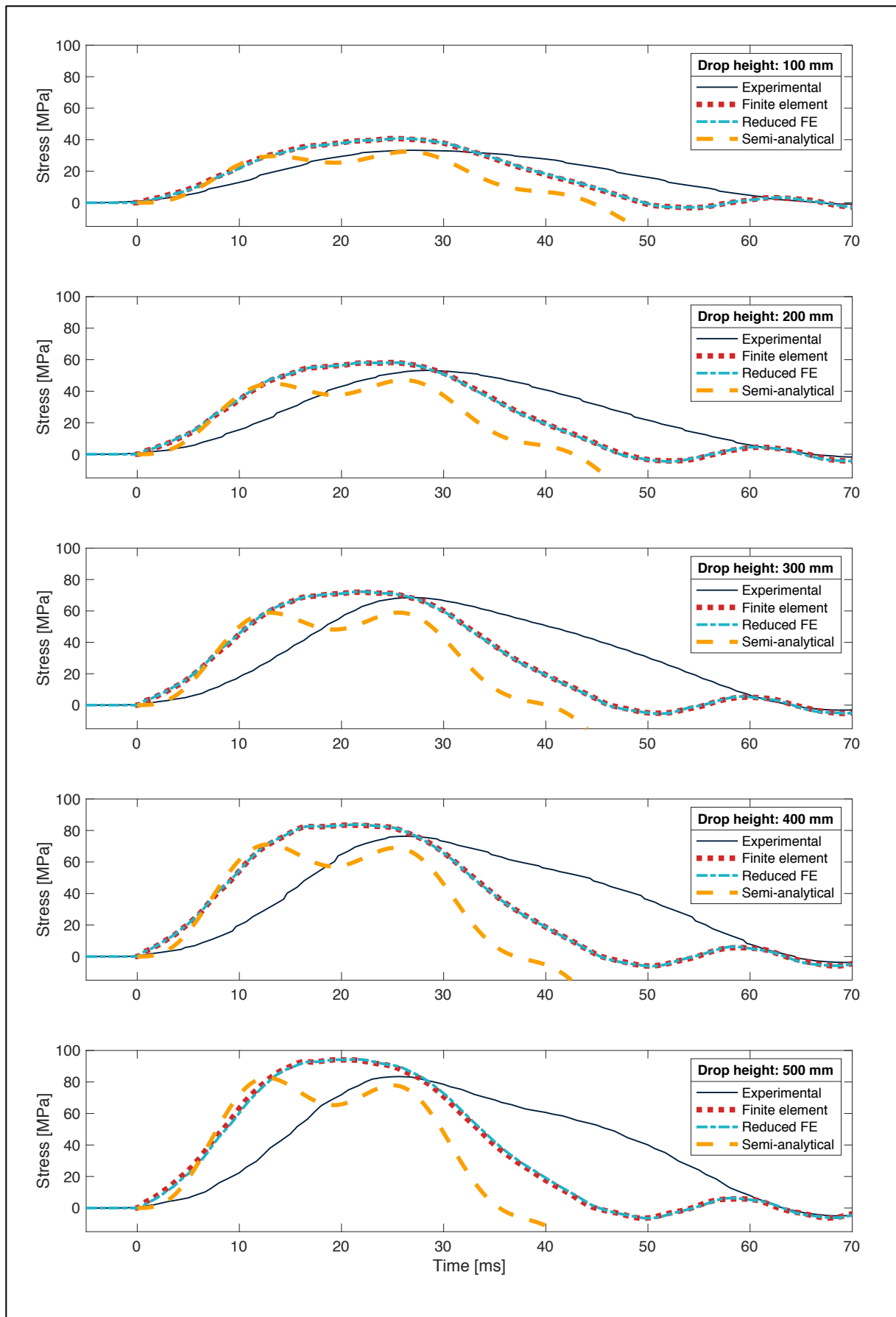


Figure 10-6: Collated results of principal stress at glass specimen impact location for various impactor drop heights. The data sets correspond to bolted laminated specimens with a thickness profile of 6 mm ESG + 1.6 mm SGP + 6 mm ESG.

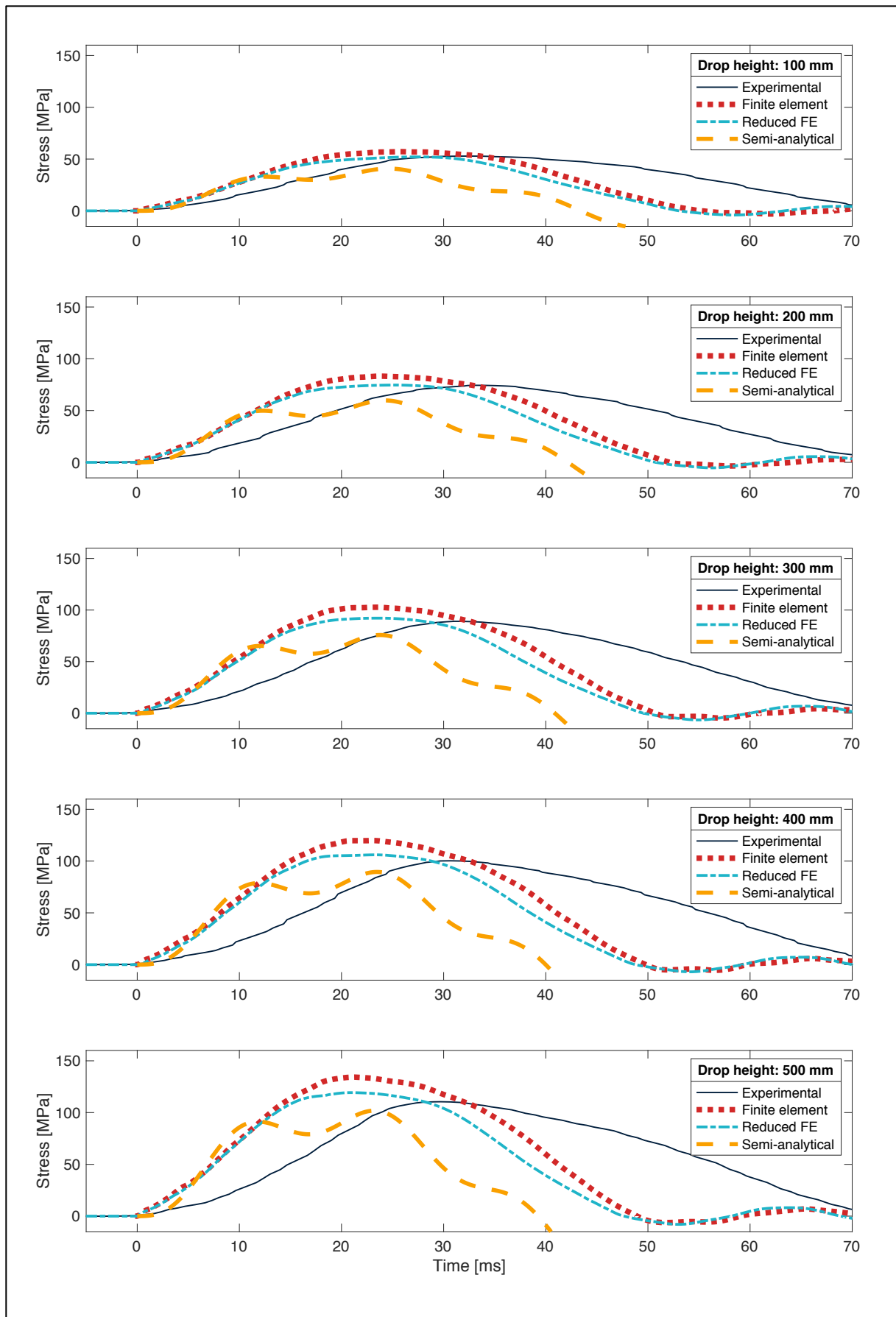


Figure 10-7: Collated results of principal stress at glass specimen impact location for various impactor drop heights. The data sets correspond to clamped laminated specimens with a thickness profile of 5 mm ESG + 1.6 mm PVB + 5 mm ESG.

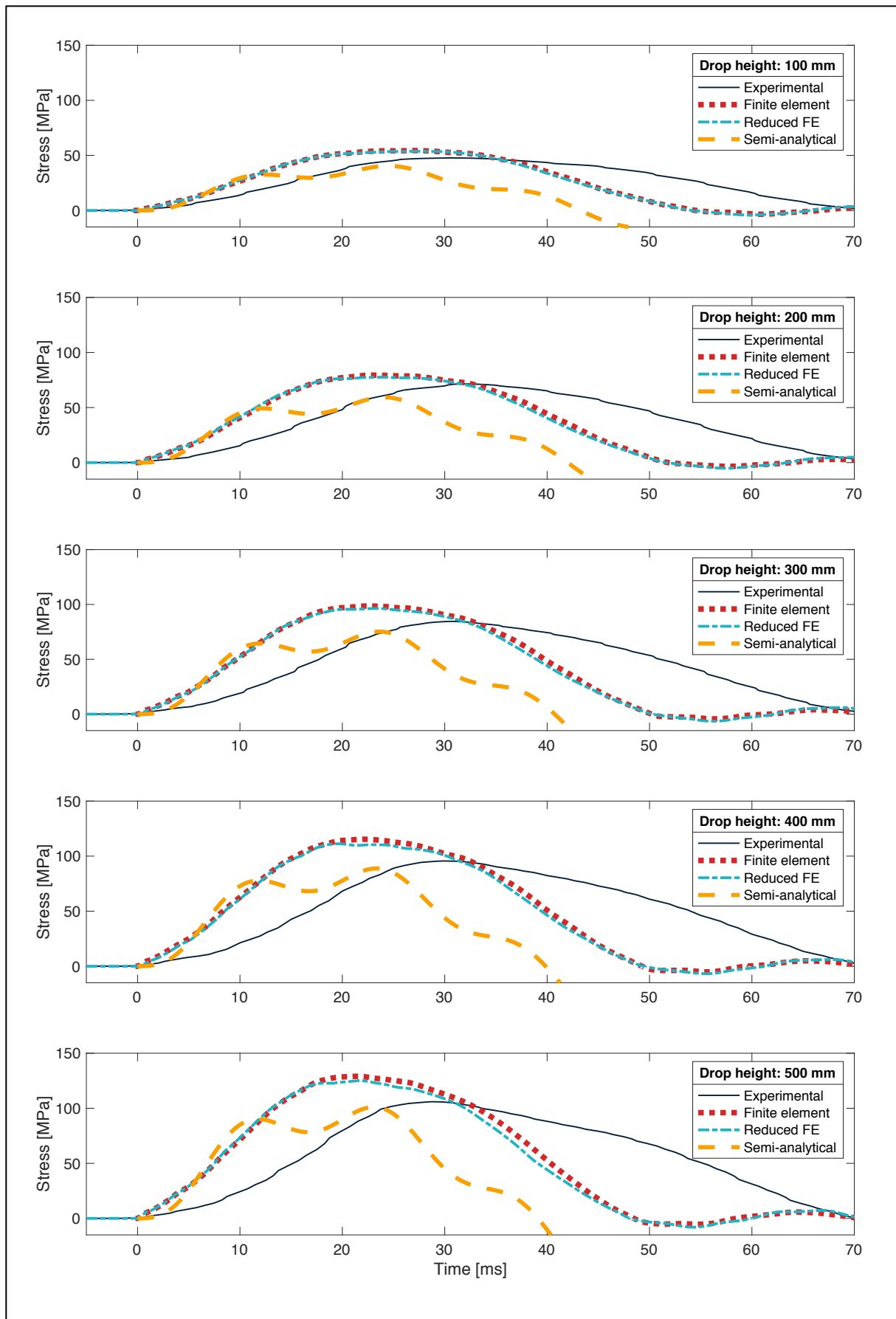


Figure 10-8: Collated results of principal stress at glass specimen impact location for various impactor drop heights. The data sets correspond to clamped laminated specimens with a thickness profile of 5 mm ESG + 1.6 mm SGP + 5 mm ESG.

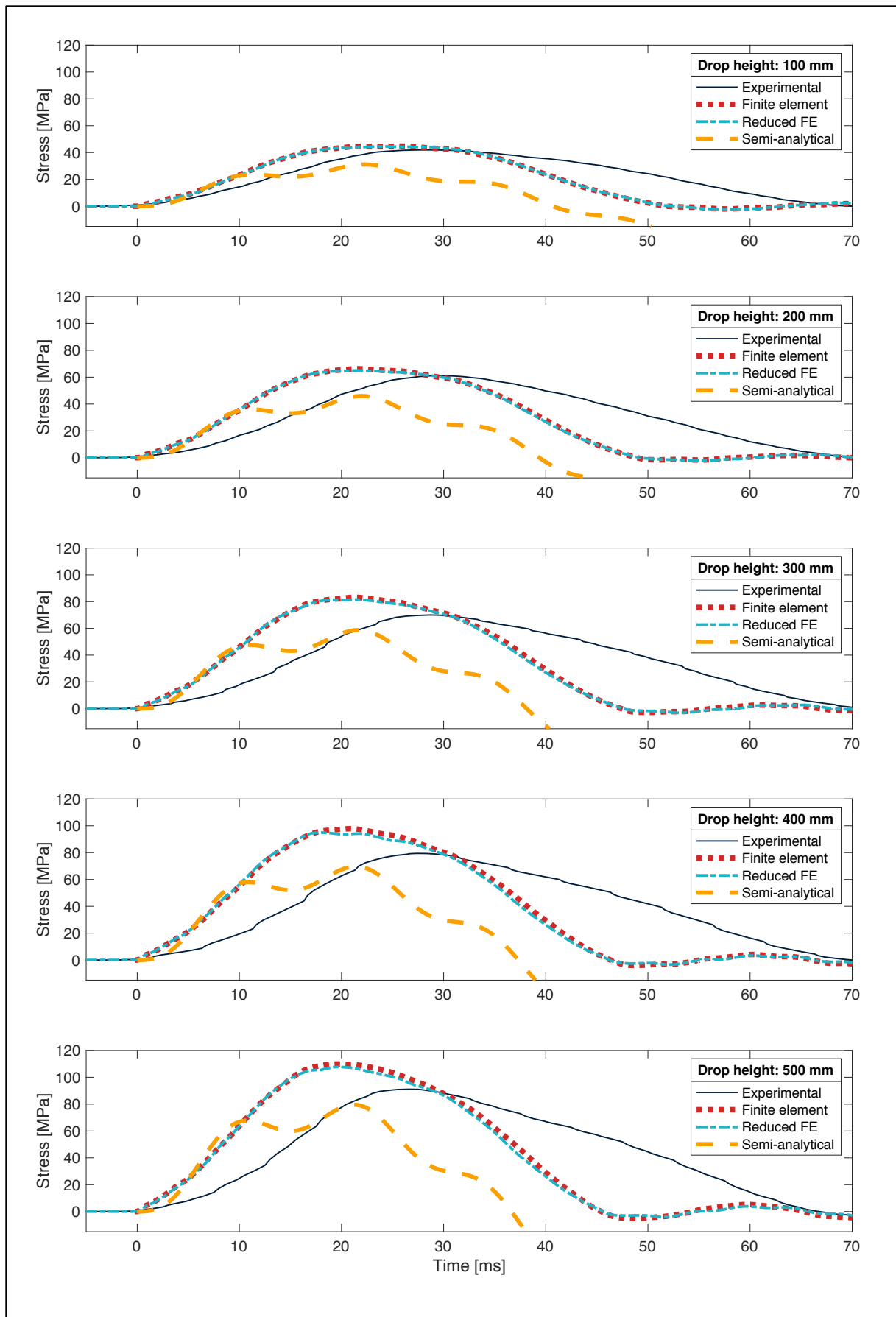


Figure 10-9: Collated results of principal stress at glass specimen impact location for various impactor drop heights. The data sets correspond to clamped laminated specimens with a thickness profile of 6 mm ESG + 1.6 mm PVB + 6 mm ESG.

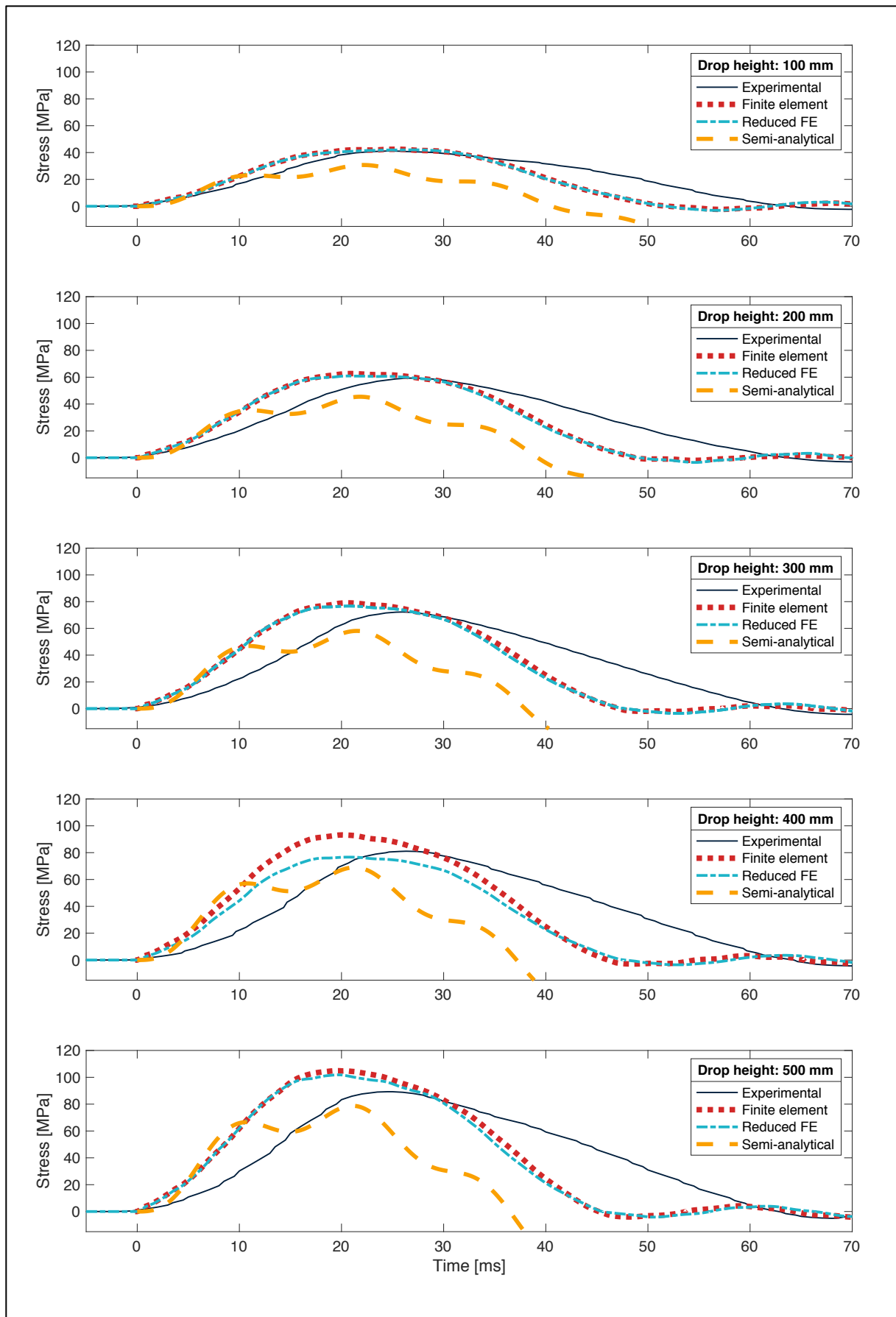


Figure 10-10: Collated results of principal stress at glass specimen impact location for various impactor drop heights. The data sets correspond to clamped laminated specimens with a thickness profile of 6 mm ESG + 1.6 mm SGP + 6 mm ESG.

10.3 Maximum Stresses and Equivalent Static Results

Given that glass is a brittle material, the maximum stresses are of decisive importance, irrespective of the timepoints at which they occur. These maxima are therefore presented for all time series in Figures 10-11 to 10-13. As the transient aspect is removed, this is also an opportunity to present the results of the reduced finite element models with equivalent static loads.

The maxima illustrated in the figures make clear that increased stress with rising drop height is successfully captured across all models. In absolute terms, the deviations in stress maxima are also limited, excluding those of the reduced models with equivalent static loads.

The equivalent static models have been formulated as a proof-of-concept. It is noted that the stresses deviate considerably for Method 2 in the bolted and clamped setups, and that Method 1 and Method 2 are in good agreement with one another for the simply supported setup. To limit superfluous work, Method 1 is therefore only tested for the simply supported setup.

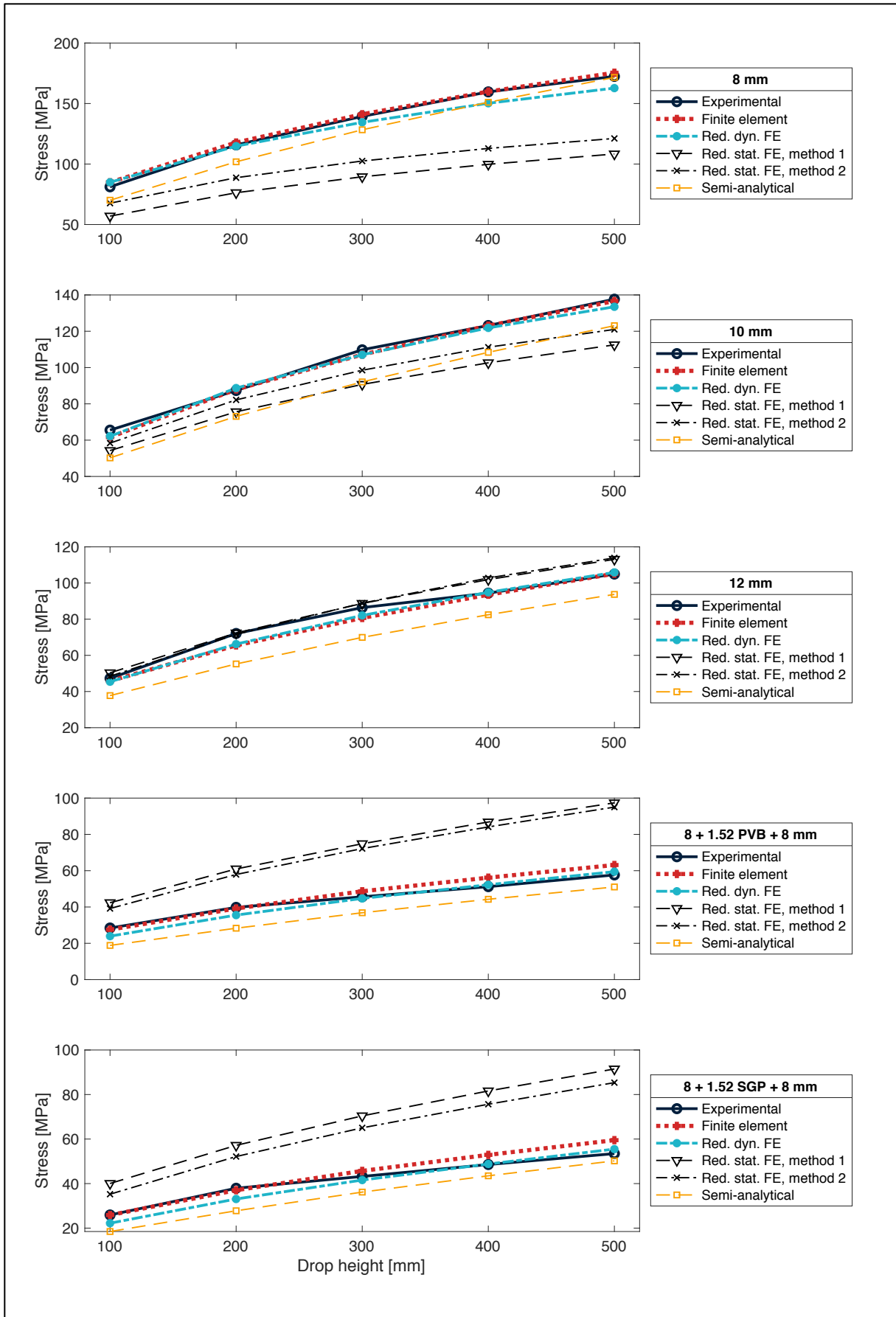


Figure 10-11: Collated results of maximum principal stress at glass specimen impact location for various impactor drop heights. The data sets correspond to the simply supported setup.

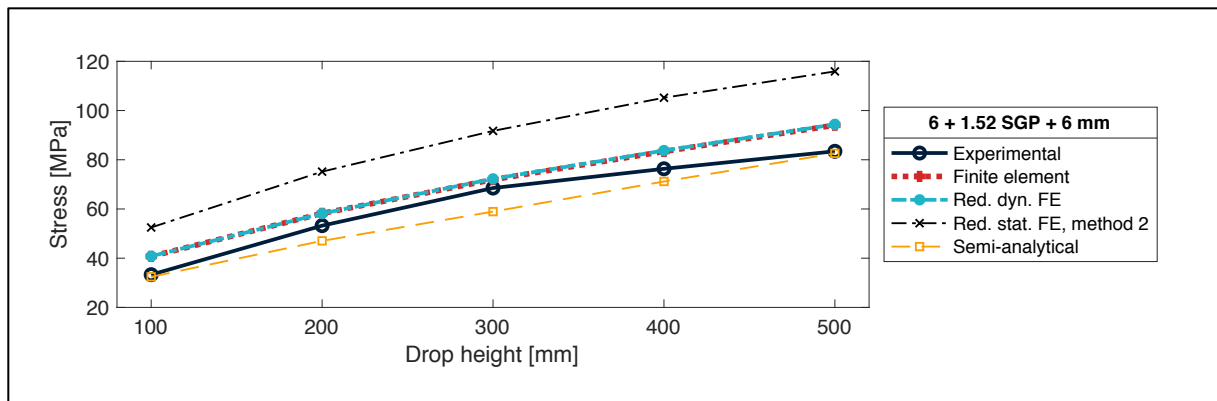


Figure 10-12: Collated results of maximum principal stress at glass specimen impact location for various impactor drop heights. The data sets correspond to the simply supported setup.

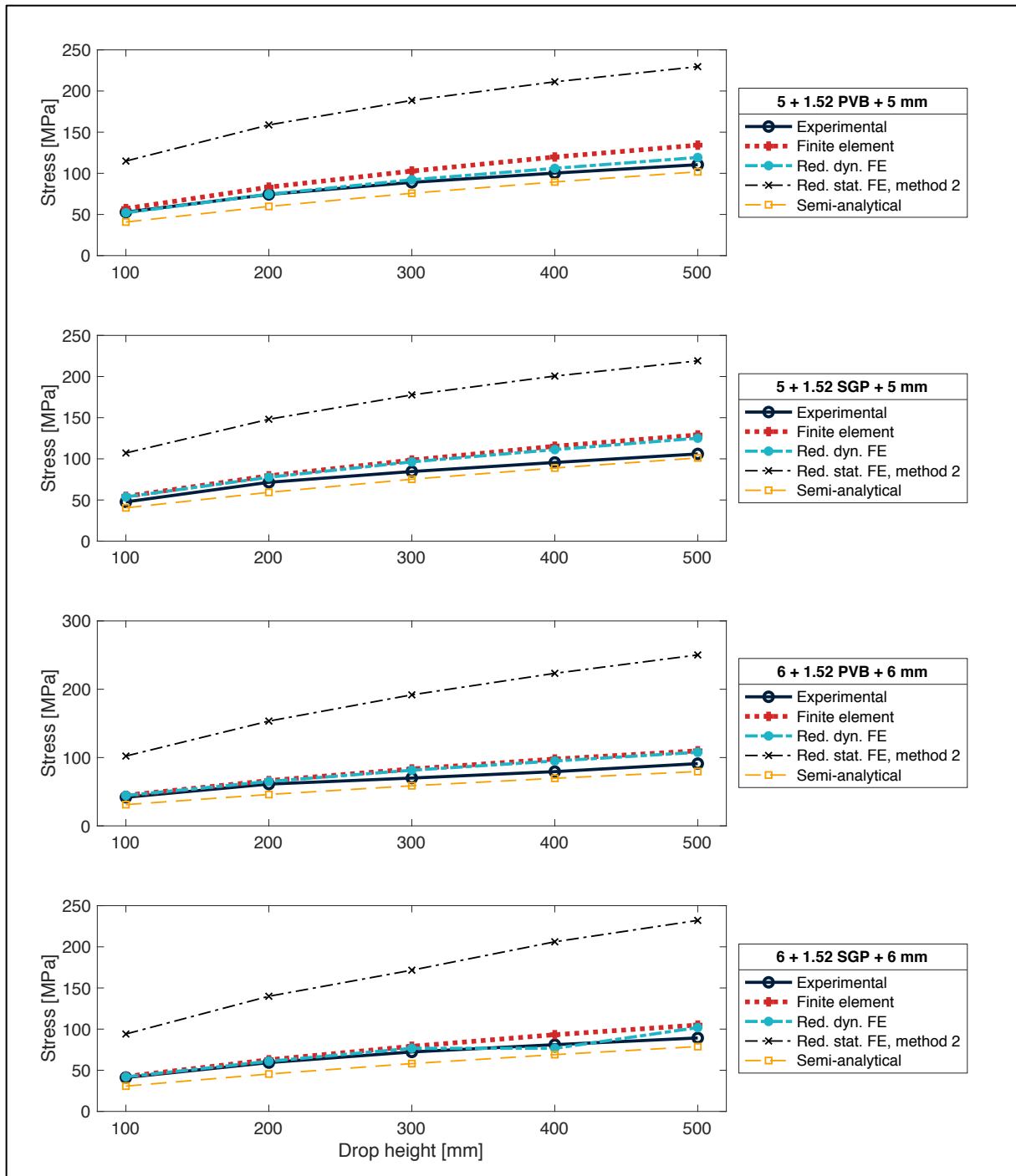


Figure 10-13: Collated results of maximum principal stress at glass specimen impact location for various impactor drop heights. The data sets correspond to the simply supported setup.

10.4 Stress Deviations

To summarize the accuracy of the models with respect to maximum stress, the deviations for each glass type are averaged over the various impactor drop heights and cataloged in Table 10-2. For the dynamic finite element models, it may, at first, seem as though the deviation increases with specimen thickness—this is only half-true, as the deviations for 12 mm specimen thickness are, in fact, lower than the ones for 8 mm and 10 mm. In truth, the error

only increases dramatically once the specimens transition from a monolithic profile to a laminated one. This strongly suggests that the models do not accurately capture the viscoelastic behavior of the interlayers nor that the composite action is simulated realistically.

The reduced equivalent static models are not as accurate as the other models. Though the deviation is respectable for the monolithic specimens, it skyrockets for the laminated specimens in the simply supported setup. For the other setups, the results outputted by the static models are effectively useless, as indicated by deviations exceeding 2.0. This is not all too surprising, given that beam analogies are invoked for the static models, even though it is readily apparent that neither the bolted nor the clamped setups can be reasonably idealized into beams. In fact, they have more in common with plates than they do beams.

The semi-analytical model consistently underestimates the maximum stress, and it is the only model to do so across all glass types. One distinguishing feature of the 2DOF model is its linearity vis-à-vis the other models. It is therefore likely that this has exercised a role in the character of the results.

Table 10-2: Deviation in modeled principal stress from the experimental results, averaged for each glass specimen type across impactor drop heights. Multiplying the factors with the corresponding experimental stress gives the stress outputted by the model.

Fastener configuration	Glass profile [mm]	High-fidelity FE	Reduced dynamic	Equiv. static, method 1	Equiv. static, method 2	Semi-analytical
Simply supported	8	1.02	0.98	0.65	0.75	0.92
	10	0.98	0.98	0.83	0.90	0.84
	12	0.96	0.97	1.05	1.04	0.83
	8 + 1.6 PVB + 8	1.04	0.95	1.61	1.54	0.79
	8 + 1.6 SGP + 8	1.05	0.95	1.62	1.48	0.82
Bolted	6 + 1.6 SGP + 6	1.12	1.12	–	1.42	0.93
Clamped	5 + 1.6 PVB + 5	1.15	1.03	–	2.12	0.85
	5 + 1.6 SGP + 5	1.17	1.14	–	2.12	0.89
	6 + 1.6 PVB + 6	1.16	1.13	–	2.65	0.82
	6 + 1.6 SGP + 6	1.10	1.04	–	2.43	0.81

Disregarding the equivalent static results for the bolted and clamped setups, the results are compacted further by calculating the average deviation for each model type, see Table 10-3.

Table 10-3: Average deviation in modeled principal stress from experimental results, averaged across all glass specimen types and impactor drop heights. Multiplying the factors with the corresponding experimental stress gives the stress outputted by the model. * Note: only accounts for the simply supported setup.

High-fidelity FE	Reduced dynamic	Equiv. static, method 1	Equiv. static, method 2	Semi-analytical
1 ± 0.09	1 ± 0.06	0.64*	0.72*	0.85

11 Discussion

“I think we agree, the past is over.”

—George W. Bush

The discussion centers on the results presented in the previous chapter, and the plausible sources of error in those results. Accordingly, attention is first given to the dynamic results and the interplay between system stiffness, damping and stress. The results of the equivalent static models are then integrated into the discussion. A final Section explains the flaws undertaken in the method with respect to material modeling and nonlinear behavior, particularly with respect to the semi-analytical model.

11.1 Dynamic Results Discussion

As remarked in Section 10.2, the stress curves outputted by both the finite element simulations and the semi-analytical model exhibit slopes that are significantly higher than those from the experimental campaign. This suggests that the finite element models are not fully realistic—the mass, the stiffness, and the damping are consequently deserving of closer scrutiny. However, it is immediately clear that the masses used in the finite element models can be presumed to be correct, as the structural members used in the primary frame are standard issue, the glass specimens have well-defined densities, and the impactor mass is prescribed by EN 12600. It is therefore the latter two system parameters, the stiffness and the damping, that are of interest.

Stiffness and damping are interlinked when it comes to stress. Studying the results from the parametric study of the semi-analytical model in Section 6.7, the effects of alternating these parameters can be observed. Further complexity is introduced when considering the interplay between the two parts and their respective stiffnesses; something which was not covered by the parametric study. It is indeed true that increased stiffness of the glass will yield smaller displacements. But this does not necessarily mean that the stress in the glass will be reduced. Indeed, it is difficult to predict the change in stress that would occur from the given data if both stiffnesses were modified. However, given that the simulated stresses exhibit good agreement with their experimental counterparts, any change to stiffness in the system is likely

to damage this agreement in stress. In other words, a more realistic finite element model should demonstrate longer loading periods while maintaining the current (stress) amplitudes—this is not possible if stiffness is only examined in isolation. Integrating damping into the discussion seems to alleviate this problem; the parametric study demonstrated that increased damping (within the structural range, i.e. below 20%) has the effect of lowering the amplitude without noticeably affecting the period. Therefore, an evaluation of system stiffness must also encompass damping.

In systems undergoing free vibration, damping has a marked effect—over time. Its influence is far less pronounced during the first peak of the displacement response, see Figure 11-1. This warrants accounting for because a soft-body impact load is concerned with the first half-period of vibration, i.e. the impact pulse. The question that arises therefore is whether damping ought to at all be considered in the modeling of soft-body impact on glass structures.

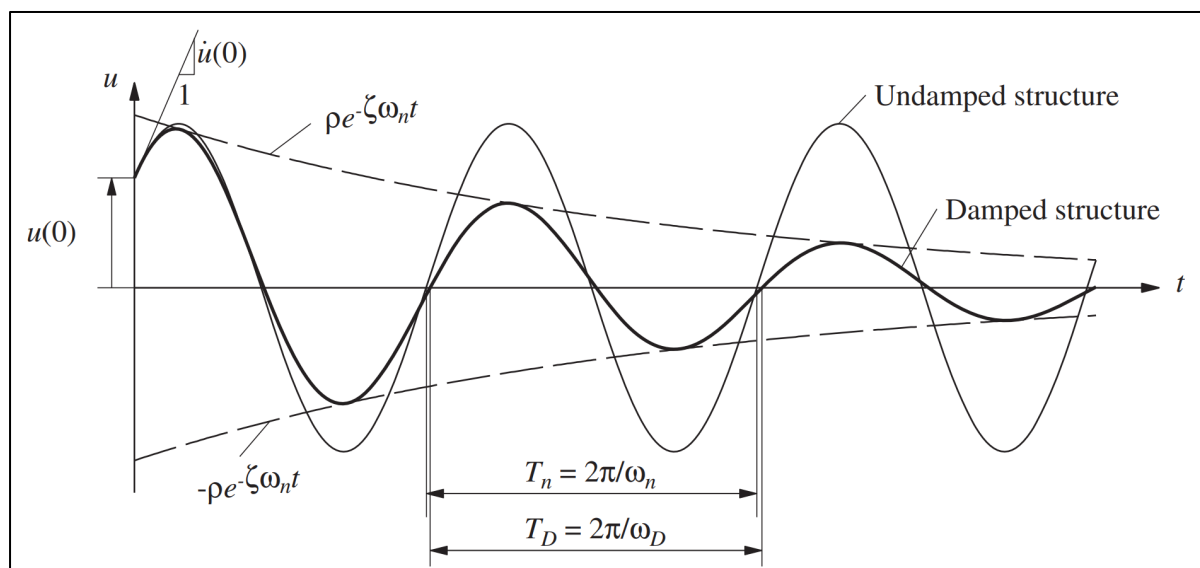


Figure 11-1: Effects of damping on free vibration. Source: Chopra (2014).

With respect to structural design codes, the answer is that damping is largely negligible because ignoring it yields somewhat conservative results with respect to impact loading (Chopra, 2014). However, if the objective is to capture the response of the structure as accurately as possible, damping deserves consideration; an admittedly bold increase in damping, from 1% to 10%, yields a reduction in pulse amplitude of approximately 12% for an arbitrary dynamic system, see Figure 11-2. It is safe to assume that the true damping of the experimental setup also exists within this range, considering that most structures have a damping ratio well below 20%.

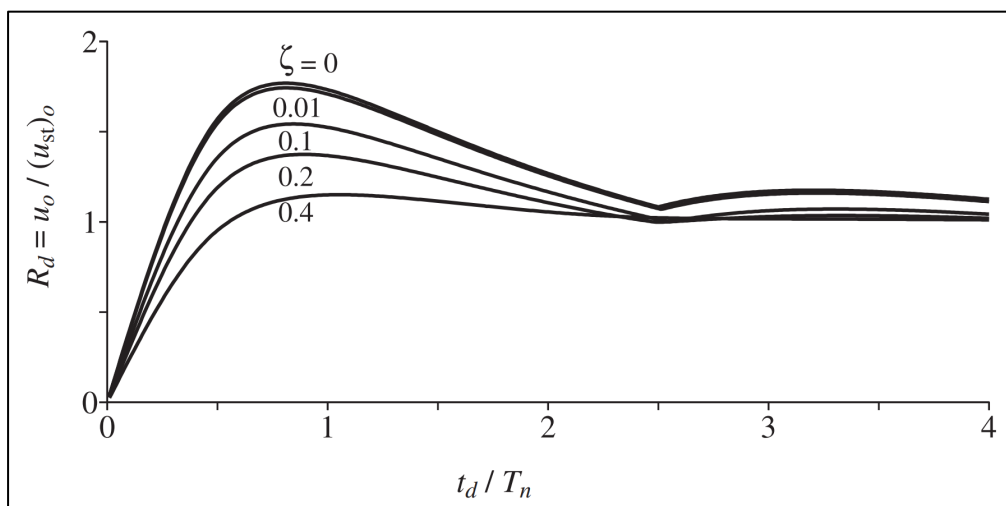


Figure 11-2: Shock spectra for a half-cycle sine pulse force for five damping values. Source: Chopra (2014).

Closer investigation of the damping is therefore merited. The sources of damping in the system can be narrowed down to the impactor, the primary frame, the fasteners, and the interlayer. Impactor damping is already defined in the finite element models (albeit approximately), unlike these other two sources. Indeed, it seems likely that damping in the steel primary frame, particularly as a result of its bolted connections, is nonzero. However, it is the interlayers and the fasteners connecting the glass to the frame, i.e. the rubber strip connection, the bolted connection, and the clamped connection, that are the obvious culprit. Looking at the fasteners, not only do they all contain EPDM rubber, which has significantly more material damping than steel or glass, but the connections are sources of friction and slip. Note that frictional slip dissipates energy, adding to the damping of a structure (Xu & Hess, 2013). Thus, it is likely that damping has not been modeled realistically.

For the interlayers, their viscoelastic properties strongly suggest damping in the system (Dassault Systèmes, 2015). This is likely why the stress deviations change when going from monolithic to laminated specimens, as this source of damping has been entirely neglected.

Adding damping to the models reduces the stress amplitudes, which may be corrected by modifying the stiffness of the system. Here, the sources of stiffness can be discretized into the impactor, the primary frame, the glass specimens, and the fasteners. Regarding the impactor, it was pointed out in Section 8.4.3 that the dynamic stiffness of the finite element impactor is lower than that of its experimental counterpart when comparing the results of the dynamic rigid impact tests. Though this is a source of error in the model, if the objective is to reduce the stiffness in the system it is not the impactor that warrants investigation, rather it is the remainder of the setup.

Judging by photographs taken of the primary frame, the bolted connections between the HEB160 beams seem sufficiently rigid to model with tie constraints in Abaqus. The fasteners and the glass, on the other hand, are on much shakier ground when it comes to stiffness. The fasteners have been subject to a line of simplifications and idealizations during the modeling

process, the cumulative effect of which has likely been to distort their true stiffness. An example of this is the pretensioning in the bolts, including those used to fasten the C-beams to the I-beams and those used in the bolted setup. The problem is particularly acute for the simply supported setup, where the bolt pretensioning caused the C-beams to rotate in the real setup, which is disregarded in the finite element models. In reality, the rotation directly affects the boundary conditions of the glass, in other words it affects a sensitive component of the setup. The Abaqus model only vaguely accounts for this by defining rigid tie constraints between the entirety of the C-beam web and the I-beam flange, which is not realistic.

In summary, the dissonance in the transient events of the models and the experimental results can be traced to the interplay between system stiffness and damping. What is remarkable is that the stiffnesses in all of the models are too large—Figures 10-1 through 10-10 illustrate that the slopes of the models are all similar to one another and are all distinct from the experimental ones. This is surprising, given that the semi-analytical model and the finite element models approach the problem from different angles, which may indicate that there are flaws in the experimental setup and data collection. Some of these were already discussed in Chapter 5, but it is worth recalling, in particular, that filtration of strain gauge data often yields strains on the smaller side. If this effect is compounded by strain rate, it may help to explain the flatter experimental stress slopes.

11.2 Equivalent Static Model Results Discussion

While the reduced dynamic models exhibit high levels of agreement with the high-fidelity finite element models, the same cannot be said for the equivalent static models. The deviations become particularly problematic for the bolted and clamped setups. This can be attributed to the beam analogies used to derive the equivalent static loads. While the simply supported setup can be reasonably idealized into a beam, admittedly one with a somewhat unusual cross-section, the same cannot be said for the other setups. These have more in common with plates; indeed, analytical methods exist for calculating the deformation in a plate with point-fixed boundary conditions. Such a method likely yields stresses that deviate less dramatically from the experimental results.

Despite the unviability of the bolted and clamped setups, the results of the simply supported setup indicate that the beam analogy works reasonably well for estimating the principal stress if the glass specimen is constrained along the length of its sides. The first static load method is more conservative than the second method, but both yield similar results. However, even for the simply supported case, the deviations increase to a factor 1.5 for the laminated specimens, again indicating flaws in the material modeling.

Despite the severity of the deviations, the flaws with the equivalent static models must be considered in the grander scheme of things. The overriding ambition of the reduced models, particularly the static models, is to demonstrate a proof-of-concept with respect to the

viability of simplified numerical approaches to modeling soft-body impact on glass. As such, their viability ought to be evaluated with respect to computational cost. Consider the following case study: for a 10 mm monolithic glass specimen fastened to the simply supported setup, and an impactor dropped from 300 mm, the computational cost, measured in CPU s, relative to the deviations are given in Table 11-1. Despite the greater deviations, it is abundantly clear that the equivalent static models are the most cost efficient. As such, while the idealizations used in the method require serious improvement, the concept of deploying equivalent static models to the problem area shows promise.

Table 11-1: Case study of computational cost relative to deviation from experimental stress. The case is 10 mm monolithic glass fastened to the simply supported setup, with a 300 mm impactor drop height.

Simulation	Deviation	Computational cost [CPU s]	Computational cost per deviation
High-fidelity FE	0.98	31100	31800
Reduced dynamic FE	0.98	8360	8570
Equiv. static FE, method 1	0.83	47.6	57.6
Equiv. static FE, method 2	0.90	47.6	53.0

11.3 Material Modeling and Nonlinearity

Sources of error have been discussed concurrently throughout the chapter. Recognizing that the models exhibit stiffnesses that are altogether too high and are governing for the displacement response, there are two ulterior categories of errors that warrant closer evaluation: the choice of material parameters, and faults in nonlinear behavior.

Each geometric component in the finite element models is prescribed material parameters that are meant to capture the true behavior of model without excessive computational cost. It therefore stands to reason that material models must always evaluate accuracy vis-à-vis computational economics. It is within this context that efforts have been continuously exerted to model the materials with equivalent linear elastic properties. If executed perfunctorily, such a campaign can obviously produce inaccurate results.

Effective linear elastic properties are chiefly prescribed by assigning an effective modulus of elasticity, E_{eff} . For materials such as glass, this is entirely consistent with the materials science presented in Chapter 3; it is less so for hyperelastic materials, such as EPDM rubber, and for viscoelastic materials, such as PVB and SGP. (It is worth pointing out that even glass exhibits some variation in Young's modulus, see Table 3-2, which comes to play an outsized role in the stress output.) Tracing realistic values of E_{eff} onto these materials is conditional on knowledge of the loading history (or strain history) and the geometry. While the geometries of the rubber components in the fasteners and the polymers in the interlayers are relatively well-defined, the loading history is not. The literature on interlayer E_{eff} is conflicting and incomplete, and

the true loading on the glass specimens during the experimental campaign was never fully established. Indeed, the theoretical values derived for E_{eff} were increased by a factor 2 during the modeling process, see Section 8.3. Judging by the increased deviation, across all models, for the laminated specimens, it is abundantly clear that the viscoelastic behavior of the interlayers has not been accurately captured. This is doubly problematic because composite action in a laminated glass panel is, among other things, a function of load duration, i.e. viscoelastic response (Fors, 2014). Abaqus treats the modeled laminated specimens as composites, which therefore may not be entirely accurate.

Similar problems arise when evaluating the EPDM rubber used in the fasteners, either as rubber strips or as gussets in the bolts and clamps. The fasteners have a decisive impact on the stresses generated by the models, yet it is the fasteners that have been subject to much of the work of simplifying the experimental setup. It is likely that the excessive stiffness discussed in Section 11.1 stems, in large part, from the equivalent compressive moduli defined for the EPDM components.

The campaign to model as many of the materials as possible with simplified effective moduli are part of a greater effort aimed at reducing the nonlinear components of the models with comparable linear equivalents. It is therefore prudent to further scrutinize this effort. Referring to the deviations cataloged in Annex F, the model stresses increase with the drop height at a higher rate than the experimental stresses, which, for many of the glass types, means that the deviations grow in tandem with drop height. This is attributed to the work done to inhibit nonlinear behavior in favor of cheaper, linear parameters. Nonlinear deformation is often not the same as its linear counterpart, and this difference grows as the problem becomes more dynamic, see Chapter 7. The studied problem of soft-body impact is emblematic of this paradigm: increased drop height implies greater impact velocity, that is to say larger inertial forces propagating under shorter load durations. Thus, the effects of nonlinearity also increase, but not at the same rate as they do in reality.

The semi-analytical model is illustrative of the nonlinearity dilemma. It is the only model to underestimate the stress maxima for all drop heights and all glass types, and it is the only fully linear model. In other words, the systemic underestimation of the stress is likely a result of the 2DOF model neglecting nonlinearity (in addition, the small amount of degrees of freedom is likely to contribute to the deviation). Indeed, the mathematics of the MDOF displacement response, \mathbf{u} , derived in Chapter 6 is entirely linear in nature. (As an aside, this may also help to explain the underlying cause behind the double impact behavior exhibited by the semi-analytical model.) While the semi-analytical model is not designed to capture the stresses as accurately as its numerical counterparts—its aim is more pedagogical in nature, and its role is more of an analytical expedient than a true structural design resource—it is worth examining improvements to it. Chief among those is replacing the beam analogy with a plate analogy. While the former is a reasonable idealization of the simply supported setup, the point fixings of the bolts and clamps better lend themselves to plate theory. The differential equations

described by Kirchhoff-Love plate theory, in particular, are better equipped to model the deflection of the glass than Euler-Bernoulli beam theory. And, in keeping with the spirit of the semi-analytical model, these equations can also be calculated relatively easily.

12 Conclusion

“We shall not cease from exploration, and the end of all our exploring will be to arrive where we started and know the place for the first time.”

—*T.S. Eliot*

The concluding chapter assembles the key takeaways and insights of the study and puts them into the context of original research objectives. This is then reframed to recount for the study’s wider implications for, and applications in, engineering. The methodological limitations of the study are then reviewed, from which avenues for further research are derived and suggested.

12.1 Chief Conclusions

It is recalled that the purpose of this thesis is to investigate the viability of a numerical method for verifying the resistance of an arbitrary glass panel to soft-body impact. The imperative for such a numerical method is driven home by the fact that contemporary verification methods rely on cumbersome, and expensive, experimental impact tests. Given that glass is a highly brittle material, it is the accurate capture of principal stresses that are of greatest interest. The work presented and discussed in the previous chapters have demonstrated that numerical methods, that is to say finite element modeling, is, indeed, a viable approach.

All three fastener configurations—simply supported, bolted, and clamped—have been constructed in Abaqus as high-fidelity (high-detail) models. The stress output by the high-fidelity models exhibit high levels of agreement with their experimental counterparts, deviating on average by 9%. This should be considered in the context of the multiple uncertainties prevalent in the experimental campaign and subsequent data processing.

Reducing the finite element models by replacing all geometry, save for the glass and the impactor body, with springs of equivalent translational and rotational stiffness further yields good agreement in stress. The reduced dynamic models deviate on average by 6% from the experiments, and only 4% from their high-fidelity finite element counterparts. The reduced dynamic models reduce the computational cost considerably, almost by a factor 4. This affirms the viability of the equivalent-spring approach.

Reducing the finite element models further by replacing the impactor and the dynamic analysis with an equivalent static load yields mixed results. For the simply supported setup, the stresses are underestimated by approximately 30%, while the stresses are overestimated by a factor 2 for the other setups. The source of these deviations is the beam analogy used to derive the equivalent static load. In other words, improving the method for deriving the static load, such as by invoking plate theory, is likely to improve the results. Put into the context of almost negligible computational cost, the equivalent static models warrant further investigation.

Though not originally intended as such, a semi-analytical model, consisting of a two-degree-of-freedom viscously damped spring system and beam analogies, yields respectable agreement with the experimental stresses, underestimating them by an average of 15%. The underestimation is attributed to the linearity of the semi-analytical model.

In summary, the thesis has demonstrated that a numerical approach is a viable complement to, if not an outright replacement for, the experimental impact test currently employed to verify the resistance of glass structures to soft-body impact. As a result, the method warrants further investigation.

12.2 Engineering Implications

The experimental test method used in European member states to classify and verify glass specimens with respect to soft-body impact, EN 12600, is expensive and cumbersome. This can be mitigated by using numerical models. Not only has the study demonstrated the viability of numerical models, it has also proven that ulterior boundary conditions can be simulated, not just those stipulated by EN 12600. In so doing, a numerical approach promises to be cheaper, faster, and applicable to a more universal range of fasteners than the experimental standard. This can be done using high-fidelity models or with reduced dynamic models. If additional research is devoted to deriving an appropriate static load, it may also be possible to model soft-body impact on glass structures with static models, thereby rendering computational costs almost negligible.

As a remark, the choice to use continuum solid shell elements to model the glass and interlayers was remarkably successful. This deserves consideration, as this element is relatively new, but proved that it is both inexpensive and accurate for modeling glass.

12.3 Limitations and Avenues for Further Research

Despite the scope of the study, numerous simplifications and idealizations have been made that warrant addressing. Furthermore, some methodological mistakes also deserve accounting for. A summary of the factors that substantially limited the study is therefore presented as follows, with suggestions for future research.

First and foremost, a thorough investigation on the subject of damping is proposed. As discussed in Section 11.1, the viscoelastic properties of the interlayers in the laminated glass panels, along with the EPDM rubber found in the fasteners, are of decisive importance to the system response. The approach taken in terms of material modeling therefore limits the validity of the results, both in terms of utilizing effective moduli of elasticity and the neglect of damping. The damping, in particular, is problematic because it is obvious that the interlayers are responsible for significant damping in the system. Put bluntly, it is possible that the good agreement in experimental and simulated stress is the result of numerous errors counteracting each other, one of which is the damping dilemma. To address this, experimental testing is required.

The reduced models are characterized by springs, whose stiffnesses holds uncertainties. A more complete theoretical derivation of the spring stiffness would reduce some of those uncertainties. This is important because the reduced dynamic models yielded accurate results at significantly lower expense compared to the high-fidelity models. It is therefore the reduced models that warrant investigation. For the equivalent static models, the equivalent loads derived would benefit from further investigation. Both approaches taken in Section 9.3 are simplified and very rough estimates. Those methods are not viable for design at the moment, but this is largely attributed to poor engineering judgment when deriving the static loads. A more theoretically relevant derivation would likely improve the results, such as by utilizing Kirchhoff-Love plate theory. Therefore, it is proposed that a different approach for determining equivalent loads is to be found.

In addition, the use of explicit solvers should be investigated. The implicit solver was used for all of the numerical models and, as discussed earlier, is not necessarily the correct choice. If the impact event were only to be investigated up until the timepoint at which maximum principal stress occurs, an explicit solver may prove preferable. This is especially the case if more realistic material models were to be included.

13 References

“I once sent a dozen of my friends a telegram saying ‘flee at once – all is discovered.’ They all left town immediately.”

—Mark Twain

- Akin, J., 2017. *Impact Load Factors for Static Analysis*, Houston: Rice University, Department of Mechanical Engineering.
- ASCE, 2017. *ASCE standard ASCE/SEI 4-16: Seismic analysis of safety-related nuclear structures*. Virginia: American Society of Civil Engineers.
- Bang-Jian, L., Quan-Bao, W. & Deng-Ping, D., 2018. Strain measurement errors with digital image correlation due to the Savitzky–Golay filter-based method. *Measurement Science and Technology*, 29(8).
- Belis, J., Louter, C., Nielsen, J. H. & Scheider, J., 2019. Architectural Glass. In: L. Calvez, J. Hu & J. D. Musgraves, eds. *Springer Handbook of Glass*. Cham: Springer Nature Switzerland AG, pp. 1779-1819.
- Boeykens, G. & Van den Bosch, R., 2014. *Numerical simulation of a pendulum impact setup for laminated glass*, Ghent: Universiteit Gent.
- Bourhis, E. L., 2008. *Glass: Mechanics and Technology*. Weinheim: Wiley-VCH.
- Burström, P. G. & Nilvér, K., 2018. *Byggnadsmaterial - Tillverkning, egenskaper och användning*. 3rd ed. Lund: Studentlitteratur AB.
- Button, D. & Pye, B., 1993. *Glass in Building*. Oxford: Butterworth-Heinemann Ltd..
- CEN, 2002. *EN 12600:2002 Glass in building - Pendulum test - Impact test method and classification for flat glass*, Brussels: European Committee for Standardization.
- CEN, 2016. *EN 572 Glass in building - Basic soda-lime silicate glass products - Part 1. Definitions and general physical and mechanical properties*, Brussels: European Committee for Standardization.
-

- Chopra, A. K., 2014. *Dynamics of Structures. Theory and Applications to Earthquake Engineering*. 4th ed. Essex: Pearson.
- Conradt, R., 2019. Thermodynamics and Kinetics of Glass. In: L. Calvez, J. Hu & J. D. Musgraves, eds. *Springer Handbook of Glass*. Cham: Springer Nature Switzerland AG, pp. 51-77.
- Custom Glass Products, 2020. *Understanding the Differences Between Annealed, Tempered, and Heat-Strengthened Glass*. [Online]
Available at: <https://cgpglass.com/custom-glass-blog/understanding-the-differences-between-annealed-tempered-and-heat-strengthened-glass/>
[Accessed 21 May 2020].
- Dassault Systèmes, 2014. *Getting Started with Abaqus: Interactive Edition*. Providence: Dassault Systèmes.
- Dassault Systèmes, 2015. *Abaqus 2016 Online Documentation*. Providence: Dassault Systèmes.
- Dassault Systèmes, 2020. *Introduction to Abaqus: Abaqus 2020*. Providence: Dassault Systèmes.
- Dattakumar, S. S. & Ganeshan, V., 2017. *Converting dynamic impact events to equivalent static loads in vehicle chassis*. Göteborg: Department of Applied Mechanics, Chalmers University of Technology.
- Dutt, A., 2015. *Effect of Mesh Size on Finite Element Analysis of Beam*. Punjab: Lovely Professional University Jalandhar.
- Falk, T. et al., 2011. *Boken om glas: hantverket, tekniken och konsten*. Stockholm: Infotain & Infobook Sweden.
- Flow Science, 2020. *Implicit vs. Explicit Numerical Methods*. [Online]
Available at: <https://www.flow3d.com/resources/cfd-101/numerical-issues/implicit-versus-explicit-numerical-methods/>
[Accessed 10 05 2020].
- Fors, C., 2014. *MECHANICAL PROPERTIES OF INTERLAYERS IN LAMINATED GLASS*, Lund: Division of Structural Mechanics.
- Fröling, M., 2013. *Strength Design Methods for Glass Structures*, Lund: Department of Construction Sciences, Lund University.
- Gonçalves, M. C., 2015. Glass. In: M. C. Gonçalves & F. Margarido, eds. *Materials for Construction and Civil Engineering*. Cham: Springer International Publishing Switzerland, pp. 335-396.
- Greaves, G., 1985. EXAFS and the structure of glass. *Journal of Non-Crystalline Solids*, 71(1-3), pp. 203-217.
- Joint Research Center of the European Commission, 2014. *Guidance for European Structural Design of Glass Components: Support to the implementation, harmonization, and further*

development of the Eurocodes, Luxembourg: Joint Research Centre of the European Commission.

Kelly, P., 2020. *Solid mechanics part I: An introduction to solid mechanics*. s.l.:Solid mechanics lecture notes, University of Auckland.

Kinsella, D., 2018. *MODELLING OF ANNEALED GLASS FRACTURE*, Lund: Division of Structural Mechanics.

Kozłowski, M., 2019. Experimental and numerical assessment of structural behaviour of glass balustrade subjected to soft body impact. *Composite Structures*, Volume 229.

Kozłowski, M., Persson, K. & Honfi, D. P. N., 2020. *Structural Behaviour of Glass Panels Under Soft-body Impact*. Ghent, Ghent University.

Kuraray, 2020. *Technical Information, Elastic Properties Data Sheet*. [Online] [Accessed 3 April 2020].

Lindley, T. B., 1978. *Engineering Design with Natural Rubber*. 4th ed. Brickendonbury: The Malaysian Rubber Producers Research Association.

Liu, G. & Quek, S., 2014. *The Finite Element Method*. Second Edition ed. New York: Elsevier.

Moreland, D. W., 2009. *Safety Design for Space Systems*. New York: Elsevier.

National Board of Housing, Building and Planning, 2019. *Boverket's building regulations - mandatory provisions and general recommendations, BBR*, Karlskrona: Boverket.

Ottosen, N. & Petersson, H., 1992. *Introduction to the Finite Element Method*. London: Pearson Education.

Ozer, H., 2007. A comparative analysis of Mindlin and Kirchhoff bending solutions for nonlinearly tapered annular plate with free edges. *Arch Appl Mech*, Issue 77, pp. 393-405.

Peksen, M., 2018. *Multiphysics Modelling*. New York: Elsevier.

Pelfrane, J., Dam, S. V., Kuntsche, J. & Paepegem, W. V., 2016. *Numerical simulation of the EN 12600 pendulum test for structural glass*. Ghent, Ghent University.

Plumbridge, W. J., Matela, R. J. & Westwater, A., 2003. *Structural Integrity and Reliability in Electronics*. New York: Kluwer Academic Publishers.

Ramos, A. et al., 2015. *Analysis of Structural Glass Panels Under Impact Loading Using Operational Modal Analysis*. Gijón, 6th International Operational Modal Analysis Conference.

Rodichev, Y. & Veer, F., 2016. Fracture Resistance, Surface Defects and Structural Strength of Glass.. *Challenging Glass Conference Proceedings*, pp. 363-374.

13 References

- Serafinavicius, T., Kvedaras, A. K. & Sauciuvenas, G., 2013. Bending Behavior of Structural Glass Laminated with Different Interlayers. *Mechanics of Composite Materials*, 49(4), pp. 437-446.
- Sienkiewicz, M., Kucinska-Lipka, J., Helena, J. & Balas, A., 2012. Progress in used tyres management in the European Union: A review. *Waste Management*, 32(10), pp. 1742-1751.
- Vu-Quoc, L. & Tan, X., 2003. Optimal solid shells for non-linear analyses. *Computer methods in applied mechanics and engineering*, Issue 192, pp. 1017-1059.
- Xu, W. & Hess, D. P., 2013. Effect of Fastener Preload on Structural Damping. *Journal of Failure Analysis and Prevention*, Volume 13, pp. 744-747.

A Processed Experimental Data: Principal Stress at Glass Specimen Impact Location

The experimental stresses were computed using data from strain gauges and $E = 72$ GPa. The strain gauges were placed on the opposite surface of the glass specimens, at the location of impact.

Annex A Processed Experimental Data: Principal Stress at Glass Specimen Impact Location

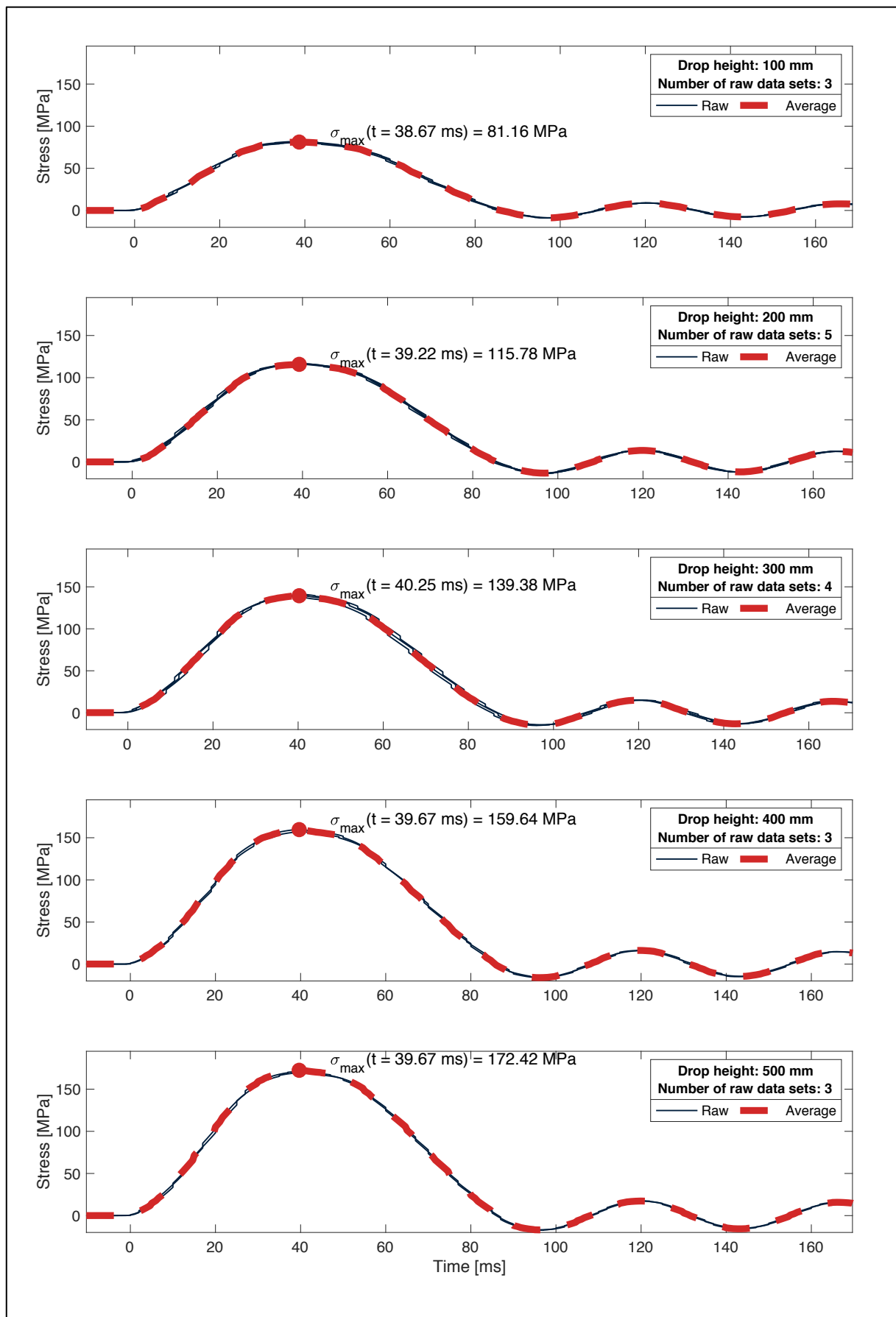


Figure A-1: Principal stress at glass specimen impact location for various impactor drop heights. The data are derived from a strain gauge positioned at the tensile face of the specimens during the experimental campaign. The data set corresponds to simply supported monolithic specimens with a thickness profile of 8 mm.

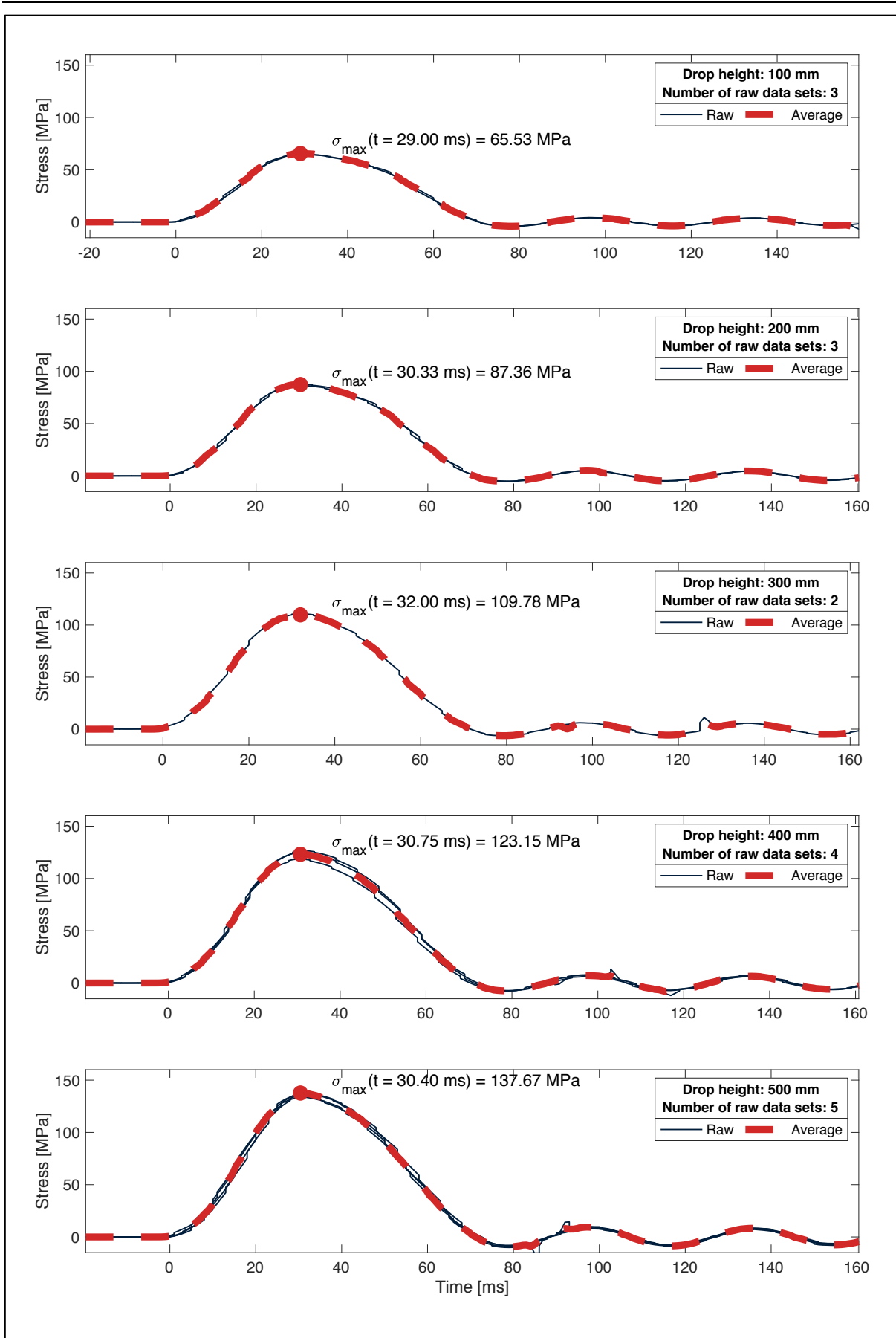


Figure A-2: Principal stress at glass specimen impact location for various impactor drop heights. The data are derived from a strain gauge positioned at the tensile face of the specimens during the experimental campaign. The data set corresponds to simply supported monolithic specimens with a thickness profile of 10 mm.

Annex A Processed Experimental Data: Principal Stress at Glass Specimen Impact Location

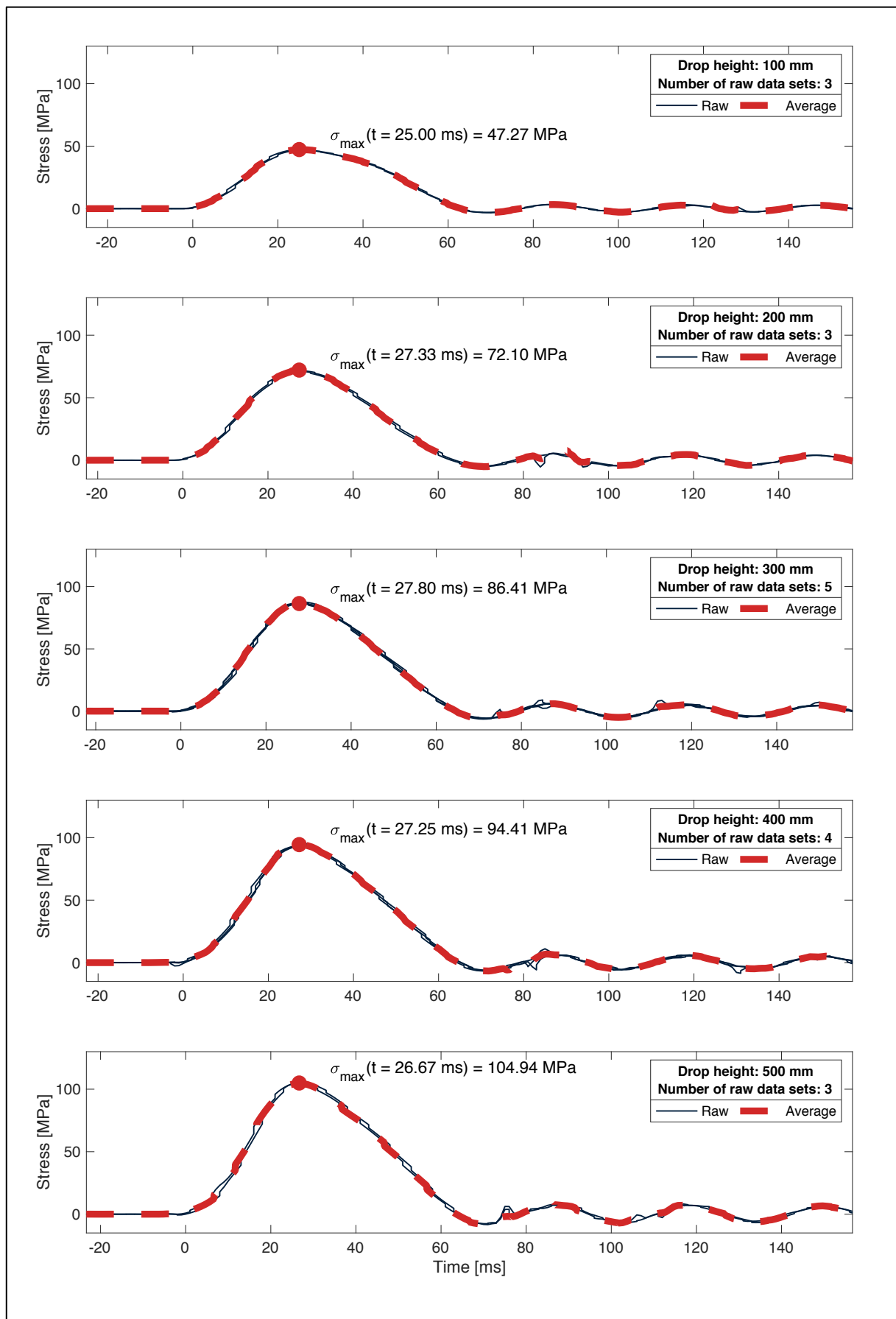


Figure A-3: Principal stress at glass specimen impact location for various impactor drop heights. The data are derived from a strain gauge positioned at the tensile face of the specimens during the experimental campaign. The data set corresponds to simply supported monolithic specimens with a thickness profile of 12 mm.

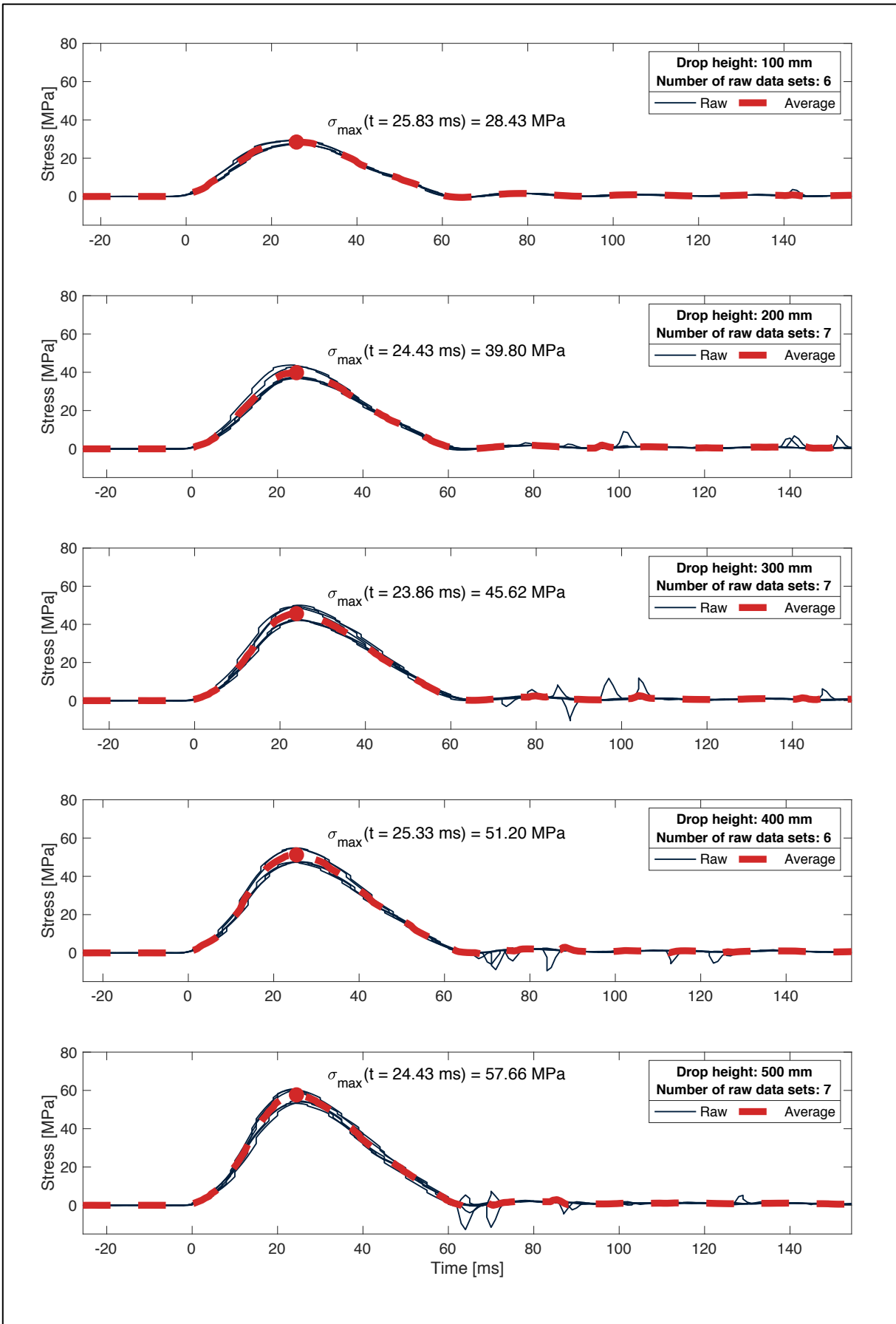


Figure A-4: Principal stress at glass specimen impact location for various impactor drop heights. The data are derived from a strain gauge positioned at the tensile face of the specimens during the experimental campaign. The data set corresponds to simply supported laminated specimens with a thickness profile of 8 mm ESG/TVG + 1.6 mm PVB + 8 mm ESG/TVG.

Annex A Processed Experimental Data: Principal Stress at Glass Specimen Impact Location

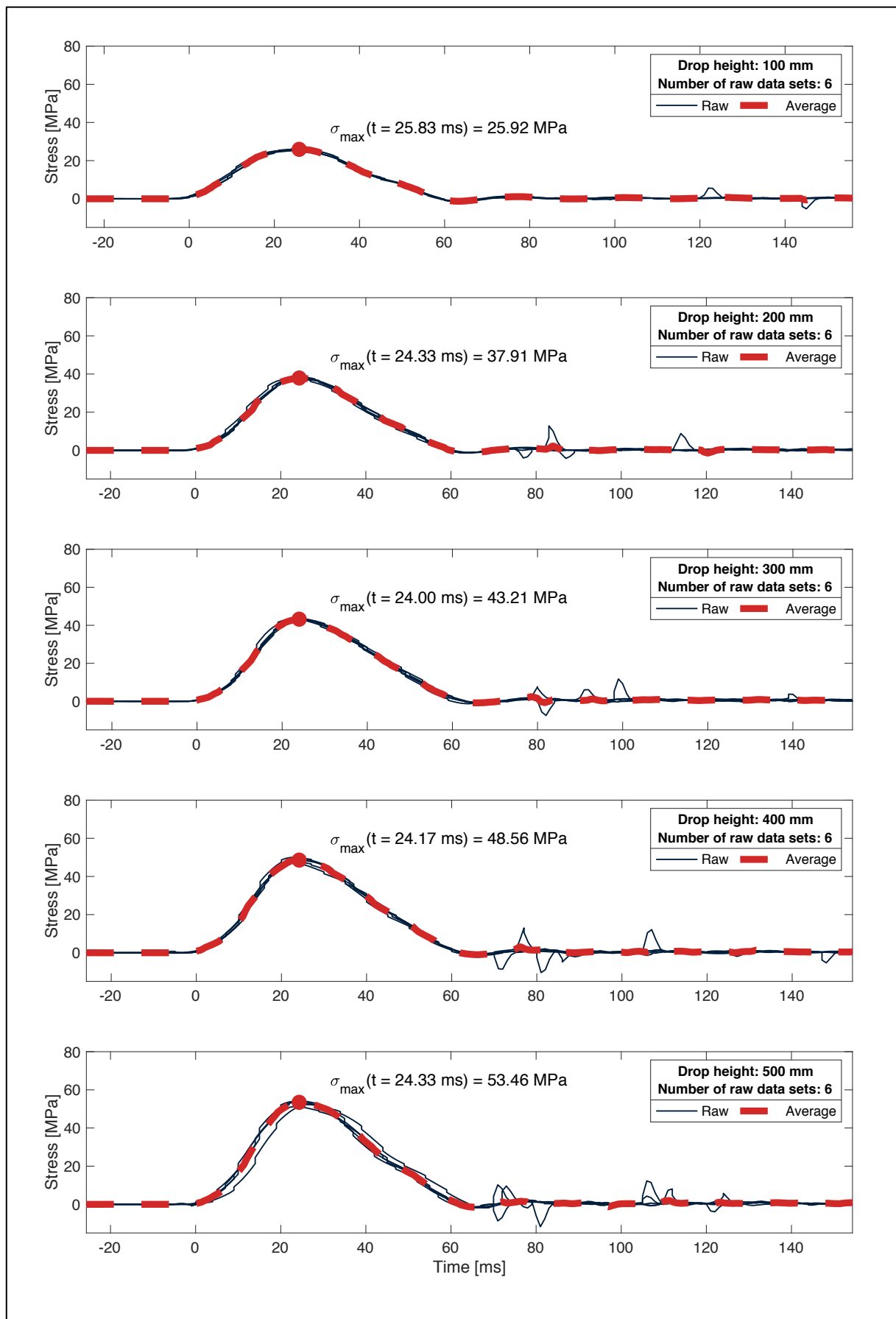


Figure A-5: Principal stress at glass specimen impact location for various impactor drop heights. The data are derived from a strain gauge positioned at the tensile face of the specimens during the experimental campaign. The data set corresponds to simply supported laminated specimens with a thickness profile of 8 mm ESG/TVG + 1.6 mm SGP + 8 mm ESG/TVG.

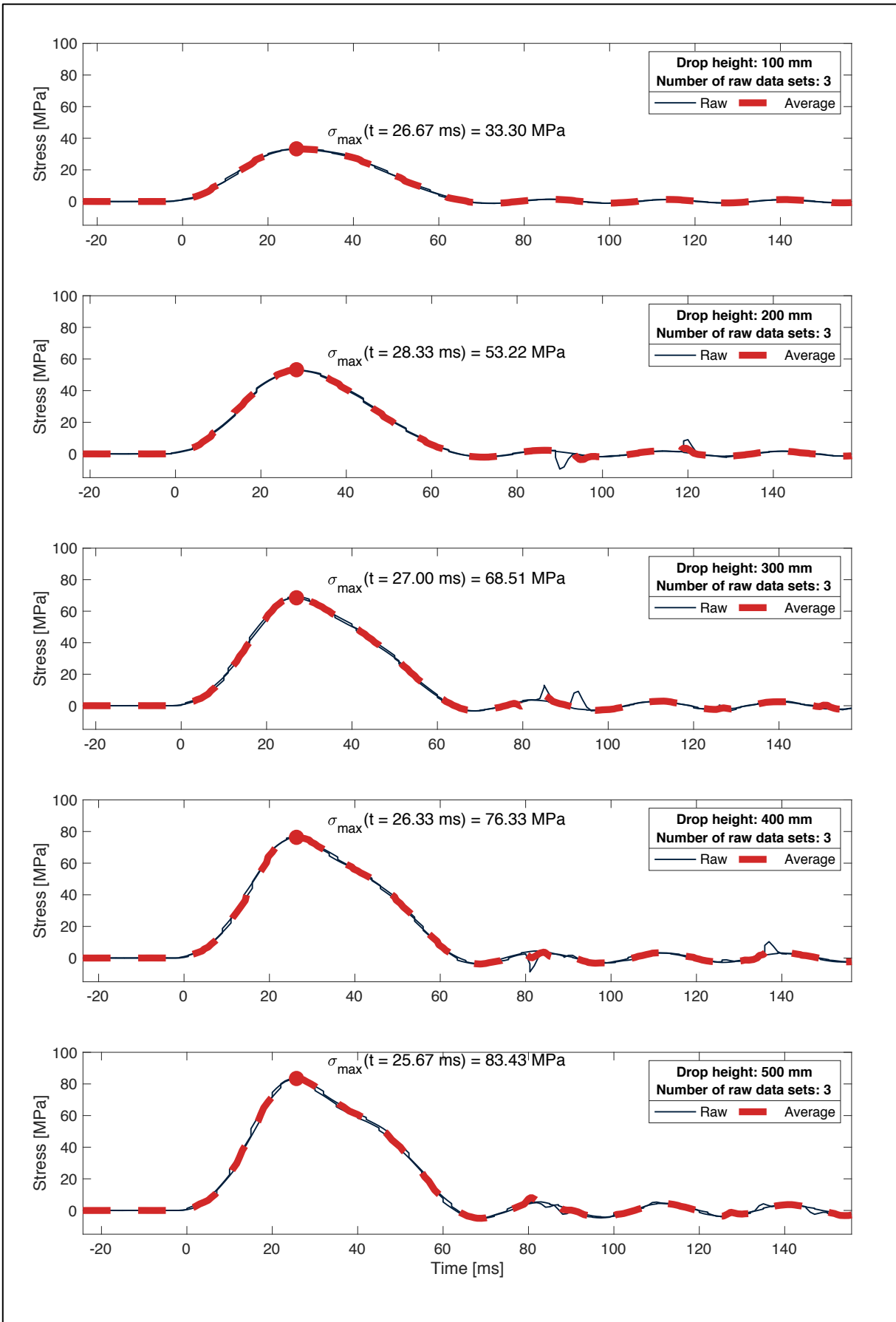


Figure A-6: Principal stress at glass specimen impact location for various impactor drop heights. The data are derived from a strain gauge positioned at the tensile face of the specimens during the experimental campaign. The data set corresponds to bolted laminated specimens with a thickness profile of 6 mm ESG + 1.6 mm SGP + 6 mm ESG.

Annex A Processed Experimental Data: Principal Stress at Glass Specimen Impact Location

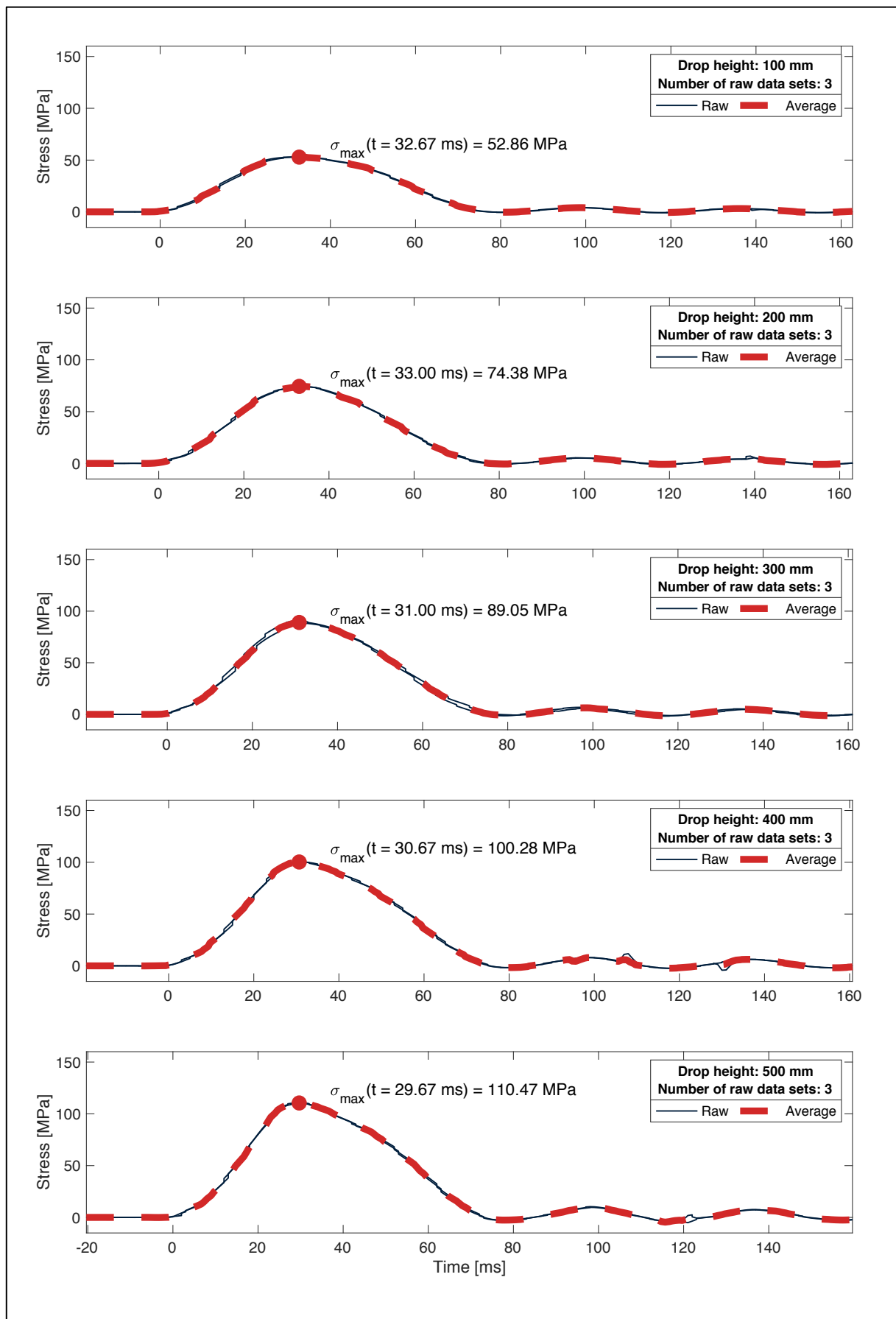


Figure A-7: Principal stress at glass specimen impact location for various impactor drop heights. The data are derived from a strain gauge positioned at the tensile face of the specimens during the experimental campaign. The data set corresponds to clamped laminated specimens with a thickness profile of 5 mm ESG + 1.6 mm PVB + 5 mm ESG.

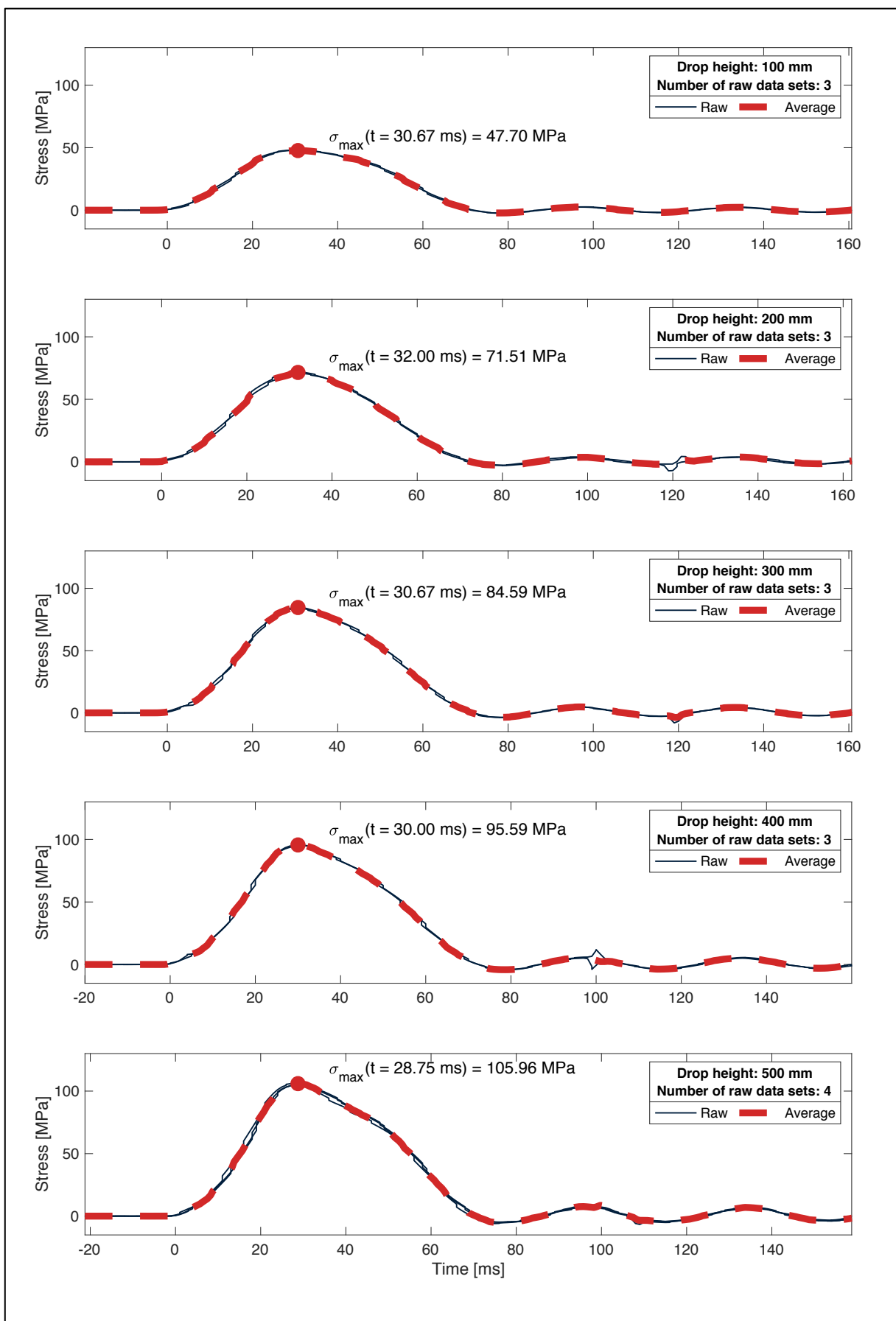


Figure A-8: Principal stress at glass specimen impact location for various impactor drop heights. The data are derived from a strain gauge positioned at the tensile face of the specimens during the experimental campaign. The data set corresponds to clamped laminated specimens with a thickness profile of 5 mm ESG + 1.6 mm SGP + 5 mm ESG.

Annex A Processed Experimental Data: Principal Stress at Glass Specimen Impact Location

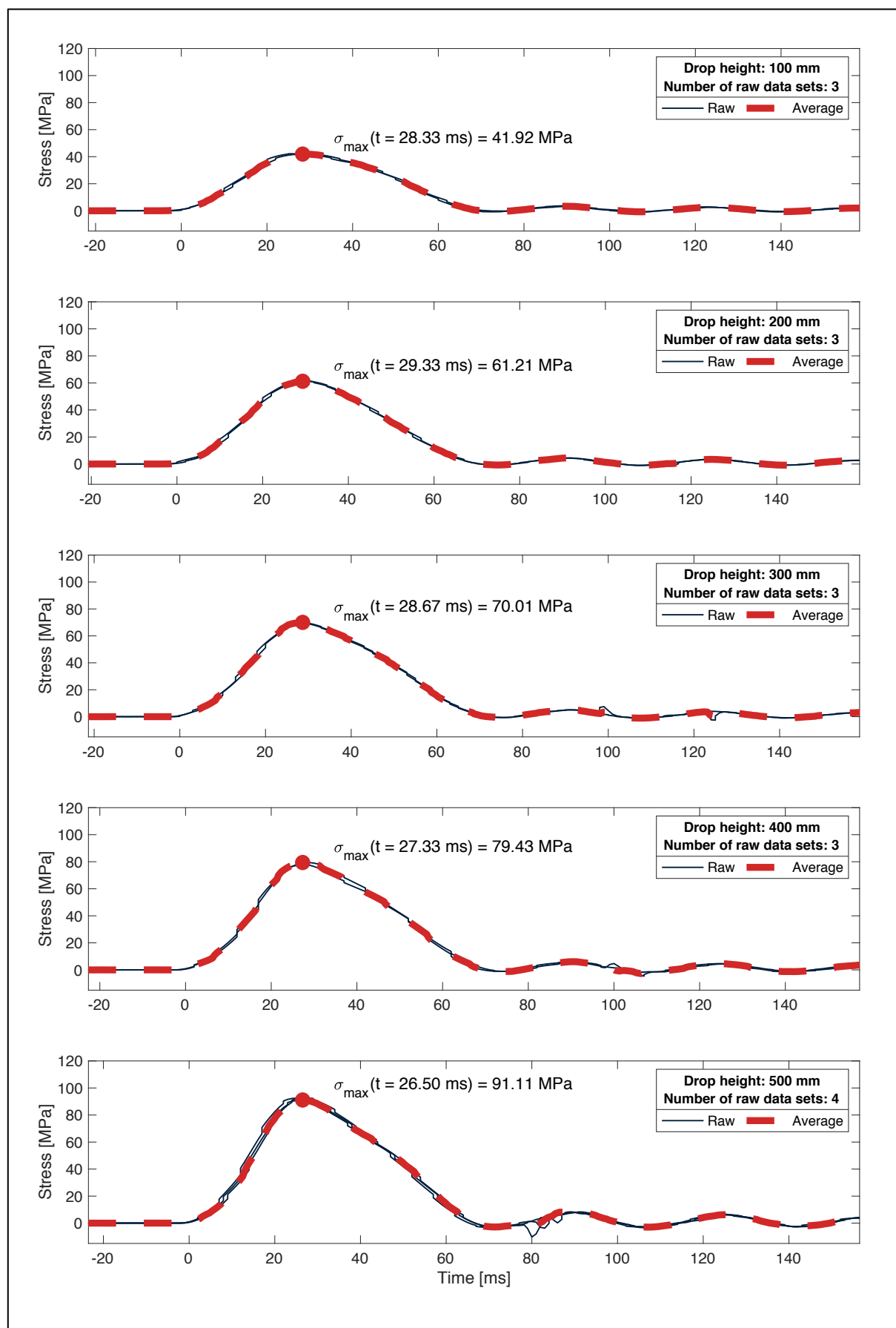


Figure A-9: Principal stress at glass specimen impact location for various impactor drop heights. The data are derived from a strain gauge positioned at the tensile face of the specimens during the experimental campaign. The data set corresponds to clamped laminated specimens with a thickness profile of 6 mm ESG + 1.6 mm PVB + 6 mm ESG.



Figure A-10: Principal stress at glass specimen impact location for various impactor drop heights. The data are derived from a strain gauge positioned at the tensile face of the specimens during the experimental campaign. The data set corresponds to clamped laminated specimens with a thickness profile of 6 mm ESG + 1.6 mm SGP + 6 mm ESG.

B Processed Experimental Data: Acceleration of Glass Specimen at Impact Location

The experimental accelerations were computed using data from accelerometers that were then processed using Savitsky-Golay filtering. The accelerometers were placed on the opposite surface of the glass specimens, at the location of impact. The graphs show, in light gray, the unfiltered accelerations.

Annex B Processed Experimental Data: Acceleration of Glass Specimen at Impact Location

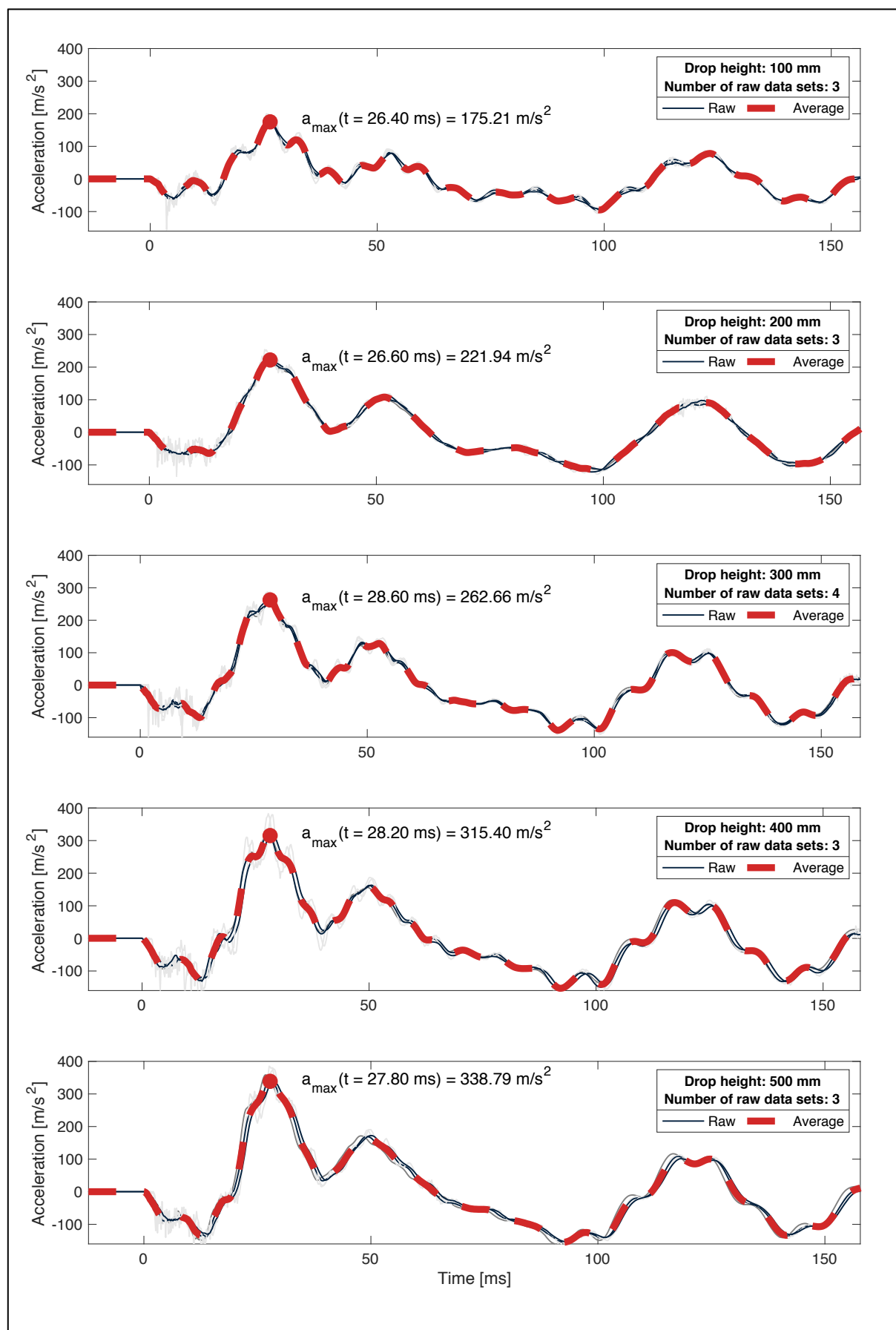


Figure B-1: Out-of-plane acceleration of glass specimen at impact location for various impactor drop heights. The data are derived from an accelerometer during the experimental campaign. The data set corresponds to simply supported monolithic specimens with a thickness profile of 8 mm.

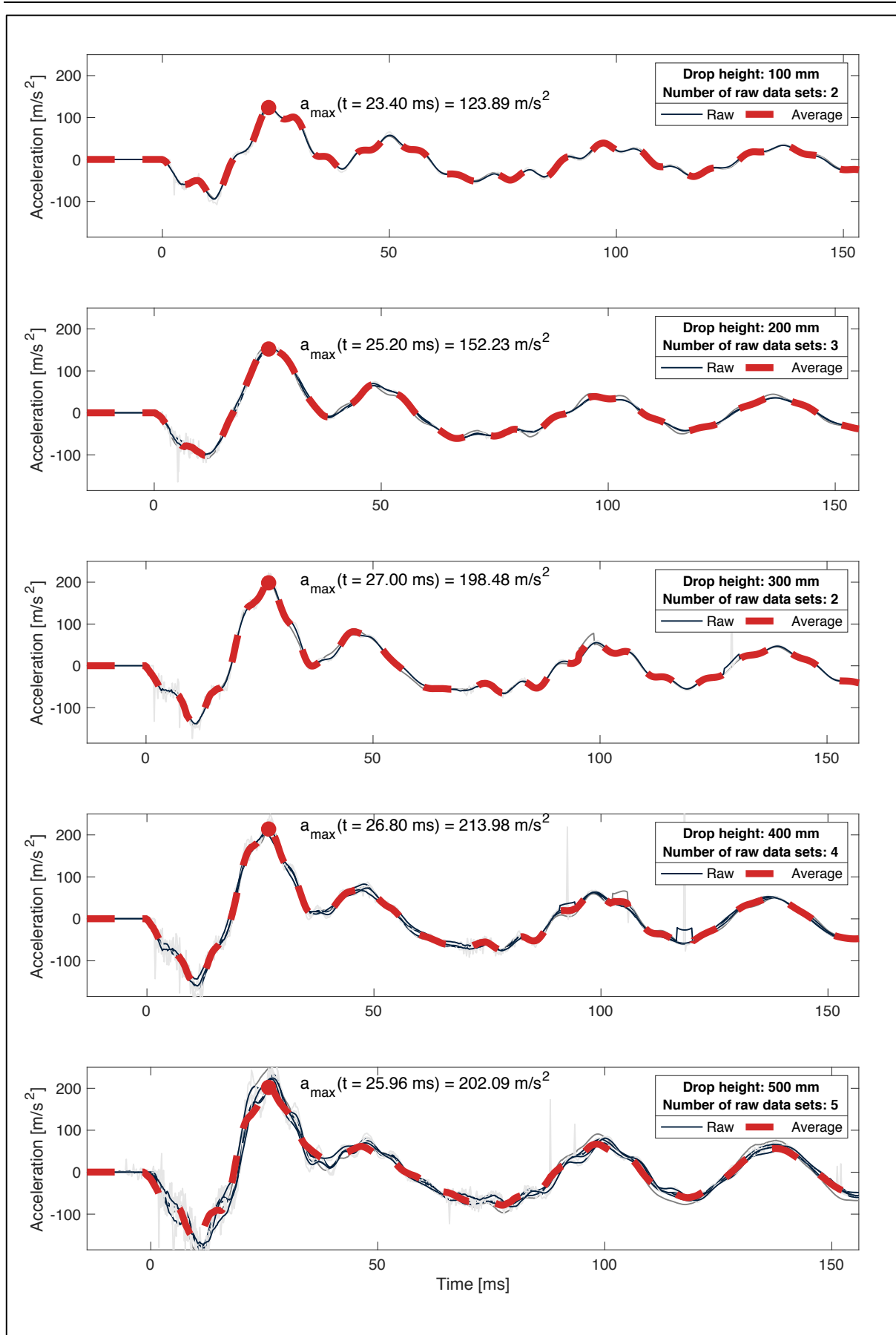


Figure B-2: Out-of-plane acceleration of glass specimen at impact location for various impactor drop heights. The data are derived from an accelerometer during the experimental campaign. The data set corresponds to simply supported monolithic specimens with a thickness profile of 10 mm.

Annex B Processed Experimental Data: Acceleration of Glass Specimen at Impact Location

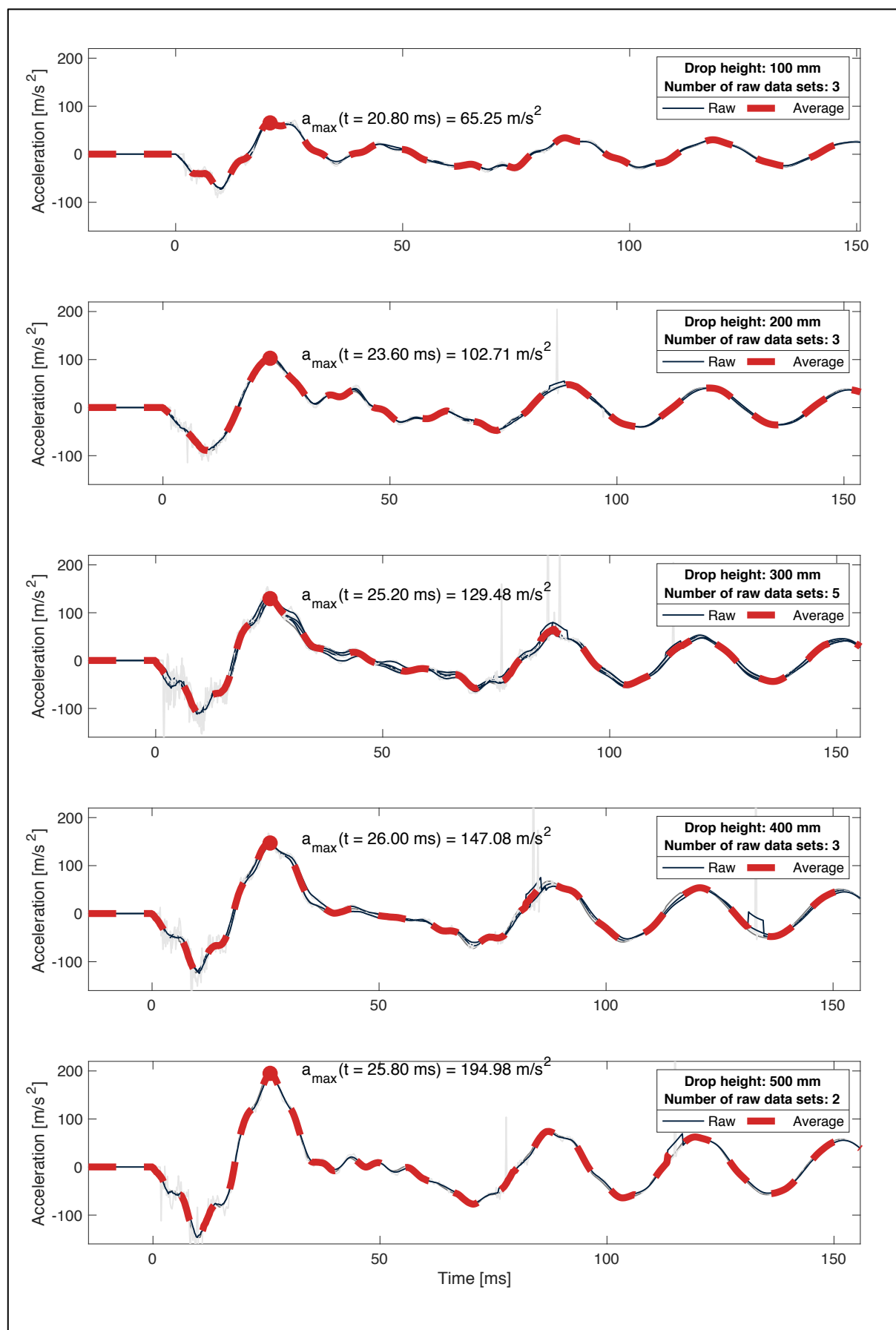


Figure B-3: Out-of-plane acceleration of glass specimen at impact location for various impactor drop heights. The data are derived from an accelerometer during the experimental campaign. The data set corresponds to simply supported monolithic specimens with a thickness profile of 12 mm.

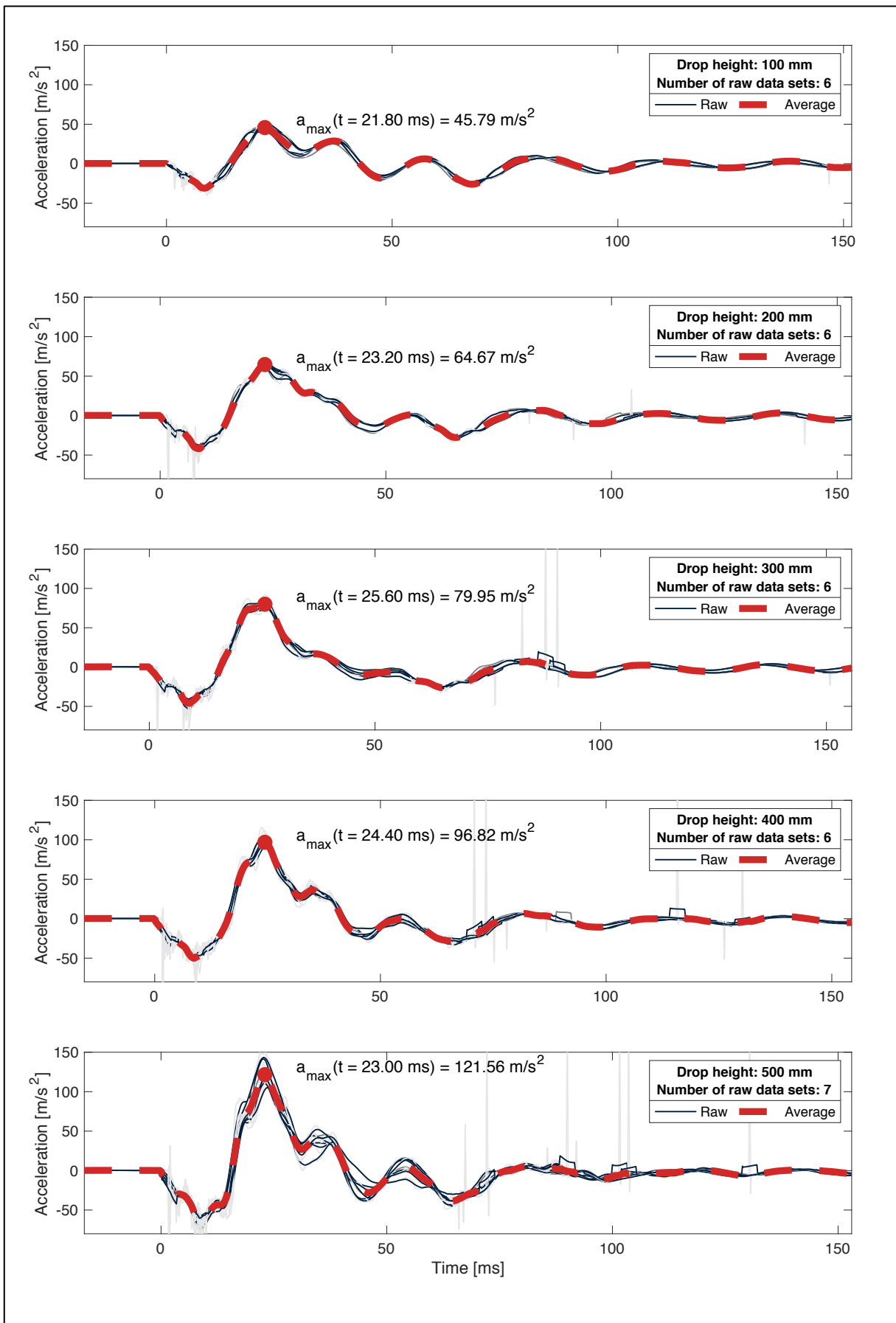


Figure B-4: Out-of-plane acceleration of glass specimen at impact location for various impactor drop heights. The data are derived from an accelerometer during the experimental campaign. The data set corresponds to simply supported laminated specimens with a thickness profile of 8 mm ESG/TVG + 1.6 mm PVB + 8 mm ESG/TVG.

Annex B Processed Experimental Data: Acceleration of Glass Specimen at Impact Location

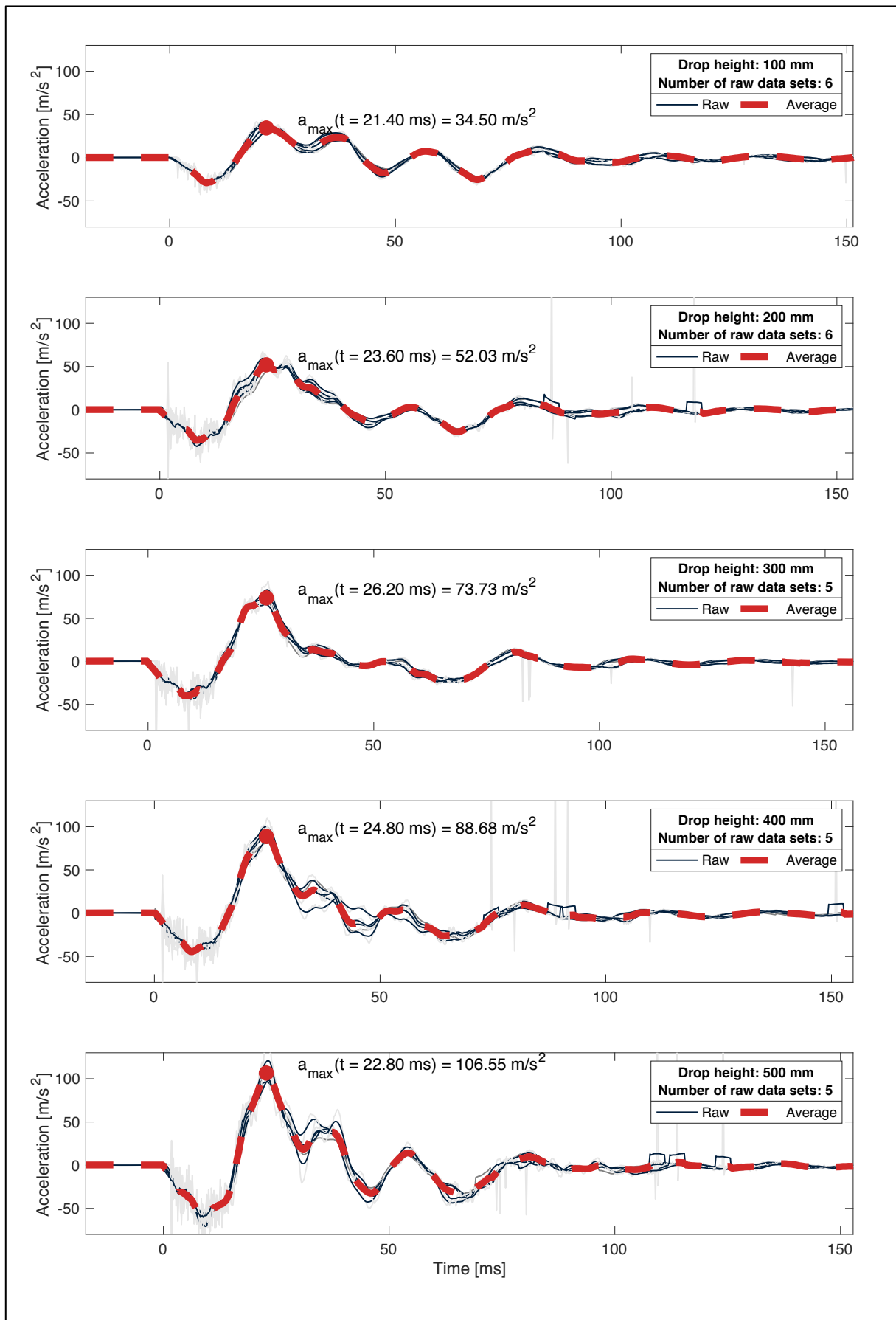


Figure B-5: Out-of-plane acceleration of glass specimen at impact location for various impactor drop heights. The data are derived from an accelerometer during the experimental campaign. The data set corresponds to simply supported laminated specimens with a thickness profile of 8 mm ESG/TVG + 1.6 mm SGP + 8 mm ESG/TVG.

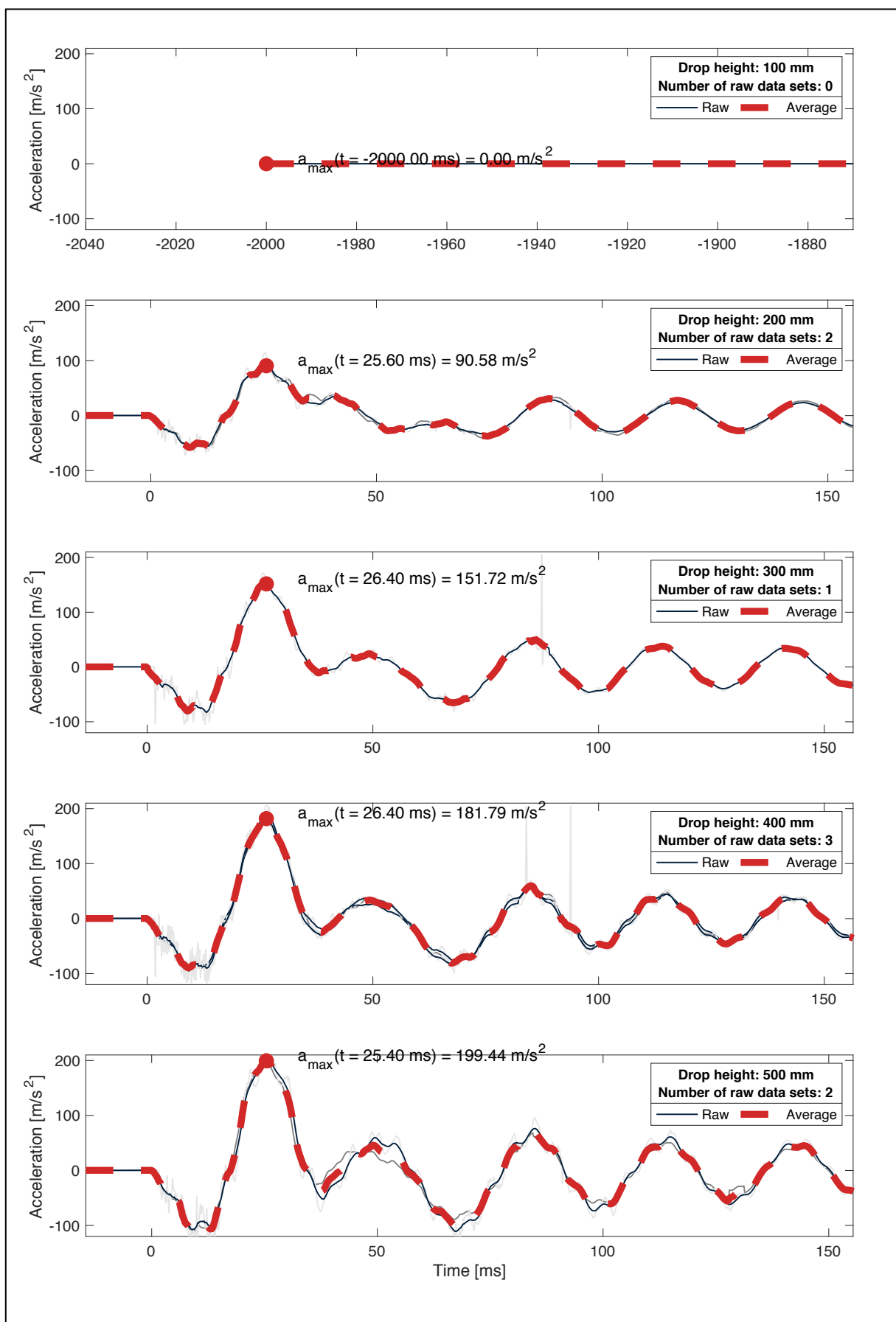


Figure B-6: Out-of-plane acceleration of glass specimen at impact location for various impactor drop heights. The data are derived from an accelerometer during the experimental campaign. The data set corresponds to bolted laminated specimens with a thickness profile of 6 mm ESG + 1.6 mm SGP + 6 mm ESG.

Annex B Processed Experimental Data: Acceleration of Glass Specimen at Impact Location

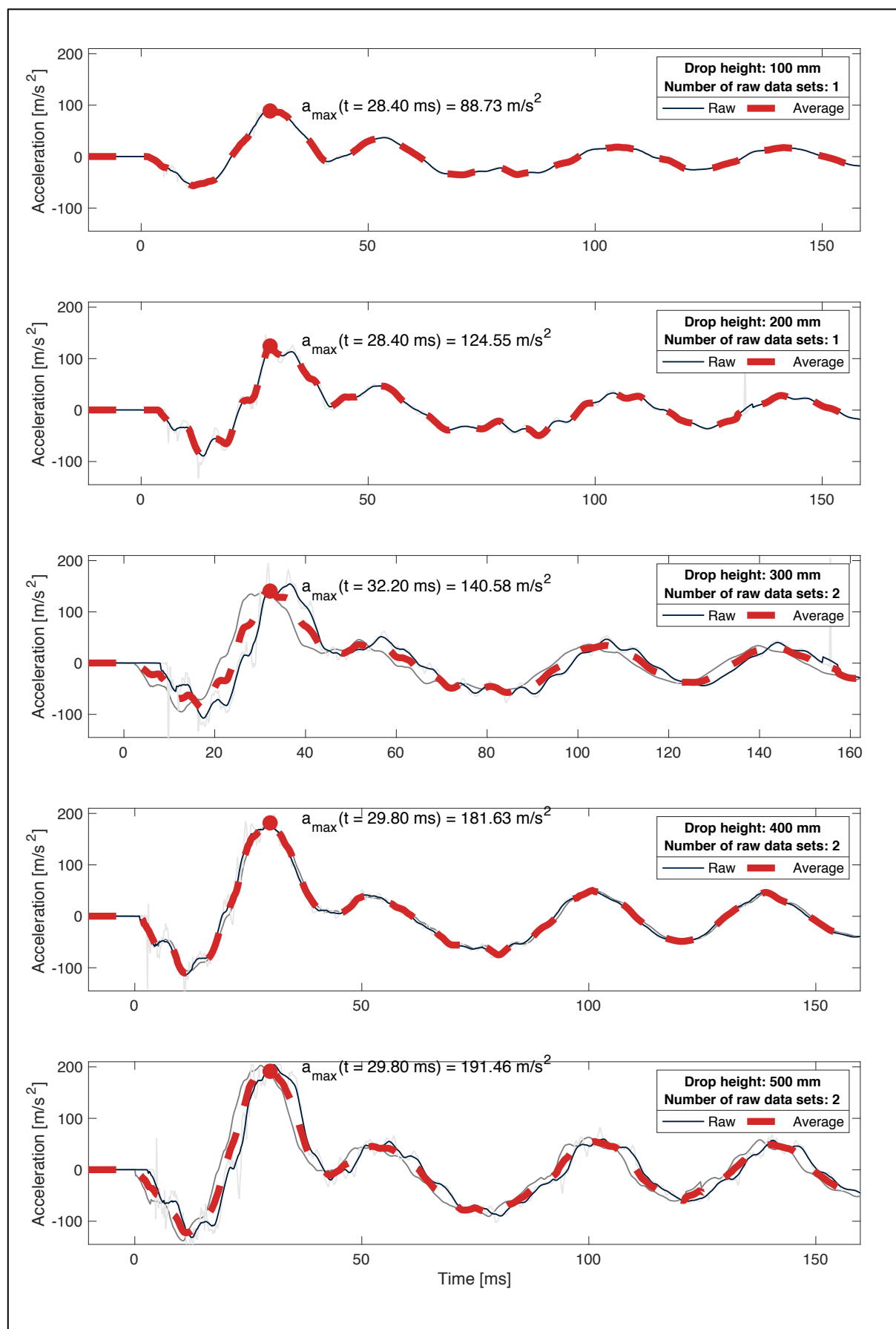


Figure B-7: Out-of-plane acceleration of glass specimen at impact location for various impactor drop heights. The data are derived from an accelerometer during the experimental campaign. The data set corresponds to clamped laminated specimens with a thickness profile of 5 mm ESG + 1.6 mm PVB + 5 mm ESG.

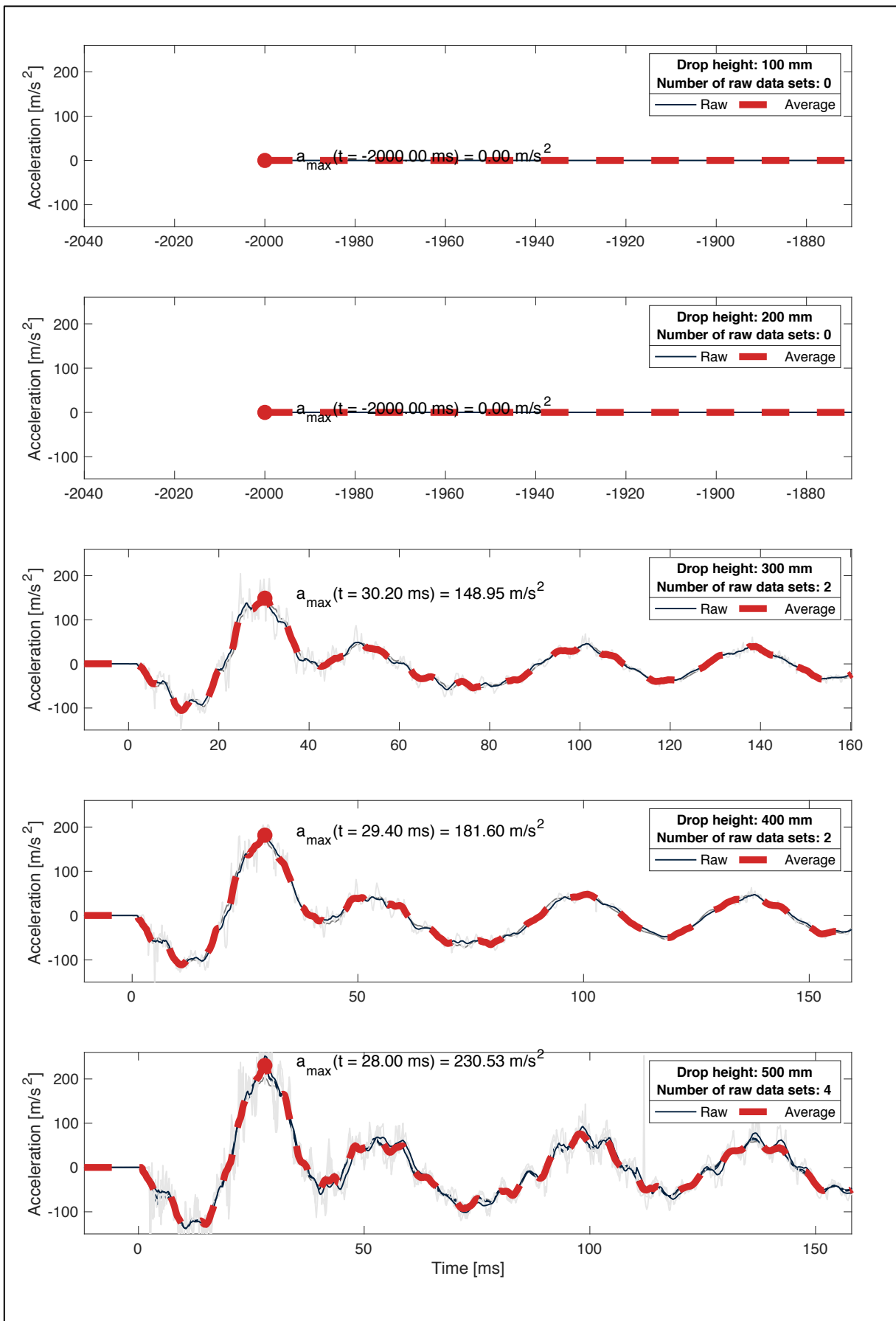


Figure B-8: Out-of-plane acceleration of glass specimen at impact location for various impactor drop heights. The data are derived from an accelerometer during the experimental campaign. The data set corresponds to clamped laminated specimens with a thickness profile of 5 mm ESG + 1.6 mm SGP + 5 mm ESG.

Annex B Processed Experimental Data: Acceleration of Glass Specimen at Impact Location

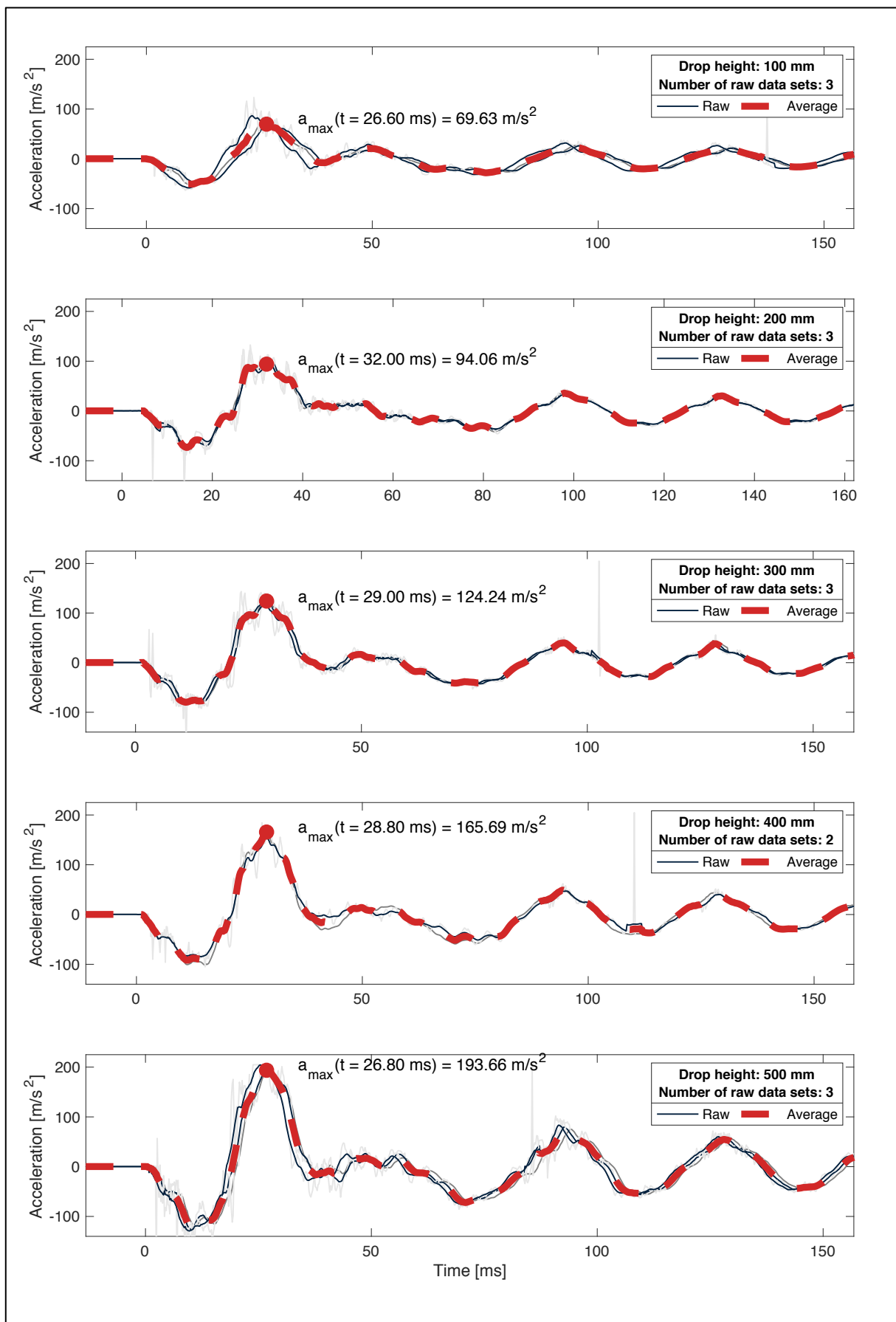


Figure B-9: Out-of-plane acceleration of glass specimen at impact location for various impactor drop heights. The data are derived from an accelerometer during the experimental campaign. The data set corresponds to clamped laminated specimens with a thickness profile of 6 mm ESG + 1.6 mm PVB + 6 mm ESG.

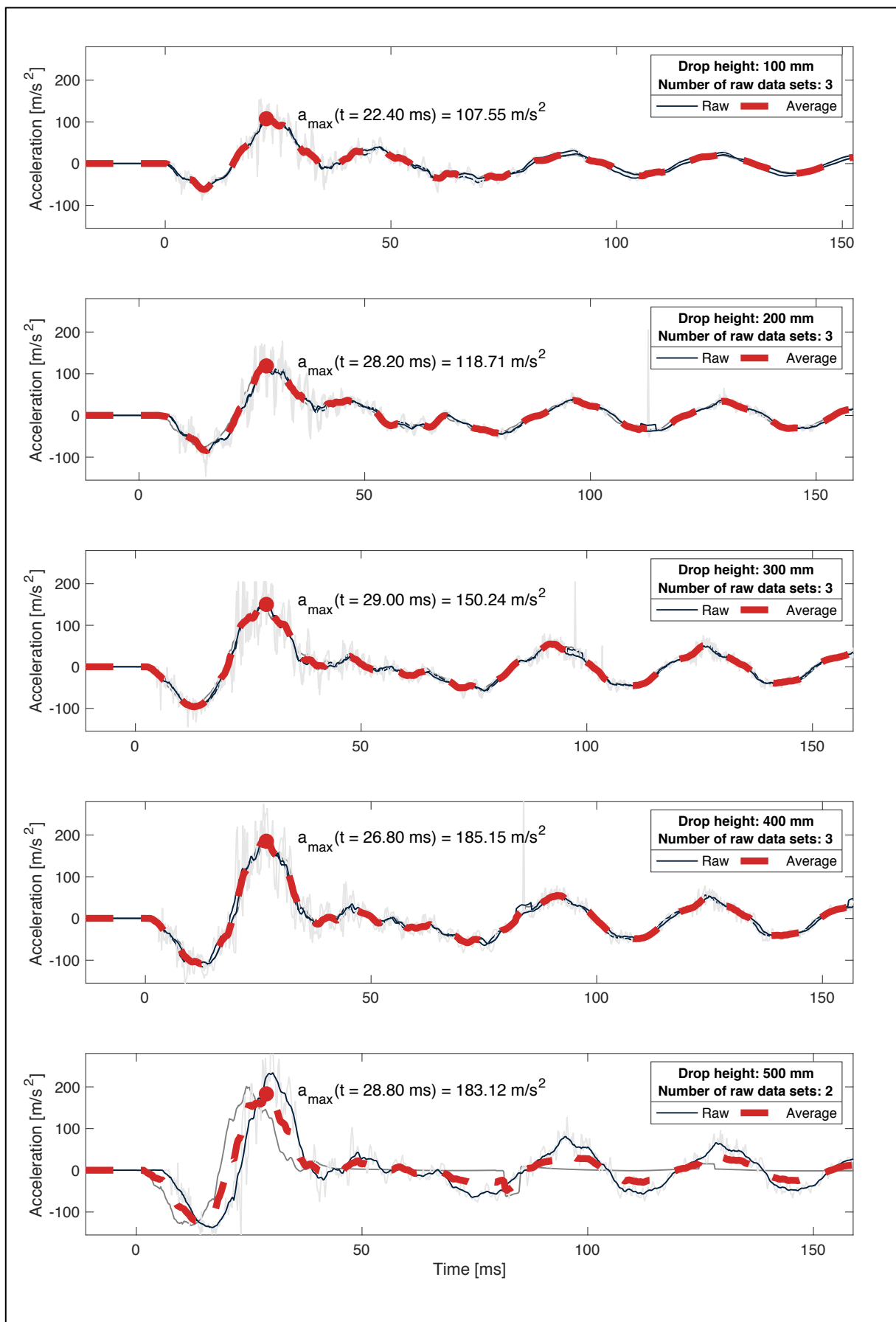


Figure B-10: Out-of-plane acceleration of glass specimen at impact location for various impactor drop heights. The data are derived from an accelerometer during the experimental campaign. The data set corresponds to clamped laminated specimens with a thickness profile of 6 mm ESG + 1.6 mm SGP + 6 mm ESG.

C Derivation of Beam Deflection Response to Atypical Load Configurations

The impactor swinging into the glass pane can be modeled as a beam subjected to an atypical load configuration, i.e. one that is not found in beam tables. This Annex documents the derivation of the beam's deflection response to one such load configuration. Two support conditions are considered: a simply supported beam, see Section C.1 and a beam fixed at both ends, see Section C.2.

C.1 Simply Supported Beam Subjected to Symmetrically Discontinuous Loading

A simply supported beam is subjected to a uniformly distributed load acting along a length c of the beam in a symmetric fashion, see Figure C-1. The indices used in the derivation are illustrated in the figure.

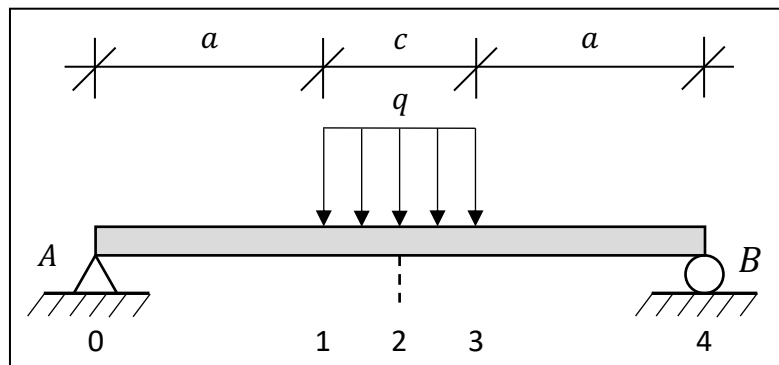


Figure C-1: Sketch of a simply supported beam subjected to symmetrically discontinuous loading

For section 0-1 of the beam, the moment distribution is given by

$$M_{0-1} = q \frac{x c}{2} \quad (C-1)$$

Recalling the relationship between moment and the elastic curve of a beam, Eq. (C-1) yields, through integration, the deflection response for section 0-1:

$$\frac{d^2 v_{0-1}}{dx^2} = \frac{1}{EI} M_{0-1} \quad (C-2)$$

$$\Rightarrow \frac{dv_{0-1}}{dx} = \theta_{0-1} = \frac{q}{EI} \left(\frac{x^2 c}{4} + C_1 \right) \quad (C-3)$$

$$\Rightarrow v_{0-1} = \frac{q}{EI} \left(\frac{x^3 c}{12} + C_1 x + C_2 \right) \quad (C-4)$$

where $\{C_1, C_2\} \in \mathbb{R}$. For a simply supported beam, the kinematic boundary conditions are known to be $\theta(0) = 0$ and $v(0) = 0$. These are prescribed to Eq. (C-3) and (C-4), respectively, such that

$$\begin{cases} \theta(0) = \frac{q c L^2}{12 EI} \left(\frac{c^2}{4 L^2} - \frac{3}{4} \right) \\ v(0) = 0 \end{cases}$$

$$\Leftrightarrow \begin{cases} C_1 = \frac{c L^2}{12} \left(\frac{c^2}{4 L^2} - \frac{3}{4} \right) \\ C_2 = 0 \end{cases}$$

The constants C_1 and C_2 have now been solved. Shifting focus to section 1-3 in Figure C-1, the moment function is given by

$$M_{1-3} = q \left(-\frac{a^2}{2} + \left(a + \frac{c}{2} \right) x - \frac{x^2}{2} \right) \quad (C-5)$$

As was done for section 0-1, the relationship between deflection and moment is invoked, yielding, through integration, the deflection response for section 1-3:

$$\frac{d^2 v_{1-3}}{dx^2} = \frac{1}{EI} M_{1-3} \quad (C-6)$$

$$\Rightarrow \frac{dv_{1-3}}{dx} = \theta_{1-3} = \frac{q}{EI} \left(-\frac{a^2}{2} x + \left(a + \frac{c}{2} \right) \frac{x^2}{2} - \frac{x^3}{6} + C_3 \right) \quad (C-7)$$

$$\Rightarrow v_{1-3} = \frac{q}{EI} \left(-\frac{a^2}{4} x^2 + \left(a + \frac{c}{2} \right) \frac{x^3}{6} - \frac{x^4}{24} + C_3 x + C_4 \right) \quad (C-8)$$

where $\{C_3, C_4\} \in \mathbb{R}$. There are no additional boundary conditions that can be prescribed to the system. However, point 1 along the length of the beam represents a singularity, with the constituent singularity conditions $\theta_{1-} = \theta_{1+}$ and $v_{1-} = v_{1+}$. Utilizing Eq. (C-3), (C-4), (C-7), and (C-8), the terms in these conditions are determined to be

$$\begin{cases} \theta_{1^-} = \theta_{0-1}(x = a) = \frac{q}{EI} \left(\frac{a^2 c}{4} + \frac{c L^2}{12} \left(\frac{c^2}{4 L^2} - \frac{3}{4} \right) \right) \\ \theta_{1^+} = \theta_{1-3}(x = a) = \frac{q}{EI} \left(-\frac{a^3}{2} + \left(a + \frac{c}{2} \right) \frac{a^2}{2} - \frac{a^3}{6} + C_3 \right) \\ v_{1^-} = v_{0-1}(x = a) = \frac{q}{EI} \left(\frac{a^3 c}{12} + \frac{c L^2 a}{12} \left(\frac{c^2}{4 L^2} - \frac{3}{4} \right) \right) \\ v_{1^+} = v_{1-3}(x = a) = \frac{q}{EI} \left(-\frac{a^4}{4} + \left(a + \frac{c}{2} \right) \frac{a^3}{6} - \frac{a^4}{24} + C_3 a + C_4 \right) \end{cases} \quad (\text{C-9})$$

Solving the system yields the constants C_3 and C_4 :

$$\begin{cases} \theta_{1^-} = \theta_{1^+} \\ v_{1^-} = v_{1^+} \end{cases} \Leftrightarrow \begin{cases} C_3 = -\frac{c L^2}{16} + \frac{c^3}{48} + \frac{a^3}{6} \\ C_4 = -\frac{a^4}{24} \end{cases} \quad (\text{C-10})$$

Having solved for C_3 and C_4 , insertion of Eq. (C-10) into Eq. (C-8) finally yields the deflection response of the beam to the predefined load configuration:

$$v_{1-3}(x) = \frac{q}{EI} \left(-\frac{a^4}{24} + \left(-\frac{c L^2}{16} + \frac{c^3}{48} + \frac{a^3}{6} \right) x - \frac{a^2}{4} x^2 + \left(a + \frac{c}{2} \right) \frac{x^3}{6} - \frac{x^4}{24} \right) \quad (\text{C-11})$$

Note, especially, that for $x = L/2$, and observing that $a = 0.5 \cdot (L - a)$, Eq. (C-11) can be simplified to

$$v_{1-3}(x = L/2) = \frac{q}{EI} \left(-\frac{1}{48} L^3 c + \frac{1}{96} L c^3 - \frac{1}{384} c^4 \right) \quad (\text{C-12})$$

This expression is sufficient to determine the maximum deflection of the beam, and thereby compute the stiffness of the glass panel semi-analytically, see Section 6.5.

C.2 Beam Fixed at Both Ends Subjected to Symmetrically Discontinuous Loading

A beam with fixed supports at both ends is subjected to a uniformly distributed load acting along a length c of the beam in a symmetric fashion, see Figure C-2. The indices used in the derivation are illustrated in the figure.

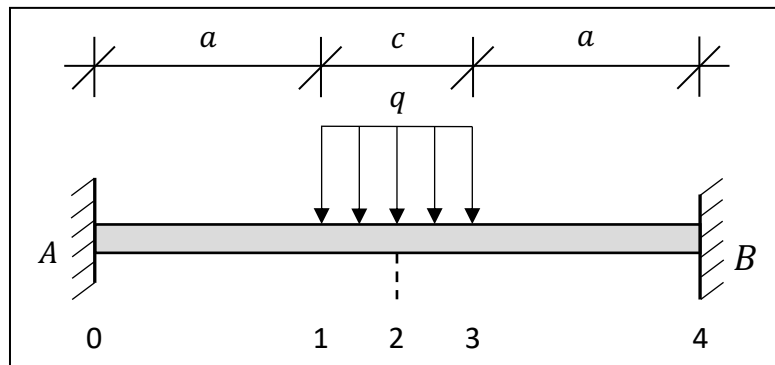


Figure C-2: Sketch of a beam fixed at both ends subjected to symmetrically discontinuous loading.

This load configuration can be deconstructed into three load configurations, see Figure C-3.

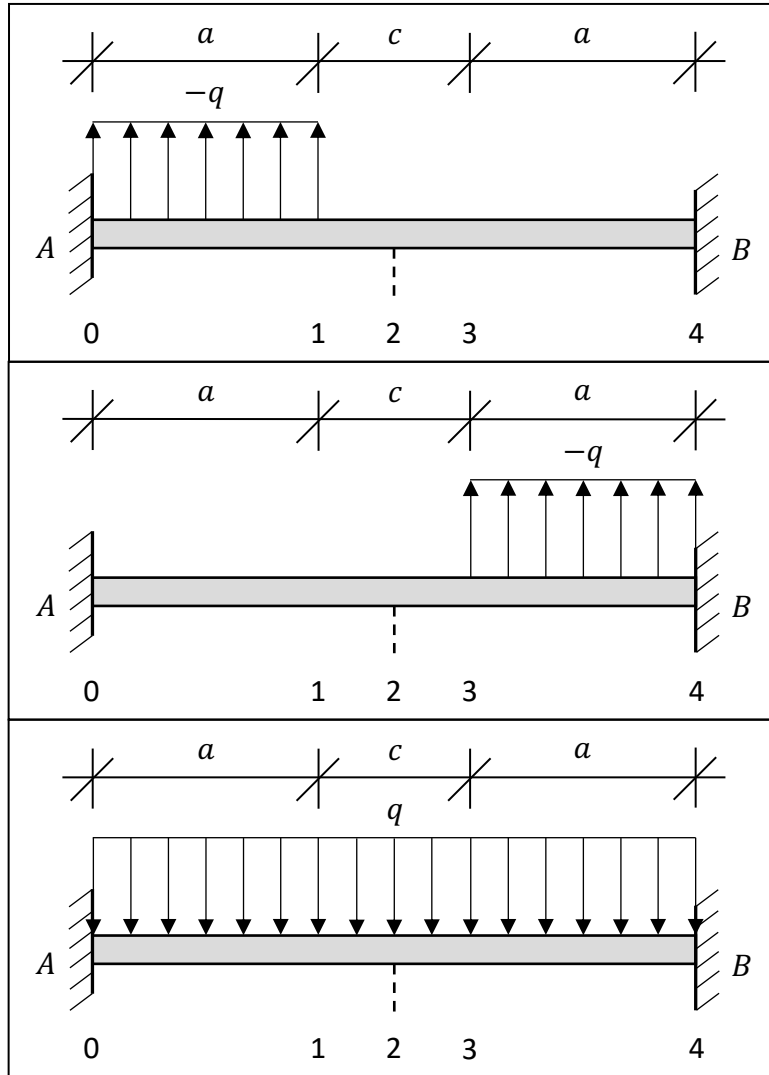


Figure C-3: Component load configurations: load configuration I (top), load configuration II (center) and load configuration III (bottom) are to be superposed.

For section 0-1 of the beam, the moment distribution, with respect to load configuration I, is given by

$$M_{0-1}^I = M_A^I + R_A^I x + \frac{q x^2}{2} \quad (C-13)$$

where

$$M_A^I = \frac{q a^2}{12} \left(3 \frac{a^2}{L^2} - 8 \frac{a}{L} + 6 \right) \quad (C-14)$$

$$R_A^I = -q a \left(1 - \frac{a^2}{L^2} + \frac{a^3}{2 L^3} \right) \quad (C-15)$$

Thus, the moment distribution is found to be

$$\begin{aligned}
 M_{0-1}^I &= \frac{q a^2}{12} \left(3 \frac{a^2}{L^2} - 8 \frac{a}{L} + 6 \right) - q a \left(1 - \frac{a^2}{L^2} + \frac{a^3}{2 L^3} \right) x + \frac{q x^2}{2} = \\
 &= q \left(-\frac{2 a^3}{3 L} + \frac{a^2}{2} + \left(-a + \frac{a^3}{L^2} \right) x + \frac{x^2}{2} \right)
 \end{aligned} \tag{C-16}$$

For section 1-4 of load configuration I, the moment distribution is given by

$$M_{1-4}^I = M_B^I + R_B^I (L - x) \tag{C-17}$$

where

$$M_B^I = \frac{q a^3}{12 L} \left(4 - 3 \frac{a}{L} \right) \tag{C-18}$$

$$R_B^I = -q a \left(\frac{a^2}{L^2} + \frac{a^3}{2 L^3} \right) \tag{C-19}$$

Thus, the moment distribution is found to be

$$\begin{aligned}
 M_{1-4}^I &= \frac{q a^3}{12 L} \left(4 - 3 \frac{a}{L} \right) - q a \left(\frac{a^2}{L^2} + \frac{a^3}{2 L^3} \right) (L - x) = \\
 &= q \left(-\frac{2 a^3}{3 L} + \frac{a^4}{4 L^2} + \left(\frac{a^3}{L^2} - \frac{a^4}{2 L^3} \right) x \right)
 \end{aligned} \tag{C-20}$$

Utilizing symmetry, the moment distribution along section 0-3 for load configuration II can be immediately derived as

$$\begin{aligned}
 M_{0-3}^{II} &= M_A^{II} + R_A^{II} x = \\
 &= q \left(\frac{a^3}{3 L} - \frac{a^4}{4 L^2} + \left(-\frac{a^3}{L^2} + \frac{a^4}{2 L^3} \right) x \right)
 \end{aligned} \tag{C-21}$$

For load configuration III, beam tables reveal the moment distribution to be

$$M_{0-4}^{III} = q \left(-\frac{L^2}{12} + \frac{L}{2} x - \frac{1}{2} x^2 \right) \tag{C-22}$$

Taken together, load configurations I, II, and III give the moment distribution of the beam at section 0-1 through the superposed function

$$M_{0-1}^{\text{super}} = M_{0-1}^I + M_{0-3}^{II} + M_{0-4}^{III} =$$

$$= q \left(-\frac{L^2}{12} + \frac{a^2}{2} - \frac{a^3}{3L} + \left(\frac{L}{2} - a\right)x \right) \quad (\text{C-23})$$

Recalling the relationship between moment and the elastic curve of a beam, Eq. (C-23) yields, through integration, the superposed deflection response for section 0-1:

$$\frac{d^2 v_{0-1}^{\text{super}}}{dx^2} = \frac{1}{EI} M_{0-1}^{\text{super}} \quad (\text{C-24})$$

$$\Rightarrow \frac{dv_{0-1}^{\text{super}}}{dx} = \theta_{0-1}^{\text{super}} = \frac{q}{EI} \left(\left(-\frac{L^2}{12} + \frac{a^2}{2} - \frac{a^3}{3L} \right) x + \left(\frac{L}{2} - a \right) \frac{x^2}{2} + C_1 \right) \quad (\text{C-25})$$

$$\Rightarrow v_{0-1}^{\text{super}} = \frac{q}{EI} \left(\left(-\frac{L^2}{12} + \frac{a^2}{2} - \frac{a^3}{3L} \right) \frac{x^2}{2} + \left(\frac{L}{2} - a \right) \frac{x^3}{6} + C_1 x + C_2 \right) \quad (\text{C-26})$$

where $\{C_1, C_2\} \in \mathbb{R}$. For a fixed beam, the kinematic boundary conditions are known to be $\theta(0) = 0$ and $v(0) = 0$. These are prescribed to Eq. (C-25) and (C-26), respectively, such that

$$\begin{aligned} & \begin{cases} \theta(0) = 0 \\ v(0) = 0 \end{cases} \\ \Leftrightarrow & \begin{cases} C_1 = 0 \\ C_2 = 0 \end{cases} \end{aligned} \quad (\text{C-27})$$

The constants C_1 and C_2 have now been solved. Shifting focus to section 1-3, here, too, the moment distribution is given by a superposed function,

$$\begin{aligned} M_{1-3}^{\text{super}} &= M_{1-4}^{\text{I}} + M_{0-3}^{\text{II}} + M_{0-4}^{\text{III}} = \\ &= q \left(-\frac{L^2}{12} - \frac{a^3}{3L} + \frac{Lx}{2} - \frac{x^2}{2} \right) \end{aligned} \quad (\text{C-28})$$

As was done for section 0-1, the relationship between deflection and moment is invoked, yielding, through integration, the superposed deflection response for section 1-3:

$$\frac{d^2 v_{1-3}^{\text{super}}}{dx^2} = \frac{1}{EI} M_{1-3}^{\text{super}} \quad (\text{C-29})$$

$$\Rightarrow \frac{dv_{1-3}^{\text{super}}}{dx} = \theta_{1-3}^{\text{super}} = \frac{q}{EI} \left(\left(-\frac{L^2}{12} - \frac{a^3}{3L} \right) x + \frac{Lx^2}{4} - \frac{x^3}{6} + C_3 \right) \quad (\text{C-30})$$

$$\Rightarrow v_{1-3}^{\text{super}} = \frac{q}{EI} \left(\left(-\frac{L^2}{12} - \frac{a^3}{3L} \right) \frac{x^2}{2} + \frac{Lx^3}{12} - \frac{x^4}{24} + C_3 x + C_4 \right) \quad (\text{C-31})$$

where $\{C_3, C_4\} \in \mathbb{R}$. There are no additional boundary conditions that can be prescribed to the system. However, point 1 along the length of the beam represents a singularity, with the constituent singularity conditions $\theta_{1-} = \theta_{1+}$ and $v_{1-} = v_{1+}$. Utilizing Eq. (C-25), (C-26), (C-30), and (C-31), the terms in these conditions are determined to be

$$\begin{cases} \theta_{1-} = \theta_{0-1}^{\text{super}}(a) = \frac{q}{EI} \left(\left(-\frac{L^2}{12} + \frac{a^2}{2} - \frac{a^3}{3L} \right) a + \left(\frac{L}{2} - a \right) \frac{a^2}{2} \right) \\ \theta_{1+} = \theta_{1-3}^{\text{super}}(a) = \frac{q}{EI} \left(\left(-\frac{L^2}{12} - \frac{a^3}{3L} \right) a + \frac{L a^2}{4} - \frac{a^3}{6} + C_3 \right) \\ v_{1-} = v_{0-1}^{\text{super}}(a) = \frac{q}{EI} \left(\left(-\frac{L^2}{12} + \frac{a^2}{2} - \frac{a^3}{3L} \right) \frac{a^2}{2} + \left(\frac{L}{2} - a \right) \frac{a^3}{6} \right) \\ v_{1+} = v_{1-3}^{\text{super}}(a) = \frac{q}{EI} \left(\left(-\frac{L^2}{12} - \frac{a^3}{3L} \right) \frac{a^2}{2} + \frac{L a^3}{12} - \frac{a^4}{24} + C_3 a + C_4 \right) \end{cases} \quad (\text{C-32})$$

Solving the system yields the constants C_3 and C_4 :

$$\begin{cases} \theta_{1-} = \theta_{1+} \\ v_{1-} = v_{1+} \end{cases} \Leftrightarrow \begin{cases} C_3 = \frac{a^3}{6} \\ C_4 = -\frac{a^4}{24} \end{cases} \quad (\text{C-33})$$

Having solved for C_3 and C_4 , insertion of Eq. (C-33) into Eq. (C-31) finally yields the deflection response of the beam to the predefined load configuration:

$$v_{1-3}(x) = \frac{q}{EI} \left(-\frac{a^4}{24} + \frac{a^3}{6} x + \left(-\frac{L^2}{24} - \frac{a^4}{6L} \right) x^2 + \frac{L x^3}{12} - \frac{x^4}{24} \right) \quad (\text{C-34})$$

Note, especially, that for $x = L/2$, and observing that $a = 0.5 \cdot (L - a)$, Eq. (C-34) can be simplified to

$$v_{1-3}(x = L/2) = \frac{q}{192 EI} \left(-L^3 c + L c^3 - \frac{1}{2} c^4 \right) \quad (\text{C-35})$$

This expression is sufficient to determine the maximum deflection of the beam, and thereby compute the stiffness of the glass panel semi-analytically, see Section 6.5.

D Collated Results: Out-of-plane Acceleration of Glass Specimens

The experimental accelerations were computed using data from accelerometers that were then processed using Savitsky-Golay filtering. The accelerometers were placed on the opposite surface of the glass specimens, at the location of impact. The numerical accelerations are extracted from the high-fidelity finite element models at a node corresponding to the location of the accelerometer.

Annex D Collated Results: Out-of-plane Acceleration of Glass Specimens

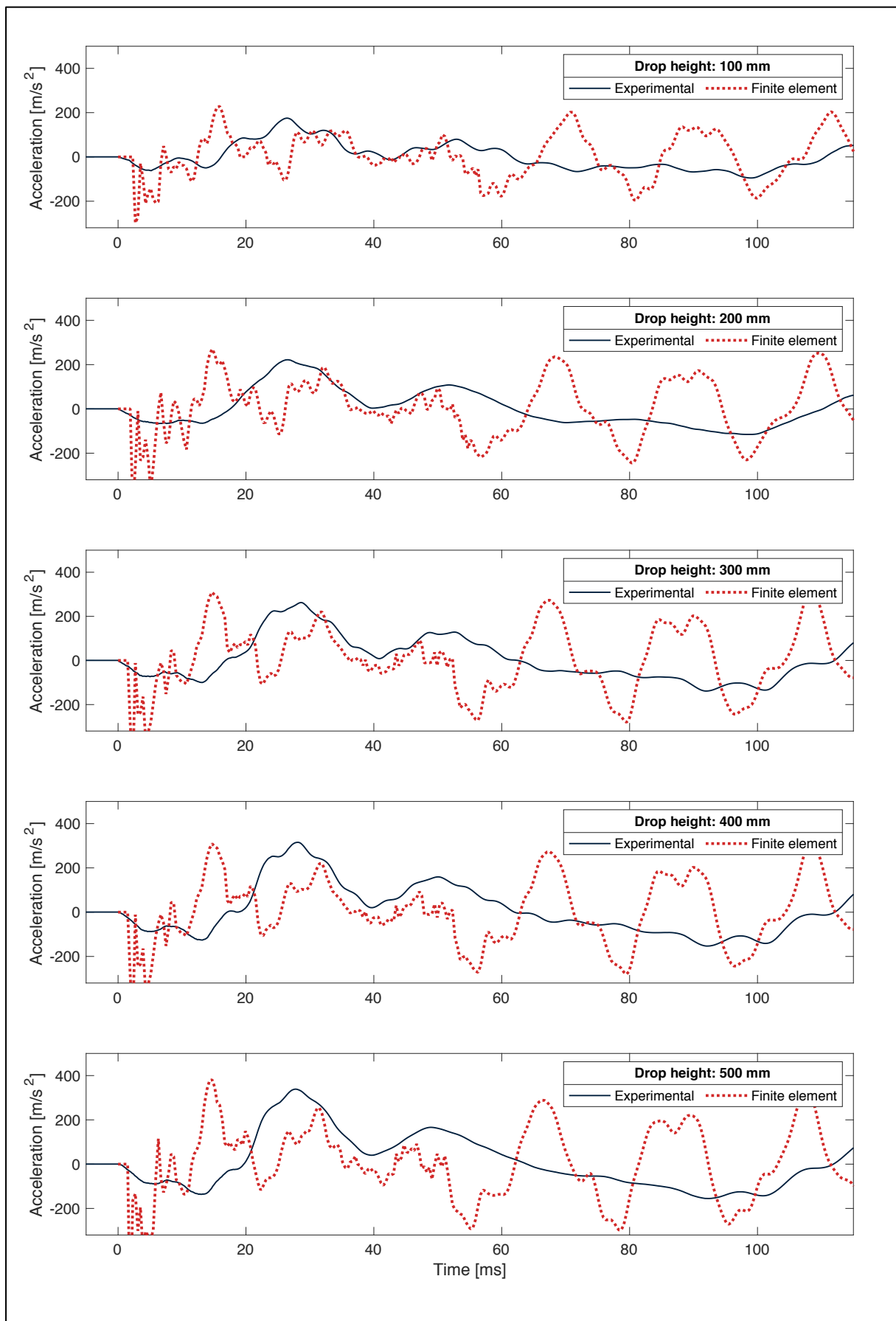


Figure D-1: Collated results for out-of-plane acceleration of glass specimen at impact location for various impactor drop heights. The data set corresponds to simply supported monolithic specimens with a thickness profile of 8 mm.

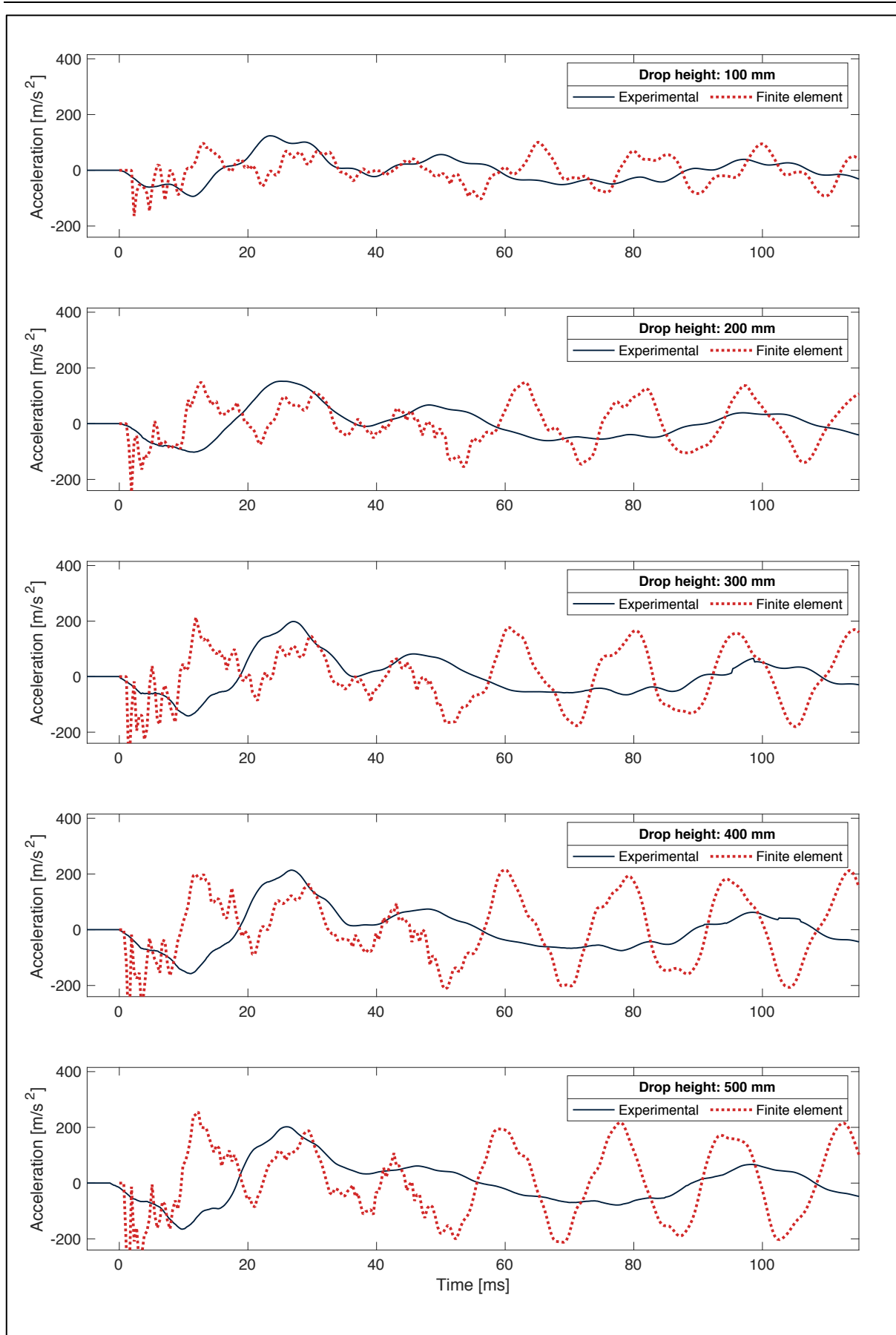


Figure D-2: Collated results for out-of-plane acceleration of glass specimen at impact location for various impactor drop heights. The data set corresponds to simply supported monolithic specimens with a thickness profile of 10 mm.

Annex D Collated Results: Out-of-plane Acceleration of Glass Specimens

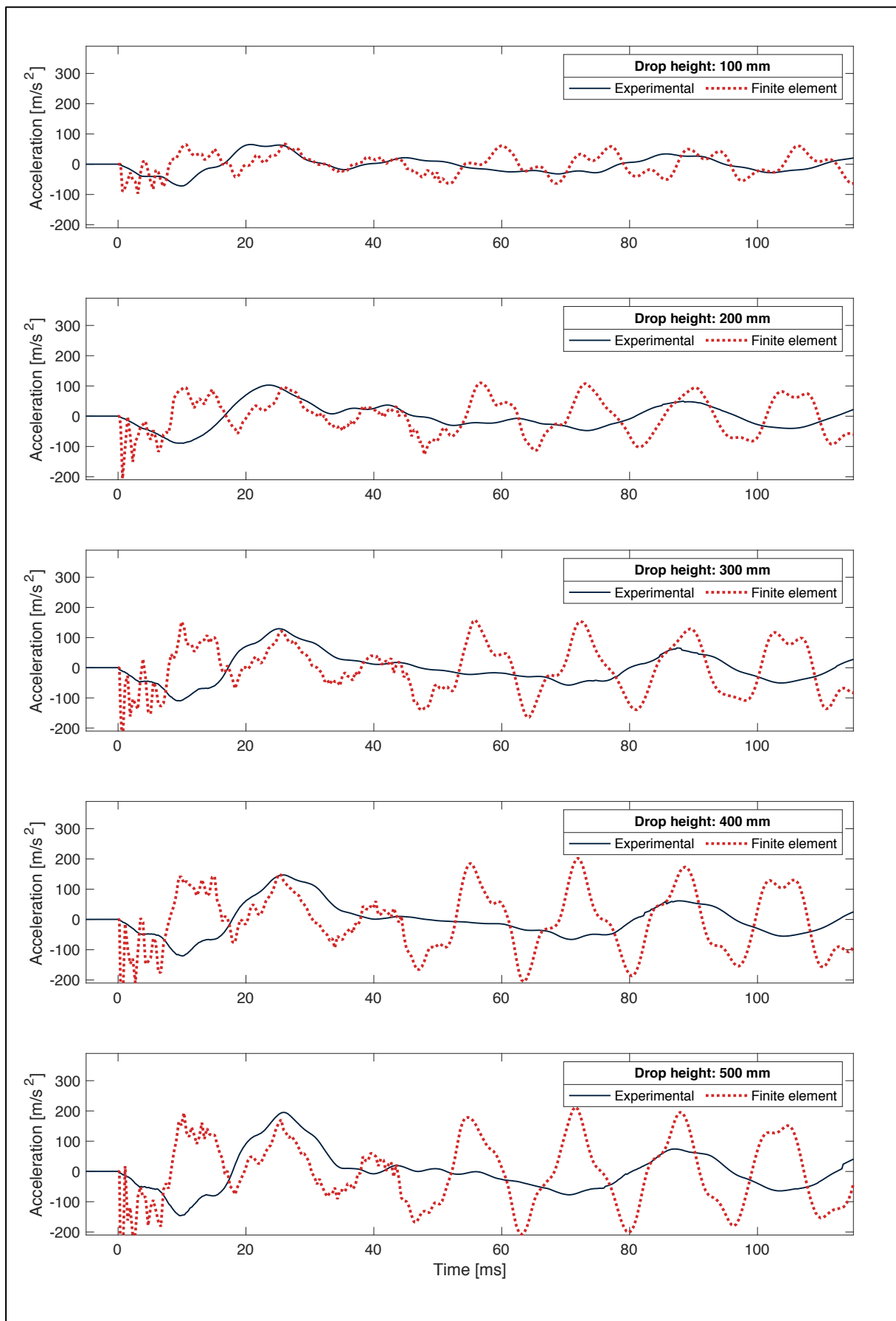


Figure D-3: Collated results for out-of-plane acceleration of glass specimen at impact location for various impactor drop heights. The data set corresponds to simply supported monolithic specimens with a thickness profile of 12 mm.

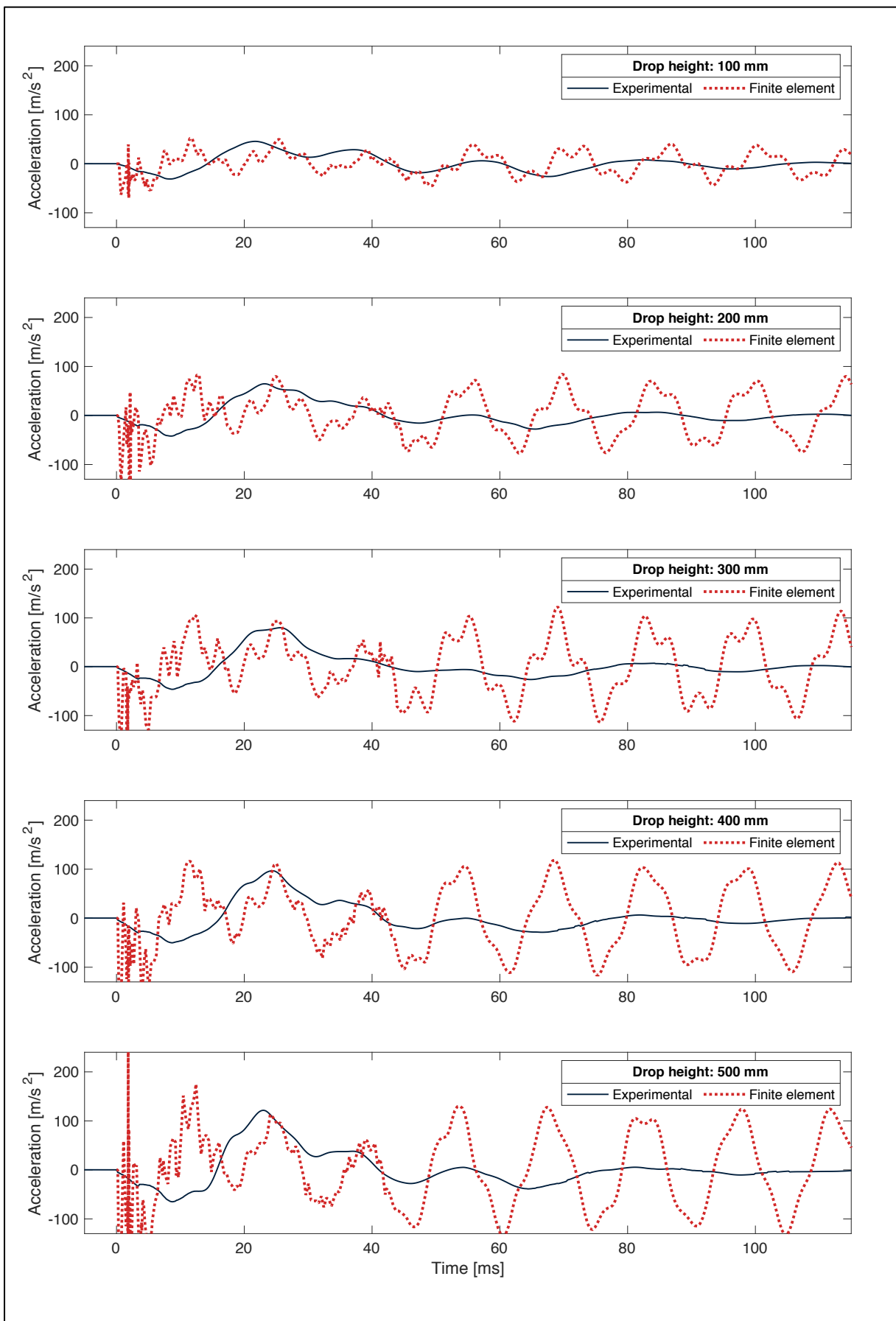


Figure D-4: Collated results for out-of-plane acceleration of glass specimen at impact location for various impactor drop heights. The data set corresponds to simply supported laminated specimens with a thickness profile of 8 mm ESG/TVG + 1.6 mm PVB + 8 mm ESG/TVG.

Annex D Collated Results: Out-of-plane Acceleration of Glass Specimens

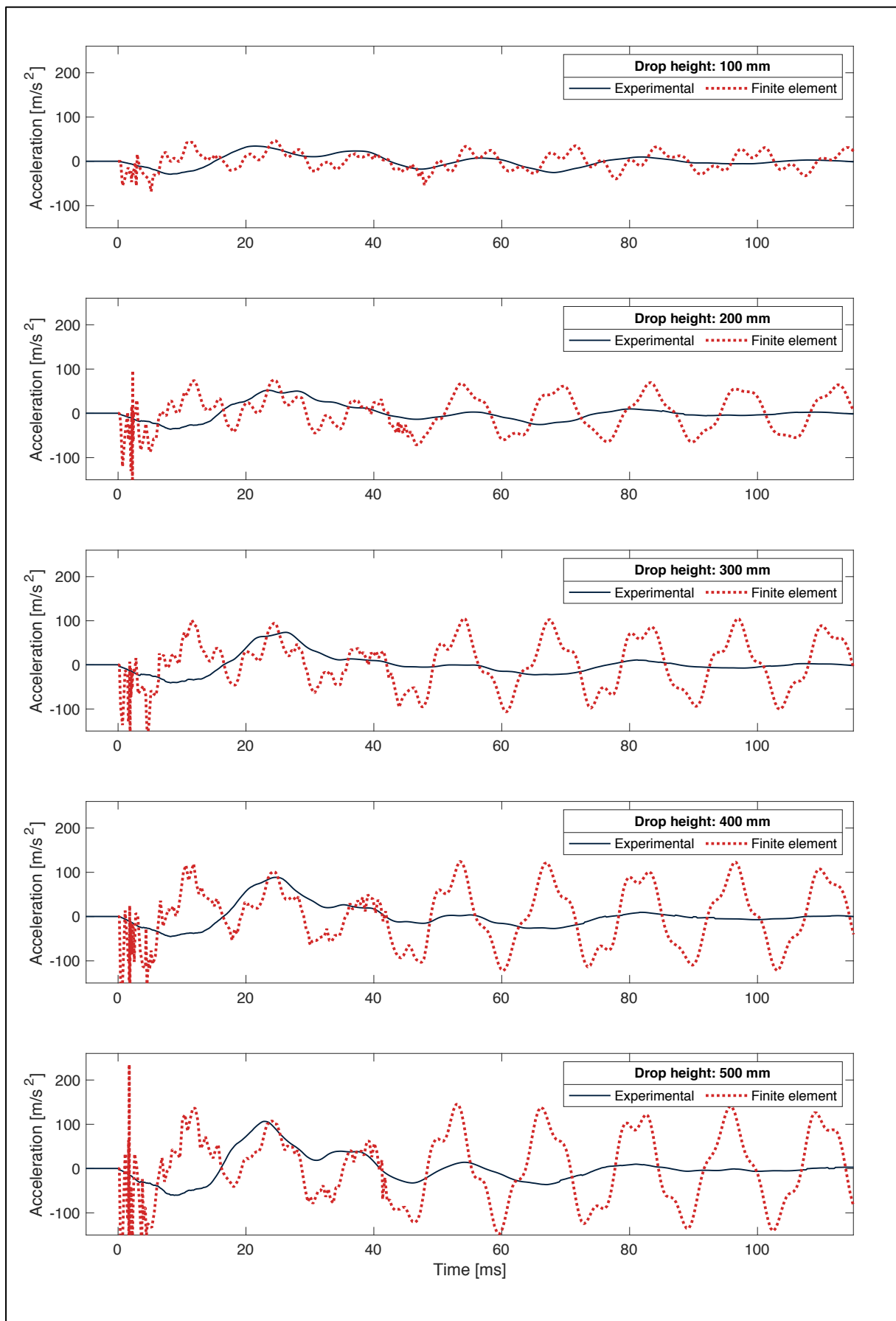


Figure D-5: Collated results for out-of-plane acceleration of glass specimen at impact location for various impactor drop heights. The data set corresponds to simply supported laminated specimens with a thickness profile of 8 mm ESG/TVG + 1.6 mm SGP + 8 mm ESG/TVG.

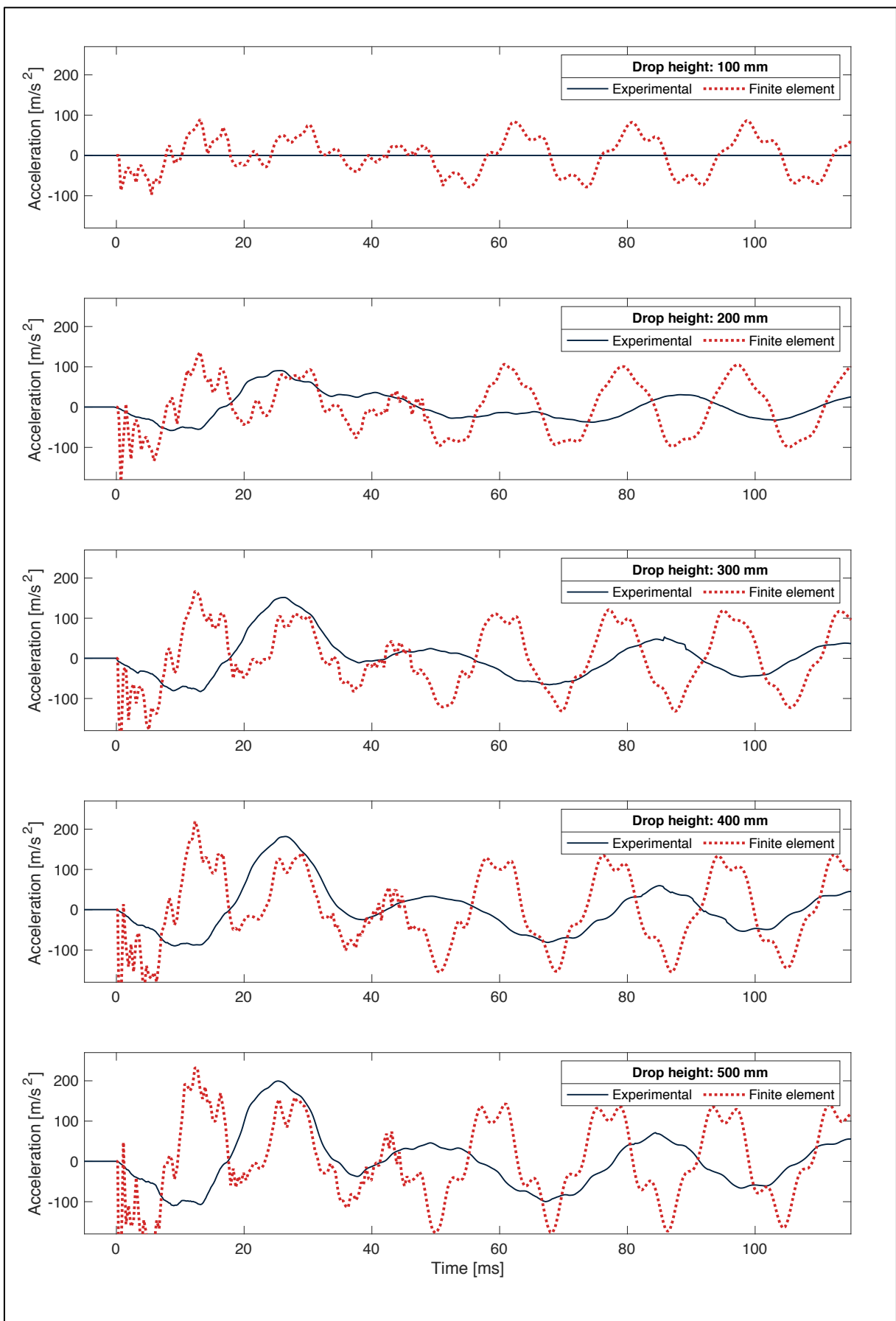


Figure D-6: Collated results for out-of-plane acceleration of glass specimen at impact location for various impactor drop heights. The data set corresponds to bolted laminated specimens with a thickness profile of 6 mm ESG + 1.6 mm SGP + 6 mm ESG.

Annex D Collated Results: Out-of-plane Acceleration of Glass Specimens

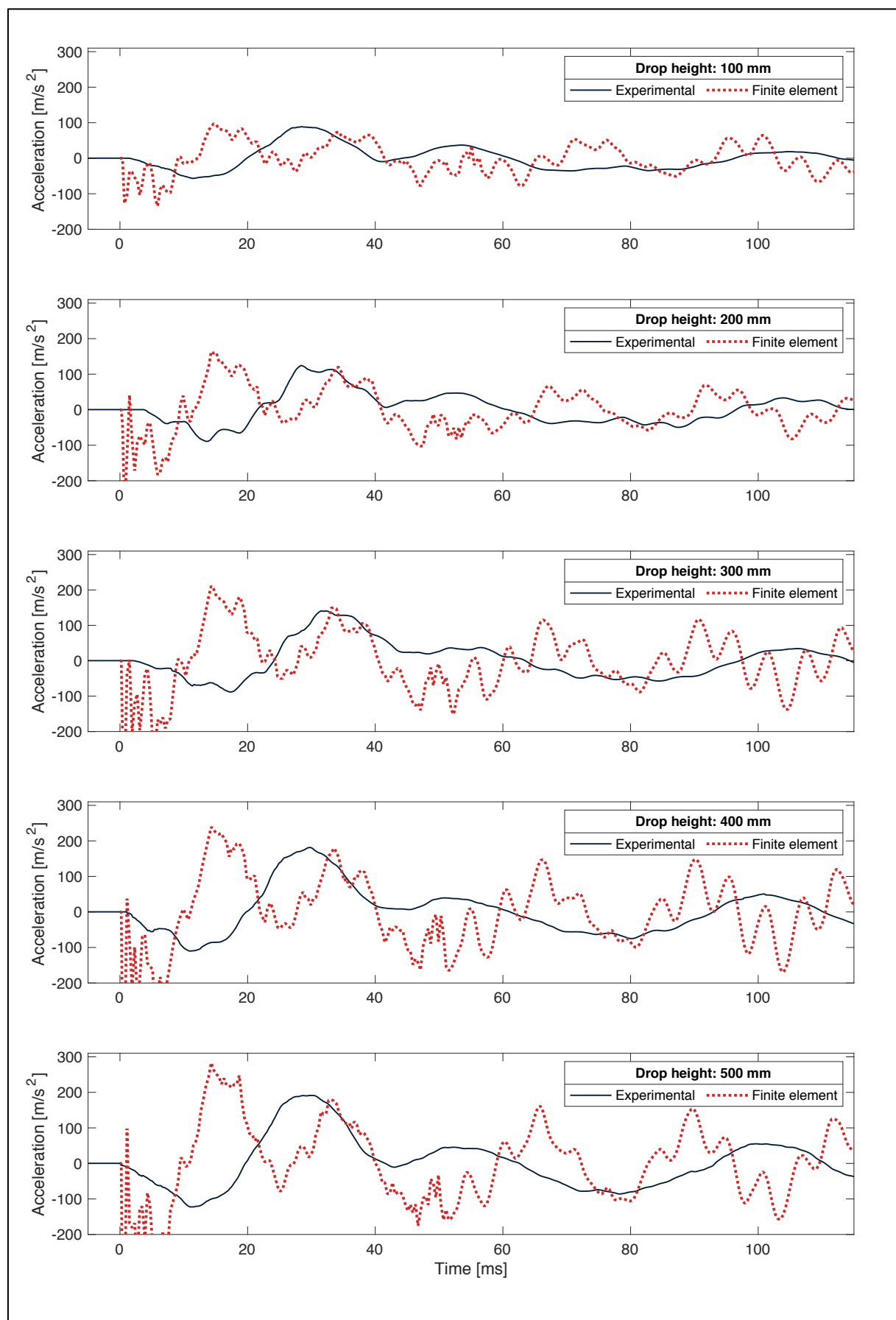


Figure D-7: Collated results for out-of-plane acceleration of glass specimen at impact location for various impactor drop heights. The data set corresponds to clamped laminated specimens with a thickness profile of 5 mm ESG + 1.6 mm PVB + 8 mm ESG.

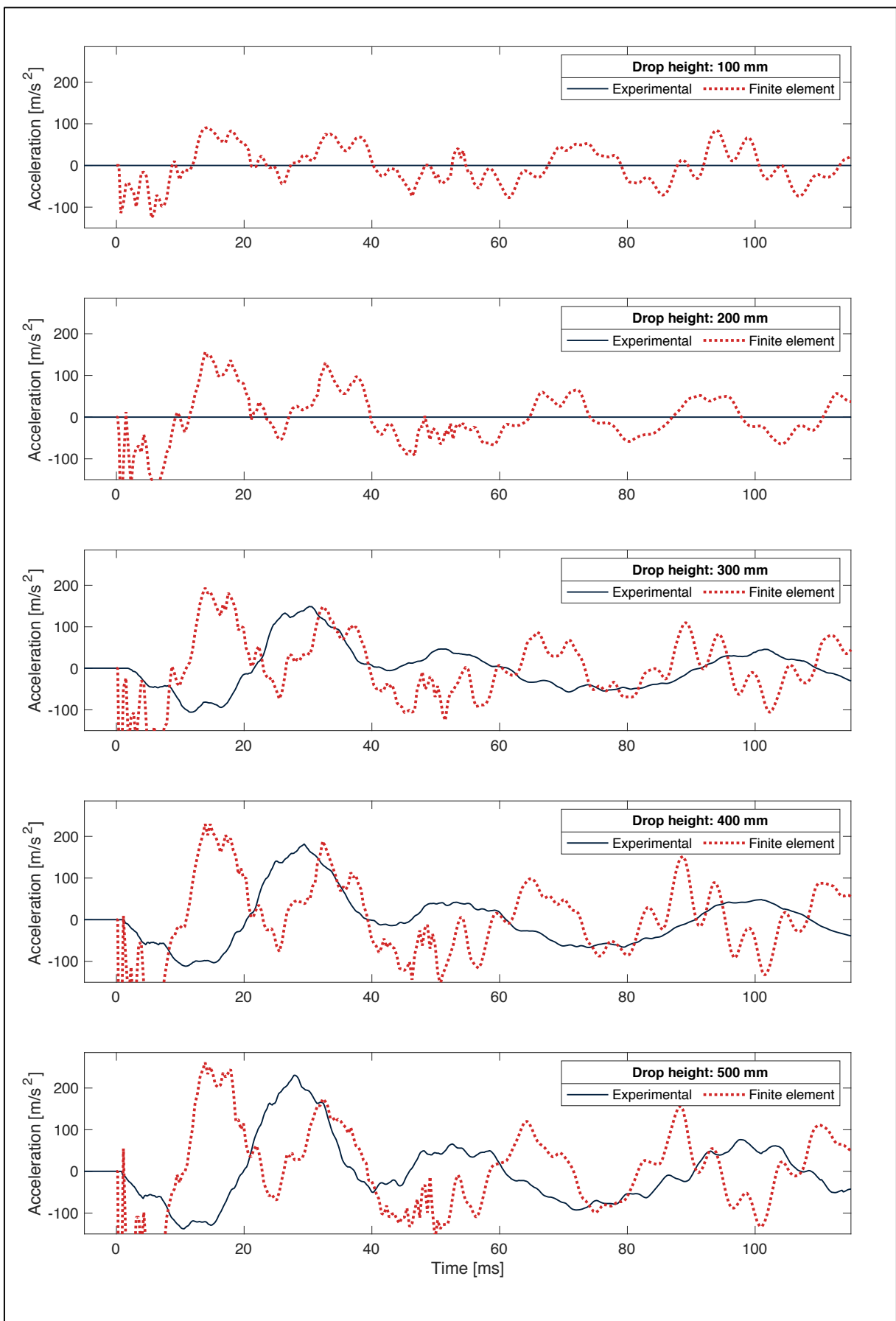


Figure D-8: Collated results for out-of-plane acceleration of glass specimen at impact location for various impactor drop heights. The data set corresponds to clamped laminated specimens with a thickness profile of 5 mm ESG + 1.6 mm SGP + 8 mm ESG.

Annex D Collated Results: Out-of-plane Acceleration of Glass Specimens

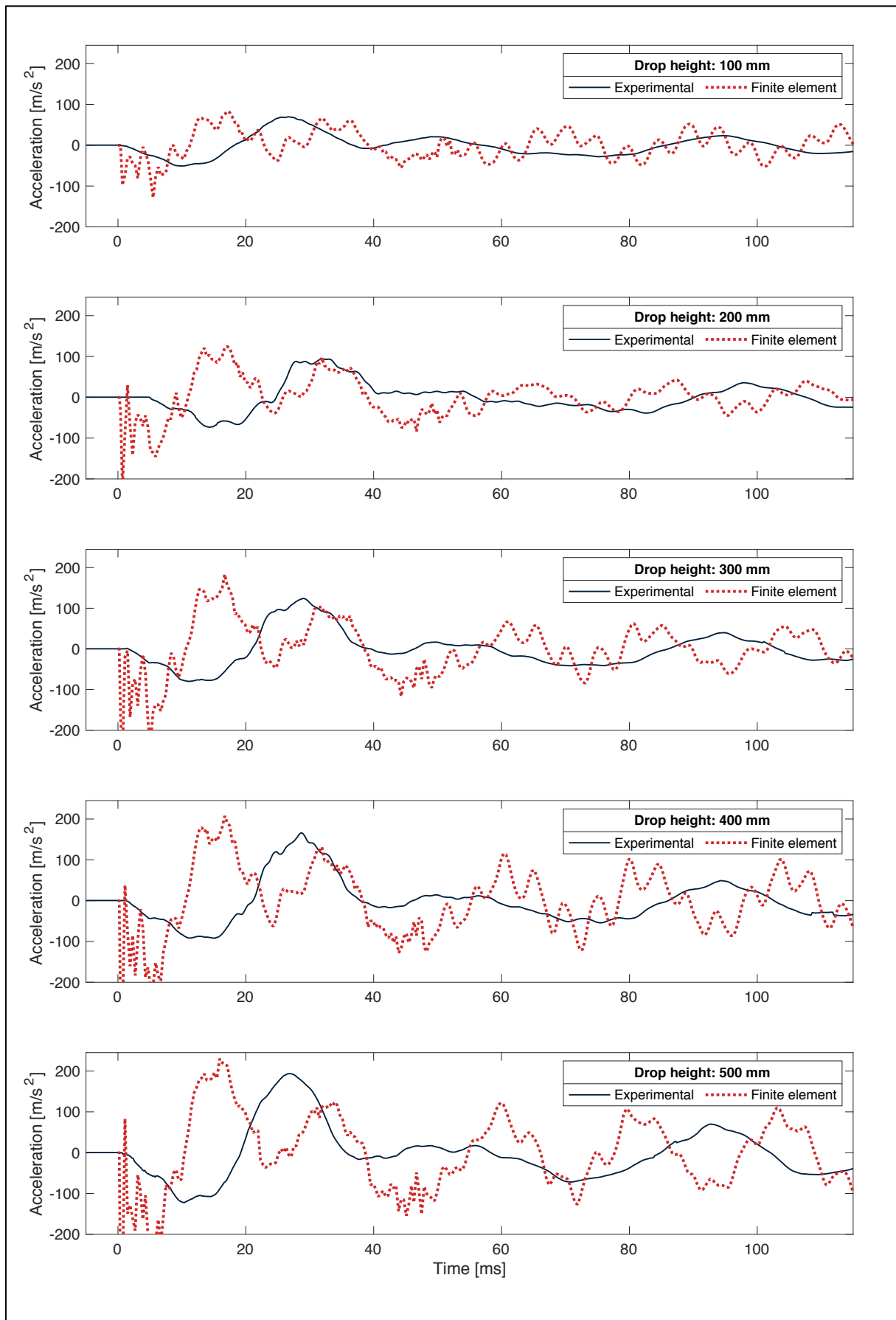


Figure D-9: Collated results for out-of-plane acceleration of glass specimen at impact location for various impactor drop heights. The data set corresponds to clamped laminated specimens with a thickness profile of 6 mm ESG + 1.6 mm PVB + 6 mm ESG.

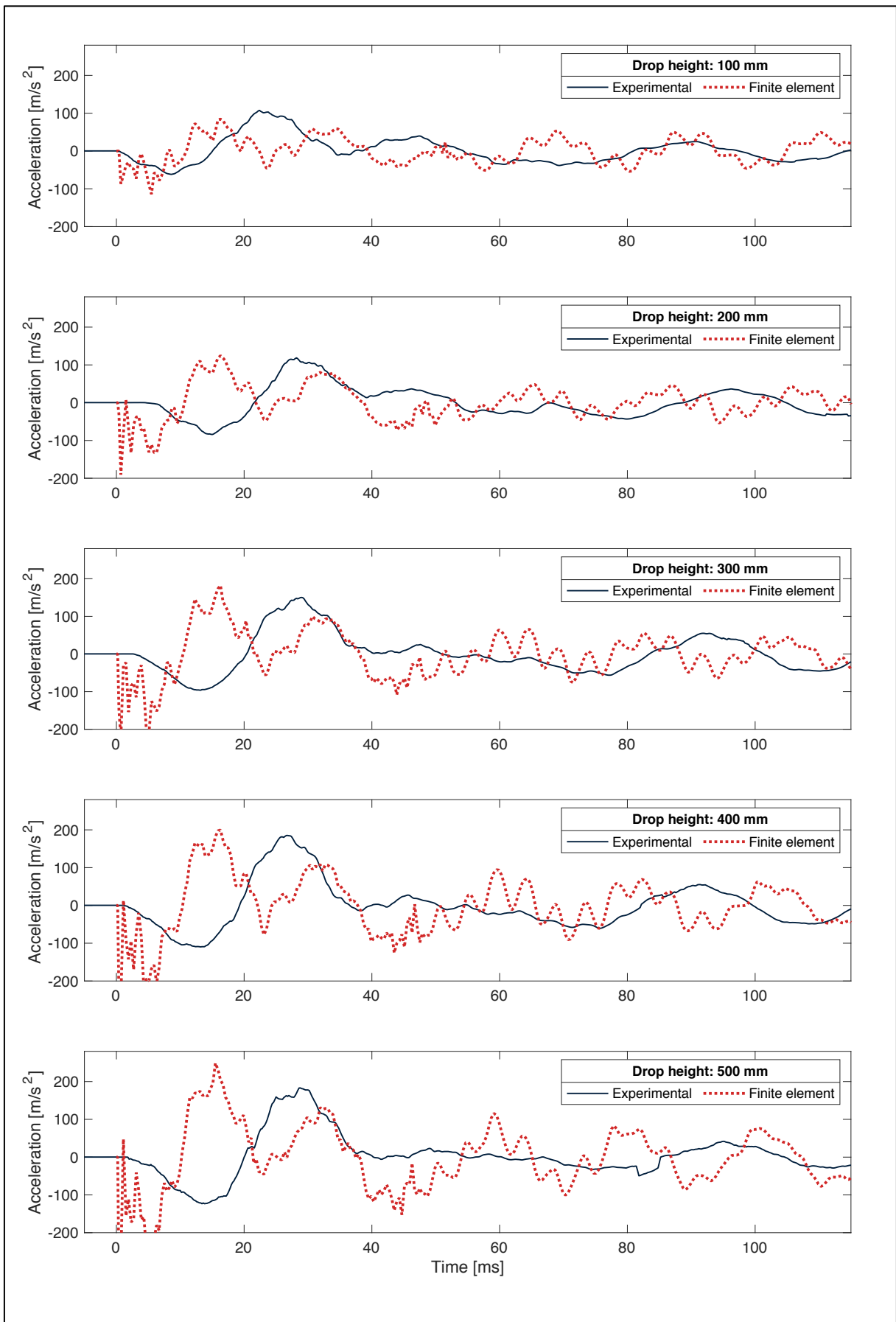


Figure D-10: Collated results for out-of-plane acceleration of glass specimen at impact location for various impactor drop heights. The data set corresponds to clamped laminated specimens with a thickness profile of 6 mm ESG + 1.6 mm SGP + 6 mm ESG.

E Equivalent Static Loads

This Annex tabulates the equivalent static loads used in the equivalent static finite element models. The input data are also presented. The methods used to calculate the loads are derived in Section 9.3.

Annex E Equivalent Static Loads

Table E-1: Equivalent static loads for the simply supported setup.

Profile [mm]	Drop height [mm]	Amplified impactor self-weight static load			Semi-analytical static load		
		δ_{stat} [mm]	n_{DIF} [-]	F_{eq} [kN]	$u_{FE,comp}$ [mm]	k_{stat} [kN/m]	F_{eq} [kN]
8	100	4.3	6.8	3.35	8.8	465	4.10
	200	4.3	9.7	4.74	12.4	465	5.74
	300	4.3	11.8	5.81	15.0	465	6.96
	400	4.3	13.7	6.71	17.1	465	7.95
	500	4.3	15.3	7.50	18.9	465	8.80
10	100	0.6	17.8	8.76	5.6	908	5.05
	200	0.6	25.2	12.38	8.0	908	7.26
	300	0.6	30.9	15.16	9.8	908	8.94
	400	0.6	35.7	17.51	11.4	908	10.33
	500	0.6	39.9	19.58	12.6	908	11.47
12	100	0.4	23.5	11.51	3.8	1570	5.94
	200	0.4	33.2	16.28	5.5	1570	8.62
	300	0.4	40.6	19.93	6.8	1570	10.69
	400	0.4	46.9	23.02	7.9	1570	12.44
	500	0.4	52.5	25.73	8.8	1570	13.88
8 + 1.6 PVB + 8	100	0.4	21.9	10.73	2.1	4760	9.95
	200	0.4	30.9	15.18	3.0	4760	14.52
	300	0.4	37.9	18.59	3.8	4760	17.96
	400	0.4	43.8	21.47	4.4	4760	20.81
	500	0.4	48.9	24.00	4.9	4760	23.44
8 + 1.6 SGP + 8	100	0.4	22.2	10.87	2.0	4890	9.59
	200	0.4	31.3	15.38	2.9	4890	14.06
	300	0.4	38.4	18.83	3.6	4890	17.43
	400	0.4	44.3	21.75	4.1	4890	20.19
	500	0.4	49.6	24.31	4.7	4890	22.72

Table E-1: Equivalent static loads for the bolted setup.

Profile [mm]	Drop height [mm]	Amplified impactor self-weight static load			Semi-analytical static load		
		δ_{stat} [mm]	n_{DIF} [-]	F_{eq} [kN]	$u_{\text{FE,comp}}$ [mm]	k_{stat} [kN/m]	F_{eq} [kN]
6 + 1.6 SGP + 6	100	–	–	–	4.2	1660	7.00
	200	–	–	–	6.1	1660	10.09
	300	–	–	–	7.5	1660	12.42
	400	–	–	–	8.7	1660	14.40
	500	–	–	–	9.6	1660	16.01

Annex E Equivalent Static Loads

Table E-1: Equivalent static loads for the clamped setup.

Profile [mm]	Drop height [mm]	Amplified impactor self-weight static load			Semi-analytical static load		
		δ_{stat} [mm]	n_{DIF} [-]	F_{eq} [kN]	$u_{FE,comp}$ [mm]	k_{stat} [kN/m]	F_{eq} [kN]
5 + 1.6 PVB +	100	–	–	–	7.3	1380	10.00
	200	–	–	–	10.8	1380	14.88
	300	–	–	–	13.6	1380	18.72
	400	–	–	–	15.9	1380	21.96
	500	–	–	–	18.0	1380	24.78
5 + 1.6 SGP +	100	–	–	–	6.9	1400	9.67
	200	–	–	–	10.1	1400	14.16
	300	–	–	–	12.7	1400	17.88
	400	–	–	–	15.0	1400	21.03
	500	–	–	–	17.0	1400	23.79
6 + 1.6 PVB +	100	–	–	–	5.1	2210	11.34
	200	–	–	–	7.8	2210	17.37
	300	–	–	–	10.0	2210	22.20
	400	–	–	–	11.9	2210	26.39
	500	–	–	–	13.6	2210	30.14
6 + 1.6 SGP +	100	–	–	–	4.9	2260	10.97
	200	–	–	–	7.3	2260	16.54
	300	–	–	–	9.4	2260	21.18
	400	–	–	–	11.2	2260	25.23
	500	–	–	–	12.8	2260	28.88

F Stress Deviations

This Annex catalogs the stress deviation factor for each of the models with respect to the stress yielded by the experimental campaign. In other words, a stress outputted by one of the models can be calculated by multiplying the listed deviation factor with the corresponding experimental stress.

The deviations are sorted into tables for each setup.

Note that the results of the semi-analytical model are presented for all setups, but the model is not configured to function realistically for the bolted and clamped setups. They are presented all the same, for the sake of completeness.

Annex F Stress Deviations

Table F-1: Collated stress deviations for the simply supported setup.

Profile [mm]	Drop height [mm]	Experimental [MPa]	High- fidelity FE	Reduced dynamic FE	Equiv. static, method 1	Equiv. static, method 2	Semi- analytical
8	100	81.2	1.05	1.05	0.70	0.83	0.86
	200	115.8	1.02	0.99	0.66	0.77	0.88
	300	139.4	1.01	0.96	0.64	0.74	0.92
	400	159.6	1.05	0.94	0.63	0.71	0.95
	500	172.4	1.02	0.94	0.63	0.70	0.99
10	100	65.5	0.94	0.95	0.83	0.89	0.77
	200	87.4	1.01	1.02	0.87	0.94	0.84
	300	109.8	0.98	0.98	0.83	0.90	0.84
	400	123.1	1.00	0.99	0.83	0.90	0.88
	500	137.7	0.99	0.97	0.82	0.88	0.89
12	100	47.3	0.97	0.96	1.06	1.02	0.80
	200	72.1	0.91	0.92	1.00	0.99	0.77
	300	86.4	0.93	0.95	1.03	1.03	0.81
	400	94.4	0.99	1.00	1.08	1.09	0.87
	500	104.9	1.00	1.01	1.08	1.09	0.89
8 + 1.6 PVB + 8	100	28.4	0.97	0.84	1.49	1.38	0.66
	200	39.8	0.98	0.89	1.53	1.46	0.71
	300	45.6	1.07	0.98	1.64	1.58	0.81
	400	51.2	1.10	1.02	1.70	1.64	0.86
	500	57.7	1.09	1.03	1.69	1.65	0.89
8 + 1.6 SGP + 8	100	25.9	1.00	0.86	1.55	1.36	0.71
	200	37.9	0.98	0.87	1.51	1.38	0.73
	300	43.2	1.06	0.96	1.63	1.51	0.84
	400	48.6	1.09	1.00	1.68	1.56	0.90
	500	53.5	1.11	1.04	1.71	1.60	0.94

Table F-1: Collated stress deviations for the bolted setup.

Profile [mm]	Drop height [mm]	Experimental [MPa]	High- fidelity FE	Reduced dynamic FE	Equiv. static, method 1	Equiv. static, method 2	Semi- analytical
6 + 1.6 SGP + 6	100	33.3	1.22	1.23	–	1.58	0.9
	200	53.2	1.09	1.09	–	1.41	0.8
	300	68.5	1.05	1.05	–	1.34	0.8
	400	76.3	1.09	1.10	–	1.38	0.9
	500	83.4	1.13	1.13	–	1.39	0.9

Annex F Stress Deviations

Table F-1: Collated stress deviations for the clamped setup.

Profile [mm]	Drop height [mm]	Experimental [MPa]	High- fidelity FE	Reduced dynamic FE	Equiv. static, method 1	Equiv. static, method 2	Semi- analytical
5 + 1.6 PVB + 5	100	52.9	1.08	0.98	–	2.17	0.7
	200	74.4	1.12	1.00	–	2.14	0.8
	300	89.1	1.15	1.03	–	2.12	0.8
	400	100.3	1.20	1.06	–	2.11	0.8
	500	110.5	1.21	1.08	–	2.08	0.9
5 + 1.6 SGP + 5	100	47.7	1.14	1.13	–	2.25	0.8
	200	71.5	1.11	1.09	–	2.07	0.8
	300	84.6	1.16	1.14	–	2.10	0.8
	400	95.6	1.21	1.16	–	2.10	0.9
	500	106.0	1.22	1.18	–	2.07	0.9
6 + 1.6 PVB + 6	100	41.9	1.07	1.06	–	2.44	0.7
	200	61.2	1.08	1.06	–	2.51	0.7
	300	70.0	1.19	1.16	–	2.74	0.8
	400	79.4	1.23	1.20	–	2.81	0.8
	500	91.1	1.21	1.18	–	2.75	0.8
6 + 1.6 SGP + 6	100	41.2	1.03	1.02	–	2.28	0.7
	200	59.3	1.06	1.03	–	2.36	0.7
	300	72.3	1.10	1.06	–	2.37	0.8
	400	81.1	1.15	0.95	–	2.54	0.8
	500	89.3	1.18	1.14	–	2.60	0.8